

# **Highly controlled deposition of organic magnets on metal-oxide surfaces**

## **Dissertation**

der Mathematisch-Naturwissenschaftlichen Fakultät  
der Eberhard Karls Universität Tübingen

zur Erlangung des Grades eines  
Doktors der Naturwissenschaften

(Dr. rer. nat.)

vorgelegt von

Reza Kakavandi

aus dem Kermanshah/ Iran

Tübingen

2015



Tag der mündlichen Prüfung: 09.10.2015

Dekan der Math.-Nat. Fakultät: Prof. Dr. W. Rosenstiel

1. Berichterstatter: PD. Dr. Maria Benedetta Casu

2. Berichterstatter: Prof. Dr. Reinhold Fink

Prüfungskommission:

PD. Dr. Maria Benedetta Casu

Prof. Dr. Reinhold Fink

Prof. Dr. Monika Fleischer

Prof. Dr. Udo Weimar



I hereby declare that I have produced the work entitled “*Highly controlled deposition of organic magnets on metal-oxide surfaces*”, submitted for the award of a doctorate, on my own (without external help), have used only the sources and aids indicated and have marked passages included from other works, whether verbatim or in content, as such. I swear upon oath that these statements are true and that I have not concealed anything. I am aware that making a false declaration under oath is punishable by a term of imprisonment of up to three years or by a fine.

Tübingen, den .....

Datum / Date

.....

Unterschrift /Signature



**To my Hannah**



# Contents

List of Figures .....	iv
List of Tables .....	ix
List of Abbreviations and Symbols .....	x
Abstract .....	11
Abstract .....	13
Chapter 1 .....	15
Introduction .....	15
1.1 Introduction .....	15
1.2 The structure of the work .....	18
Chapter 2 .....	19
Theoretical and experimental background .....	19
2.1 Overview .....	19
2.2 Organic molecular beam deposition .....	19
2.3 Growth modes .....	20
2.4 X-Ray Photoelectron Spectroscopy .....	22
2.4.1 Inelastic Mean Free Path .....	26
2.4.2 Quantitative analysis of XPS Spectra .....	29
2.5 Near Edge X-Ray Absorption Fine Structure .....	29
2.5.1 NEXAFS measurements .....	32
2.6 Atomic Force Microscopy .....	34
Chapter 3 .....	37
Materials and characterization techniques .....	37
3.1 Overview .....	37

3.2 Molecules .....	37
3.2.1 NitPyn .....	38
3.2.2 PPN .....	39
3.2.3 Bisnitroxide Diradical Molecule .....	40
3.3 Substrates .....	41
3.3.1 TiO <sub>2</sub> .....	41
3.3.2 SiO <sub>2</sub> /Si(111) .....	43
3.4 Ultra High Vacuum environment .....	44
3.4.1 X-Ray tube and synchrotron radiation .....	45
3.4.2 End-station in BESSY .....	50
3.5 Atomic Force Microscopy .....	50
3.6 Data analysis .....	50
3.7 TiO <sub>2</sub> single crystal .....	51
3.8 SiO <sub>2</sub> /Si(111) .....	52
Chapter 4 .....	53
Results and discussion .....	53
4.1 Overview .....	53
4.2 Clean rutile TiO <sub>2</sub> (110) single crystals .....	53
4.3 Hydroxylated rutile TiO <sub>2</sub> (110) single crystal .....	57
4.4 NitPyn deposition on TiO <sub>2</sub> (110) single crystal .....	59
4.4.1 XPS measurements .....	59
4.4.2 NEXAFS measurements .....	81
4.5 NitPyn deposition on SiO <sub>2</sub> /Si(111) surface .....	89
4.5.1 XPS measurement .....	89
4.6 PPN deposition on SiO <sub>2</sub> /Si(111) .....	101
4.6.1 XPS Measurement .....	102
4.6.2 NEXAFS .....	118

4.6.3 Growth mode.....	122
4.7 PPN deposition on TiO <sub>2</sub> (110) single crystal.....	123
4.7.1 Multilayer.....	123
4.7.2 Growth mode.....	130
4.8 Bisnitroxide Diradical .....	132
Chapter 5 .....	135
Conclusions and Outlook .....	135
5.1 Conclusions.....	135
5.2 Outlook.....	137
Chapter 6 .....	139
References.....	139
Chapter 7 .....	153
Appendix I.....	153
Appendix II .....	155
NitPyn deposited on TiO <sub>2</sub> (110) single crystal.....	158
NitPyn deposited on SiO <sub>2</sub> / Si(111).....	174
PPN deposited on TiO <sub>2</sub> (110) single crystal.....	184
List of Publications .....	215
Credits .....	217
Acknowledgements.....	219
Curriculum Vitae.....	221

# List of Figures

<b>Figure 2.1:</b> Cross section views of the three primary modes of thin film growth including (a)The layer by layer growth mode (FM), (b) The island growth mode (VW) and (c) The layer plus island growth mode (SK) .....	21
<b>Figure 2.2:</b> Schematic view of the photoemission process in the single particle picture. ....	23
<b>Figure 2.3:</b> Schematic representation of the basis of the photo-electric effect .....	24
<b>Figure 2.4:</b> Universal curve of the IMFP for electrons based on experimental data for various materials .....	26
<b>Figure 2.5:</b> Schematic representation of the basis of near edge adsorption fine structure spectroscopy.....	32
<b>Figure 2.6:</b> Representation of $p^*$ orbitals with respect to the electric field vector, $E$ , and the normal of the surface, $n$ . The angle of incidence changes from glancing ( $20^\circ$ ) to normal ( $90^\circ$ ) with the electric field vector oriented perpendicular to the direction of propagation in the $xz$ plane. Orbitals 1 through 3 represent $p^*$ orbitals along the $z$ , $x$ , $y$ axes, respectively.....	33
<b>Figure 2.7:</b> Schematic structure of an AFM experiment. The sample is scanned with an atomically sharp tip .....	35
<b>Figure 2.8:</b> Schematic representation of contact mode (left) and non-contact mode of operation in AFM.....	35
<b>Figure 3.1:</b> Schematic representation of NitPyn. ....	38
<b>Figure 3.2:</b> The conformation of a NitPyn in its crystal.....	39
<b>Figure 3.3:</b> Schematic representation of PPN. ....	39
<b>Figure 3.4:</b> The unit cell of PPN: the $b$ -axis is the long axis.....	40
<b>Figure 3.5:</b> Schematic representation of Bisnitroxide di radical. ....	41
<b>Figure 3.6:</b> Bulk structure of rutile.....	42
<b>Figure 3.7:</b> Ball-and-stick model of two terraces of $TiO_2(110)$ . ....	42
<b>Figure 3.8:</b> A top view of the atomic arrangement for the $(111)$ plane of Si atom. ....	43
<b>Figure 3.9:</b> Schematic of X-ray monochromator.....	46
<b>Figure 3.10:</b> Our XPS station. The apparatus consists of three separately pumped chambers. Left the preparation chamber, in the middle the analysis chamber also on to recognize hemispherical analyzer and right another chamber for preparation of the organic thin-film systems.....	48
<b>Figure 3.11:</b> Schematic view of a planar undulator magnet with alternating polarity of the magnetic field and of the sine like trajectory of the electrons. ....	49
<b>Figure 4.1:</b> Survey spectrum of the rutile $TiO_2(110)$ single crystal. ....	54

<b>Figure 4.2:</b> Ti 2p core level spectrum of the heavily reduced TiO <sub>2</sub> (110) single crystal.....	55
<b>Figure 4.3:</b> O 1s core level spectrum of the TiO <sub>2</sub> (110) single crystal. ....	56
<b>Figure 4.4:</b> Ti 2p core level spectrum of the clean TiO <sub>2</sub> (110) single crystal surface.....	57
<b>Figure 4.5:</b> Ti 2p core level spectrum of the heavily reduced TiO <sub>2</sub> (110) single crystal surface. ...	58
<b>Figure 4.6:</b> Survey spectrum of a nominally 2 nm thin film of NitPyn on the rutile TiO <sub>2</sub> (110) single crystal.....	60
<b>Figure 4.7:</b> C 1s core level spectrum of a 2 nm nominally thick film of NitPyn deposited on TiO <sub>2</sub> (110) single crystal. ....	61
<b>Figure 4.8:</b> C 1s core level spectrum of a 2.5 nm nominally thick film of NitPyn deposited on TiO <sub>2</sub> (110) single crystal. ....	63
<b>Figure 4.9:</b> N 1s core level spectrum of a 2 nm nominally thick film of NitPyn deposited on TiO <sub>2</sub> (110). ....	64
<b>Figure 4.10:</b> Survey spectrum of a 0.3 nm nominally thick film of NitPyn deposited on TiO <sub>2</sub> (110) single crystal. ....	67
<b>Figure 4.11:</b> C 1s core level photoelectron spectra of 0.3 nm (left) and 0.5 nm (right) nominally thick film of NitPyn deposited on TiO <sub>2</sub> (110) single crystal.....	68
<b>Figure 4.12:</b> N 1s core level photoelectron spectrum of a 0.3 nm nominally thick film of NitPyn deposited on TiO <sub>2</sub> (110) single crystal.....	69
<b>Figure 4.13:</b> N 1s core level photoelectron spectrum of a 0.5 nm nominally thick film of NitPyn deposited on TiO <sub>2</sub> (110) single crystal.....	70
<b>Figure 4.14:</b> N 1s core level photoelectron spectra of a 0.3 nm nominally thick film of NitPyn deposited on TiO <sub>2</sub> (110) single crystal with density of Ti <sup>3+</sup> 3d states of (left) 17% and (right) 3%. ....	71
<b>Figure 4.15:</b> O 1s core level spectrum after deposition 2 nm nominally thick NitPyn film.....	72
<b>Figure 4.16:</b> Photoemission spectra of C 1s core level for NitPyn deposited on the TiO <sub>2</sub> (110) with incident photon energies of 330 eV (left), 640 (middle) and 1000 eV (right) .....	75
<b>Figure 4.17:</b> C 1s core level spectra of a 2.5 nm nominally thick film of NitPyn taken at different photon energies. ....	77
<b>Figure 4.18:</b> Photoemission spectra of the N 1s core level for NitPyn deposited on the TiO <sub>2</sub> (110) with incident photon energies of 640 eV (left) and 1000 eV (right).....	80
<b>Figure 4.19:</b> N 1s core level spectra of 0.5 nm (left) and 1.5 nm (right) nominally thick film of NitPyn deposited on TiO <sub>2</sub> (110) single crystal (excitation energy= 1000 eV). ....	81
<b>Figure 4.20:</b> Crystal structure of NitPyn .....	83
<b>Figure 4.21:</b> C-K edge NEXAFS spectra obtained from thin film in multilayer regimes . The spectra are taken in grazing incidence for p-pol (red curve) and s-pol (black curve) polarization. ....	84

<b>Figure 4.22:</b> N-K edge NEXAFS spectra obtained from thin film in multilayer regimes. ....	85
<b>Figure 4.23:</b> C-K edge NEXAFS spectra obtained from thin film in the sub-monolayer regimes (0.3 nm).....	86
<b>Figure 4.24:</b> N-K edge NEXAFS spectra obtained from thin film in the sub-monolayer regimes (0.3nm).....	87
<b>Figure 4.25:</b> Attenuation of Ti 2p XP signal corresponding to the saturation signal as function of time during NitPyn deposition on TiO <sub>2</sub> (110) at RT.....	88
<b>Figure 4.26:</b> 2 $\mu$ m $\times$ 2 $\mu$ m AFM image of a 1 nm nominally thick layer of NitPyn deposited on the surface of TiO <sub>2</sub> (110) single crystal. ....	89
<b>Figure 4.27:</b> Survey spectrum of a 6 nm nominally thin film NitPyn on the SiO <sub>2</sub> /Si(111).....	90
<b>Figure 4.28:</b> C 1s core level spectrum of a nominally 6 nm thick film of NitPyn deposited on SiO <sub>2</sub> /Si(111).....	91
<b>Figure 4.29:</b> N 1s core level spectra of a 6 nm thick film of NitPyn on SiO <sub>2</sub> /Si(111).....	93
<b>Figure 4.30:</b> Room temperature ESR characterization of the samples. Spectra of a nominally 4 nm thick film (lower trace-left) and of the residual powder after sublimation (upper trace-left). ....	94
<b>Figure 4.31:</b> Angular dependence of the linewidth obtained by best fit of the spectra by Lorentzian lineshape for the 4 nm thick film. $\theta = 0^\circ$ when the magnetic field is applied parallel to the Si surface. Angular dependence of the double integral of the Lorentzian curves obtained by best fit of the spectra of the 4 nm thick film: Intensities are normalized as 1.00 at $\theta = 0^\circ$ , when the magnetic field is applied parallel to the Si surface. ....	95
<b>Figure 4.32:</b> C 1s core level spectrum of a nominally 0.6 nm thick film of NitPyn deposited on SiO <sub>2</sub> /Si(111).....	96
<b>Figure 4.33:</b> N 1s core level spectrum of a nominally 0.6 nm thick film of NitPyn deposited on SiO <sub>2</sub> /Si(111).....	97
<b>Figure 4.34:</b> C-K edge NEXAFS spectra of a 15 nm nominally thin film of NitPyn. ....	99
<b>Figure 4.35:</b> Attenuation of Si 2p XP signal corresponding to the saturation signal as function of time during NitPyn deposition on SiO <sub>2</sub> /Si(111)at RT. ....	100
<b>Figure 4.36:</b> 2 $\mu$ m $\times$ 2 $\mu$ m AFM image of a 40 nm nominally thick layer of NitPyn deposited on the surface of SiO <sub>2</sub> /Si(111). ....	101
<b>Figure 4.37:</b> Survey spectrum of a 1 nm nominally thin film PPN on the SiO <sub>2</sub> /Si(111). ....	103
<b>Figure 4.38:</b> C 1s core level spectra of a nominally 3.3 nm thick film of PPN deposited on SiO <sub>2</sub> /Si(111).....	105
<b>Figure 4.39:</b> N 1s core level spectrum of a nominally 3.3 nm thick film of PPN deposited on SiO <sub>2</sub> /Si(111).....	105

<b>Figure 4.40:</b> (Left) EPR spectrum obtained from the solution of the PPN residual powders present in the cell after several cycles of evaporation. (Right). EPR spectrum of a solution obtained from washing one of the thin films with toluene. ....	107
<b>Figure 4.41:</b> C 1s core level spectrum of a nominally 0.5 nm thick film of PPN deposited on SiO <sub>2</sub> /Si(111). ....	109
<b>Figure 4.42:</b> N 1s core level spectrum of a nominally 0.5 nm thick film of PPN deposited on SiO <sub>2</sub> /Si(111). ....	109
<b>Figure 4.43:</b> Thickness dependent C 1s (left) and N 1s (right) core level spectra of the PPN thin films deposited on SiO <sub>2</sub> /Si(111) surfaces. ....	111
<b>Figure 4.44:</b> C 1s core level spectrum of a nominally 1.3 nm thick film of PPN deposited on SiO <sub>2</sub> /Si(111) after 30 min in the vacuum condition. ....	113
<b>Figure 4.45:</b> N 1s core level spectrum of a nominally 1.3 nm thick film of PPN deposited on SiO <sub>2</sub> /Si(111) after 30 min in the vacuum condition. ....	113
<b>Figure 4.46:</b> N 1s core level spectrum of a nominally 1.3 nm thick film of PPN deposited on SiO <sub>2</sub> /Si(111) after 1200 min in vacuum. ....	115
<b>Figure 4.47:</b> Temporal evolution of the Si 2p and C 1s XPS signals for a 1.3 nm nominally thin film after deposition. ....	115
<b>Figure 4.48:</b> C 1s core level spectra of a nominally 1.3 nm thick film of PPN deposited on SiO <sub>2</sub> /Si(111) after 25h of air exposure. ....	117
<b>Figure 4.49:</b> C 1s core level spectra of a freshly evaporated film of PPN deposited on the SiO <sub>2</sub> /Si(111) (blue curve) and after 25 h of air exposure (red curve). ....	117
<b>Figure 4.50:</b> N 1s core level spectra of a freshly evaporated film of PPN deposited on the SiO <sub>2</sub> /Si(111) (blue curve) and after 25 h of air exposure (red curve). ....	118
<b>Figure 4.51:</b> C-K edge NEXAFS spectra obtained from a 12 nm nominally thick film of PPN deposited on SiO <sub>2</sub> /Si(111). ....	120
<b>Figure 4.52:</b> The unit cell of the PPN molecule. ....	120
<b>Figure 4.53:</b> N-K edge NEXAFS spectrum obtained from a 12 nm nominally thick film of the PPN on SiO <sub>2</sub> /Si(111) surface. The spectrum is taken in grazing incidence for p-polarization. ....	121
<b>Figure 4.54:</b> Attenuation of Si 2p XP signal corresponding to the saturation signal as function of time during PPN deposition on SiO <sub>2</sub> /Si(111) at RT. ....	122
<b>Figure 4.55:</b> 2μm × 2μm AFM image of a 12 nm nominally thick layer of PPN deposited on the surface of SiO <sub>2</sub> /Si(111). ....	123
<b>Figure 4.56:</b> Survey spectrum of a nominally 4 nm thin film of PPN on rutile TiO <sub>2</sub> (110) single crystal. ....	124

<b>Figure 4.57:</b> C 1s core level spectrum of a nominally 11.8 nm thick film of PPN deposited on TiO <sub>2</sub> (110) single crystal. ....	126
<b>Figure 4.58:</b> N 1s core level spectrum of a nominally 11.8 nm thick film of PPN deposited on the TiO <sub>2</sub> (110) single crystal. ....	127
<b>Figure 4.59:</b> C 1s core level spectrum of a nominally 0.8 nm thick film of PPN deposited on TiO <sub>2</sub> (110) single crystal. ....	128
<b>Figure 4.60:</b> N 1s core levelspectrum of a nominally 0.8 nm thick film of PPN deposited on TiO <sub>2</sub> (110)single crystal. ....	129
<b>Figure 4.61:</b> Thickness dependent C 1s (left) and N 1s (right) core level spectra of the PPN thin films deposited on TiO <sub>2</sub> (110) single crystals. ....	130
<b>Figure 4.62:</b> Attenuation of Ti 2p XP signal corresponding to the saturation signal as function of time during PPN deposition on the TiO <sub>2</sub> (110) at RT. ....	131
<b>Figure 4.63:</b> 2μm ×2μm AFM image of a nominally 4 nm thick layer of PPN deposited on the TiO <sub>2</sub> (110) single crystal. ....	131
<b>Figure 4.64:</b> Survey spectra of bisnitroxide diradical thin film on the SiO <sub>2</sub> /Si(111) before (red curve) and after 2.5 h deposition (black curve).....	132
<b>Figure 4.65:</b> C 1s core level spectra of bisnitroxide diradical powder (upper panel –right), deposited on the TiO <sub>2</sub> (110) single crystal (upper panel –left) and deposited on the SiO <sub>2</sub> /Si(111) (lower panel). ....	133
<b>Figure 4.66:</b> N 1s core level spectra of bisnitroxide biradical powder (upper panel –right ), deposited on the TiO <sub>2</sub> (110) single crystal (upper panel – left) and deposited on the SiO <sub>2</sub> /Si(111) (lower panel). ....	134

# List of Tables

<b>Table 4.1:</b> Assignment of the measured components by peak fitting analysis in Ti 2p core level spectrum; $E_{B-abs}$ , and $E_{B-rel}$ denote absolute and relative binding energies. ....	55
<b>Table 4.2:</b> Binding energy of the different components of the C 1s core level spectrum and shake-up satellites in NitPyn deposited on the $TiO_2(110)$ single crystal.....	62
<b>Table 4.3:</b> Binding energy of the N 1s core level spectrum and the shake-up satellites in NitPyn deposited on the $TiO_2(110)$ single crystal.....	65
<b>Table 4.5:</b> Energy position and relative intensity of the C 1s core level spectrum and shake-up satellites in NitPyn thin film, with nominally 6 nm thickness deposited on the $SiO_2/Si(111)$ .....	92
<b>Table 4.6:</b> Energy position and relative intensity of the different components of the N 1s core level spectrum and shake-up satellite of NitPyn, with nominally 6 nm thickness, deposited on the $SiO_2/Si(111)$ . ....	93
<b>Table 4.7:</b> Energy position and relative intensity of the different components of the C 1s core level spectrum and shake-up satellites in NitPyn thin film, with nominally 0.6 nm thickness, deposited on the $SiO_2/Si(111)$ . ....	97
<b>Table 4.8:</b> Energy position and relative intensity of the N 1s core level spectrum and shake-up satellite of NitPyn thin film, with nominally 0.6 nm thickness, deposited on the $SiO_2/Si(111)$ . ....	98
<b>Table 4.9:</b> Energy position and relative intensity of the C 1s core level spectrum and shake-up satellites of a nominally 3.3 nm thick film of PPN deposited on the $SiO_2/Si(111)$ .....	104
<b>Table 4.10:</b> Energy position and relative intensity of the different contributions in the N 1s core level spectrum and shake-up satellites of a nominally 3.3 nm thick film of PPN deposited on the $SiO_2/Si(111)$ .....	106
<b>Table 4.11:</b> Energy position and relative intensity of the different contributions in the N 1s core level spectrum and shake-up satellites of a nominally 1.3 nm thick film of PPN deposited on the $SiO_2/Si(111)$ after 1200 min in vacuum.....	114
<b>Table 4.12:</b> Energy position and relative intensity of the different contributions in the C 1s core level spectrum and shake-up satellites of a nominally 11.8 nm thick film PPN deposited on the $TiO_2(110)$ single crystal.....	125
<b>Table 4.13:</b> Energy position and relative intensity of the N 1s core level spectrum and shake-up satellites of a nominally 11.8 nm thick film PPN deposited on the $TiO_2(110)$ . ....	127
<b>Table 4.14:</b> Binding energy of the N 1s core level spectrum and shake-up satellites of a nominally 0.8 nm thick film PPN deposited on the $TiO_2(110)$ single crystal. ....	128

# List of Abbreviations and Symbols

2D	Two - dimensional
3D	Three-dimensional
AFM	Atomic Force Microscopy
BESSY	The Berliner Elektronenspeicherring-Gesellschaft für Synchrotronstrahlung
CHA	Concentric Hemispherical Analyzer
$E_{kin}$	Kinetic energy
$E_b$	Binding energy
EPR	Electron Paramagnetic Resonance
ESCA	Electron Spectroscopy for Chemical Analysis
EF	Fermi Energy
FWHM	Full Width at Half Maximum
FM	Frank- van der Merve
HOMO	Highest Occupied Molecular Orbital
K	Kelvin
LEED	Low Energy Electron Diffraction
OFET	Organic Field-Effect Transistor
OLED	Organic Light Emitting Diode
Linac	Linear Accelerator
LUMO	Lowest Unoccupied Molecular Orbital
NEXAFS	Near Edge X-ray Adsorption Fine Structure
NitPyn	4, 4, 5, 5,-tetramethyl-2-(pyrenyl)-imidazoline-1-oxy-3-oxide, organic radical
OMBD	Organic Molecular Beam Deposition
PES	Photoelectron Spectroscopy
PEY	Partial Electron Yield
PPN	1-[4-(3-oxide-1-oxyl-4, 4, 5, 5-tetramethylimidazolin-2-yl) pyrazol-1'-yl] - pyrene
RF	Radio Frequency
S	Sensitivity Factor
S	Satellite
SCLS	Surface Core Level Shift
SK	Stranski-Krastanov
SOMO	Singly Occupied Molecular Orbital
STM	Scanning Tunneling Microscopy
TEY	Total Electron Yield
UHV	Ultra-High Vacuum
XPS	X-ray Photoelectron Spectroscopy
VW	Volmer-Weber
$h\nu$	Energy of the incident radiation
$\gamma_o$	Surface free energy of over layer – vacuum interface
$\gamma_s$	Surface free energy of substrate – vacuum interface
$\gamma_{s/o}$	Surface free energy of substrate – over layer interface
$\phi$	Work function
$\sigma$	Photoionization cross-section
$\lambda$	Inelastic mean free path
$\lambda$	Wavelength

# Abstract

Organische molekulare Magnete sind eine aufkommende Klasse von Materialien mit möglicher Anwendung in der Spintronik.

Die Adsorptionseigenschaften dieser Quantenmagnete und ihre Verarbeitung zu Dünnschichtsystemen sind sowohl für besseres Grundlagenverständnis der physikalischen Prozesse, als auch für mögliche kommerzielle Anwendungen von großem Interesse.

Der Fokus dieser Thesis liegt auf dem Wachstum von Dünnschichten verschiedener Dicke aus metallfreien organischen Magneten auf der Oberfläche verschiedener Metalloxidsubstrate im Ultrahochvakuum (UHV), sowie der Untersuchung der elektronischen Struktur, sowie der paramagnetischen Eigenschaften der Moleküle.

Wir haben den paramagnetischen Charakter von Dünnschichten eines paramagnetischen Pyren-Derivates des Nitronyl Nitroxid Radikals (NitPyn) auf  $\text{TiO}_2(110)$  Einkristallen erforscht und herausgefunden, dass die paramagnetischen Eigenschaften der NitPyn Moleküle vom lokalen Hydroxylierungsgrad des Substrates abhängen.

Die erste Monolage kann hierbei als Puffer fungieren, auf dem intakte organische Magnete wachsen können.

Mit den spektroskopischen Techniken X-ray photoelectron spectroscopy (XPS) und near-edge X-ray absorption fine structure (NEXAFS), haben wir herausgefunden, dass die paramagnetische Eigenschaften der Moleküle beim Übergang zum Dünnschichtmaterial erhalten bleiben.

Weiterhin haben wir die elektronische Struktur und die paramagnetischen Eigenschaften von NitPyn Dünnschichten, die auf  $\text{SiO}_2/\text{Si}(111)$  aufgedampft wurden, mithilfe von XPS und NEXAFS aufgeklärt. Unsere Resultate sprechen dafür, dass die Moleküle ihren Radikalcharakter sowohl bei Filmdicken von Sub-Monolagen, als auch bei mehreren Molekülschichten behalten. Weiterhin gibt es keine Anzeichen für eine präferierte Orientierung der NitPyn-Moleküle auf  $\text{SiO}_2/\text{Si}(111)$ .

PPN ist das andere Pyrenderivat des Nitronyl-Nitroxid Radikals, das in dieser Arbeit untersucht wurde. PPN Moleküle wurden auf  $\text{TiO}_2(110)$  Einkristallen und  $\text{SiO}_2/\text{Si}(111)$  aufgebracht.

Auch bei diesem Molekültyp wurde die elektronische Struktur und die paramagnetischen Eigenschaften der Dünnschichten untersucht. Die Ergebnisse deuten darauf hin, dass die magnetischen Eigenschaften der Moleküle sowohl bei Sub-Monolagen als auch bei dickeren Schichten auf SiO<sub>2</sub>/Si(111) erhalten bleiben.

Die Filme zeichnen sich durch hohe strukturelle Ordnung, sowie hoher Stabilität, sowohl im Vakuum, als auch an der Luft aus, was dieses Fluorophor-Nitroxid Radikal zu einem vielversprechenden Kandidaten für eine Anwendung in der Elektronik macht.

# Abstract

Purely organic magnetic molecules are a class of emerging materials interesting for their potential use in spintronics. Thin film processing and the mechanism of adsorption of these class of quantum magnets is of great interest whether one considers possible commercial applications or fundamental physical interactions.

This thesis focuses primarily on the growing of thin films of metal-free organic magnets on the surface of different metal-oxide substrates in ultra-high vacuum (UHV) in a wide range of thickness. Their electronic structure and the paramagnetic character of the molecules were investigated.

We explore the paramagnetic character of thin films of a paramagnetic pyrene derivative of the nitronyl nitroxide radical (NitPyn) of NitPyn radical deposited on  $\text{TiO}_2(110)$  single crystals. We find that the molecules keep/lose their paramagnetic character depending on the local substrate hydroxylation. The first molecular layer may act as a “buffer” on which intact organic magnets are grown.

By using X-ray photoelectron spectroscopy and near-edge X-ray absorption fine structure (NEXAFS) spectroscopy, we find that the paramagnetic character is kept going from molecule to material. In particular, we evidence the transitions related to the singly occupied molecular orbital, as expected in open shell materials.

We also study the electronic structure and paramagnetic nature of thin films of NitPyn deposited on  $\text{SiO}_2/\text{Si}(111)$  by using XPS and NEXAFS. Our study implies that the molecules keep their radical character in the sub-monolayer and multi-layer regime of thickness. We also find that there is no preferential orientation in NitPyn thin films on  $\text{SiO}_2/\text{Si}(111)$ .

PPN is the other pyrene derivative of the nitronyl nitroxide radical that we have investigated which was deposited on  $\text{TiO}_2(110)$  single crystals and  $\text{SiO}_2/\text{Si}(111)$ . Also in this case, the electronic structure and the paramagnetic character of thin films of deposited PPN were investigated, identifying that the magnetic properties of the molecules are preserved on  $\text{SiO}_2/\text{Si}(111)$  in the low coverage and high coverage. The films are characterized by a high structural order, coupled to strong vacuum and air stability that make this fluorophore-nitroxide radical an extremely promising candidate for applications in electronics.



# Chapter 1

## Introduction

### 1.1 Introduction

We live in the age of digital and information revolutions which have a causal relationship to the design of organic devices capable of performing a wide spectrum of functions as well as appearance of novel devices ranging from light portable electronic devices, computers and magnetic levitation trains to wearable devices and intelligent machines [1-12].

Magnetic materials, as fundamental components of the processing units of the majority of modern devices, have influential impacts on the expanding of modern technologies. Magnets have long been employed, to a large extent, since the beginning of human civilization and their extraordinary important role plus their applications are recently undergoing rapid development. Over the past several decades, by broadening the spectrum of their applications, in particular after discovering the capability of magnetism in the information processing and long-term data storage, magnets have become active and crucial components in our modern life [13].

Development of the knowledge of magnetism is continuing and this field is still in the focus of attention of a huge number of scientists. Suitable strategies in introducing magnetic materials comprised in part or wholly molecular components, in which, data could be stored, transmitted, and retrieved as alternative approach to conventional classic magnets [14-16]. The end of the last millennium has seen the correlation between unravelling different aspects of magnetism and emerging fields such as molecular electronics. Spintronic and organic electronics are two disciplines with revolutionary potential ranging from computing at the molecular level and increasing integration densities to quantum information processing [17].

Organic magnets are defined as the molecule exhibiting bulk magnetic ordering and possessing unpaired electron spins which are responsible for magnetic properties of the molecule [18]. Molecular magnets are on the one hand, the ultimate few nanometers object through which

electronic transport can take place, being in the nanometer scale, molecules share many characteristics with atoms, such as discrete quantized energy spectra and angular momentum. On the other hand they are large enough to be chemically attached to the other molecules with which they can exchange electrons [19]. Organic based magnets are especially interesting because magnetism, in this case, originates from unpaired electron spins residing in p-orbitals which are spatially delocalized over specific parts of the molecules and contribute to the magnetic ordering. In other words, unpaired electrons participate in coordinated quantum-mechanical behavior which means that the molecule coordinate spins of the unpaired electrons to produce magnetism and is thus quantum mechanical in nature [20,21].

By considering the aforementioned properties of the molecular magnets, they can be employed, on one hand, to bridge spintronic and molecular electronics as two rapidly progressing paradigms on the other, to satisfy a variety of new needs in modern technologies. For example, organic molecules, as the fundamental building blocks of the molecular magnets, are structurally and electronically very flexible. Due to the wealth of exciting possibilities offered by organic molecules, one of the main ultimate goals of molecular magnetism can be packing reconfigurable quantum centers, aligning magnetic moments of the molecules over large volumes to harness the collective magnetic properties of spin carriers in conjunction with devising molecular-scale electronic and magnetic devices based on the spin of molecules [22,23].

Organic radicals are a class of organic based magnets which consist of light elements like C, H, N, O, and S. A promising property of the metal-free magnets is their stability against chemical reaction and charge transfer in these open-shell structures originating from the delocalization of the unpaired electrons over the radical part of the molecule [24]. Since 1991, after realizing the  $\beta$  phase of p-nitrophenyl nitronyl nitroxide ( $C_{13}H_{16}N_3O_4$ ) as the first example of a metal-free ferromagnet, these class of organic based magnets have been the subject of intense research [25,26]. These magnetic properties can be manipulated by controlling their synthesis. As a result, an intense effort has been devoted to systematically synthesize a wide range of purely organic magnets. In parallel, analytical tools such as spectroscopic and microscopic techniques in the quest of characterization and imaging of the metal-free magnetic molecules have been introduced and explored [27,28].

By considering their magnetic properties, their stability together with their purely organic nature, the technological applications of these class of molecules is easily foreseen. In this regards, the use of individual purely organic magnetic molecules has gained much attentions as the fundamental units of possible new generation of organic devices, such as dense and efficient memories, spin probes, spin labels and organic batteries [29]. The most promising aspects is the ease of synthesis and isolation, beside the facile tailoring of the properties of the molecules [30,31]. Organic magnets of mesoscopic dimensions were previously organized on the surfaces as single molecule and were investigated as single molecule or single crystal, in wet environment [32,33]. Although purely organic magnets have experienced rapid developing, this area is still young. An appealing step is the use of their capabilities in the field of information storage and sensors. Thus, it is time to develop a strategic use of metal-free molecular magnets in a nanoscale assembly. The assembly of organic molecular magnets offers the opportunity to get an insight into the electronic structure and the magnetic character of the molecule as thin films in the solid state by investigation of the intermolecular interactions and molecule-surface interactions [34-36]. This correlation will enable new opportunities to link structural thin film properties to device performance.

However, it has been reported that the intermolecular interactions, substrate temperature and molecule-surface interactions have influential impacts on the thin film formation [37,38] while nucleation and island dimensions are influenced by preparation parameters [39,40]. The substrate morphology may determine also the arrangement of the molecules in the thin films [41-43]. Therefore, controlling preparation parameters, nucleation and growth of thin films of purely organic magnets is of crucial importance to get a deep insight into the thin film properties and, ultimately, to step towards applications.

In the past, the awareness of instability and high reactivity of this class of magnetic molecules may have been the reason why little attention is drawn to study the evaporation of organic radicals [41,44,45]. Overcoming this fundamental obstacle would facilitate device fabrication. This is a strategic step because fulfilling this mission may lead to the integrating novel generation of the molecular magnets and promising quantum sensors; something between science fiction and state -of-the art [46].

## 1.2 The structure of the work

In this work, we investigate the electronic structure and magnetic properties of thin film of pyrene-derivatives of the nitronyl nitroxide radical (NitPyn), 1-[4-(3-oxide-1-oxy-4, 4, 5, 5-tetramethylimidazolin-2-yl) pyrazol-1'-yl]-pyrene (PPN) and 1,2,8,9-tetrahydro-2,2,4,4,6,6,8,8-octamethyl-4H,6H-benzo[1,2-d;5,4-d']bis-(1,3-oxazine)-1,9-dioxy deposited on rutile TiO<sub>2</sub>(110) single crystals and SiO<sub>2</sub>/Si(111) wafer by means of X-ray Photoelectron Spectroscopy (XPS), Near Edge X-ray Absorption Fine Structure (NEXAFS) Spectroscopy and Atomic Force Microscopy (AFM).

Chapter II introduces the employed techniques and the necessary theoretical background related to the applied experimental techniques. Chapter III starts by introducing the utilized molecules followed by reviewing the instrumentation, the sample preparation and data processing. Chapter IV comprise the results of XPS, NEXAFS and AFM measurements and the subsequent discussions. In this case, the chapter is divided into three parts. Each part starts with the investigation of the electronic structure with the analysis of the core level spectra and it is followed by the analysis of the NEXAFS spectra focusing mainly on magnetic character and orientation of the molecules. Finally, each part ends with the study of the growth mode and the morphology by means of XPS and AFM. Chapter V concludes this work with a summary of the obtained results and gives an outlook the work.

# Chapter 2

## Theoretical and experimental background

### 2.1 Overview

This chapter focuses on the physical background related to the applied experimental techniques to the extensive investigation of the electronic, magnetic and chemical properties of the thin films, as well as, the theoretical basics.

Section 2.2 describes the basic physical background of the organic molecular beam deposition (OMBD), which has been utilized for thin film preparation. The chapter is followed by description of the mechanism of thin film growths (Section 2.3). Sections 2.4 to 2.6 present the principles of spectroscopic techniques including XPS and NEXAFS and microscopic technique such as AFM that has been used for thin film characterization.

### 2.2 Organic molecular beam deposition

Organic molecular beam deposition (OMBD) is a physical vapor deposition technique being employed for producing high quality thin films of rather small molecules in a wide range of thicknesses from sub monolayer to multilayers [<sup>47-49</sup>].

The essence underlying OMBD consists of a molecular beam, while gas phase of molecules are distributed angularly, produced by vaporization of the organic solid source in ultra-high vacuum (UHV) and deposit on the substrate without undergoing intermediate chemical interactions [<sup>50,51</sup>]. UHV is the essential environment for OMBD to get a good operational growth control [<sup>52</sup>].

Evaporation starts by heating up the effusion cell, thereby precision-heating of crucible containing the highly purified condensed organic source occurs while the cell is maintained at a fixed temperature during evaporation. The evaporated molecular beam passes through an orifice [<sup>53</sup>], while the molecules are in thermodynamic equilibrium with the melted molecules [<sup>54</sup>]. All the molecules must have sufficiently high vapor pressure to allow evaporation from a Knudsen cell

[<sup>55</sup>]. By decreasing the density of the gaseous molecules (presented in the path of molecular beam) in UHV, the mean free path of the sublimated molecules which has to exceed the cell-substrate distance, considerably increases. Hence the evaporant travels a straight line towards the substrate. The evaporated molecules are deposited on an atomically clean substrate at room temperature (RT). It allows obtaining ultra-high pure thin films. Controlling and monitoring the rate of deposition, by applied electrical current and a quartz microbalance, yields homogenous thin films. The effusion cell is the heart of molecular beam deposition, to achieve flux stability and uniformity and also material purity [<sup>56</sup>]. Temperature fluctuations in the range of  $\mp 2\text{K}$  during evaporation result in stability of the organic molecular deposition. The cell has to be outgassed in vacuum environment and the substance is purified using thermal gradient sublimation [<sup>57</sup>].

## 2.3 Growth modes

Organic thin films are grown on a broad spectrum of substrates by OMBD. The growth mode of the organic thin films are classified typically in three major modes due to different ways of condensation of the vapor phase of the substance on the surface. Growth mode and molecular orientation of the organic molecules deposited on the surface of the substrates have influential impact on the electronic structure of the molecule [<sup>38, 58, 59</sup>].

Depending on competition between surface free energy and interface energy of the molecule and the substrate, thin films grow following [<sup>60, 61</sup>]:

- 1: The layer by layer growth mode (or Frank-van der Merve, FM)
- 2: The island growth mode (or Volmer-Weber, VW)
- 3: The layer plus island growth mode (or Stranski-Krastanov, SK)

These three modes of thin film growth is shown in the Figure 2.1.

In the Frank-van der Merve growth mode, the interaction between surface and layer atoms/molecule are stronger than the interatomic interactions between the neighboring atoms/molecule in the film [<sup>62, 63</sup>]. The initial layer spreads over the substrate entirely. This means that, the initial layer wets the surface of the substrate completely due to very low contact angle which is equivalent to the high surface energy of the substrate [<sup>37, 64</sup>]. Wetting lowers the surface energy

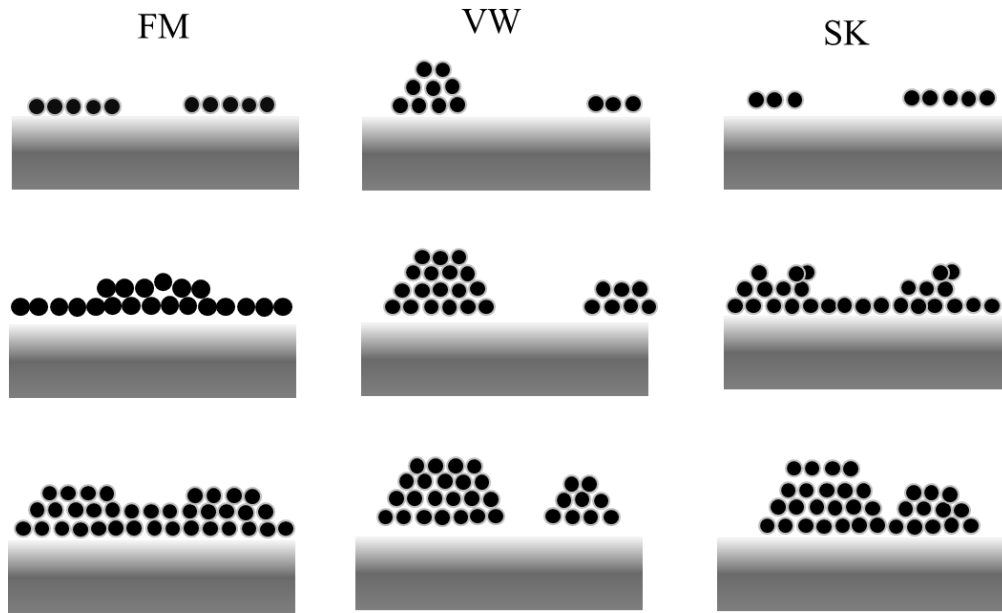


**Figure 2.1:** Cross section views of the three primary modes of thin film growth including (a) The layer by layer growth mode (FM), (b) The island growth mode (VW) and (c) The layer plus island growth mode (SK) [68].

of the substrate so that, results in formation of two-dimensional thin film [65,66]. The new layer assembles only when the growth process of the previous strained layer is completed. This kind of atomic/ molecular assembly result in smooth thin film formation [67].

In the Volmer-Weber growth mode, neighboring atoms or molecules in thin film are coupled to each other more strongly than to the atoms or molecules of the surface. In other words, the growing film does not wet surface of the substrate entirely therefore, the film itself minimizes its surface. In the VW growth mode, low surface energy of the substrate is favorable condition for three-dimensional growth of the film [69].

The Stranski-Krastanov growth mode is an intermediary process between FM and VW modes [16]. The S-K growth mode consists of two stages. This mode starts initially by formation of one or several 2D layers (FM modes) because of high surface energy of the substrate and due to either strain induction in thin films or any other factor perturbing the monotonic decrease in  $E_b$ , it transits to 3D island formation (VW modes) when exceeding a critical thickness [70]. In this mode of thin film growth, lattice spacing of the ultrathin layers and the substrate are not identical [71]. Since surface energy of the substrate is higher than sum of the surface energy of the

film and the interfacial energy, the first deposited layer(s) wets the surface entirely. After reaching thickness to supercritical value, by vanishing interfacial energy, the surface energy of the substrate approaches the surface energy of the deposited film hence results in 3D islanding of the arriving molecules on top of initial thin films [65].

The different growth modes can be explained in terms of surface or interface energy criteria,  $\gamma$ .

$$\gamma_s = \gamma_{s/o} + \gamma_o \cos \phi \quad (2.1)$$

$\gamma_o$ : surface free energy of over layer – vacuum interface

$\gamma_s$ : surface free energy of substrate – vacuum interface

$\gamma_{s/o}$ : surface free energy of substrate – over layer interface

If  $\phi = 0$  or  $\phi > 0$  then the thin film grows in layer or island mode, respectively.

## 2.4 X-Ray Photoelectron Spectroscopy

The electromagnetic radiation – matter interaction is the basis of a large variety of spectroscopies. In this type of interaction, depending on the frequency of the electromagnetic radiation, three events are expected to occur: reflection, propagation of the electromagnetic radiation through the material and absorption. In particular, the interaction of the electromagnetic radiation with matter is the source of several phenomena such as photoelectric effect, Thomson scattering and Compton scattering [72].

Photoelectron spectroscopy (PES) is a standard analytical technique inspired by the photoelectric effect [73,74]. Owing to its capability to provide both qualitative elemental identification and quantitative composition of the outer 10 nm or less of any solid surface, PES has been extensively used in the past decades and is still vastly employed in order to unravel electronic structures, bonding states of the elements and chemical properties of the matter. The surface sensitivity of PES arises from the relatively short inelastic mean free path (IMFP) of the electrons in the solids. The universal mean-free path curve indicates that this number is few tens of angstroms for XPS [75].

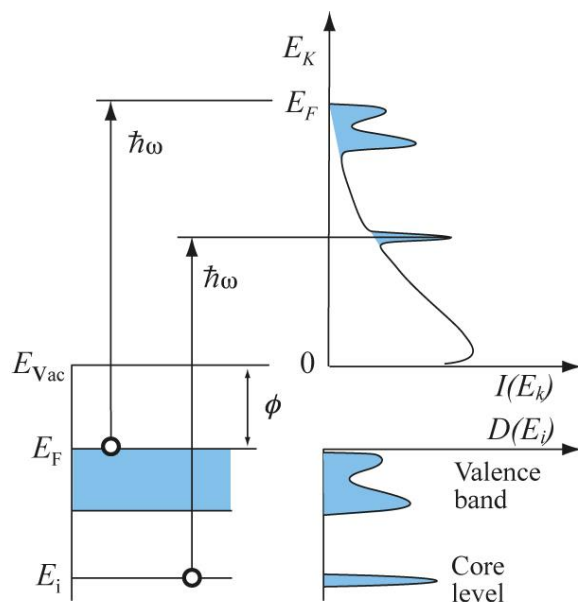


**Figure 2.2:** Schematic view of the photoemission process in the single particle picture [76].

In a simple description, radiation will be absorbed for incident energy larger than the  $E_b$  of the emitted electron in the system. Referring to the photoelectric effect, absorption a quantum of energy with frequency greater than a critical threshold frequency by an electron initially bound to an atom leads to transferring energies from photons to electron [77]. In other words, excitation occurs only if the energy of the electromagnetic radiation is greater than the  $E_b$  of the photoelectrons. This electron is referred to as “photoelectron”.

Photo-excited electrons from valence and core energy levels possess enough energy to exceed the work function of the specimen to be ejected out of the atom or solid towards vacuum. The kinetic energy of the emitted electrons is the quantity that will be measured in XPS measurement.

For theoretical description of a photoemission process. In this thesis, we employ a single particle model rather than a many-body approach in order to avoid the complexity of the many-body approach [78]. In this model, the “sudden approximation” is used which assumes that during photo-ejection process, an electron is removed from the (n-1) electron system in an infinitely short

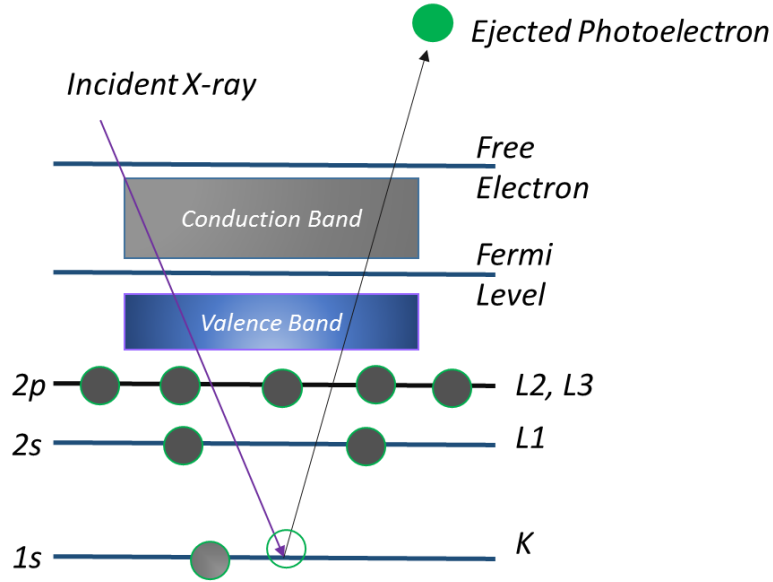


**Figure 2.3:** Schematic representation of the basis of the photo-electric effect [80].

time that only negligible interaction between final states and initial states exist [78, 79].

The emitted electrons have kinetic energy  $E_{kin}$  determined by Einstein relationship [81]

$$E_{kin} = h\nu - E_b \quad (2.2)$$

with  $h\nu$  being the energy of the incident radiation (a known value) and  $E_b$  being the binding energy of the electron in the atom.

The  $E_b$  of the atomic orbital from which the electron originates is mainly determined by measuring the  $E_{kin}$  of the electrons departing the system. Radiation will be absorbed for incident energy larger than the  $E_b$  of the emitted electron in the system. Referring to the photoelectric effect, electrons are emitted only when the energy of the electromagnetic radiation is greater than the  $E_b$  of a specific electron in different chemical environments. This is not identical and it changes by environment. Since  $h\nu$  is a fixed parameter for a given excitation energy during photoemission phenomena,  $E_{kin}$  of the emitted electron is higher, lower its  $E_b$  and vice versa. While for electrons from a certain element in a certain chemical state, the  $E_{kin}$  of the photoelectrons varies with excitation energy of the incident radiation.

$E_b$  can be written as the energy difference between the (n-1) electron final state and the (n) electron initial state called by  $E_f(n-1)$  and  $E_f(n)$  respectively<sup>[82]</sup>:

$$E_b = E_f(n-1) - E_i(n) \quad (2.3)$$

By assuming that no rearrangement takes place in the system, the difference between final state and initial state would be the negative orbital energy of the core level,  $\epsilon_{kt}$  this energy is the basis of the Koopmans' theorem <sup>[20, 83]</sup>. Koopmans' theorem states that ionization energy out of orbital  $\epsilon_{kt}$  is given by  $-\epsilon_i$  provided that the orbitals of the ions are identical to those of the neutral ground states <sup>[84]</sup>. Since, photoelectron emission results in a core-hole creation, as a consequence, the system reacts to the existence of the created core-hole by minimizing the energy of its ionized state. Energy reduction caused by this rearrangement is the relaxation energy of the electronic wave function of the molecule (relaxation energy) <sup>[85]</sup>.

The photoemission process is intrinsically a quantum physical phenomenon. In attempt to understand photoemission, this process has to be described in term of a quantum physical approach. Therefore, in the semi-classical model, photoemission process is divided into three sequential steps: <sup>[86]</sup>

- 1: Photo excitation of the electron inside the bulk.
- 2: Diffusion of the excited electron to the surface of the bulk.
- 3: Transmission of the electron into the vacuum through the surface.

Only those electrons that have enough  $E_{kin}$  are able to escape from the surface of the material toward vacuum level without energy loss.

A XPS spectrum is a plot of the number of photoelectrons detected by a detector versus the  $E_b$  of the electronic states of atom. Each element produces a characteristic set of spectroscopic lines at characteristic  $E_b$  <sup>[87]</sup>. The intensity of the peak corresponds to the number of the detected electrons and to the amount of the element while its  $E_b$  is related to the environment of the atoms.

## 2.4.1 Inelastic Mean Free Path

In XPS measurements, the sample is subjected to irradiation of the photons in the X-ray range. The limited distance which X-rays can readily travel through the sample is the penetration depth. While X-rays with certain amount of energy are able to penetrate into the solids, electrons exhibit remarkably less penetration depth [88]. Penetration depth for X-ray and electrons that carry the same amount of energy in the same solid are approximately 1000 nm and 10 nm, respectively [88].

Penetration depth is defined as the depth from which 95% of the electrons are scattered before reaching the surface of the sample. Penetration depth is equal to three times IMFP [89]. A fraction of the photo-emitted electrons are adsorbed by the material when they travel through the solid, therefore, the number of escaped electrons decreases by increasing the thickness of the layers in the path of the solid that the electron pass through. The decrease in the number of photo emitted electrons as a function thickness is described by the Beers law.

The IMFP of a photoelectron in a solid is the thickness of matter in which the incident electron flux is attenuated by the factor of  $1/e$  or on the other hand  $1/e$  of initial electrons with a given energy lose their energy during traveling this distance[90]. IMFP is dependent on the  $E_{kin}$  of the electrons. It varies in the range of 1-3.5 nm for Al  $K_{\alpha}$  radiation [91] so the penetration depth is in the range of 3-10 nm. IMFP has been used to quantitatively interpret the inelastic scattering of the detected electrons. This parameter is used to describe surface sensitivity of the XPS technique [89, 92, 93].

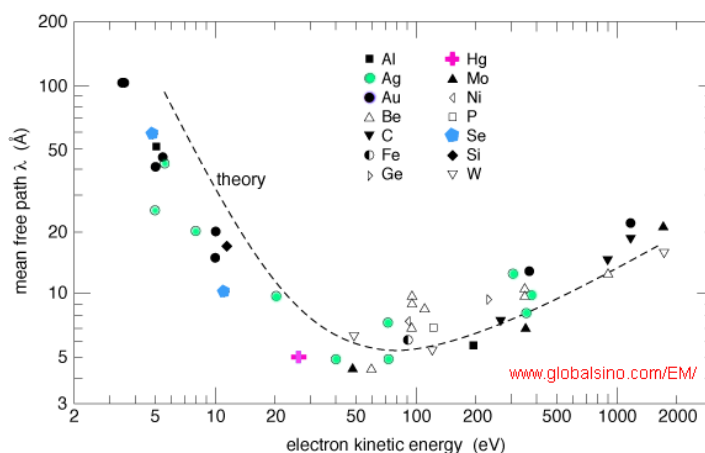


**Figure 2.4:** Universal curve of the IMFP for electrons based on experimental data for various materials [94].

The photogenerated electrons, depending on the depth that they come from, are classified into three groups:

- 1: The electrons which are emitted from the atoms at the surface. These electrons have not lost any energy during escaping from surface of the solid. These kind of electrons contribute to the main line in the XPS spectra.
- 2: The photo emitted electrons that lost some fraction of their  $E_{kin}$  because of inelastic scattering during travelling through the matter. These kinds of electrons still have sufficient energy to escape from the surface of the material. The contribution of these electrons is exhibited in the background signal.
- 3: The electron that lost their energy entirely.

Therefore, the signal at a given electron energy stems from both kinds of electrons, i.e. electrons which their  $E_{kin}$  is maintained and the electrons that undergo different inelastic interactions with the atoms which constitute the sample. The later results in a continuously stepped background in the spectra. Dealing with the background has been one of the primary problems in quantitative chemical analysis of XPS spectra including elemental identification and quantification of the chemical states [<sup>95, 96</sup>]. Several different strategies have been employed to define the background via accounting correctly the contribution of inelastically scattered photoelectrons. Some of the most used are:

- 1: Linear routine
- 2: Shirley routine
- 3: Tougaard routine

In this thesis, we have used the linear routine and the model purposed by Shirley for quantification of all the core level photoemission spectra [<sup>97</sup>].

The emitted electrons from the sample are collected with an analyzer and ultimately, they will be analyzed with respect to their  $E_{kins}$ . X-ray photoelectron charging causes decreasing the  $E_{kin}$  of the ejected electrons by the electronic field and consequently shifts the photoelectron spectra to the higher  $E_b$  direction (a few eV). Broadening of the XPS spectrum is another influence

of the charging effect. This positive potential is determined by the photoelectric current of the electrons leaving the sample, the current through the sample holder toward the investigated sample as well as the flow of the Auger and secondary electrons from the Al-window onto the sample. In addition to the photoelectron and Auger electron peak, other peaks are detected. Following: [98, 99].

- 1: Satellite peaks (without monochromator)
- 2: Plasmon loss peak shake-up
- 3: Shake-off, and multiple splitting [100]

Whenever an atom is subjected to the X-ray irradiation with enough energy, core orbitals of the atom are photo-ejected which leads to the core-hole formation. Introduction core-hole into the electronic structure of the photoelectron emitting atom results in to the sudden changes in the atomic potential. These sudden changes are associated with excitation of valence electrons from the highest occupied molecular orbital (HOMO) to the lowest unoccupied molecular orbitals (LUMO). The sudden rearrangement of outer shell electrons in atom is called relaxation [101]. Photo-ejection of the core orbitals results in increasing nuclear charge of the atom and ultimately the coulombic potential experienced by the less tightly bound orbitals in the atom alters suddenly [102]. The remaining electrons respond to the increment in atomic potential dynamically via a substantial reorganization of the electrons in photoemission process [103]. This multi electron excitation is usually explained in terms of the sudden approximation [104, 105]. In this context, the final state is represented not only as the normal hole state but as combination of this state and excited initial state-wave functions [99, 106].

Shake-up and shake-off process are known as two main final states effects in the XPS. Valence electron transition during the initial core ionization gives rise to the shake-up when relaxation phenomenon involves excitation of one electron to a higher level which was previously unfilled [107]. Concerning  $E_{\text{kin}}$  loss of the photoelectrons, relaxation results in an excited state a few eV above the ground state thus shake-up satellite appears as a peak at few eV higher  $E_b$  with respect to the main peaks [108].

Shake-off takes place when valence electrons are ionized completely then excited to an unbounded continuum states and appears as a continue energy distribution in background [103].

### 2.4.2 Quantitative analysis of XPS Spectra

In order to quantitatively analyzing the XPS spectra, the intensity of the obtained peak have to be converted to the atomic concentrations. There are many factors that have impact on the intensity of the signal for a given photon energy and consequently the quantifying XPS: The cross-section for emission, the escape depth of the electron emitted from the atom, number of photo-emitting atoms and the transmission function of the spectrometer [109]. The intensity of the signal is referred to as the integrated area under the peak following the subtraction of a background. The relation between the aforementioned parameters and the intensity of the XPS signal is obtained according to the following formula [110].

$$I(h\nu, E) = \Phi_0 \cdot \sigma(h\nu) \cdot n \cdot A_{ij} \cdot \lambda(E) \cdot T(E), \quad (2.5)$$

where  $\lambda$  is the IMFP,  $\Phi_0$  is instrumental constant,  $T$  is transmission function,  $n$  is the number of atoms,  $A_{ij}$  is the angular asymmetry factor of orbital  $j$  of element  $i$  and  $\sigma$  is the photoionization cross-section which represents the probability of the ionization of a subshell [110].

By considering ( $I_1 / I_2$ ), the ratio between two elements (element1 and element2), as following:

$$I_1 / I_2 = N_1 \cdot \sigma_1 \cdot \lambda_1 \cdot T_1 / N_2 \cdot \sigma_2 \cdot \lambda_2 \cdot T_2, \quad (2.6)$$

the atomic percentage of the elements concerned can be determined by dividing the peak area by the sensitivity factor ( $S$ ) and expressing it as a fraction of the summation of all normalized intensities

$$N_1 / N_2 = (I_1 / S_1) / (I_2 / S_2), \quad (2.7)$$

where  $S$  is the sensitivity factor  $S_i = \sigma_i \cdot \lambda_i \cdot T_i$

## 2.5 Near Edge X-Ray Absorption Fine Structure

NEXAFS spectroscopy is a synchrotron-based technique that allows quantitative elemental analysis of the surface. It was devised in 1980s and revolutionized the field of surface science. The reason for this is that this comparatively young technique can exploit simultaneously electronic structure, in particular unoccupied density of states, of the molecule and the average spatial orientation of the molecular plan, as well as, geometric properties and local charge distribution

[<sup>11</sup>]. Exploitation of electronic structure is possible through the absorption mechanism of soft X-ray photon near an absorption edge [<sup>12</sup>]. Since NEXAFS measurements require continuously tunable photon energy, synchrotron radiation is the necessary source for these kinds of measurements [<sup>13</sup>]. NEXAFS process, like XPS, is based on photoelectric effect. The essential phenomenon underlying NEXAFS is the energy absorption of the electromagnetic radiation in the X-Ray range according to Einstein relationship [<sup>14</sup>], absorption of incident radiation is found to take place only if its energy is larger than the  $E_b$  of the electron to the atom which means that photon energy can excite the core electrons from initial states to partially filled or empty states above the Fermi level. Therefore, peak position and spectral line shape in NEXAFS spectra are directly related to the nature of unoccupied states [<sup>15</sup>]. A schematic view of the NEXAFS process is illustrated in Figure 2.6. X-ray absorption is, in many aspects, similar to optical absorption process. According to the Beer-Lambert rule, the intensity of the X-ray transmitted through the specimen decreases due to absorption. NEXAFS is measured by scanning the photon energy in the energy region below and up to 50 eV above the absorption edge [<sup>16</sup>].

The fundamental description of the X-rays – matter interaction is given by the Fermi's golden rule [<sup>17</sup>]. Fermi's golden rule is a way to calculate the perturbation-based transition rate between an initial energy eigenstate ( $\psi^i(N)$ ) to a continuum of energy eigenstate ( $\psi^f(N)$ ) of a  $N$  electrons quantum system with unit incident photon flux. On the other hand, NEXAFS measures the optical dipole transitions from a core level to unoccupied states. The transition rate in NEXAFS as well as in optical absorption can be described by the Fermi's golden rule:

$$W_{if} \propto |\langle \psi^f(N) | H' | \psi^i(N) \rangle|^2 \rho_f \quad (2.8)$$

$\rho_f$  is the density of states and the matrix element is  $M_{if} = \langle \psi^f(N) | H' | \psi^i(N) \rangle$

The perturbation operator is

$$H' = \frac{e}{2m} (A \cdot P + P \cdot A), \quad (2.9)$$

$P$  is the momentum operator of the electron and  $A$  is the vector potential of the exciting electromagnetic wave which describes a plane wave with unit vector,  $\hat{e}$ .  $A$  can be expressed as

$$\hat{A}(\vec{r}, \vec{t}) = \vec{e} \cdot A_0 \cdot e^{i(\vec{k} \cdot \vec{r} - \omega t)}, \quad (2.10)$$

$\vec{e}$  is the polarization direction of the light and based on the fact that the wavelength of the electromagnetic radiation is much larger than the size of the atom  $\vec{\nabla} \cdot \hat{A} = 0$  and  $H' = 2(A \cdot P)$ . The dipole matrix element is

$$M_{if} \approx \langle \psi_f(N) | \vec{e} \cdot \hat{P} | \psi_i(N) \rangle \quad (2.11)$$

In a molecule a K-shell excitation is the excitation of a 1s core electron to unoccupied states such as  $\pi^*$  or  $\sigma^*$  [118]. The aforementioned transitions are named as  $\pi^*$  transition or  $\sigma^*$  transition [119]. Therefore corresponding to these transitions, sharp structures below the ionization energy are observed in the NEXAFS spectra [119]. Below we discuss the way in which molecular orientation referring to the substrates is obtained by analyzing the NEXAFS features. In the molecular systems, NEXAFS spectra are characterized by resonances due to the excitation of the inner shell of specific atomic species to an empty molecular orbital or state [120]. The  $\pi^*$  and the  $\sigma^*$  resonances can be described in a molecular orbital picture such as dipole transition from occupied s states to the p component of the  $\pi^*$  and the  $\sigma^*$  final states [118].

Molecular orientation can be determined quantitatively using the sensitivity of NEXAFS spectroscopy to molecular orientation [39, 121]. NEXAFS measures the dependence of the photo-excitation cross section on the orientation of the electric field vector of the incoming linearly polarized X-ray with respect to the transition dipole moment of the probed molecular orbital. This phenomenon is known as linear dichroism [122]. The concept of dipole selection rule can be used not only in explanation of the dichroic NEXAFS but in determining the molecular orientation [118]. The dipole moment of the  $\pi^*$  transition is oriented perpendicular to molecule plane which means the  $\pi^*$  orbitals have maximum orbital amplitude normal to the bond direction while dipole moment of the  $\sigma^*$  transition is aligned in parallel to molecular plan; the maximum orbital amplitude of the  $\sigma^*$  orbitals is along the bond axis. The transition intensities are dependent on the orientation of the transition dipole momentum relative to the orientation of the molecule, consequently the transition intensities of the  $\pi^*$  or the  $\sigma^*$  and hence  $\pi^*$  or  $\sigma^*$  resonances of interest are largest if the electric field vector of the incoming linearly polarized X-ray is along the  $\pi^*$  or  $\sigma^*$  orbitals, respectively.

It can be directly shown from the dipole selection rules that for a vector-type orbital, the resonance intensity along the direction of the dominant component of the incident electric field is given by [123]

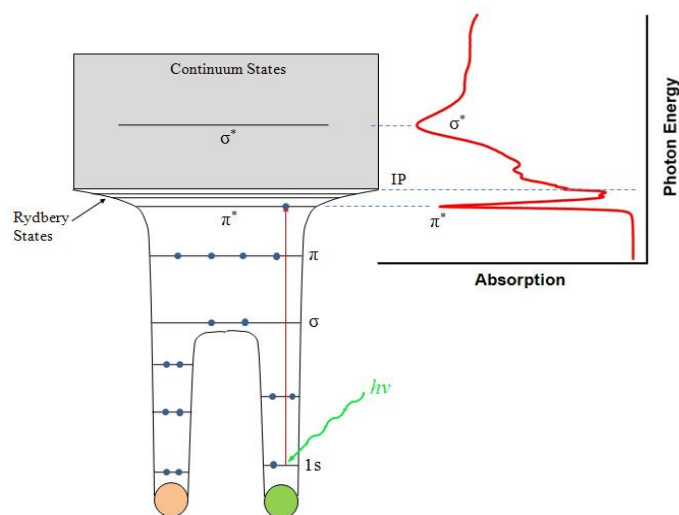


**Figure 2.5:** Schematic representation of the basis of near edge adsorption fine structure spectroscopy.

$$I \propto (\cos^2 \Theta \sin^2 \alpha + 2 \sin^2 \Theta \cos^2 \alpha), \quad (2.12)$$

$\alpha$  is angle between the normal to the surface and the orbital and  $\Theta$  is angle between the incident radiation and the normal to the surface. For determining the orientation of the vector orbital relative to the surface, the angle  $\alpha$  is determined from the following equation.

$$\frac{1}{\tan^2 \alpha} = \frac{1}{2p} \left( p - \frac{1-q}{\sin^2 \Theta_2 - q \sin^2 \Theta_1} \right), \quad (2.13)$$

where  $p$  is the polarization degree and  $q$  is the ratio between the intensity of the chosen resonances for the two different polarizations,

$$q = \frac{I(\Theta_2)}{I(\Theta_1)} \quad (2.14)$$

### 2.5.1 NEXAFS measurements

Owing to the requirement for X-rays with tunable energy, high brightness and intensity, synchrotron radiation providing the full range of wavelengths is the only suitable source of radiation for NEXAFS spectroscopy [124]. The excited states decay in two channels via refilling

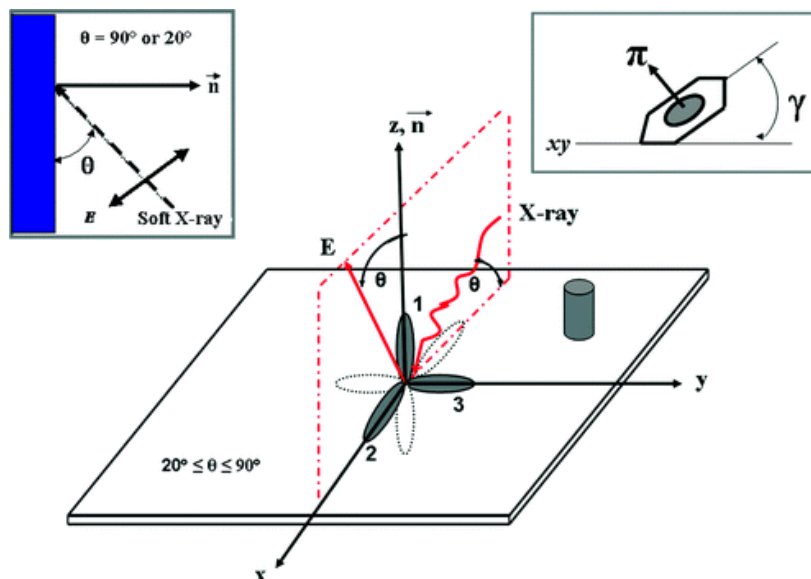


**Figure 2.6:** Representation of  $p^*$  orbitals with respect to the electric field vector,  $E$ , and the normal of the surface,  $n$ . The angle of incidence changes from glancing ( $20^\circ$ ) to normal ( $90^\circ$ ) with the electric field vector oriented perpendicular to the direction of propagation in the  $xz$  plane. Orbitals 1 through 3 represent  $p^*$  orbitals along the  $z$ ,  $x$ ,  $y$  axes, respectively [125].

the core-hole by higher energy electrons either radiative, by emission X-ray fluorescent, or non-radiative by Auger electrons emission [72,121]. Both radiative and non-radiative emission identify the existence of core-hole; measuring the absorption cross section [121]. Either radiative or non-radiative channels can in principle be detected. In this thesis we are interested in the later channel hence we focus on electron detection.

We have used two different electron detection modes:

1. Total Electron Yield (PEY)
2. Partial Electron Yield (PEY)

During the decay of the photo-excited electron to its ground state its energy is transferred to nearby electron [126]. The electrons in the range of the probing depth of TEY (3-10 nm), are photo-ejected. Photo-ejection of electrons emerged from the surface causes a net positive charge. The charged sample is grounded in order to neutralize the net current flowing from the sample and neutralization is monitored. With TEY detection mode all contributing electrons including Auger electrons and secondary electrons are measured [72,121,124]. TEY mode yields high signal intensity

whereas, in correlation to existence of high signal intensity, considerably high background appears due to low  $E_{\text{kin}}$  of detected electrons [127].

PEY is adopted to detect the respective energies of the electrons. PEY method collects a fraction of the total electrons that have  $E_{\text{kin}}$  larger than a threshold energy by filtering out the secondary electrons and the Auger electrons from other lower energy absorption edges [128] using a channeltron electron multiplier and an electron energy analyzer. This mode of detection provides high quality spectra [129]. Low signal-to-background ratio is the disadvantage of the TEY mode of detection which is dominated by secondary electrons while, in the PEY mode signal-to-background ratio enhances dramatically. In the PEY mode, a negative retarding field is applied to the grid in front of the electron detector to increase the signal-to-background ratio. The direct consequence of applying a retarding field is the reduction background signal [72, 130].

## 2.6 Atomic Force Microscopy

AFM belongs to the class of scanning probe microscopy that allows extremely high resolution topographical imaging of the sample surface, in the range of sub-nanometer, by measuring the force between the outermost atoms of the sharp tip of a cantilever and atoms of the sample [131, 132]. It is used in a wide spectrum of natural and applied science from biology to material science, chemistry and physics [133, 134]. The main advantage of the AFM with respect to the other scanning probe microscopies, in particular Scanning Tunneling Microscopy (STM) is that in AFM, measurements in the ambient pressure are possible. AFM is usually employed to investigate the mechanism of growth of thin layers on a surface as well as morphology of the grown thin films. Three modes of scanning are possible: contact mode, non-contact mode and tapping mode. Contact mode AFM is mainly used to probe hard surfaces [135]. In contact mode the ultra-small probe tip is in contact with the surface of the sample. Approaching the sample with the tip in the sub-nanometer range, their electronic orbitals overlap. On the basis of the Pauli exclusion principle, between the investigated surface and the tip in atomic distance, there is a very strong repulsive force [136].

In noncontact mode, the tip scans over the surface at a certain distance [134]. Hence the image is constructed from long range attractive van der Waals forces interaction between the tip and the Tapping mode AFM (TM-AFM), which is a combination of contact mode and non-contact mode, is a type of amplitude modulation (AM) technique.

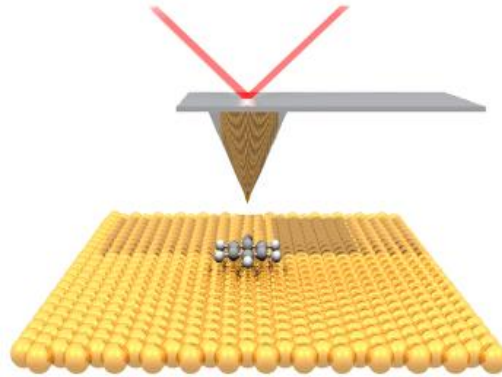


**Figure 2.7:** Schematic structure of an AFM experiment<sup>[137]</sup>.

It performs surface analysis in a very high sensitive condition of operation by taking advantage of relatively large amplitude vibration of the probe <sup>[138]</sup>. The amplitude of vibration is 100 to 200 nm in TM-AFM operation mode while it is 10 nm in other modes of operation <sup>[139]</sup>. The large amplitude oscillation causes high-lateral forces between the cantilever and the surface which will be solved by brief intermittent contact of the tip and the sample <sup>[140]</sup>. The surface is probed with a tip by means of a piezoelectric element and topographic image of the surface will be formed as a consequence of tip-surface interaction. The tip is attached to a cantilever. Depending on the strength of the interaction, the cantilever undergoes a certain deflection, which is detected by a laser beam. The laser beam hits the back of the cantilever while it is deflected toward a photodiode, as shown in Figure 2.8.

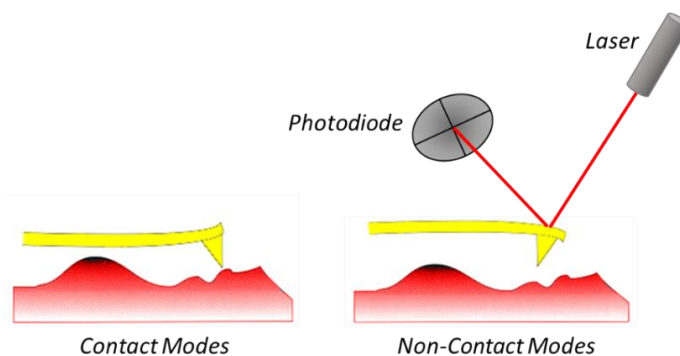


**Figure 2.8:** Schematic representation of contact mode and non-contact mode of operation in AFM <sup>[141]</sup>.



# Chapter 3

## Materials and characterization techniques

### 3.1 Overview

Three metal-free magnetic molecules have been investigated in this work. In this chapter the physical and chemical properties of the molecules and the substrates are introduced.

SiO<sub>2</sub>/Si(111) and TiO<sub>2</sub>(110) single crystal are the two substrates used in our experiments. The molecular and crystal structures of the TiO<sub>2</sub>(110) single crystal as well as preparation techniques are reviewed. Section 3.3.2 introduces the structure of the amorphous SiO<sub>2</sub>/Si(111) briefly.

The XPS measurements of the present work have been performed either in the laboratory at the Institute of Physical and Theoretical Chemistry (IPTC) in Tuebingen or at BESSYII in Berlin. In section 3.4.1 the home spectrometer including its different chambers is extensively discussed. The NEXAFS measurements have been done at the BESSYII facility. In section 3.4.2 we explain the instruments we have used for XPS and NEXAFS measurement at the BESSY II.

### 3.2 Molecules

In this thesis we have investigated three different metal free magnetic molecules. Purely organic radicals are defined as molecules composed of the light elements, mostly C, H, N, and O that have (at least one) unpaired valence electrons or open shell structure [<sup>142</sup>].

Neutral organic radicals possess an odd number of electrons which means that they have an unpaired electron which consequently makes the organic radicals highly reactive. They are unstable species due to their open-shell structures, because, they prefer to reach a closed-shell structure configuration. The unpaired electron as a site of high spin density is capable to take part in reactions such as recombination in the attempt to distribute the spin density with other reactants leading to loss of the open shell structure [<sup>142</sup>]. Several strategies are used to make organic radicals more stable including adding aromatic rings to delocalize the unpaired electrons or introducing

bulky substituent [143].

### 3.2.1 NitPyn

4, 4, 5, 5-tetramethyl-2-(pyrenyl)-imidazoline-1-oxy-3 – oxide, (NitPyn) is a stable free radical in ambient condition which exhibit a magnetic moment. NitPyn belongs to the category of nitronyl nitroxide radicals, a well-known class of stable radicals [144]. The molecular skeleton of NitPyn has two main groups: a pyrene moiety which governs the electronic structure and consequently controls the intermolecular interactions and the nitroxide radical bound to the carbon atoms of the nitrone group which is responsible for good stabilization of the spin [145]. The  $sp^2$  hybridization of  $\alpha$ -C leads to the delocalization of  $\pi$ -electrons. The length, width and thickness of the pyrene substituent part of NitPyn is 11.66Å, 9.279Å, and 3.888Å respectively [146].

Nitroxides have substantial spin density on both N and O atoms, which can be illustrated by one of the two resonance structures [144]. Although some electron spin density is distributed over the rest of the molecule, the unpaired electron is delocalized mainly over the two equivalent N-O groups [147]. The unpaired electron is located in an antibonding  $\pi^*$ -orbital. The delocalization of the unpaired electron over several atoms stabilizes the  $\pi^*$ -orbital (SOMO) therefore, nitronyl nitroxide is very stable compared to other free radicals.

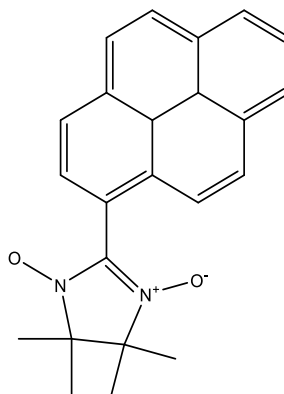


**Figure 3.1:** Schematic representation of NitPyn.

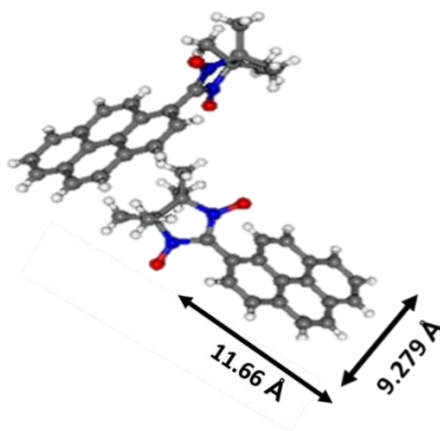


**Figure 3.2:** The conformation of a NitPyn in its crystal.

### 3.2.2 PPN

Another interesting metal-free paramagnetic molecule that has been employed and investigated in this thesis is 1-[4-(3-oxide-1-oxyl -4, 4, 5, 5-tetramethylimidazolin-2-yl) pyrazol-1'-yl]-pyrene, (PPN). The molecular formula of PPN is  $C_{26}H_{23}N_4O_2$ . The molecular structure of PPN consist of three main groups: a pyrene unit that controls the intermolecular interactions of the molecule, a pyrazole bridging block which is linked to the radical unit and nitroxide radical which is responsible for good stabilization of the spin due to delocalization of unpaired electron distributed over two N-oxides [<sup>148</sup>]. The overlapping of  $2p_z$  orbitals of nitrogen and oxygen atoms leads to the  $\pi$  N—O bond, it can be represented as following resonance structure (Figure 3.3) [<sup>149</sup>].

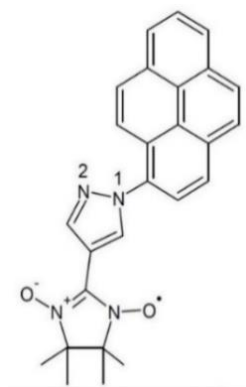


**Figure 3.3:** Schematic representation of PPN.

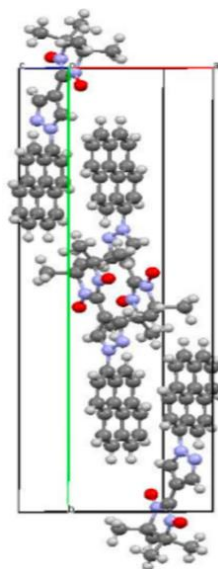


**Figure 3.4:** The unit cell of PPN: the b-axis is the long axis.

The spin density in nitroxide radicals mainly reside on nitrogen and oxygen atoms, but slightly higher on oxygen because of the presence of a nodal plane in  $\pi$  SOMO [150]. The Curie temperature of the molecule is  $T_c = 0.3$  K [26].

### 3.2.3 Bisnitroxide Diradical Molecule

1,2,8,9-tetrahydro-2,2,4,4,6,6,8,8-octamethyl-4H,6H-benzo[1,2-d;5,4-d']bis-(1,3-oxazine)-1,9-dioxy is a bisnitroxide diradical in which the radical centers are not widely separated [151].

The molecular skeleton of bisnitroxide contains two nitroxide groups in meta-position to one another and is expected to exist as a triplet in the ground state [152]. Bisnitroxide diradical is characterized by two unpaired electrons in anti-bonding  $\pi^*$  orbital mobile over the whole molecule but mainly delocalized over the two equivalent N-O groups although some unpaired electron spin density is also distributed over the rest of the molecule [153]. The nitroxides are coplanar with m-phenylene, forming an exchange coupling pathway leading to strong ferromagnetic coupling. In such diradicals with planar conformation efficient delocalization of spin density from the two nitroxides into m-phenylene is expected [28].

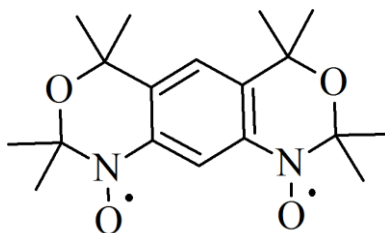


**Figure 3.5:** Schematic representation of Bisnitroxide di radical.

This organic magnet crystallizes with one molecule per asymmetric unit in monoclinic crystal structure with  $a=8.7862 \text{ \AA}$ ,  $b=8.0998 \text{ \AA}$ , and  $c=24.100 \text{ \AA}$ . Bisnitroxide is one of very few examples of existing stable radicals linked by  $sp^3$  carbons in ambient condition that exhibit strong antiferromagnetic coupling. Stability of this organic magnet makes it a promising target for organic-based magnetic materials.

### 3.3 Substrates

Metal oxides have attracted great deal of interests over the last decades for their important technological applications in biocompatible materials, photocatalysis, energy storage and microelectronics [21, 146–149]. Metal oxides comprise a class of materials containing metal element bounds to oxygen atoms. The metal elements are able to form a large diversity of oxide components [158] manifesting a remarkable range of material properties. For instance, electrical properties of metal oxides span over a wide range from insulators to high temperature superconductors [11, 159, 160]. In this thesis, two well-studied metal oxides are employed as substrates: titanium dioxide and silicon dioxide.

#### 3.3.1 $\text{TiO}_2$

Titanium dioxide commonly known as titania ( $\text{TiO}_2$ ) is a reducible wide band gap metal oxide [161]. Its surface has been more extensively studied than those of any other metal oxide materials. Owing to its unique physical and chemical structure on one hand and its scientific and pivotal technological applications, on the other hand, it has been the focus of multidisciplinary efforts [162]. High affinity of  $\text{TiO}_2$  for reduction results in the existence of  $\text{TiO}_x$  in different degrees of oxidation. Besides different compositions,  $\text{TiO}_2$  crystallizes mainly in three different crystallographic phases, namely, rutile, brookite, and anatase [163, 164].

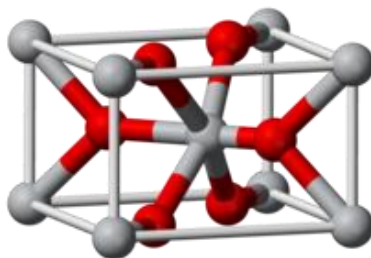


**Figure 3.6:** Bulk structure of rutile [165].

Instability at the relatively elevated temperature and semiconducting nature are two main properties of the single-crystalline  $\text{TiO}_2$  which offers challenges in preparation procedure. Because of these properties, surface analysis with charge particle spectroscopic techniques as well as mounting and cleaning the surface of  $\text{TiO}_2$  single crystals containing various amounts and type of defects in UHV is difficult. However, high affinity of  $\text{TiO}_2$  single crystal for reduction suppresses charging effect at the surface of the crystal and hence facilitates surface analysis by XPS.

### 3.3.1.1 The rutile $\text{TiO}_2(110)$ single crystal

Deciphering the relationship between surface atomic structure in great detail and chemical and physical properties of inorganic single crystals surfaces have long been one of the main challenges in surface chemistry [165]. This knowledge which is obtained by studying both bulk and surface of the single crystals, paved the way for exploring mechanisms of organic molecules adsorption and also nucleation and growth of the molecule on the surface of the single crystals.

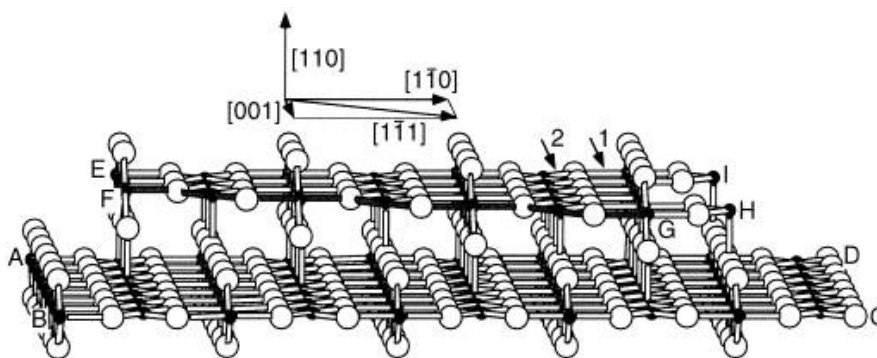


**Figure 3.7:** Ball-and-stick model of two terraces of  $\text{TiO}_2(110)$ . Small black balls represent Ti atoms, and large white balls represent oxygen atoms.

Rutile with the (110) face is the most thermodynamically stable crystallographic structure of  $\text{TiO}_2$  and also the easiest to prepare, among all different phases of  $\text{TiO}_2$  single crystals [166]. Due to its availability and stability, rutile has been employed as benchmark surface and substrate of deposition of already most of the organic molecules [158,167,168]. The perfect  $\text{TiO}_2(110)$  surface is charge neutral and contains alternative rows of six-folded (6f) -as in the bulk-and five-fold (5f) coordinated  $\text{Ti}^{4+}$  bounded with three (as in the bulk) and the outermost two-fold coordinated  $\text{O}^{2-}$  atoms along the [001] direction. Bridging oxygen atoms with three-fold coordination miss one bond to titanium and hence are twofold. The bridging oxygen atoms are located on top of the six-fold coordinated Ti ions. The interaction of organic molecules with inorganic surfaces is of fundamental importance in wide range of scientific discipline.

### 3.3.2 $\text{SiO}_2/\text{Si}(111)$

Recently numerous theoretical and experimental studies were dedicated to metal oxides such as  $\text{Si}(111)$  covered by its native oxide [169–171]. The research interest in highly (p or n) doped  $\text{SiO}_2/\text{Si}(111)$  as one of the leading materials, is driven by its manifold applications such as field effect transistor or MOSFET technology [172,173]. Specifically the conductive silicon substrate is used as gate electrode and the oxide acts as a gate dielectric [174–176]. The thickness of the ultrathin  $\text{SiO}_2$  layer in the range of 1-2 nm thickness on  $\text{Si}(111)$  wafer can be the source of significant electrical properties affecting the performance of the devices. It should be noted that the growth of native oxide is influenced by the structural and morphological characteristic of the silicon and can be explained with a strained epitaxial growth.

In addition to deposition of metal-free organic magnets on rutile single crystal, they are deposited on amorphous  $\text{SiO}_2/\text{Si}(111)$ . Comparing the two different metal oxides with different

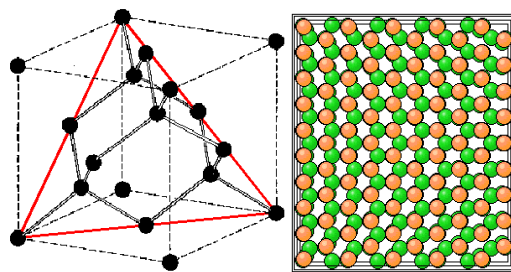


**Figure 3.8:** A top view of the atomic arrangement for the (111) plane of Si atom [171,177].

crystalline structure as a substrate for a given molecule expand our knowledge about the role of the physical and chemical properties of the substrate on the electronic structure as well as paramagnetic character of the deposited molecules. Beyond studying the electronic structure, SiO<sub>2</sub>/Si(111) substrate has been selected to understanding the influence of SiO<sub>2</sub>/Si(111) with amorphous structure on the over layer growth mechanism.

### 3.4 Ultra High Vacuum environment

UHV environment is the basic prerequisite for almost every surface sensitive analysis and careful preparation of atomically clean surfaces. The key importance of UHV stems from the fact that preparation and analysis of nanoscale structures requires a level of purity that will not be achieved through normal cleaning procedure. In surface sensitive techniques thanks to the sampling depth of only few atomic layers, impurities mostly coming from residual gas in vacuum environment play a noticeable role in the quality of the obtained spectra. Considerable efforts have been devoted to maintain the cleanness of the surface. For this purpose, pressure in the range of  $10^{-9}$  mbar or even lower is essential to keep the surface clean [168]. Most of the required instruments for carrying out XPS analysis such as X-ray source, electron analyzer and detectors operate only in UHV environment. Within XPS experiments, the most important consideration in designing the chambers should be the following [178].

- 1: Minimizing all external electrostatic and magnetic fields.
- 2: Providing conditions in which photoelectrons can pass through the sample and the detector distance.
- 3: Contaminants on the surface must be eliminated during analysis.

Standard bake-out of the chambers is needed to improve the base vacuum of the chambers by gradually increase the temperature of the chambers. Time and temperature of bake-out differs in different systems as well as different chambers of the system. For example, the bake-out temperature for evaporation chamber of our system increases up to around 450 K for typically 12-18 h. The moisture and contaminant adsorbed on the side wall of the chambers will take longer time to be desorbed. Bake-out removes absorbed gas (mainly water) from the inner surface of the chamber [179].

A load lock chamber is a small volume chamber being employed for loading and unloading the sample and is considered to be mildly contaminated because of its connection with ambient atmosphere during loading and unloading the sample. This chamber is attached to a UHV vessel to change and to transfer the sample to the preparation chamber. The base pressure of the load lock chamber is about  $10^{-7}$  mbar and is achieved by a membrane and a turbo molecular pumps.

The preparation chamber is a conventional stainless-steel chamber equipped with an ion-gun for Ar ion bombardment and resistive current heating for annealing to the preparation of atomically well-defined surfaces. This chamber connected to the load lock chamber on one side and to the analysis chamber on the other side, is vacuum-isolated by mechanical gate valves. The preparation chamber has a transferable manipulator to prepare and transfer the sample, respectively. The base pressure of approximately  $10^{-10}$  mbar is achieved by using a rotary pump, turbo molecular pump, titanium sublimation pump and bake-out procedure. In-situ surface preparation is performed via Ar ion sputtering and further annealing to remove contamination from the surface of the single crystal and achieve the surface reconstruction.

### **3.4.1 X-Ray tube and synchrotron radiation**

The heated filament as the negative end of the X-ray tube provides high accelerated electron (potential up to 15 KeV) toward a water cooled target anode.

A large number of materials could be essentially used as anode and the X-Ray source depends on the selected anodes. However, due to some specific purposes, this choice is restricted. The crucial consideration in choosing the anode is its stability and conductivity during electron bombardment [178]. In addition, the anode should have photon productivity. High photon energy depends on core level energy. The energy distribution of the X-ray is known as line width. The line width is a characteristic factor for the determination of the resolution of the instrument and also is another essential parameter for selection anodes. The line width of the anode of choice should not limit the required energy resolution of the XPS technique (lower than 1.0 eV) [180]. On the base of these conditions, Al (1486.6 eV) and Mg (1253.6 eV) are the most used materials as X-ray sources.

Thermo-emitted electrons will be generated and accelerated toward to energy electron analyzer. The generated soft X-ray emission is quite complex. It consists of a sharp X-ray line although weaker lines are also observed. It could be divided into two main parts. An intense part of radiation

arise from single line such as  $K_{\alpha}$  providing monoenergetic X-ray source, while satellite lines, such as  $K_{\beta}$ , are also found and a weak part of the radiation leading to the continuous energy distribution of Bremsstrahlung which is of no use in XPS and contribute to the background of the XPS spectrum. These low energy electrons result from inelastic collisions between incident electrons and electrons belong to the surface. The sample is protected from unwanted Bremsstrahlung radiation from anode and also from heating effect by inserting a thin Al window ( $= 2 \mu\text{m}$ ) at the exit aperture of the X-ray source to suppress Bremsstrahlung radiation, and also to prevent stray electrons entering the energy analyzer. The unwanted portion of the radiation which pass through the Al foil is detected in the background spectrum.

The analysis chamber is the heart of the experiment. The design concept of an analysis chamber is based on a monochromator, an electron energy analyzer and a detector. The standard X-ray created in the X-ray tube are directed to the monochromator and reflected as a monochromatized. The monochromatized X-ray illuminates the sample. The emitted photoelectrons are focused by an electronic lens system, including lenses for analysis area definition and lenses for energy adjustment. Consequently, the  $E_{\text{kin}}$  of the electrons is reduced to the narrow range of the pass energy to have a constant resolution.

The monochromator is a principle component in PES related techniques. Its main function is monochromatizing the X-ray spectra via improving resolution, removing satellite lines, improving the signal to noise ratio by elimination of Bremsstrahlung radiation and satellites,

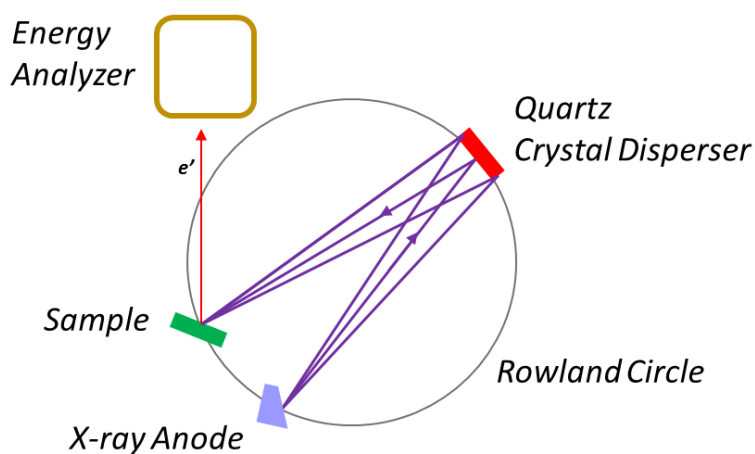


**Figure 3.9:** Schematic of X-ray monochromator.

minimizing sample damage, and separation of the  $K_{\alpha 1}$  doublet. This performance leads to narrowing the X-ray line. An X-ray monochromator operates based on the Bragg-diffraction of the X-ray using concave single crystals. The Bragg-diffraction states that photon (as a plane wave) scattering will undergo constructive interference. Hence, the crystal will appear to have reflected the X-ray if

$$n\lambda = 2d \sin\varphi, \quad (3.1)$$

where  $n$  is the diffraction order,  $\lambda$  is the wavelength,  $d$  is the crystal atomic spacing and  $\varphi$  is the angle of diffraction. The lattice spacing in  $10\bar{1}0$  in quartz single crystal is  $4.255 \text{ \AA}$  [88]. Hence, the corresponding Bragg angle for the first order of diffraction for Al  $K_{\alpha}$  X-ray with the wave length of  $0.8333 \text{ nm}$  is  $78.5^{\circ}$ .  $K_{\alpha}$  radiation means that the emitted X-rays originate from transition of an electron from L shell to the hole which was created during photoemission process in K shell [181]. The physical properties of quartz combined with its suitable interplanar distance and availability as a single crystal makes it the only material for X-ray monochromators in combination with Al  $K_{\alpha}$  radiation.

The X-ray monochromator utilized in our lab consists of 24 quartz crystals which are kept at RT. The geometry is based on a Rowland circle for high performance with multiple toroidal array of quartz  $10\bar{1}0$  single crystal. In the process of X-ray monochromation, since wavelength and consequently the energy of the Al  $K_{\alpha 1}$  and  $K_{\alpha 2}$  X-ray is different, based on the Bragg diffraction, the Al  $K_{\alpha 2}$  X-ray is filtered out. This filtration results in a focused X-ray beam at the surface of the sample. The energy spread of the monochromatized X-ray is narrower than the standard source. For example, for Al  $K_{\alpha}$  X-ray half widths decrease from  $0.8 \text{ eV}$  for standard X-ray source to  $0.2 - 0.3 \text{ eV}$  for monochromated source.

In photoelectron spectroscopy, quantitative information is derived by analyzing the  $E_{\text{kin}}$  of the emitted electrons from the surface. Therefore, energy filtration requirement arises for precise analysis. For this purpose, an electron energy analyzer is advantageously employed as an energy window. It is designed to measure the energy and angular distribution of emitted electrons. The analyzer system consists of three components: the collection lens, the energy analyzer and the detector. The concentric hemispherical analyzer (CHA) is an electrostatic device being employed to disperse electrons as a function of their  $E_{\text{kin}}$  [182]. The analyzer consists of one concave and one convex metallic shells, one inside the other, while  $R_1$  and  $R_2$  are the radii of inner and outer hemisphere, respectively.

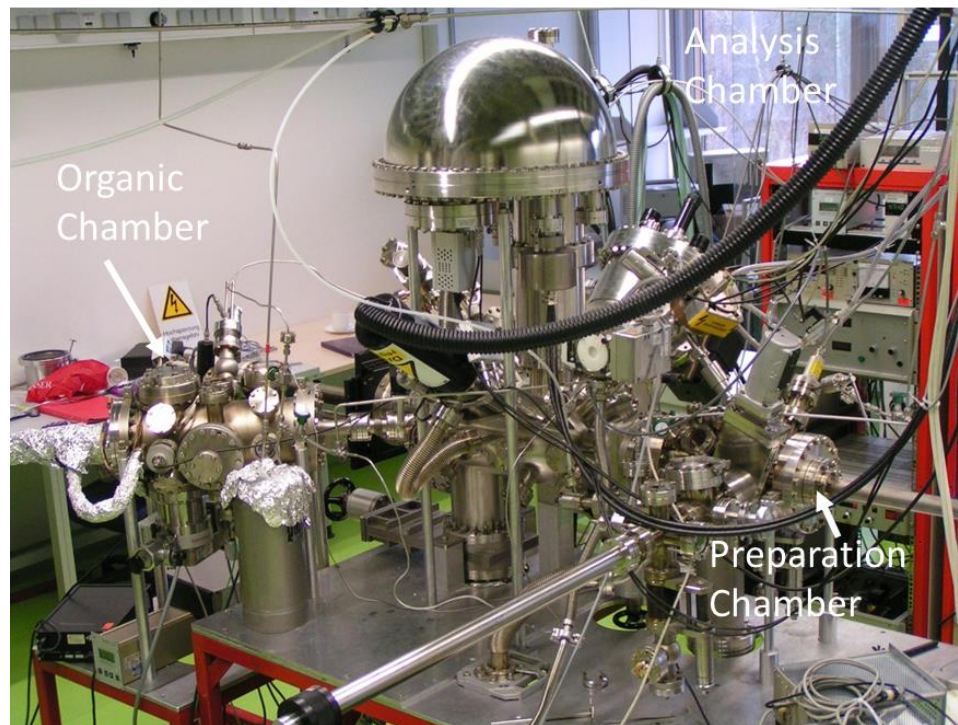


**Figure 3.10:** Our XPS station. The apparatus consists of three separately pumped chambers. Left the preparation chamber, in the middle the analysis chamber also on to recognize hemispherical analyzer and right another chamber for preparation of the organic thin-film systems.

Accelerated electrons are focused successfully to a point within the analyzer using a system composed of two electron lenses. Applying specific potentials between the hemispheres results in an equipotential surface between the hemispheres. Focused electrons with very high or low  $E_{kin}$

(and therefore, velocity) will collide to deflectors with larger and smaller radius, respectively. As a result, only electrons of the desired energy region pass through the detector aperture. The Phoibos 150 electron concentric hemispherical energy analyzer of 150 mm mean radius has been used to measure the photoelectron signal versus  $E_b$  or  $E_{kin}$ . The analyzer has 10 electrostatic lens, a concentric hemispherical capacitor and multichannel detector. Good magnetic shielding in conjunction with a very high stable power supply of the analyzer are the basic requirements to provide high collection efficiency and to enhance the energy resolution [183]. The source of electrons, booster ring, storage ring, Radio Frequency (RF) cavity and insertion devices such as wigglers and undulators are the main components of synchrotrons [184].

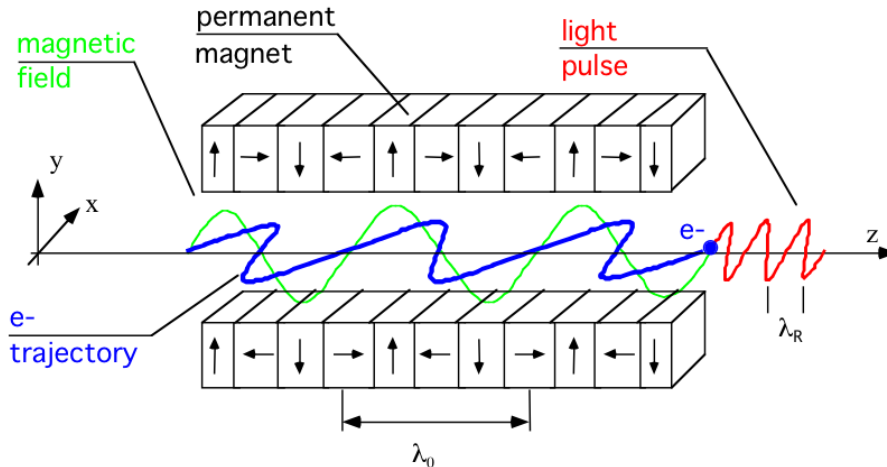


**Figure 3.11:** Schematic view of a planar undulator magnet with alternating polarity of the magnetic field and of the sine like trajectory of the electrons [185].

Photons are generated by thermionic emission from a heat filament and are accelerated up to speed close to the speed of the light by means of a linear accelerator (Linac). Accelerated electrons collide with residual gas particles in a storage ring which result in decreasing its  $E_{kin}$ . These electrons must be continuously supplied. The electrons must be accelerated to few GeV, which is the energy of the electrons in the main storage ring or to somewhat below. It occurs by periodic injection of electron from the Linac to the booster ring.

The storage ring consists of several straight sections and bending magnets positioned around the ring. The main function of the storage ring is maintaining the generated electrons carrying  $E_{kin}$  measured in the range of GeV. Since bending magnets force electrons to change their directions, they experience a centripetal acceleration which causes high flux of emission in attempt to conserve the electron momentum [184].

Undulators and wigglers are two insertion devices situated in storage ring in order to produce synchrotron radiation by changing path of the electrons. Undulators are relatively low field, planar permanent magnet hybrid devices which consist of several individual undulator segments positioned in the separate range of mm and generate radiation at specific harmonics. The undulator axis is along the direction of the beam, the magnetic field point in the y direction. The orbiting electrons lose their energy constantly via synchrotron radiation emission. Radio

Frequency (RF) cavity is an extra device positioned in the storage ring to continuously supply the power that is lost by the emitted radiation via electrons passing through RF cavities.

### **3.4.2 End-station in BESSY**

The X-ray absorption measurements and some of the X-ray photoelectron spectroscopy measurements, in particular measurements with different excitation energy of the X-ray, are carried out on the UE52-PGM undulator beam line at the synchrotron radiation facility Bessy II (Berlin). The end-station consists of two separated chambers, a preparation chamber and an analysis chamber. The base pressure in the chambers was  $2 \times 10^{-10}$  mbar. The photon energies covered a range between 100 eV to 1500 eV from. For the monochromatisation of the synchrotron radiation was used a plane grating monochromator. Most of the measurements are performed in the "single bunch" while the ring current was 20 mA at the injection. The detection of photoelectrons took place with a Scienta R4000 electron energy analyzer (resolution 0.1 eV). For excitation of the photoelectrons for the XPS measurements, three different incident photon energies 330, 640, and 1000 eV were used to vary the surface sensitivity of the experiments. All NEXAFS spectra are recorded at two different polarizations of the incident X-ray (out of-plane and in-plane). The NEXAFS spectra are measured in total electron yield and partial electron yield normalized by the clean substrate signals.

## **3.5 Atomic Force Microscopy**

The AFM measurements are performed using a Nanoscope III scanning probe microscope (Digital Instruments). All pictures are collected in tapping mode in ambient conditions. In order to exclude possible artifacts, different points of the surface of the interested thin films are probed.

## **3.6 Data analysis**

The obtained data are acquired and analyzed using Specs Lab and UNIFIT 2014 software. We used two kinds of spectra: survey spectra and elemental spectra. Survey spectra provide overall information about all the detectable elements exist at the surface of the sample [186]. Thereby, survey spectra identify which elements are present in the investigated sample and in what  $E_b$ . The upper limit in the  $E_b$  in XPS is determined by the excitation energy minus the work function. When Mg or Al are the source of the X-ray, excitation energies of the X-ray are 1253.6 eV and 1486.6

eV respectively. For all the samples being analyzed in this work, the range of the survey spectra has been determined to be in 0-1000 eV. Detailed spectra are obtained at lower pass energy (20 eV) and lower step size (0.05 eV). This means that elemental spectra are scanned in higher resolution than the survey spectra.

### 3.7 TiO<sub>2</sub> single crystal

TiO<sub>2</sub> single crystals (10×10×0.5 mm<sup>3</sup>) in (110) orientation and 99.999% purity are provided by PI-KEM LTD. The crystal is fixed on the surface of a stainless steel sample holder by spot-welding three wolfram wires in which tantalum filaments, as a radiative heater, was tightly installed behind the sample holder and so TiO<sub>2</sub>(110) single crystal. Mounting the sample holder in this way guarantees electrical conduction.

Reading of the temperature is calibrate by a pyrometer. A clean well-characterized rutile TiO<sub>2</sub>(110) surface is achieved by repeated cycles of Ar ion sputtering and annealing to give rise to the (1×1) surface reconstruction and to reduce the intensity of 3d gap states.

Ar ion sputtering is adopted to clean the substrate using Ar ions with acceleration voltage of 600 V for 30 min at RT. The Ar pressure is in the range of  $5 \times 10^{-5}$  mbar. Because of the deep ion penetration of Ar<sup>+</sup>, several layers of the single crystals are damaged. Ar<sup>+</sup> bombardment is performed by sputtering oxygen from the surface, thus, altering the Ti/O ratio and producing a number of reduced Ti states (Ti<sup>3+</sup>, Ti<sup>2+</sup>). Oxygen sputtering varies the coordination number of the surface atoms which indicates increasing the surface energy of the crystal and, thus its instability. Oxygen depletion caused by sputtering leads to a net flow of surplus Ti cations from the instable surface toward the bulk, giving rise to oxygen vacancies both in the bulk and on the surface [27].

After sputtering, it is necessary to anneal the surface in order to desorb possible contaminations and producing atomically smooth surfaces. Annealing the sputtered surface to 800 K is started immediately after the pressure of the preparation chamber reduces to the range of the 10<sup>-9</sup> mbar. By vacuum annealing, surface is reconstructed via oxygen diffusion from bulk to the surface of the crystal. Surface reconstruction is a phenomenon of paramount importance because of its pivotal role in governing the surface energy, and so, the surface reactivity and stability. In the case of TiO<sub>2</sub>, the surface reconstruction reduces the surface energy of the crystal by increasing the concentration of the surface oxygen allows restoring the (110) (1×1) surface stoichiometry. In

this condition, the coordination number of the surface atoms reaches that of the bulk atoms: The closer to the bulk atom, the coordination number, is the more stable the surface. Sputtering and annealing are usually repeated till no trace of contaminations are detected by XPS.

An untreated crystal is transparent, indicating the presence of a small amount of oxygen vacancies in the bulk. Due to the fact that the created defects are responsible for electrical conductivity in ionic crystals, and the fact that they can alter optical properties of the surface [<sup>187</sup>], during the cleaning procedure, the color of the sample changes to gray revealing slightly reduction of the surface. The treated single crystal is sufficiently conductive that no charging effects are observed during the experiments. The clean surface was slowly cool down to 300 K and then was transferred to the analysis chamber for XPS analysis.

### **3.8 SiO<sub>2</sub>/Si(111)**

Native SiO<sub>2</sub>, grown on single-side polished Si(111) wafers with 10×10×0.5 mm<sup>3</sup> dimensions, doped resistivity of 5-10 Ω cm (boron-doped) was provided by WAKER-CHEMITRONIC GMB. The substrate was fixed to the sample holder as discussed in the case of TiO<sub>2</sub> single crystal.

# Chapter 4

## Results and discussion

### 4.1 Overview

In this chapter, we present the results of our spectroscopic studies performed on thin films of pyrene-derivatives of the nitronyl nitroxide radical (4,4,5,5-tetramethyl-2-(pyrenyl)-imidazoline-1-oxyl-3-oxide, NitPyn, 1-[4-(3-oxide-1-oxyl-4,4,5,5-tetramethylimidazolin-2-yl)pyrazol-1'-yl]-pyrene, PPN, and 1,2,8,9-tetrahydro-2,2,4,4,6,6,8,8-octamethyl-4H,6H-benzo[1,2-d;5,4-d']bis-(1,3-oxazine)-1,9-dioxy) deposited on rutile  $\text{TiO}_2(110)$  single crystals and native  $\text{SiO}_2$ , grown on Si(111) wafer. Morphological analysis and growth modes determination is studied with AFM images.

### 4.2 Clean rutile $\text{TiO}_2(110)$ single crystals

The main purpose of this thesis is to study the effect of molecular adsorption on the aforementioned substrates and on the adsorbed molecules. In an ideally controlled experiment are studied the electronic structure of a clean substrate, before deposition of the organic molecules. Subsequently, the electronic structure of the substrate upon adsorption of the organic molecules is extensively analyzed. This enable us to understand the mutual effects of molecular adsorption on the substrate and the deposited molecules film. The effects are studied in the light of physical and chemical properties of the substrates and the thin films as well as the magnetic properties in case of the organic magnets. We start by investigating rutile  $\text{TiO}_2(110)$  single crystals and then exploiting the amorphous native  $\text{SiO}_2$ , grown on single – side polished p-Si(111) wafers.

As mentioned in chapter 3.7, atomically clean and well-ordered  $\text{TiO}_2(110)$  single crystals are obtained by cleaning the substrate in a systematic way including alternating cycles of sputtering and annealing. The purity of the substrate is of pivotal importance prior to deposition of the molecules in UHV condition. Figure 4.1 shows a XPS survey spectrum of a  $\text{TiO}_2(110)$  single

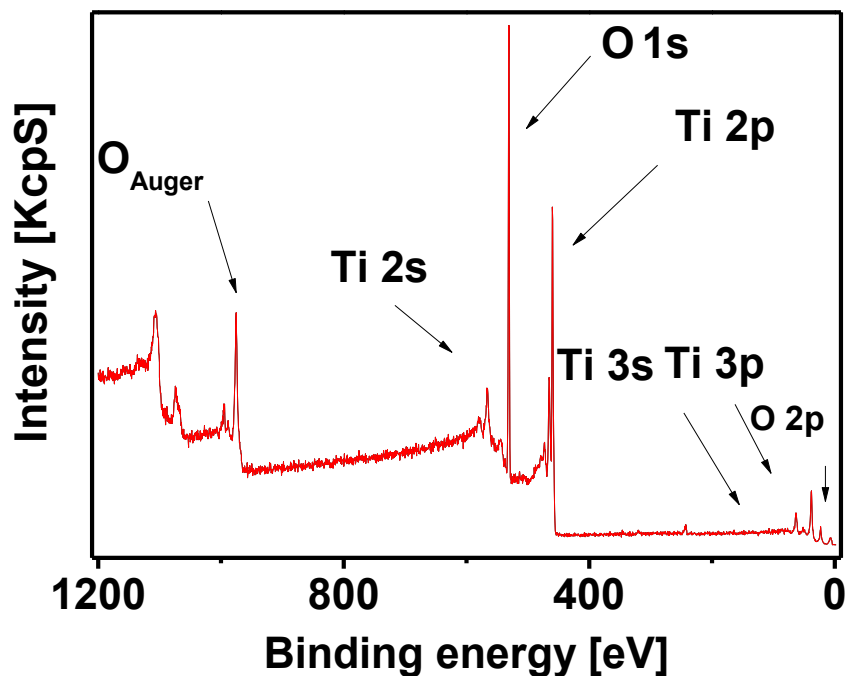


**Figure 4.1:** Survey spectrum of the rutile  $\text{TiO}_2(110)$  single crystal.

crystal after several cycles of sputtering and annealing. As shown in Figure 4.1, neither carbon nor other contaminations have been detected in the survey spectrum: the sample is contamination-free and it is ready to be used as atomically clean substrate for deposition of the molecules. A survey spectrum, provides an overview about the elements that are present in the structure of the sample. Thus, in the case of  $\text{TiO}_2(110)$ , Ti 2p and O 1s core level spectra are recorded in high energy resolution mode (pass energy of 20 eV). Now, for a more detailed analysis of the surface, we look at the elemental spectra of titanium and oxygen. Figure 4.2 shows the Ti 2p core level spectrum of the stoichiometric clean rutile  $\text{TiO}_2(110)$  single crystal surface which gives rise to the two strong sharp signals centered at 458.5 eV and 464.2 eV indicative of the  $\text{Ti}^{4+} 2p_{3/2}$  and  $\text{Ti}^{4+} 2p_{1/2}$  states of the  $\text{Ti}^{4+}$ , respectively. The spin-orbit splitting between  $\text{Ti}^{4+} 2p_{3/2}$  and  $\text{Ti}^{4+} 2p_{1/2}$  is found to be 5.7 eV. This is in nice agreement with the published values obtained in  $\text{TiO}_2$  single crystal [188]. In addition, some satellite features are expected at 3 eV and 13 eV energy position higher than the main feature. It is well-known that during sputtering the surface of  $\text{TiO}_2(110)$  single crystal, a fraction of the two fold coordinating bridging oxygen atoms are removed leading to the oxygen deficient surfaces and then progressive reduction of a part of  $\text{Ti}^{4+}$  ions to the 3+ or 2+ oxidation states [165, 189].

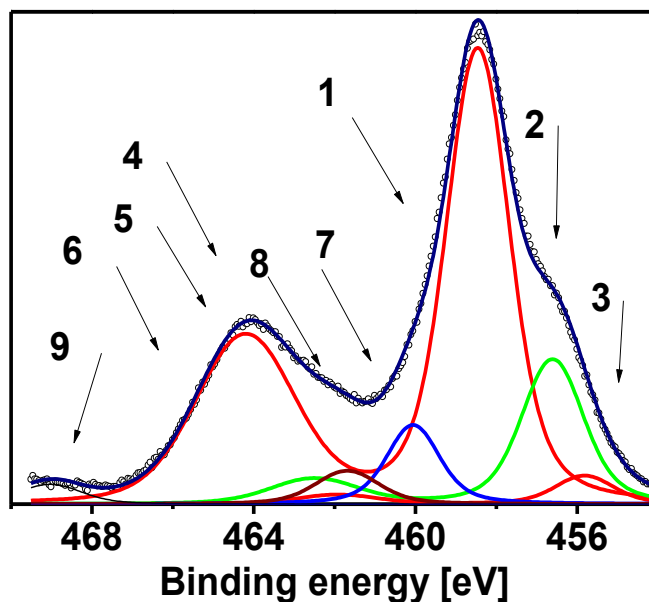


**Figure 4.2:** Ti 2p core level spectrum of the heavily reduced  $\text{TiO}_2(110)$  single crystal.

**Table 4.1:** Assignment of the measured components by peak fitting analysis in Ti 2p core level spectrum;  $E_{B, \text{abs}}$ , and  $E_{B, \text{rel}}$  denote absolute and relative binding energies.

Component	$E_b$ and assignment
(1)	$E_{B, \text{abs}} = 458.5 \text{ eV}$ ; $\text{Ti}^{4+} 2p_{3/2}$ core level- peak [ <sup>110, 196, 197</sup> ]
(2)	$E_{B, \text{rel}} = -1.8 \text{ eV}$ ; $\text{Ti}^{3+} 2p_{3/2}$ core level- peak [ <sup>191, 196</sup> ]
(3)	$E_{B, \text{rel}} = -3.4 \text{ eV}$ ; $\text{Ti}^{2+} 2p_{3/2}$ core level- peak [ <sup>191</sup> ]
(4)	$E_{B, \text{rel}} = 5.7 \text{ eV}$ ; $\text{Ti}^{4+} 2p_{1/2}$ core level- peak; Spin-Orbit splitting [ <sup>110, 196, 197</sup> ]
(5)	$E_{B, \text{rel}} = 4.1 \text{ eV}$ ; $\text{Ti}^{3+} 2p_{1/2}$ core level- peak; Spin-Orbit splitting [ <sup>191, 196</sup> ]
(6)	$E_{B, \text{rel}} = 2.7 \text{ eV}$ ; $\text{Ti}^{2+} 2p_{1/2}$ core level- peak; Spin-Orbit splitting [ <sup>191</sup> ]
(7)	$E_{B, \text{rel}} = 1.6 \text{ eV}$ ; $\text{Ti}_2\text{O}_3$ core level- peak [ <sup>191, 198</sup> ]
(8)	$E_{B, \text{rel}} = 3 \text{ eV}$ ; satellite structure [ <sup>198</sup> ]
(9)	$E_{B, \text{rel}} = 13 \text{ eV}$ ; satellite structure [ <sup>197</sup> ]

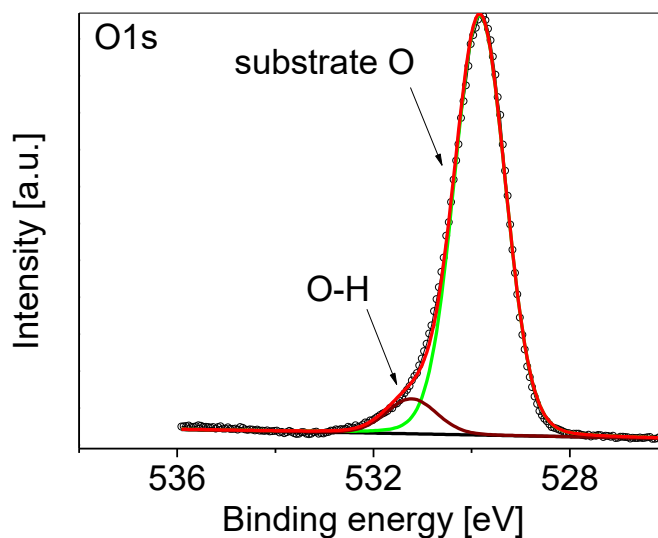


**Figure 4.3:** O 1s core level spectrum of the TiO<sub>2</sub>(110) single crystal.

Metals often have more than one oxidation state and they are able to form oxides of different stoichiometry or even mixed valance compounds in which more than one valence state is present [178]. The density of the oxygen defects located either at the surface or in the bulk of the rutile TiO<sub>2</sub>(110) varies with the parameters of the cleaning procedure cleaning procedure, such as time, energy of sputtering, annealing time and temperature [190]. The percentage of the oxygen vacancies is determined by analytically fitting the Ti 2p core level spectra [191]. In particular, the presence of oxygen defects at the surface or sub-surface of TiO<sub>2</sub>(110) single crystal is confirmed by the appearance of photoemission lines at, respectively, 1.8 eV and 3.4 eV lower E<sub>bs</sub> than the Ti<sup>4+</sup> bulk signal XPS line which implies reduced (lower valence) Ti<sup>3+</sup> and Ti<sup>2+</sup> states. Detailed information about the position of all the components of the TiO<sub>2</sub> including titanium atoms at different oxidation states and satellite features are summarize IN Table 4.1. Atoms at higher positive oxidation states exhibit higher E<sub>bs</sub> due to the extra-coulombic interaction between the photo-emitted electrons and the ion [192].

Figure 4.3 shows the O 1s core level spectrum of the reduced TiO<sub>2</sub>(110) single crystal surface which gives rise to a strong sharp signal centered at 531.08 eV and a minor feature visible at the 1.4 eV higher E<sub>bs</sub> with respect to the main line. The main feature indicates a signal from oxygen atoms belonging to the TiO<sub>2</sub>(110) single crystal. The molecular water is chemisorbed on the surface of the TiO<sub>2</sub>(110) single crystal which results in splitting the adsorbed molecule in to H

atoms and OH groups [<sup>193</sup>,<sup>194</sup>]. The minor signal at 532.48 eV from OH oxygen atoms originates from adsorption of molecular water on the TiO<sub>2</sub>(110) surface [<sup>195</sup>].

### 4.3 Hydroxylated rutile TiO<sub>2</sub>(110) single crystal

In this section the hydroxylation mechanism and its effect on the electronic structure of rutile TiO<sub>2</sub>(110) single crystal is studied. We also look at the mechanism of adsorption of NitPyn on the crystal surface. Oxygen vacancies and hydroxyl groups are the two most common point defects on the (110) surface of the rutile phase of TiO<sub>2</sub> single crystals. These defects affect the surface properties and electronic structures of TiO<sub>2</sub> [<sup>199</sup>,<sup>200</sup>]. The relative intensity ratio of Ti<sup>4+</sup> to that of Ti<sup>3+</sup> and Ti<sup>2+</sup> is regularly used to calculate the stoichiometry of TiO<sub>2</sub>(110) [<sup>191</sup>]. The E<sub>b</sub> scale has been calibrated so that all the spectra are referenced by means of Ti<sup>4+</sup> 2p<sub>3/2</sub> peak [<sup>191</sup>].

As discussed, NitPyn is a small organic molecule with an unpaired electron in the radical part. This makes it a very thermal-sensitive molecule. Because of this property, we avoid standard baking-out of the evaporator, instead we adopt a low temperature bake-out which includes heating the Knudsen cell up to 350-370 K for 18 h. A further rise in the temperature of the cell leads to degradation of the molecular structure of NitPyn. This bake-out is not enough to remove all the molecular water present in the evaporation chamber. Therefore, a small amount of residual water remains. The presences of oxygen vacancies at the two fold coordinating bridging sites of the (110)

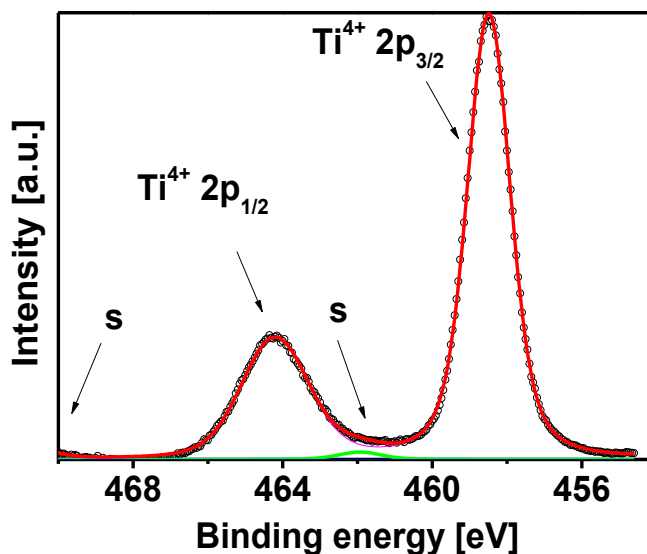


**Figure 4.4:** Ti 2p core level spectrum of the clean TiO<sub>2</sub>(110) single crystal surface.

surface of the rutile  $\text{TiO}_2$  favors molecular water adsorption on the vacancy sites which results in conversion of the  $\text{Ti}^{4+}$  sites to the  $\text{Ti}^{3+}$  defects [201, 202].

The molecular structure of water is unperturbed on substrate surface adsorption [203]. Adsorption of molecular water while electronic structure remains intact usually occurs on top of the defect-free surfaces and is interpreted as physisorption or weak chemisorption of the molecular water [204, 205]. In this case, adsorbed molecule, owing to the molecular water-substrate interactions may desorb from the surface of the substrate. On the other hand, there are several theoretical and experimental studies that have agreed on the scenario that the molecular water dissociatively adsorbs on the surface of the substrates [204, 205]. In this case, water splits into OH and H species. In our experiments, where the defective  $\text{TiO}_2(110)$  single crystal is used as a substrate, the highly reactive surface of the  $\text{TiO}_2(110)$  single crystal favors dissociative adsorption of the molecular water [204, 206]. The OH species interacts with the vacant sites, (110) surfaces contains fivefold coordinated Ti atoms along the [001], causing the adsorption to occur along the [001] direction in the bridging configurations [207]. The remaining H atoms, hydroxylate adjacent bridging O atoms. Dissociative adsorption of the molecular water is a consequences of the formation of the two kinds of bridging hydroxyl groups per initial vacancy [208, 209]. Missing one bridging oxygen atom from

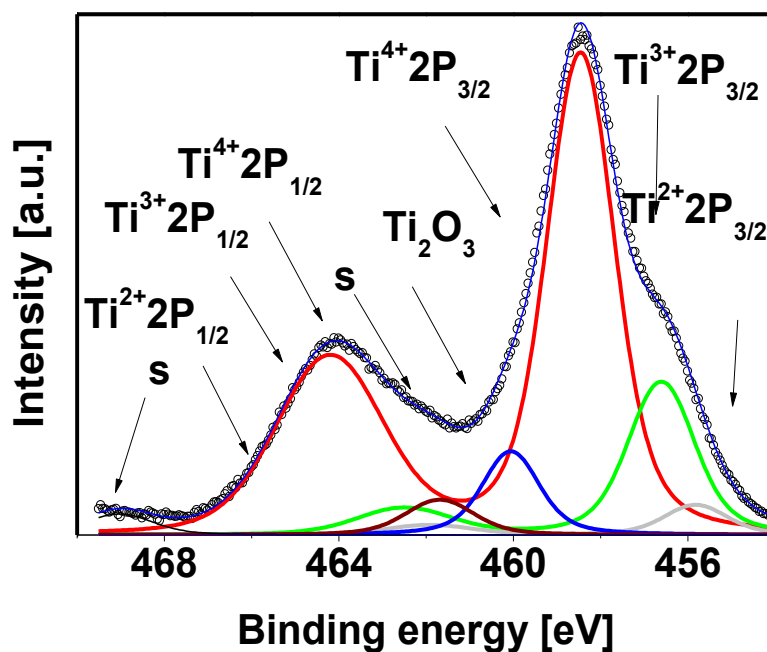


**Figure 4.5:** Ti 2p core level spectrum of the heavily reduced  $\text{TiO}_2(110)$  single crystal surface.

surface or subsurface of the TiO<sub>2</sub>(110) single crystal, introduces one oxygen atom and two Ti<sup>3+</sup> occupied states in the surface or subsurface of the same crystal. The molecules are strongly bound to the adsorption sites of the surface and the sub-surface of the TiO<sub>2</sub>(110) single crystal. This inhibits the chemisorbed species from spontaneously desorption at RT [209]. A prerequisite for the dissociation of molecular water to occur is its mobility and ability to reach the adsorption sites [209].

## 4.4 NitPyn deposition on TiO<sub>2</sub>(110) single crystal

In this section, we focus on the study of a thick film of NitPyn deposited on the nearly defect-free rutile. We investigate the surface of the thin film within an information depth for which the molecules do not interact with the TiO<sub>2</sub>(110) substrate. Understanding the physical and chemical properties of the molecules when their electronic structure is unperturbed represent the first necessary characterization of a system.

### 4.4.1 XPS measurements

#### 4.4.1.1 High coverage

The analysis of the films of NitPyn deposited on the TiO<sub>2</sub>(110) single crystal starts with the XPS survey spectrum. As shown in Figure 4.6, the significant intensity of the peaks related to the C 1s and the N 1s core level spectra illustrates that the molecule has been successfully deposited on the clean rutile TiO<sub>2</sub>(110) single crystal.

In order to determine the ratio between the C atom and the N atom in the structure of NitPyn, we need to compare the intensity of the C 1s (I<sub>1</sub>) and N 1s (I<sub>2</sub>) core level spectra taking into account the sensitivity factor of the 1s orbital of the C and N atoms in our set of experiments (0.25 and 0.4, respectively) as discussed in chapter 2.4.2.

The integrated signal intensities of the C 1s and N 1s core level spectra are calculated as follows:

$$C\ 1s / N\ 1s = (I_C / S_C) / (I_N / S_N) = 11.25$$

The chemical formula of NitPyn (C<sub>23</sub>H<sub>21</sub>N<sub>2</sub>O<sub>2</sub>) with 23 carbon atoms and 2 nitrogen atoms implies stoichiometric C / N ratio is equal to 11.5. Therefore, we can conclude that the ratio of the

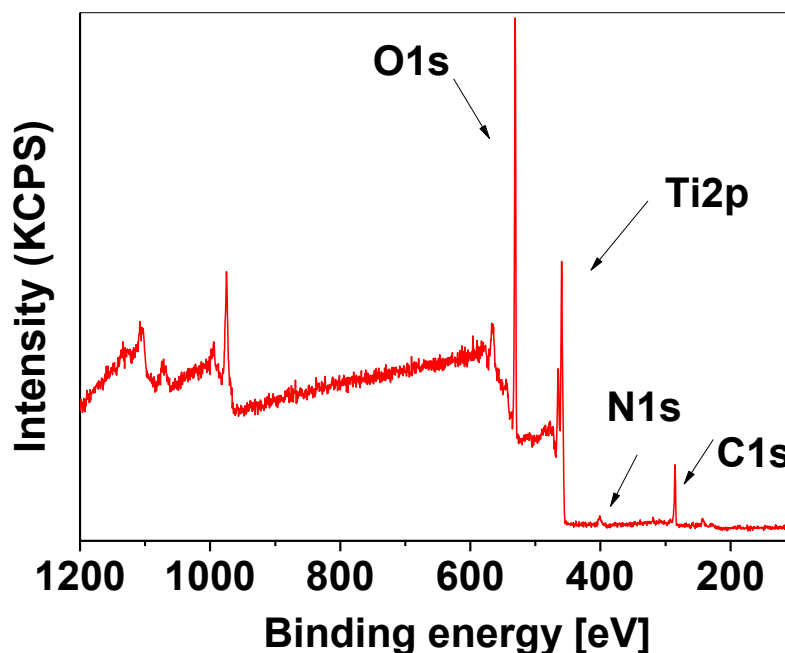


**Figure 4.6:** Survey spectrum of a nominally 2 nm thin film of NitPyn on the rutile  $\text{TiO}_2(110)$  single crystal.

integrated signal intensities of the C 1s and N 1s core level spectra meets the expected stoichiometric ratio.

Curve-fitting and analyzing the experimental curves facilitates a deeper insight into the photoemission spectra <sup>[210]</sup>. The complexity of the C 1s core level spectrum is mainly due to the presence of carbon atoms with different environments in the structure of the molecule.

Curve-fitting provides an opportunity to resolve the individual spectral lines. The most striking observation in Figure 4.7 is that the C 1s core level spectrum of NitPyn consists mainly of two contributions including the main line at around 284.6 eV and the second feature evident as a shoulder at higher  $E_b$  at around 286.6 eV. The ratio between the two integrated signals is 19:3.

To perform peak-fitting of the photoemission lines, we used asymmetric Voigt line-shape profiles characterized by a constant Lorentzian width which is fixed (80 meV for C 1s). These values of the are in good agreement with the intrinsic life time for the core-hole states in organic molecules<sup>[211–213]</sup>. The Gaussian widths for C-C, C-H, and  $\text{CH}_3$  is 0.97 eV and for the C-N components is 1.20 eV.

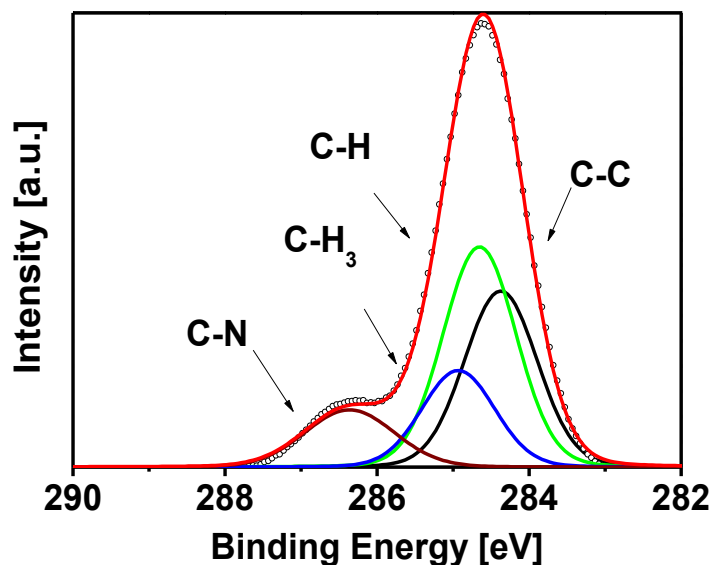


**Figure 4.7:** C 1s core level spectrum of a 2 nm nominally thick film of NitPyn deposited on TiO<sub>2</sub>(110) single crystal.

The main line of the C 1s core level spectrum, as displayed in the Figure 4.7, can be assigned to three chemically different carbon atoms. The different contributions belong to the aromatic rings (C-C and C-H) and to the methyl groups (CH<sub>3</sub>). The peak at lower E<sub>b</sub> belongs to the double-bonded carbon atoms (C=C), C-H is visible at 0.28 eV higher energy, indicates a more efficient screening of the core-hole for the internal C-C ring bonds [210]. The peak at 0.56 eV higher E<sub>b</sub>s with reference to the C=C contribution assigned to the carbon atoms belong to the methyl groups (CH<sub>3</sub>). The CH<sub>3</sub> peak appeared at higher E<sub>b</sub> due to an increased number of hydrogen atoms with respect to CH. The contribution related to the carbon atoms bound to nitrogen atoms (C-N) is evident at 1.98 eV higher E<sub>b</sub> with respect to the C=C contribution. The significant higher E<sub>b</sub> of the C-N can be understood in terms of difference in the electronegativity of the nitrogen and carbon atoms. The relatively high electronegativity of the nitrogen atom withdraws the electrons, and reduces the charge density on the C-N bond. This results in the increasing of E<sub>b</sub> of the photoelectron emitted from carbon atoms bound to the nitrogen atoms as compared to the other components [214]. As mentioned, NitPyn molecule is formed by 23 carbon atoms, 2 nitrogen atoms and 2 oxygen atoms, which leads to the atomic percentage of 85.2%, 7.4%, and 7.4% respectively. We find that the resulting percentages are in agreement with the integral signal intensities obtained by analyzing the XPS curve. As already mentioned, the ratio of the integrated signal intensities

between the two main parts of the spectrum is 19:3. The contributions to the main line in the lower  $E_b$  are set to have 9:7:4 ratio (C-H: C-C:  $\text{CH}_3$ ) according to the stoichiometry of the molecule. In addition to the four outlined components in the C 1s core level spectrum, two further features with much lower intensity are introduced. They are photoelectron shake-up structures and their energy positions with respect to the main photoemission line are at 1.2 eV and 3.2 eV. These are consequences of the relaxation of the electronic system following core-hole formation [108,215]. The satellites are correlated to the shake-up excitation between orbitals mainly localized on the aromatic carbon atoms ( $S_1$  at 285.40 eV in Figure 4.7), as well as, on the carbon atoms bound to the nitrogen atoms, ( $S_2$  at 287.40 eV in Figure 4.7). The satellite structures cannot be understood in a simple initial state picture due to the modified chemical environment. An interpretation that they originated from strong dynamic multi-electron shake-up excitations in the PES final states gives a detailed picture on the excited states of the core ionized system [216]. Core-hole formation induces a reduction in the symmetry of the electronic system for example; The benzene ring has six fold spatial symmetry ( $D_{6h}$ ) with all the six C-C bonds equivalent but in the core-hole description (when considering the localized core-hole events) the molecular symmetry decreases to  $C_{2v}$  [217]. Therefore, there are a large number of nonequivalent carbon atoms during core ionization that contribute to the satellite spectrum. The ionization at different carbon sites may give different contributions to the shake-up spectra [41]. This concept has been comprehensively discussed by Rocco et al and Schoell et al [214,217]. The first satellite feature ( $S_1$ ) can be conventionally assigned to the excitation of an electron from the HOMO to the LUMO. This shake-

**Table 4.2:** Binding energy of the different components of the C 1s core level spectrum and shake-up satellites in NitPyn deposited on the  $\text{TiO}_2(110)$  single crystal.

	<b>Energy</b> (eV)	<b>Lorentzian Width</b> (eV)	<b>Gaussian Width</b> (eV)	<b>Intensity</b> (%)
<b>C-C</b>	284.28	0.08	0.97	30.70
<b>C-H</b>	284.54	0.08	0.97	38.10
<b>CH<sub>3</sub></b>	284.82	0.08	0.97	16.80
<b>C-N</b>	286.25	0.08	1.20	11.30
<b>S<sub>1</sub></b>	285.40	0.08	0.97	2.90

up excitation i.e., the relaxation after the photoemission process, is attributed to the excitation having same energies and determines the excitation of an outer shell electron from the HOMO to LUMO levels [218]. The  $S_1$  satellite can be related to the first HOMO-LUMO shake-up. Its energy position is 1.2 eV higher with respect to the C 1s main line. This value is lower than the corresponding HOMO-LUMO optical gap obtained by spectroscopic measurements (2.3 eV) [108]. The HOMO-LUMO shake-up transition is a typical phenomenon for polyaromatic systems such as perylene-based molecules [43]. The value of 1.2 eV is in agreement with the value obtained for tetracene [217].

The main reason for the difference between the first HOMO-LUMO shake-up and the HOMO-LUMO optical gap is that the photo-generated core-hole is delocalized over the large aromatic system. The mechanism of core-hole screening is enhanced due to the delocalization of the core-hole over a large aromatic system [217]. There are several factors that influence the intensity of the shake-up satellites. The excitation among electrons of the valence bands and the satellite intensities are correlated, the influential factors can thus be related to the ability of the system to react to the creation of core-hole. As it will be discussed in detail in further sections of

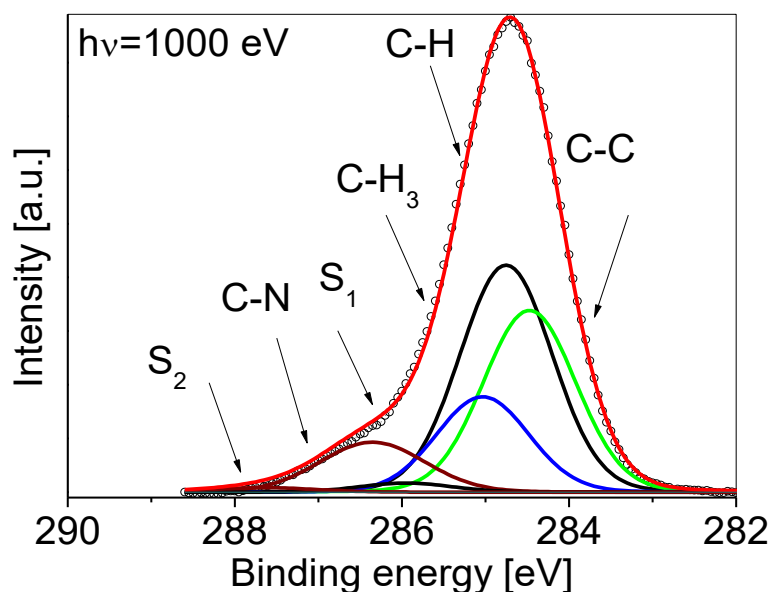


**Figure 4.8:** C 1s core level spectrum of a 2.5 nm nominally thick film of NitPyn deposited on  $\text{TiO}_2(110)$  single crystal.

this chapter, the mentioned factors can be divided into two main groups [214]: First, the intramolecular contribution arising from the capability of the electrons to respond to the alteration of the electronic structure of the molecule as core-hole screening. Second, the reaction of the whole system including the molecule of interest and the molecular surrounding, known as intermolecular contribution [219]. We also notice the presence of a second satellite feature at 287.40 eV. According to stoichiometry arguments, this  $S_2$  satellite may be related to C–N contributions. Now, we look at the N 1s core level spectrum the same time. The N 1s core level spectra are of prime importance in our experiments because N atoms carry the information on the paramagnetic character of NitPyn due to delocalization of the unpaired electron over N–O groups. The analysis of the N 1s core level spectrum delivers vital information about its radical. As Figure 4.9 shows, the main line of the N 1s core level spectrum is centered at 401.92 eV which is in close correlation with the energy position observed for the N 1s main line in the NitPyn thin films deposited on the Au(111) single crystals [211]. NitPyn has an unpaired electron delocalized over the two N–O groups in the nitronyl nitroxide radical which are chemically equivalent. One single intense peak is expected to be observed, as in the case of the N 1s core level spectrum in Figure 4.9. The delocalization of the unpaired electrons within NitPyn causes the electrons to redistribute over the N–O groups. This structure is known as a mesomeric structure [220,221]. In contrast to the Lewis structure which exhibits a region with relatively high electron densities between two nuclei, the charge density in

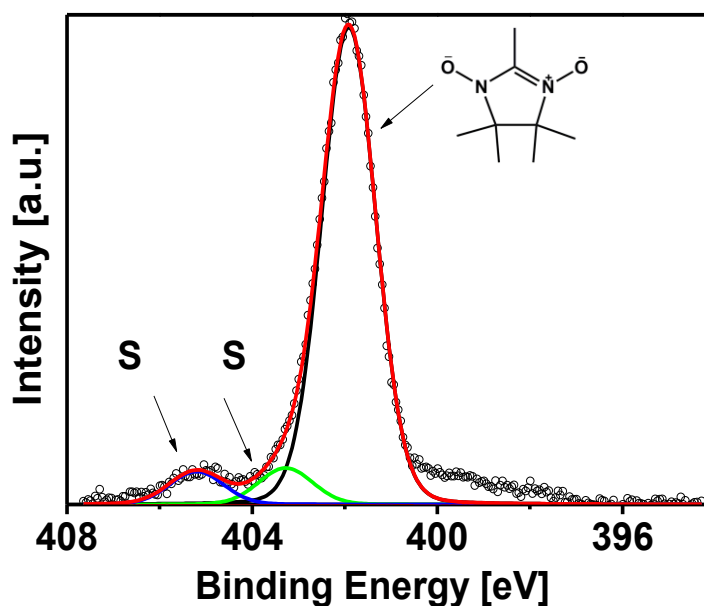


**Figure 4.9:** N 1s core level spectrum of a 2 nm nominally thick film of NitPyn deposited on TiO<sub>2</sub>(110).

this case is distributed over a larger area (over two N-O groups) [222]. Electron delocalization, in the framework of mesomerism, results in the permanent polarization in the ground state of NitPyn [223]. Electron delocalization over the N-O groups lowers the energy of the molecule, thus, makes it more stable. Similarly to the C 1s core level photoemission spectrum, two well-separated features are visible at 1.4 eV and 2.9 eV higher  $E_b$ s than the N 1s core level spectrum of the mesomeric nitrogen (see Figure 4.9). The correspondence between the satellites visible in the N 1s core level spectrum and those in the C 1s XPS spectrum, clearly indicates that the shake-up excitation between orbitals localized on the aromatic parts of NitPyn strongly couples to the N 1s excitation of the nitrogen atoms. Comparing the spectrum in the Figure 4.9 with the spectra of the powder or physisorbed NitPyn molecules [41], we observe that they are similar which implies that the molecules, in the multi-layer films, retain their molecular structure [211]. Figure 4.9 also shows a signal tail in the lower  $E_b$  with respect to the main peak. This signal is assigned to the interfacial contributions such as nitrogen atoms bound to the titanium atoms of the substrate, (Ti-N), or to the hydrogen atoms (N-H). These contributions are dominant at the molecule-substrate interface and we are going to discuss them in the next paragraph.

As it will be discussed in paragraph 4.4.3, the study of the growth mode of the thin film shows that the NitPyn molecule grows first as layer(s) on the bare TiO<sub>2</sub>(110) single crystal. As it exceeds a certain thickness, the molecules assemble as islands on top of the previous layers. Therefore, it is possible to observe the interfacial contributions in also rather thick films. The counterbalance between molecule-substrate and molecule-molecule interactions determines the extent to which the growth mode switches from layer-by-layer to island formation. The existence of interfacial contribution at high coverage hints at the fact that the thin film grows on the TiO<sub>2</sub>(110) single

**Table 4.3:** Binding energy of the N 1s core level spectrum and the shake-up satellites in NitPyn deposited on the TiO<sub>2</sub>(110) single crystal.

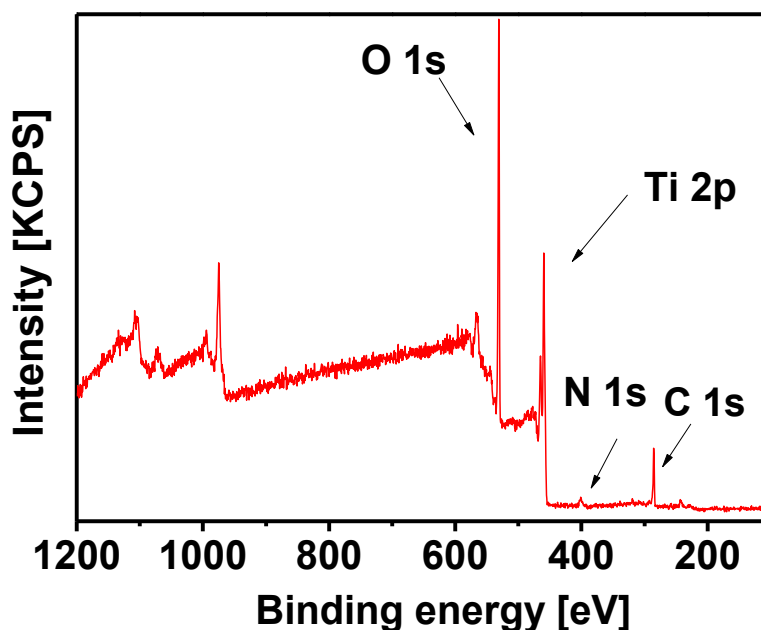
	Energy (eV)	Lorentzian Width (eV)	Gaussian Width (eV)	Intensity (%)
<b>N</b>	401.92	0.1	1.32	87.33
<b>S<sub>1</sub></b>	403.32	0.1	1.32	6.67
<b>S<sub>2</sub></b>	405.20	0.1	1.32	5.00

crystal by S-K growth mode. Further systematic analysis is required to confirm this claim and will be presented also by using AFM investigations in the paragraph 4.4.3.

#### 4.4.1.2 Low coverage

In this paragraph, after the investigation of the high coverage NitPyn thin films, we focus on the study of the same molecule in the sub-monolayer regime. Figure 4.11 shows the recorded C 1s core level photoemission spectra obtained for samples of different nominal thicknesses of NitPyn thin films in the sub-monolayer coverage. Similarly to the C 1s core level spectrum of the multilayer thin film, the C 1s core level spectrum of sub-monolayer films of NitPyn consists of four different components. A nice agreement of the relative intensities of the four components of the C 1s core level spectrum with the stoichiometry of the molecule (See Appendix I, II) implies that the molecular structure of NitPyn remains intact during evaporation and during deposition on the surface of the TiO<sub>2</sub>(110) single crystals.

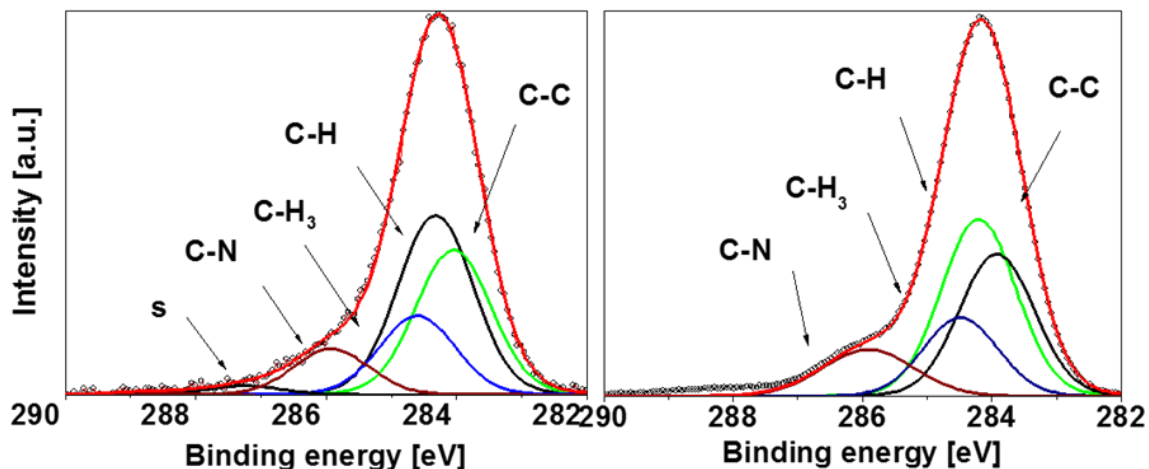
The nominal thickness of the grown thin films on the rutile single crystals are 0.3 and 0.5 nm. By considering that pyrene molecule is 11.66 Å large, 9.279 Å broad, and 3.888 Å thick [224], an assembly in the range from 3 to 10 Å lies in the sub-monolayer regime unless we assume that the molecules adsorb completely flat on the substrate. Our NEXAFS investigation of the orientation of NitPyn with respect to the surface of the substrate in the sub-monolayer coverage (paragraph 4.4.2.2.2), shows that this is not the case [35]. As Figure 4.10 shows, a significant peak intensity related to the C 1s and the N 1s core level spectra indicates a successful deposition of the NitPyn on the surface of the atomically clean TiO<sub>2</sub>(110) single crystal. We aim at investigating whether the molecule is adsorbed on the surface via chemical or physical absorption. If the molecular orbitals of the adsorbed molecules are perturbed, it means that the wave functions of the molecular orbitals of the molecule hybridized, due to strong chemical interactions between the molecules and the substrate, or because of weak physical interaction, the wave functions of the molecular orbitals remain largely unperturbed [224]. The agreement between the relative intensities of the four components of the C 1s core level spectrum (Figure 4.11) and the quantitative composition of the molecule indicates that the deposited molecules in the sub-monolayer coverage, interact with the surface of the TiO<sub>2</sub>(110) single crystal but the pyrene substituents of NitPyn remain unperturbed upon adsorption on the substrate. This observation indicates a lack of strong interaction of the



**Figure 4.10:** Survey spectrum of a 0.3 nm nominally thick film of NitPyn deposited on TiO<sub>2</sub>(110) single crystal.

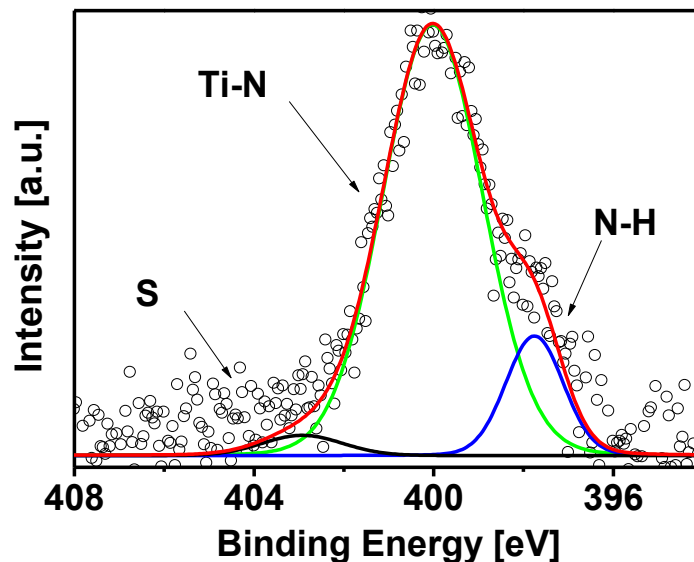
pyrene unit of the molecule with the substrate. We conclude that the radical part of the molecule interacts with the substrate while the pyrene unit of NitPyn is not strongly influenced by the substrate. The analysis of the N 1s core level spectra of the molecule in the sub-monolayer regime of thickness provides first-hand information about the molecule-substrate interface, as well as, the mechanism of NitPyn adsorption.

Figure 4.12 and Figure 4.13 illustrate the N 1s core level spectra of the thin films with different thicknesses in the sub-monolayer coverage. We are able to identify three contributions due to the photoelectrons emitted from nitrogen atoms bound to the oxygen atoms (N-O), nitrogen atoms interacting with the empty d-orbitals of Ti<sup>4+</sup> cations (Ti-N) and nitrogen atoms bound to the hydrogen atoms (N-H). The XPS N 1s core level spectra are characterized by two phenomena at the NitPyn- TiO<sub>2</sub>(110) interface: The E<sub>b</sub> of the main peak shifts toward lower values with respect to the E<sub>b</sub> of the main peak of the N 1s core level spectra recorded for NitPyn deposited on the Au(111) [210]. This value is 401.9 eV for 1.0 nm thick film on TiO<sub>2</sub>(110) and 402.2 eV on the Au(111). The 0.3 eV shift to the lower E<sub>b</sub>s for the sub-monolayer coverage is most likely due to the chemical interaction between N atoms of the NitPyn and the adsorption sites of the TiO<sub>2</sub>(110)



**Figure 4.11:** C 1s core level photoelectron spectra of 0.3 nm (left) and 0.5 nm (right) nominally thick film of NitPyn deposited on TiO<sub>2</sub>(110) single crystal.

single crystal. When two atoms bind together, changes in the  $E_{bs}$  not only take place for the valence electrons but the core electrons also experience changes in  $E_{bs}$ . Figure 4.12 and Figure 4.13 show the complex spectral line in the N 1s core level spectra of 0.3 nm and 0.5 nm nominally thick films of NitPyn. Two lines at 400 eV and 398 eV that are related to the N-H and Ti-N contributions, respectively, are identified for the spectrum recorded for nominally 0.3 nm thick film. The assignments agree with the interpretation of the N 1s core level spectra of a wide variety of organic molecules adsorbed on the rutile TiO<sub>2</sub>(110) single crystal surface [27, 226, 227]. The study of the thin films with different thicknesses from 0.3 nm to 1.0 nm (Figure 4.12 and Figure 4.13), shows that by increasing the film thickness, a peak is visible at 401.9 eV and upon further increasing of the thickness of the thin film. It is dominant relatively to the other contributions (N-H and Ti-N). The study of the N 1s core level spectra of the unperturbed NitPyn deposited on gold and sapphire demonstrate that this peak corresponds to the mesomeric nitrogen atoms [108, 210]. As mentioned in the paragraph 4.2, sputtering of the surface of the TiO<sub>2</sub>(110) give rises to the oxygen vacancies with a broad range of density depending on the cleaning procedure. These oxygen vacancies, even at very low percentages, in the nearly defect-free surfaces, are the origin of Ti<sup>3+</sup> 3d states contributions. Vacancies favor adsorption of molecular water either in the intact or dissociated form. Adsorption of molecular water on the TiO<sub>2</sub>(110) single crystal surface, leads to the partial



**Figure 4.12:** N 1s core level photoelectron spectrum of a 0.3 nm nominally thick film of NitPyn deposited on TiO<sub>2</sub>(110).

hydroxylation of the surface, and, consequently the coexistence of clean and hydroxylated surface regions in TiO<sub>2</sub>(110) single crystals [200, 201].

The behavior of the nitronyl nitroxide radical derivative in solution, could be useful to understand the behavior of NitPyn during evaporation and deposition on the surface of the substrate. Ultimately, it can elucidate the mechanism of the adsorption of the molecule at this interfaces. Ullman and co-workers showed that nitronyl nitroxide radical derivatives in solution tend to spontaneously lose an oxygen atom of the N-O groups without further decomposition [227]. According to their report, the radicals are highly stable and losing an oxygen atoms does not lead to further decomposition of the molecule. The compounds can be reconverted to the initial structure with appropriate chloroperbenzoic acid treatment [227]. All compounds (independently of their substituent) may be reversibly protonated without decomposition [228]. Therefore, at the interface, the evaporated molecules first lose the oxygen atom located in the N-O group, spontaneously, without further decomposition, then the nitrogen atom will bind either to the hydrogen atoms of the O-H group of the hydroxylated surface or to the titanium atoms of the atomically clean surface. Thus, the initial mode of the adsorption of the organic molecule involves reaction of the nitrogen atoms with the titanium atoms on the substrate surface, as well as, hydrogen

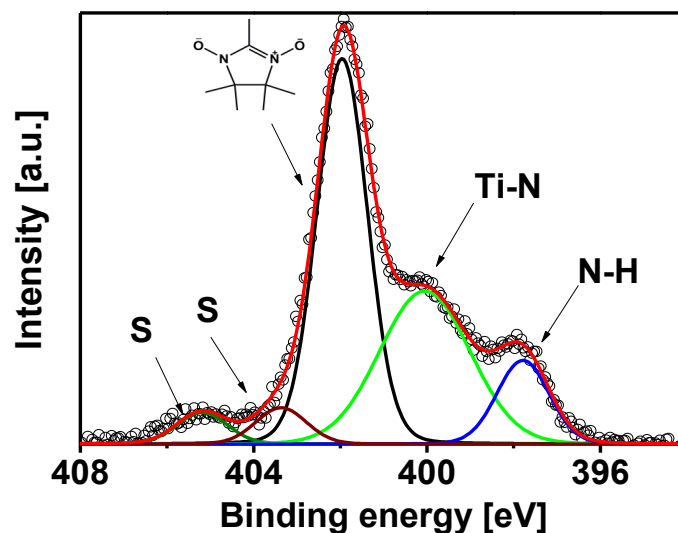


**Figure 4.13:** N 1s core level photoelectron spectrum of a 0.5 nm nominally thick film of NitPyn deposited on TiO<sub>2</sub>(110) single crystal.

sites. A (110) surface contains fivefold coordinated Ti atoms along [001], the molecule adsorption is expected to occur a long [011] direction in bridging configuration.

#### 4.4.1.3 N 1s core level spectra of NitPyn on the TiO<sub>2</sub>(110) single crystal with different density of defects

The relation between adsorption of the molecular water and the density of the oxygen vacancy at the surface or subsurface of rutile has not been entirely elucidated yet. To study the evolution of adsorbed thin films with varying defect population, thin film of 3 Å nominal thicknesses of NitPyn is deposited on the two different rutile (110) single crystals. The density of the oxygen vacancy at the two surfaces are 1.5% (nearly perfect surface) and 8.5% (vacancy rich surface) respectively. By considering the fact that missing one bridging oxygen atom from surface or subsurface of the TiO<sub>2</sub>(110) single crystal, introduces one oxygen atom vacancy and two Ti<sup>3+</sup> states in the surface or subsurface of the single crystal, the density of the oxygen vacancy equal to 1.5% and 8.5% correspond to the 3% and 17% of the Ti<sup>3+</sup> states, respectively.

Comparing the left and the right part of the Figure 4.14 shows that the integrated signal intensity of the N-H in the heavily reduced surface is higher than the intensity of the signal intensity on a nearly perfect surface. This finding shows that there is a direct correlation between the density of the oxygen vacancy and the percentage of the molecules bound to the hydrogen atoms. Defects are found to alter the characteristic of the NitPyn and promoting adsorption on the hydroxylated

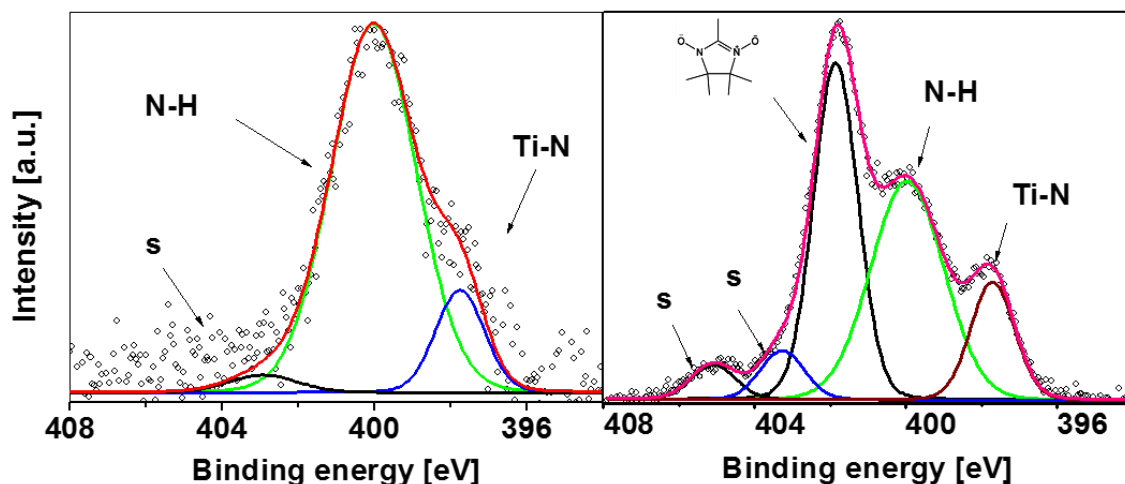


**Figure 4.14:** N 1s core level photoelectron spectra of a 0.3 nm nominally thick film of NitPyn deposited on TiO<sub>2</sub>(110) single crystal with density of Ti<sup>3+</sup>3d states of (left) 17% and (right) 3%.

sites. This analysis presents an important aspect of the adsorption of NitPyn on the rutile (110) surfaces, i.e., there is a clear tendency of the molecule to favor binding with the hydrogen atoms localized at the surface of the substrate.

#### 4.4.1.4 O 1s core level spectra

Figure 4.15 presents the O 1s core level spectrum acquired after deposition of a 2 nm NitPyn on a TiO<sub>2</sub>(110) single crystal. The O 1s spectrum is important in our experiments because of the following reason: As mentioned before, the magnetic momentum carrying unpaired electrons are delocalized mainly over the two equivalent N-O groups of this pyrene derivative. Therefore, the O 1s as N 1s core level spectra are used to ascertain the intactness of the paramagnetic nature of NitPyn. The intensity of the signal related to the oxygen atoms belonging to the substrate, O<sub>sub</sub>, decreases upon NitPyn deposition but its E<sub>b</sub> remain unchanged upon NitPyn adsorption which confirms that the oxygen vacancies are not filled by NitPyn molecules. Because of the presence of oxygen atoms both in TiO<sub>2</sub>(110) single crystals and NitPyn, distinguishing the O 1s core level spectra originated from the substrates and those arising from the NitPyn in thin layers is difficult. For sufficiently thick layers so that the thickness of the film is three times larger than the values of the IMFP of the elements of the substrate, photoelectron spectra contain only contribution of the photoelectrons from the deposited thin film. Consequently, the observed O 1s core level spectra

are conventionally assigned to the oxygen atoms of the NitPyn. Considering the difficulty in precise distinction of different O 1s contributions and in order to facilitate a systematic comparison of the paramagnetic character of the layers with different range of thicknesses, we discuss mainly the N 1s core level spectra.

Figure 4.15 shows that, besides the almost symmetrical nature of the surface O 1s signal at 531.08 eV, the spectrum contains two other components at 1.4 eV and 2.3 eV higher  $E_{bs}$  with respect to the main line, due to photoemission from surface hydroxyls formed from dissociative adsorption of the molecular water on the oxygen vacancies at the surface of the  $TiO_2(110)$  single crystal and lattice O atoms [228]. They can be distinguished in the hydroxylated substrate before deposition by their different  $E_{bs}$ . After deposition of a 2 nm thin film, a second feature accompanied by a satellite is evident at 4 eV higher  $E_b$  than the main signal and it is assigned to the signal from the O atom of this pyrene derivative, by using a peak-fit analysis.

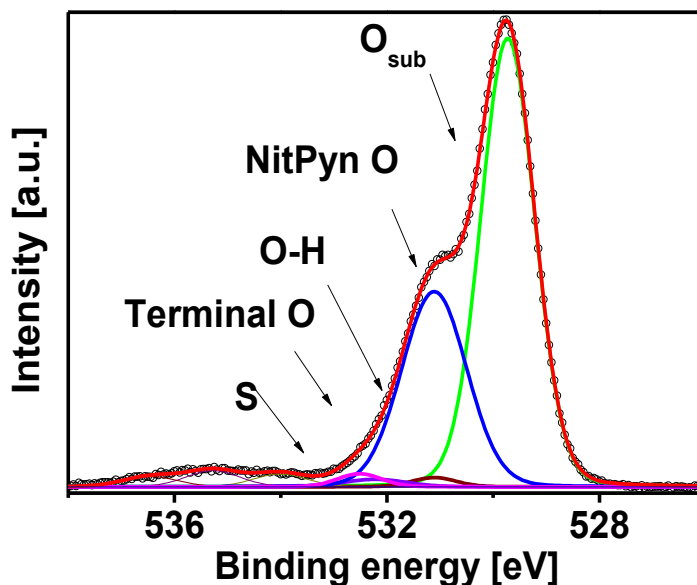


**Figure 4.15:** O 1s core level spectrum after deposition 2 nm nominally thick NitPyn film.

#### 4.4.1.5 Different excitation energy

##### 4.4.1.5.1 C 1s core level spectra

In this set of experiments we study the variation of the peak position and the shape of the C 1s core level spectra of NitPyn deposited on the surface of TiO<sub>2</sub>(110) with different thickness (from 0.3 nm to 6 nm) and probed with X-ray with a broad spectrum of excitation energies (330, 640 and 1000 eV). It is worth noting that the measured  $E_b$  depends on several factors such as chemical state, electronic level or band structure, and dynamic screening effect [229]. The main reason for employing a X-ray source with tunable excitation energy is varying the IMFP,  $\lambda$ , and thus the surface and bulk sensitivity of the measurements [230]. The other consequence of varying the photon energy is changing the C 1s cross section. Increasing excitation energy of the incident X-ray results in increasing the probability of interaction between the electromagnetic wave (which in this case lies in the X-ray wavelength range) and the atom of interest (carbon atom or nitrogen atom). Variation in the C 1s cross section also leads to an increase in the number of effects to be further accounted for. It also provides an opportunity to study the mechanism of core-hole screening [35].

Figure 4.16 shows that upon varying the excitation energy, the peak position and the shape of the C 1s core level spectra remains unchanged. This indicates an absence of the surface core level shift (SCLS) in the C 1s core level spectra. The SCLS is discussed as the core level  $E_b$  difference between atoms of the surface and the corresponding bulk atoms. In order to unravel the phenomena leading to these results, the mechanism of photoemission in organic solids should be considered. These class of solids are prominently governed by non-covalent van der Waals forces and are characterized by strong intramolecular bonds, weak intermolecular bonds and a dielectric constant which is not too high [230]. As it mentioned previously, no SCLS is observed in the C 1s XPS spectra of the thin films of NitPyn deposited on TiO<sub>2</sub>(110) surface. Here we try to count the phenomena leading to the SCLS in the organic solids.

In a core electron photoemission process, a core-hole is generated once a core electron is excited from a core level to the vacuum level due to the adsorption of a photon. The photo-generated core-hole will be localized over the molecule or molecular neighbors. Since localization of the created hole is accompanied by electrostatic polarization of the surrounding molecules in the photoemission process. Photoemission  $E_b$  is correlated with localization of the hole and hence

polarization of the vicinity of the hole. The difference between the mechanism of hole creation at the surface and the same photoemission event in the bulk of the sample results in the difference in the polarization and hence in the photoemission  $E_b$  for the surface and the bulk, as long as, the effective charge remains localized within the atoms or the molecules. In a quantitative expression, the electrostatic energies of the localized positive charges created at the surface is different with the energy of the charges in the bulk. SCLS in the organic solids are possible to be understood in terms of screening effect. There are three possibilities to address the mechanism of charge screening in the organic materials: Screening of the created charges (i) by single atom, (ii) by single molecule and (iii) by whole the system [230]. In other words, the extent to which the photo-generated charge is localized may vary over an atom, a single molecule or whole the system including under study molecule.

In the first case, the final state should be represented as atomic fully charged state and the result can be reproduced by using a model based on the point charged configuration [230]. As no SCLS being observed in the organic materials, localization of the created charge on the single atom cannot be the case in these materials.

In the second case, charge screening is possible to be interpreted in terms of charge redistribution inside the isolated molecule. In this case, the molecule relaxes its geometrical structure to compensate the metastable charged state.

The last reason for the absence of the SCLS is charge screening by whole the system [231]. In this case, the role of the intermolecular coupling, is significantly important. One interpretation for the absence of the SCLS in the organic materials is the occurrence of charge screening in an efficient way. It would mean that there is no significant difference between the mechanism of the hole creation at the surface and in the bulk of the organic solids. As a consequence, reaction of the environment to these photoemission events is the same both at the surface and in the bulk of the organic thin film. In this case, the charge will be delocalized over entire electronic system due to high degree of intermolecular coupling and core-hole screening occurs by intermolecular charge transfer between NitPyn molecules.

Figure 4.17 shows the C 1s core level spectra of a 2.5 nm nominally thick film of NitPyn taken at different photon energies. A detailed comparison of the XPS signals obtained from

different range of the surface sensitivity (from 330 eV to 1000 eV). Figure 4.17 shows that the main line in the C 1s core level spectra is identical and it does not reveal any energy shift or change in the line shape of the core level spectra related to C-C, C-H or C-H<sub>3</sub> when the molecule is probed by x-ray with tunable energy. Now, we investigate variation of the shape of the signal related to the C-N contribution. The analysis of the Figure 4.17 shows slight variations in both the intensity as well as the FWHM of the signals related to the C-N contributions. To quantitatively investigate the variation in the shape of the C-N core level line, the change in the FWHM of the C-N contribution upon increasing film thickness is studied. As fitting procedure of Figure 4.17 shows, the FWHM of the C-N contribution decreases from 1.65 eV to 1.45 eV by increasing thickness from 0.3 nm to 6 nm (see appendix II).

There are several contributions such as intrinsic life time broadening, experimental contributions, vibronic and inhomogeneous broadening that influence the line shapes in the XPS spectra of the molecules [130]. The contributions like intrinsic life time and experimental contributions are constant for all the curves. In this particular case, the differences between the FWHM of the spectra for the sub-monolayer (1.65 eV) and multi-layer coverage (1.45 eV), stems

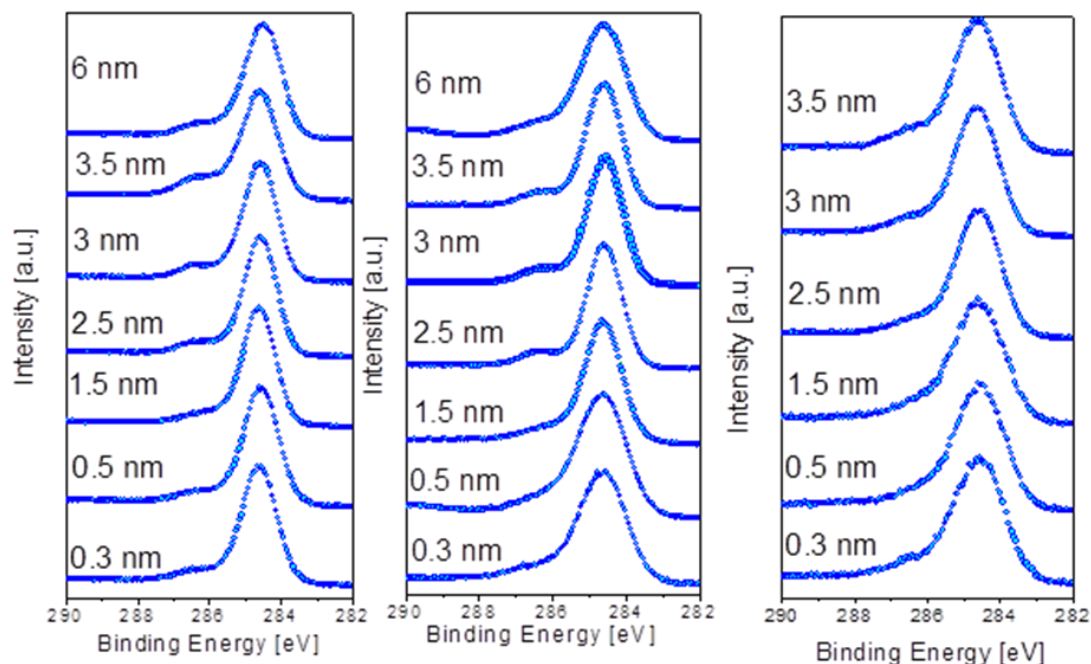


**Figure 4.16:** Photoemission spectra of C 1s core level for NitPyn deposited on the TiO<sub>2</sub>(110) with incident photon energies of 330 eV (left), 640 (middle) and 1000 eV (right).

from different molecular packing in the sub-monolayer film with respect to the thicker layers. The intensity of the satellites appearing at the higher  $E_{bs}$ , decreases inversely with the excitation energy indicating that the phenomena are not related to the SCLS but it may be related to the orientation of the molecules with respect to the surface of the substrate in the different thicknesses of the vapor-deposited thin film.

In order to understanding the origin of these behaviors, as first step, the mechanism of NitPyn adsorption on the  $TiO_2(110)$  single crystal should be considered. Study of the NitPyn- $TiO_2(110)$  interface indicates that prior to landing NitPyn on the surface of the substrate, oxygen atoms from N-O group are released and nitrogen atoms, interact with the adsorption sites [34]. Consequently, the carbon atoms bound to the nitrogen atoms are withdrawn in different levels, they experience different environments at the different layers. In particular, at the organic molecule-single crystal interface, where the nitrogen atoms are covalently bound to the adsorption sites, the chemical environment of the carbon atoms in the C-N group is different with that in the subsequent layers. In thicker layers, the influence of the strong chemical forces originated from the substrate are diminished and the weak molecule-molecule interactions are the driving force for film formation. Second, the rest of the carbon atoms in the structure of NitPyn do not interact with the surface even in the sub-monolayer regimes. NEXAFS study supports the idea of variation of

**Table 4.4:** Fit results for the energy position and relative intensity of photoemission and satellite line in the C 1s core level spectra of the NitPyn deposited on  $TiO_2(110)$  single crystal at 330 eV, 640 eV and 1000 eV.

	<b>Energy (eV)</b> <b>(<math>h\nu = 1000</math>)</b>	<b>Intensity</b> <b>(%)</b>	<b>Energy (eV)</b> <b>(<math>h\nu = 640</math>)</b>	<b>Intensity</b> <b>(%)</b>	<b>Energy (eV)</b> <b>(<math>h\nu = 330</math>)</b>	<b>Intensity</b> <b>(%)</b>
<b>C=C</b>	284.50	30.59	284.50	30.32	284.50	29.14
<b>C-H</b>	284.78	38.32	284.78	38.28	284.78	35.97
<b>C-H<sub>3</sub></b>	285.06	16.81	285.06	16.60	285.06	16.96
<b>C-N</b>	286.41	11.60	286.41	11.27	284.41	11.04
<b>S<sub>1</sub></b>	285.65	2.30	285.65	2.53	285.65	6.30
<b>S<sub>2</sub></b>	287.78	0.04	287.78	1.00	287.78	1.00

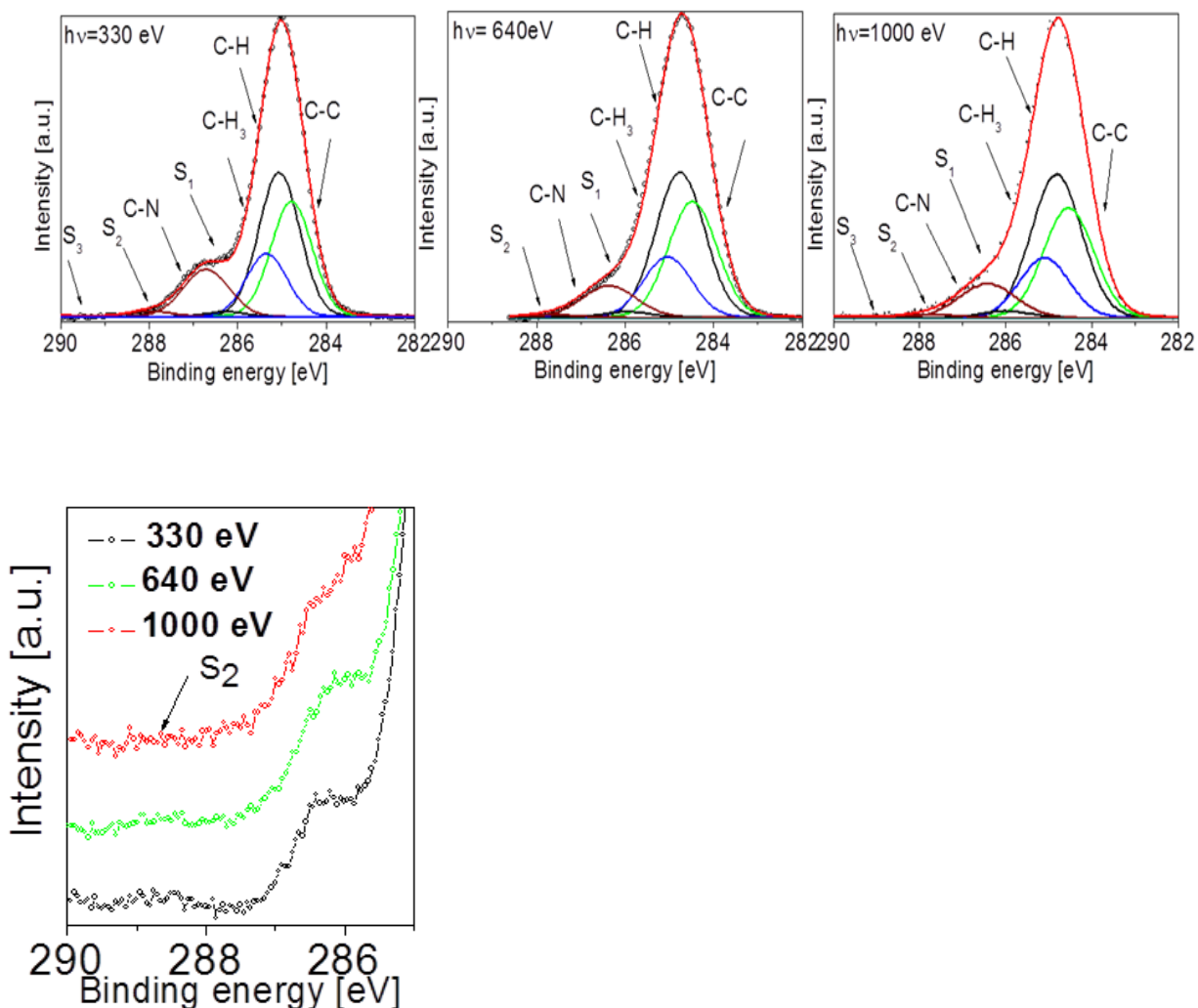


**Figure 4.17:** C 1s core level spectra of a 2.5 nm nominally thick film of NitPyn taken at different photon energies.

the molecular orientation with respect to the surface of the substrate in different layers of the vapor deposited thin film as discussed in the paragraphs 4.4.2.1.2 and 4.4.2.2.2.

#### 4.4.1.5.2 The C 1s core shake-up spectra of NitPyn

Here, we aim at extracting information about the ground state, as well as, the electronically excited states of NitPyn by analyzing the C 1s photoelectron shake-up spectra of the molecule adsorbed on the TiO<sub>2</sub>(110) single crystal. Prior to the analysis of the photoemission satellites, it should be considered that the satellites have been categorized into two main groups. The first class includes the satellites excitation cross sections relative to the single-hole ionization cross sections that stays constant while whose excitation cross sections of the second class of satellites decreases with increase the excitation energy [231]. Figure 4.17 illustrates the C 1s core level spectra of the NitPyn

which has two satellite features visible at the 1.2 eV and 3.2 eV higher Ebs with respect to the main peak. In order to better compare the satellite intensities, the spectra are normalized to the intensity of the main peak. Since the energy position of the first satellite overlaps with the main C 1s, precise quantitative analysis of the first satellite is not straightforward. The intensity of these satellite structures are 3% and 1% of the main peak respectively. These shake-up structures stem from core-ionized molecules while the core-hole is localized on the carbon atoms located in the aromatic rings (C-C and C-H) and the carbon atoms belong to the methyl groups (CH<sub>3</sub>) which is marked by S<sub>1</sub>. The other shake-up structure labeled by S<sub>2</sub> could be due mainly to the ionized core-hole localized on the carbon atoms of the C-N group. The first HOMO-LUMO shake-up satellites correlate with the electronic transitions in the photoemission final states and the optical HOMO-LUMO gap is related to the electronic transition from valence band in the neutral molecule. In the basis of the fact that both of S<sub>1</sub> and S<sub>2</sub> stem from the electronic transition, making comparison between these two HOMO-LUMO shake-up satellites would be meaningful. This comparison provides further information about the mechanism of screening of the core – hole in the electronic structure upon photo-excitation. Rocco et al investigated the variation in the intensity of the two mentioned HOMO-LUMO satellites as function of the size of the molecule and concluded that the electronic relaxation leads to stronger decreases in energy for the shake-up final state with the hole in the HOMO and an electron in the LUMO than optical HOMO-LUMO gap [217]. It is the core-hole screening by a redistribution of the charge in the larger molecules [217]. The second HOMO-LUMO shake-up (S<sub>2</sub>) for the excitation energies of 330, 640 and 1000 eV is illustrated in Figure 4.17 (lower panel). The satellite features are very similar in all excitation energies. The position of the satellites remains unchanged by varying the excitation energy. By increasing the excitation energy, the intensity of the S<sub>2</sub> decreases while behavior of the first satellite shake-up is not clear and thus, is not fully understood. In order to interpret this behavior of the S<sub>1</sub> and S<sub>2</sub> shake-up satellites as function of the excitation energy, it has to be mentioned that satellites can be classified into two groups:

1. The satellites which the excitation cross section remains constant by increasing excitation energy. This kind of energy dependence have been attributed to the lowest order correlation called direct shake-up terms. In this case, the dipole photo-emission from the core orbital is accompanied by a monopole excitation of the valence electron [231].

2. The satellites which the excitation cross section relative to the single hole ionization cross section dramatically decreases with increasing excitation energy. This variation in the intensity of the satellite as function of energy is attributed to the conjugate shake-up terms. In this case, the dipole excitation of the core electron to an unoccupied molecular orbital is in conjunction with the monopole ionization of the valence electron [231].

According to the above classification, one may conclude that in the case of NitPyn, the intensity of the first HOMO-LUMO shake-up is related to the dipole excitation of a core electron to the valence orbital while the monopole ionization of the valence electron occurs simultaneously [231,232]. This phenomena has been observed in small molecule such as carbon monoxide [231–234] and benzene [232].

#### 4.4.1.5.1 N 1s core level spectra

The next step of our experiment in the study of the variation of the  $E_b$  and the shape of the N 1s core level spectra of NitPyn deposited on the surface of the TiO<sub>2</sub>(110) single crystal with different thickness (from 0.3 nm to 6 nm) probed by X-ray with different excitation energies (640 and 1000 eV). Figure 4.18 shows that the peak position of the N 1s spectra remains unchanged by varying the excitation energy. Following a variation of the shape of the spectra by increasing the thickness of the film looks more complicated than the case of the C 1s core level spectra due to the presence of interfacial contributions. Weight of the mentioned contributions and the manner they alter by variation film thickness are not identical. Variation in the shape of the N 1s core level spectra is expected to occur in direct correlation with the variation in the C-N part of the C 1s spectra. The reason for these alterations is that in contrast to the pyrene part of the NitPyn which is not in direct contact to the substrate, the nitrogen atoms interact with the adsorption sites of the substrate. Therefore, the molecules are subjected to very strong influence of the substrate that is attenuated by increasing thickness of the film. Changes in the FWHM of the N 1s spectra of the N-O group as a function of film thickness is quantitatively investigated. As Figure 4.18 illustrates, the FWHM of the N 1s spectra of the mesomeric nitrogen atoms decrease from 1.7 eV to 1.4 eV by increasing the film thickness. The variation in the FWHM upon increasing thickness of the thin film is related to the different chemical environments of the molecules in different layers. The other reason for

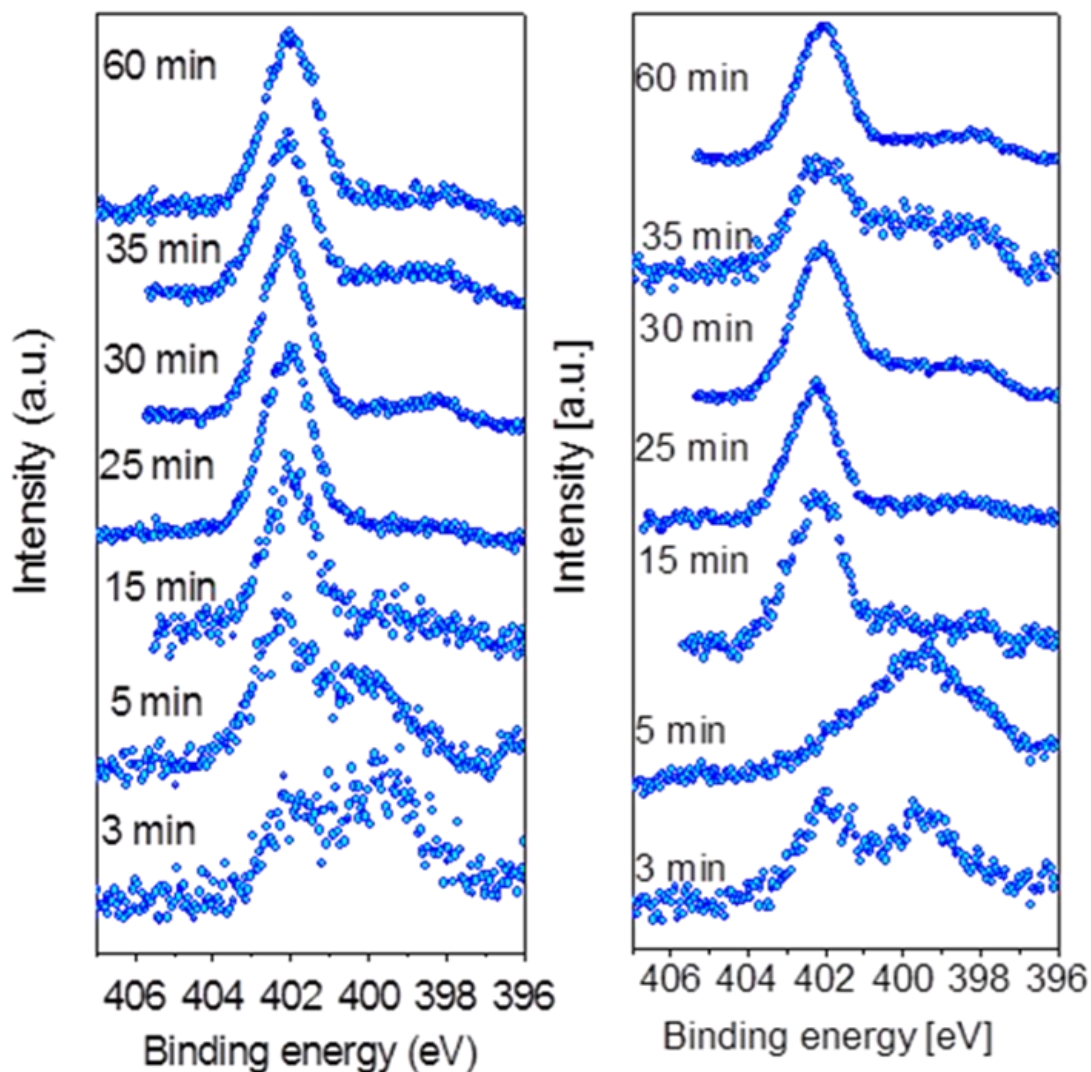


**Figure 4.18:** Photoemission spectra of the N 1s core level for NitPyn deposited on the TiO<sub>2</sub>(110) with incident photon energies of 640 eV (left) and 1000 eV (right).

variation of the shape of the mesomeric nitrogen atom is a change in the orientation of the assembled molecules with respect to the substrate by increasing film thickness. The sensitivity of the N 1s core level spectra to the perturbation of the organic radical is discussed in the previous sections. This perturbation can arise from either degradation of the molecule or the strong chemical interaction between organic radical and the substrate. NitPyn degrades to imino-nitroxide or diimino derivative products. These products are mirrored by spectroscopic lines at the lower Ebs relative to the main N 1s peak. Figure 4.19 shows a contribution line at the Ebs between 398 and 400 eV (for both samples) which its percentage is determined by XPS line analysis and it is equal to 4.8%.

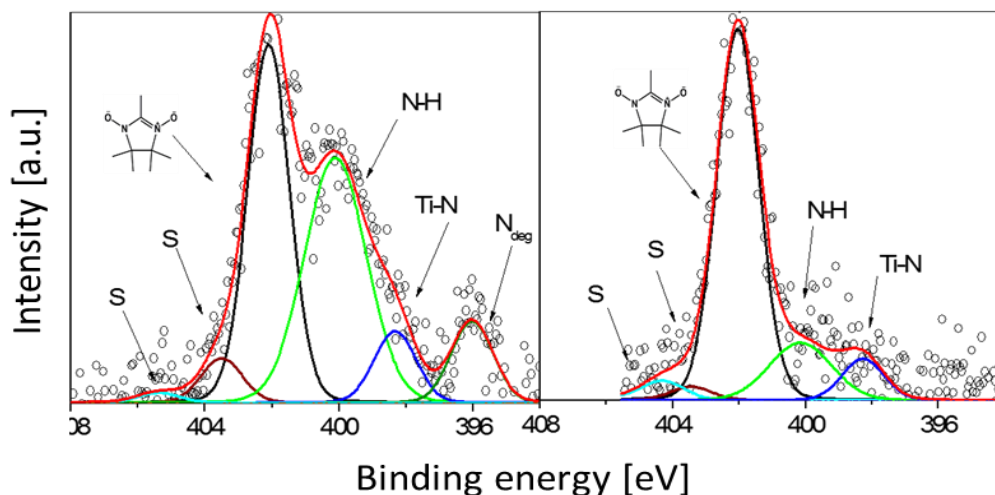


**Figure 4.19:** N 1s core level spectra of 0.5 nm (left) and 1.5 nm (right) nominally thick film of NitPyn deposited on  $\text{TiO}_2(110)$  single crystal (excitation energy= 1000 eV).

#### 4.4.2 NEXAFS measurements

To further characterize the thin film, we perform NEXAFS spectroscopy aiming at the investigation of the unoccupied states. As it is shown in previous paragraphs of this chapter, XPS is a very powerful technique employed to analyze materials and thin films by probing occupied states of the understudy molecules. In order to perform a comprehensive study, we need to combine these information with those obtained by probing the unoccupied states.

NEXAFS spectroscopy belongs to the broader class of techniques known as X-ray adsorption spectroscopy (XAS) which deals with the adsorption cross-section near the (1s) ionization step and directly probes the unoccupied states [96]. Depending on the excitation energy, the final states can be categorized to the discrete molecular orbitals when the excited electrons are adsorbed in the antibonding orbitals or may be free vacuum states in the cases that the excitation energy is sufficient to excite the electrons above the Fermi level.

The energy of the NEXAFS resonances provides information about the environment of specific chemical elements while the photon energy is scanned in a region several tens of electron volts above the edge resulting in measuring the adsorbed X-ray intensity [235]. In addition, some information can be gained from NEXAFS spectra about bonding properties as well as local charge distributions. As discussed, the other useful property of the NEXAFS spectra is to quantitative determination of the orientation of the molecules forming the thin film with respect to the plane of

the substrate [<sup>118</sup>]. In our particular case we employed this technique as a complimentary technique coupled with XPS measurements to perform a comprehensive study of the electronic and magnetic structures of the metal-free magnets by probing unoccupied states.

#### 4.4.2.1 NEXAFS spectra of multilayer

##### 4.4.2.1.1 C-K edge NEXAFS spectra of multilayer

Here, we aim at the analysis of structural properties of the molecule by studying the C-K edge NEXAFS spectra. A comparison is made between the NEXAFS spectra of NitPyn and pyrene as well as pyrene-based molecules in order to interpret the spectral features and assign the resonances in the NEXAFS spectra, [<sup>236, 237</sup>]. The comparison facilitates the characterization of the C-K edge NEXAFS spectra. These spectra are characterized by two main regions: the  $\pi^*$  region up to around 290 eV and the  $\sigma^*$  region that lies in the photon energy range above 290 eV (see Figure 4.21). We will focus on the  $\pi^*$  region resonances, which show sharper features that can be assigned to specific transitions. In the  $\pi^*$  region, three sharp resonances are observed at 284.9, 285.5 and 286.2 eV which have C=C character. This correspond to the transitions from the C 1s initial states of the C atoms to the LUMOs. There are two other features visible at 287.7 and 289.7 eV. In contrast to the previous features they have a mixed nature ( $\sigma^*(\text{C-H})$  and  $\pi^*(\text{C=C})$ ).

In the  $\sigma^*$  region, which are dominated by relatively broad lines, two resonances are visible. They have a mixed character (C-C, C=C and C-N) and  $\pi \rightarrow \pi^*$  shake-up contributions due mainly to the transitions from the 1s core levels of the C atoms to the antibonding  $\sigma^*$  orbitals of the molecule [<sup>237</sup>]. The resonances observed in the  $\sigma^*$  region are not as sharp as those visible in the  $\pi^*$  region. The reason for the difference between line shape in the two different region backs to the correlation between lorentzian width of the line shape and the final state life time which is determined by the created core-hole decay. In other words, the decay probability of the electron in the continuum states increases dramatically leading to a broadening of the line shape of the NEXAFS spectra in the  $\sigma^*$  region [<sup>119</sup>].

##### 4.4.2.1.1.1 Orientation analysis with NEXAFS spectroscopy

As we discussed earlier, NEXAFS spectra can be used to determine the average spatial orientation of the molecular plane in the vapor – deposited thin film with respect to the surface. The transition energy and the intensity of the features in the NEXAFS spectra is related to the presence of the

specific elements and their chemical environment, while, some of the specific transition also depend on the orientation of the transition dipole moment associated with the transition relative to the polarization vector of the linearly polarized X-ray beam [238]. In our particular case, by investigating the C-K edge NEXAFS dichroism, we can calculate the orientation of the molecular plane of the pyrene unit with respect to the surface of the substrate. We focus on the resonance observed at the 285.5 eV and as it is shown in Figure 4.20, this calculation yields  $48^\circ$  as the angle between the pyrene unit of NitPyn and the substrate. The average orientation of the molecular plane of the pyrene substituent is in agreement with the crystalline structure of NitPyn [149]. This arrangement is mainly consequence of the counterbalance between two different driving forces: the tendency of the molecule to have the major  $\pi$  electron sharing and the intermolecular interaction of the NitPyn with the surrounded molecules in the structure of the thin film. This has been also observed in other nitronyl nitroxide radicals [239, 240] as well as, in small molecules [241, 242].

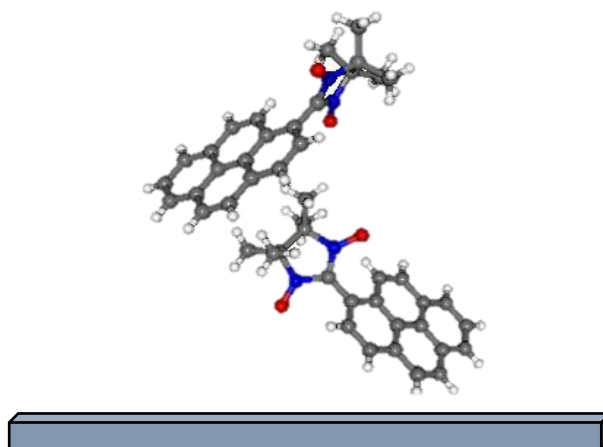


**Figure 4.20:** Crystal structure of NitPyn

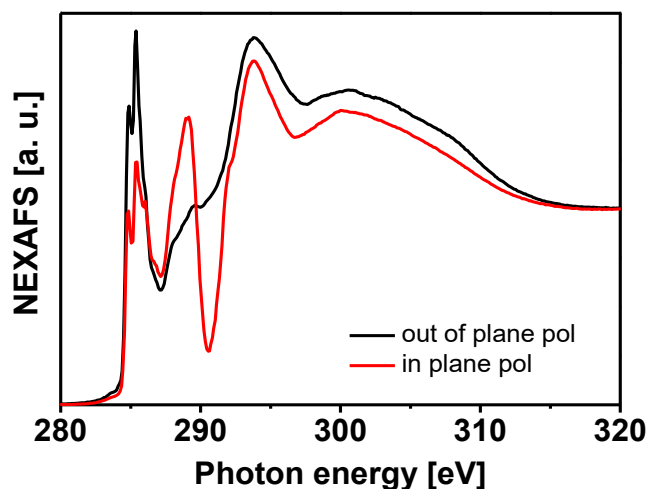


**Figure 4.21:** C-K edge NEXAFS spectra obtained from thin film in multilayer regimes (2.3 nm). The spectra are taken in grazing incidence for p-pol (red curve) and s-pol (black curve) polarization.

#### 4.4.2.1.2 N-K edge NEXAFS spectra of multilayer

The importance of the N-K edge NEXAFS spectra stems from the fact that N atoms carry information about the radical nature of the molecule, because of the delocalization of the unpaired electron over the two equivalent N-O groups. The N-K edge NEXAFS spectra (like the C-K edge NEXAFS spectra) is characterized by two main regions: The  $\pi^*$  region between 398 and 404 eV, and the  $\sigma^*$  region that lies in the photon energy range above 404 eV (as shown in the Figure 4.22). In the  $\pi^*$  region, several sharp resonances are observed that are related to the transitions from the N 1s initial states of the N atoms to the  $\pi^*$  antibonding molecular orbitals. This assignment is based on previous studies on NO [244,245], amino acids [246] and phthalocyanines [247–249]. In the  $\sigma^*$  regions, several relatively broad resonances are visible; they are due mainly to the transitions from the N 1s core levels of the N atoms to the antibonding  $\sigma^*$  orbitals of the molecule [246]. The main reason for the broad shape of the feature is that they have mixed character and various contribution such as  $\sigma^*$  (N-C) are included. As discussed, the other reason for the broadening is that the decay probability of the electron in the continuum states is remarkably higher in comparison to the  $\pi^*$  region [250]. All assigned feature in the 398 to 410 eV photon energy interval have analogy with

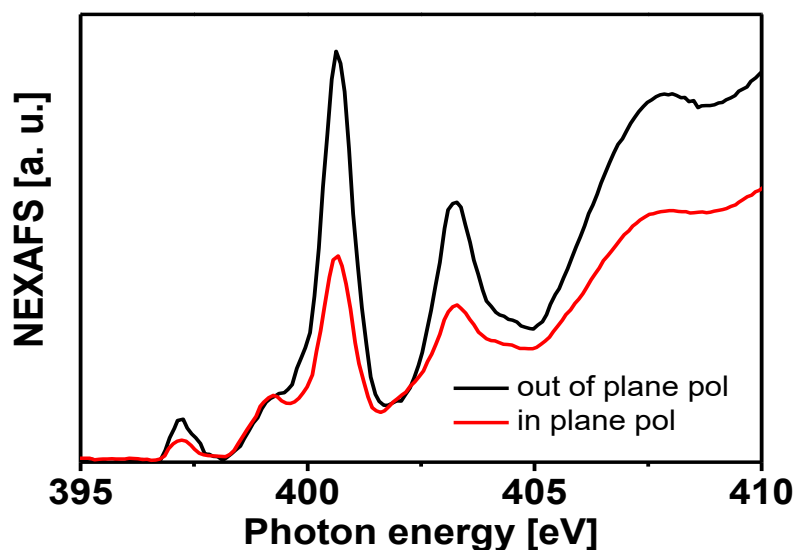


**Figure 4.22:** N-K edge NEXAFS spectra obtained from thin film in multilayer regimes (2.3 nm). The spectra are taken in grazing incidence for p-pol (red curve) and s-pol (black curve) polarization.

peak energy and behavior of the features in the N-K edge NEXAFS spectra of small organic molecules [35]. An additional feature is visible in the N-K edge NEXAFS spectra of NitPyn at the photon energy of 397.2 eV which has not been observed in the other investigated molecules. The photon energy region below 398 eV is known as “pre-edge“, the resonance corresponds to the transition of the N-K electrons from 1s orbitals to the singly occupied molecular orbitals (SOMO). As we discussed, the paramagnetic property of the molecules is related to the presence of the unpaired electrons delocalized over N-O groups. The feature at 397.2 eV corresponds to the excitation of electron from 1s orbitals to the SOMO. The direct consequence of this finding is that the unpaired electron in the N-O groups is not influenced by either evaporation of the molecule or assembly as condensed film on the TiO<sub>2</sub>(110). Consequently, we can conclude during the thin film formation, the paramagnetic properties of the thin film NitPyn molecule are preserved.

#### 4.4.2.2 NEXAFS spectra of the sub-monolayer

##### 4.4.2.2.1 C-K edge NEXAFS spectra of sub-monolayer

The C-K edge NEXAFS spectra of the thin film in the sub-monolayer regime of thickness is

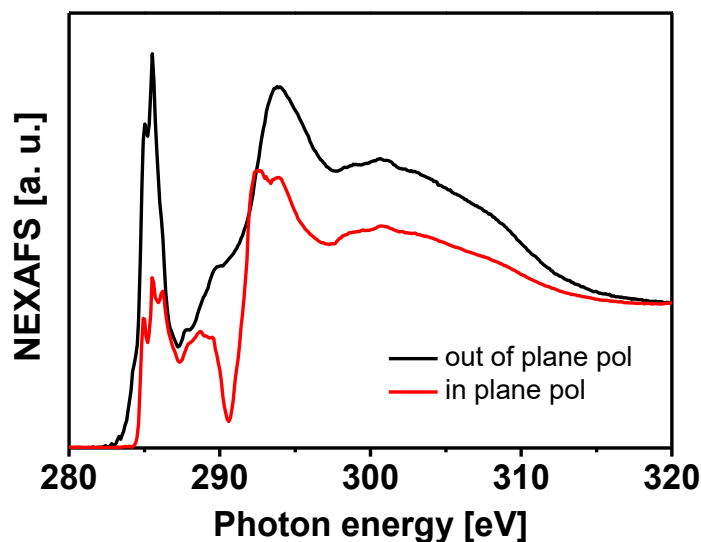


**Figure 4.23:** C-K edge NEXAFS spectra obtained from thin film in the sub-monolayer regimes (0.3 nm). The spectra are taken in grazing incidence for p-pol (black curve) and s-pol (red curve) polarization.

showed in Figure 4.23 for two different polarization directions of the incident light (in plane polarization and out of plane polarization). The resonances resemble those observed for thick films. Therefore, many conclusions obtained for thick layers can be generalized to the interface films regardless of their thickness. By our XPS investigations explained in chapter 4.4.1.2, we proved that the molecule lands on the surface of  $\text{TiO}_2(110)$  single crystal, and it interacts with the substrate through nitrogen atoms bound to the  $\text{TiO}_2(110)$ . Thereby, the similarity of the C-K edge NEXAFS spectra originate from the fact that the pyrene substituent of the molecule either in high or low coverage is not influenced by the substrate. This conclusion is confirmed by comparing the C 1s core level XPS spectra of the films in the sub-monolayer and multilayer coverage which illustrates that there is no relevant difference between the C 1s core level spectra in the two cases.

#### 4.4.2.2.2 N-K edge NEXAFS spectra of sub-monolayer

Our finding from the XPS study of the nitrogen atom in the low coverage NitPyn, reveals that the layer formed at the molecule-substrate interface has a mixture character being mainly dominated by the molecules whose radical character is perturbed. By considering the mechanism of adsorption of NitPyn at the molecule-substrate interface and compare it with the adsorption of the same molecule in the thicker layers, we expect the N-K edge NEXAFS spectra of NitPyn at the

layer next to the substrate to be different than the spectra of the subsequent layers. The comparison of Figure 4.24 with the N-K edge NEXAFS spectra of the thicker film of NitPyn shows these differences clearly. The origin of the differences is the strong chemical interactions between orbitals of the nitrogen atoms and adsorption sites results in hybridization of the molecular orbital of NitPyn and, thus, the strong deviation of the nitronyl nitroxide molecular orbitals from their unperturbed spatial distribution due to adsorption the molecule on top of the  $\text{TiO}_2(110)$  single crystal.

The direct consequence of perturbation in the NitPyn molecular orbital is that the matrix element defining the NEXAFS adsorption experiences changes [35]. In particular, in the N-K edge NEXAFS spectra obtained from thin films in the sub-monolayer regimes, a weak feature is observed in the photon energy below 398 eV known as “pre-edge” region. However, this feature is not the singly isolated feature as observed at 397.2 eV for thick films attributed to the transition of the N-K electrons to the SOMO. The presence of this weak feature in the “pre-edge” region, confirms coexistence of the molecule that assembled on the substrate while their paramagnetic nature is preserved and the molecules that have lost their paramagnetic properties due to the hybridization of the molecular orbital.

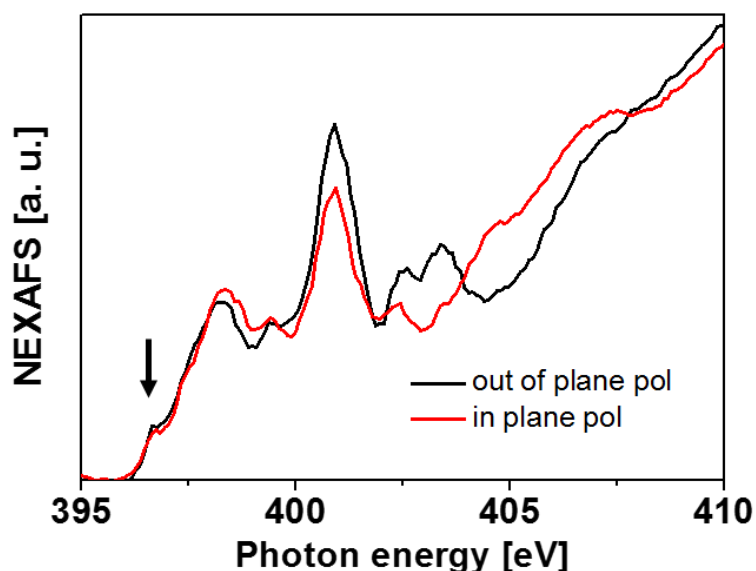


**Figure 4.24:** N-K edge NEXAFS spectra obtained from thin film in the sub-monolayer regimes (0.3 nm). The spectra are taken in grazing incidence for p-pol (black curve) and s-pol (red curve) polarization.

### 4.4.3 Growth mode

We use XPS to study the growth mode of thin film of NitPyn on  $\text{TiO}_2(110)$ . In this regard, the attenuation of the Ti 2p core level spectra versus deposition time is measured. The trend of the decreasing signal from the substrate gives us information about the mechanisms of assembly of the molecule on the substrate, thus, on the mode of growing the thin film. Figure 4.25 shows the attenuation of the Ti 2p XPS signal as a function of time during NitPyn deposition on the surface of the  $\text{TiO}_2(110)$  single crystal at RT. The resulting data are normalized to the corresponding saturation signal. Therefore, the relative intensity varies in the 0-1 interval. The variation in the intensity of the Ti 2p signal from the substrate can be classified into two modes. First, on initial adsorption of molecules, the intensity of the signal of the substrate decreases dramatically. This indicates that the molecule are forming a layer over this layer. Second, while exceeding a certain critical thickness (0.7 nm in this case), the intensity decreases gently. This shows that three dimensional islands are forming over the deposit layer(s). This point is known as S- K transition. Our XPS finding clearly shows that NitPyn grows on  $\text{TiO}_2(110)$  single crystal by the growing of layer + island i.e. S-K growth mode. To confirm our finding about this growth mode we coupled ex situ AFM measurement with the mentioned XPS study. Figure 4.26 clearly shows NitPyn island formation in agreement with our XPS finding.

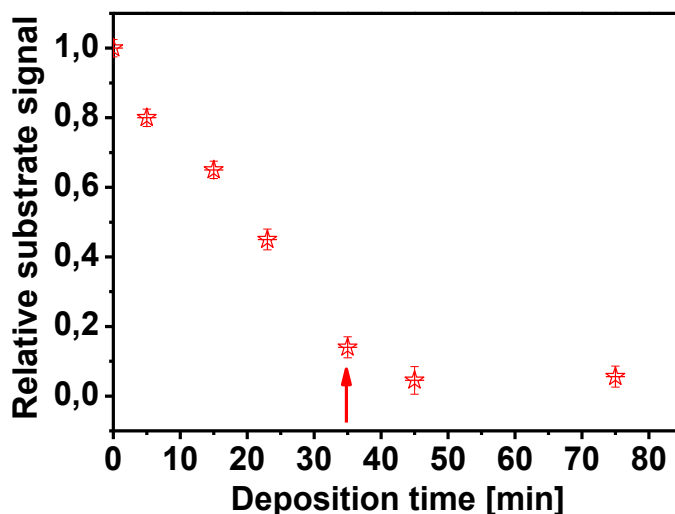


**Figure 4.25:** Attenuation of Ti 2p XP signal corresponding to the saturation signal as function of time during NitPyn deposition on  $\text{TiO}_2(110)$  at RT.

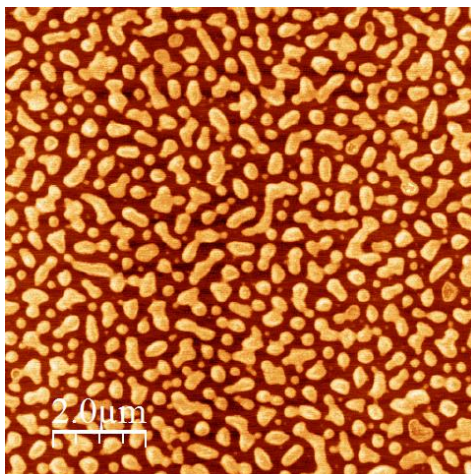


**Figure 4.26:**  $2\mu\text{m} \times 2\mu\text{m}$  AFM image of a 1 nm nominally thick layer of NitPyn deposited on the surface of  $\text{TiO}_2(110)$  single crystal.

## 4.5 NitPyn deposition on $\text{SiO}_2/\text{Si}(111)$ surface

This section deals with a comprehensive investigation on the growth of thin films of NitPyn on the  $\text{SiO}_2/\text{Si}(111)$  surface and studying the electronic structure of the system and the paramagnetic behavior of the molecules, in a vast range of film thicknesses. The results from XPS, NEXAFS, and AFM studies on the electronic structure, paramagnetic character and the mechanism of self-assembly of the organic molecule on the surface of  $\text{SiO}_2/\text{Si}(111)$  are thus compared with those obtained from the analysis of the NitPyn thin films on the  $\text{TiO}_2(110)$  single crystals. It makes possible a comprehensive investigation on the difference between growing thin film of metal-free magnets over highly oriented single crystals and flat amorphous surfaces. In the forthcoming subsections are mentioned the details of the assay and the results acquired.

### 4.5.1 XPS measurement

#### 4.5.1.1 Multilayer regime

This section starts with the XPS survey spectrum of a thin film of NitPyn on the native  $\text{SiO}_2$ . Figure 4.27 shows a survey XPS scan of a nominally 6 nm thick film of NitPyn on  $\text{SiO}_2/\text{Si}(111)$  wafer. This spectrum shows that only C, N, O and Si atoms are present in the investigated sample. A significant intensity of the peaks which are related to the C 1s as well as the N 1s core level spectra

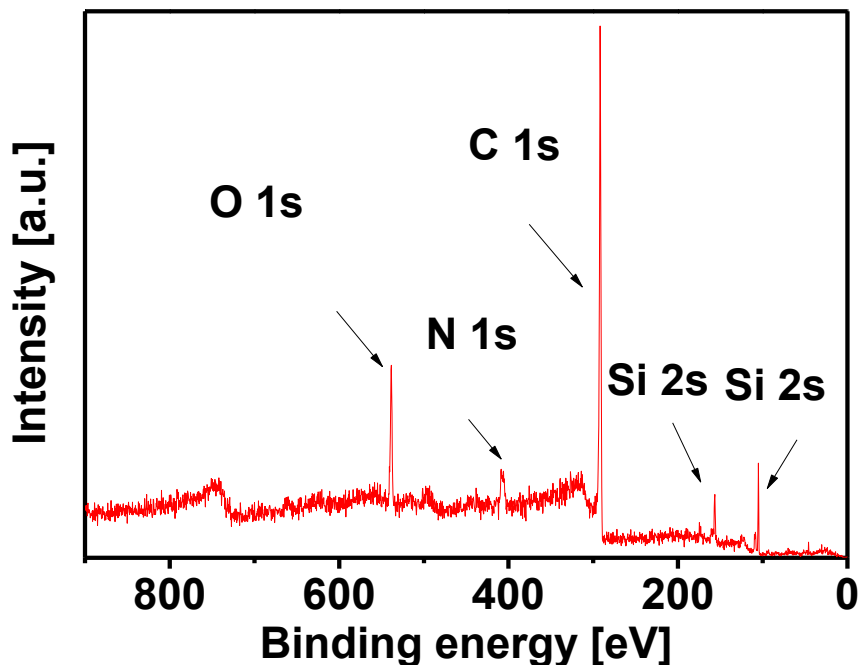


**Figure 4.27:** Survey spectrum of a 6 nm nominally thin film NitPyn on the SiO<sub>2</sub>/Si(111).

illustrates that the molecule has been successfully deposited on the clean substrate. Our stoichiometric calculations of the experimental curves show that the ratio between integral intensity of the C 1s and the N 1s core level spectra is equal to 23/2 (Appendix 1). Therefore, the ratio of the integrated signal intensities of the C 1s and N 1s core level spectra meets the expected stoichiometric ratio. It is interesting to verify whether the electronic structure of the molecules after deposition remain unchanged with respect to that before evaporation. The C 1s core level spectra can be used in order to extract information about the electronic structure of NitPyn.

The information is mainly related to the pyrene substituent. Thick films are investigated to describe the electronic structure as well as the paramagnetic properties of the layer based on NitPyn. Afterwards, films in the low coverage of thickness are studied. The ratio between the intensity of the different components of C 1s XP spectra is then calculated. The obtained quantity identifies the ratio between carbon atoms in different chemical environments. The calculated ratio is found to be in agreement with the stoichiometry of NitPyn (See Appendix I).

Figure 4.28 shows the C 1s core level photoemission spectrum of a nominally 6 nm thick film of NitPyn deposited on SiO<sub>2</sub>/Si(111). The peaks at 284.20 eV, 284.48 eV, 284.70 eV and 286.10 eV are assigned to the C=C, C-H, CH<sub>3</sub> and C-N respectively [210]. The relative intensity of

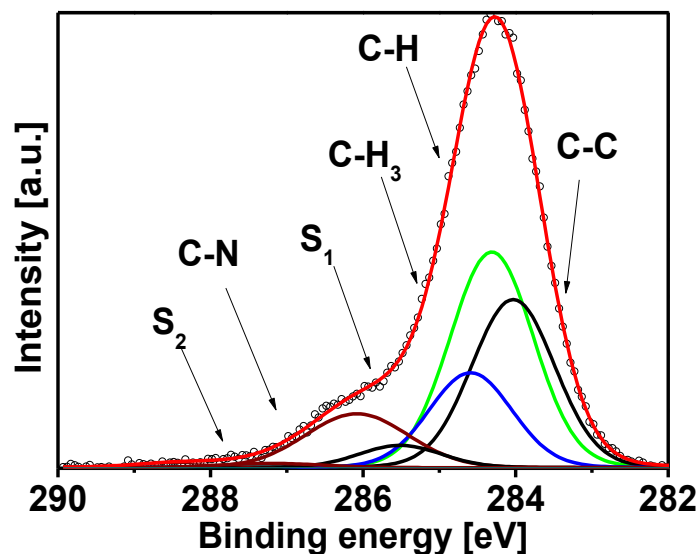


**Figure 4.28:** C 1s core level spectrum of a nominally 6 nm thick film of NitPyn deposited on SiO<sub>2</sub>/Si(111).

the components are 9:7:4:3 for C=C, C-H, CH<sub>3</sub>, and C-N contributions, respectively. This ratio is in agreement with the stoichiometry of the molecule. This means that NitPyn deposition occurs without molecular degradation. Beside the four different components in the C 1s core level spectra, Figure 4.28 displays two shake-up structures at 1.2 eV and 3.2 eV higher Ebs, relative to the main line. These features (S<sub>1</sub> and S<sub>2</sub>) can be assigned to the HOMO-LUMO shake-up satellite excitations [217]. Apart from the C 1s core level spectra, we also look at the N 1s core level spectra of the same thin film. This allows us to describe the electronic structure of the radical unit of the molecule and hence the magnetic character of the NitPyn thin film.

Figure 4.29 shows the N 1s core level spectrum of the same NitPyn thin film deposited on SiO<sub>2</sub> together with its best fit curves. The N 1s main line is visible at 402.04 eV. In addition, a clear feature attributed to the first HOMO-LUMO shake up satellite is visible at 1.4 eV higher Ebs than the main line. According to our previous discussions, (Section 4.4.1.1) the presence of the single peak in the N 1s core level spectra shows that NitPyn molecules, in the multi-layer, adsorb with the radical character of the molecules unperturbed. Figure 4.29 also shows a signal at 398.4 eV corresponding to around 4.8 % of the total intensity. The lower Ebs of the mentioned signal with respect to the main line indicates that the chemical environment of the contributing nitrogen atoms is less electronegative than the environment of the nitrogen atoms of the intact nitronyl nitroxide radical. We can infer that around 4.8 % of the organic molecules undergoes degradation to the

imino-nitroxide or diimino derivative products during evaporation or deposition or strong chemical bonding with the substrate. To understand the main source of this weak spectroscopic line complimentary study by EPR measurements is required. EPR study is performed by Mannini at the University of Florence [251].

In this series of EPR measurements, nominally 4 nm thin film are measured and the obtained spectra are compared with the spectra collected from the residual powder left in the Knudsen cell after undergoing several cycles of heating/evaporation and the solution from washing the thin films. As Figure 4.30 shows, the typical EPR signal for an organic radical, centered at  $g = 2.0067$  evidenced the persistence of the paramagnetic character of the deposited molecules. This observation is in agreement with what was reported for other thick films based on nitronyl nitroxide radicals [243, 244]. In these series of experiments, EPR measurements show that, NitPyn thin films with the nominally thickness of 4 nm have an average linewidth of 8.6 Oe, with a clear Lorentzian line shape. The observed linewidth for the deposited molecule is somewhat larger than that of a powder of the pristine radical indicating that some residual low-dimensional magnetic

**Table 4.4:** Energy position and relative intensity of the C 1s core level spectrum and shake-up satellites in NitPyn thin film, with nominally 6 nm thickness deposited on the SiO<sub>2</sub>/Si(111).

	Energy (eV)	Lorentzian Width (eV)	Gaussian Width (eV)	Intensity (%)
<b>C-C</b>	284.02	0.08	1.24	29.35
<b>C-H</b>	284.30	0.08	1.24	37.58
<b>CH<sub>3</sub></b>	284.58	0.08	1.24	17.31
<b>C-N</b>	286.01	0.08	1.54	11.59
<b>S<sub>1</sub></b>	285.50	0.08	1.24	3.14
<b>S<sub>2</sub></b>	287.58	0.08	1.24	1.03

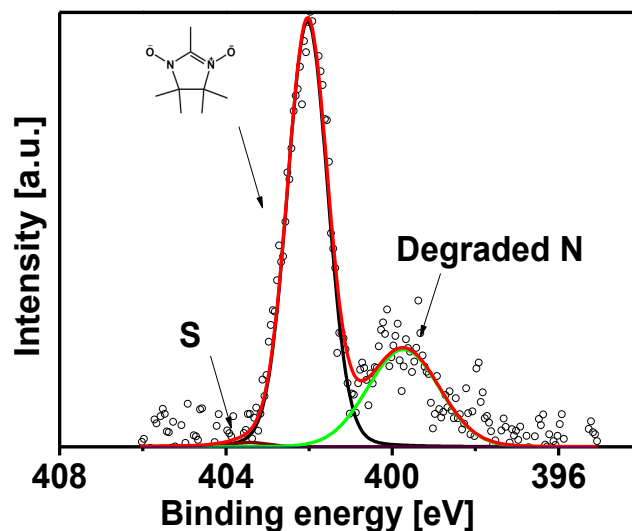


**Figure 4.29:** N 1s core level spectra of a 6 nm thick film of NitPyn on SiO<sub>2</sub>/Si(111).

character is maintained in the deposited structure. In the next steps of the EPR experiments, as Figure 4.30 shows, the line width and the double integral of the Lorentzian curves are obtained as function of the angle. A small angular dependence on the linewidth and, more importantly, on the integrated intensity of the lines is clearly visible. This is possibly due to the formation of locally ordered domains of the nitronyl nitroxide groups [245]. As we discussed in paragraph 4.5.2.1, The C-Kedge NEXAFS spectra, does not show any preferential orientation for the deposited PPN molecules. Note that the NEXAFS signal gives structural information integrated over the area sampled by the incident spot, while ESR is sensitive only to the interaction involving the paramagnetic function.

**Table 4.5:** Energy position and relative intensity of the different components of the N 1s core level spectrum and shake-up satellite of NitPyn, with nominally 6 nm thickness, deposited on the SiO<sub>2</sub>/Si(111).

	Energy (eV)	Lorentzian Width (eV)	Gaussian Width (eV)	Intensity (%)
N	402.04	0.1	1.32	87.33
N <sub>deg</sub>	398.94	0.1	1.67	4.80
S <sub>1</sub>	403.44	0.1	1.32	2.00

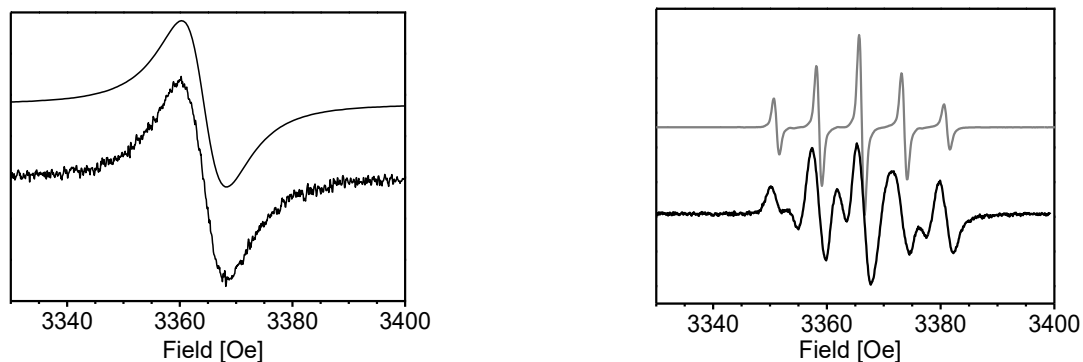


**Figure 4.30:** Room temperature ESR characterization of the samples. Spectra of a nominally 4 nm thick film (lower trace-left) and of the residual powder after sublimation (upper trace-left). Spectra obtained by dissolving the residual powder in  $\text{CH}_2\text{Cl}_2$  (upper trace-right) and by washing the Si deposited sample in the same solvent (lower trace-right).

The nature of the deposited radical is investigated by washing the  $\text{SiO}_2/\text{Si}(111)$  supported sample in  $\text{CH}_2\text{Cl}_2$ , and measuring the spectra of the resulting solution, by which the hyperfine pattern is observed (Figure 4.30). In addition to the 1:2:3:2:1 intensity pattern expected for a nitronyl nitroxide radical, weaker intensity lines are observed, which can be safely attributed to the iminonitroxide radical. This is known to yield a seven line pattern with intensity 1:1:2:1:2:1:1 due to the superposition of two of the hyperfine lines, resulting from the condition  $2a_{\text{imino}} = a_{\text{nitrox}}$  [254]. Interestingly, the residue after sublimation, once dissolved in solution, provide an ESR spectrum (Figure 4.30) which is due only to a nitronyl nitroxide radical, without traces of product degradation. This indicates that iminonitroxide is not formed during the molecular beam evaporation process, but either after the condensation, or because of the exposure of the prepared sample to the atmosphere. The former possibility is in line with the reported XPS data, showing a small amount of degraded molecules, even if one has to consider that ESR is only sensitive to paramagnetic degradation products. EPR study states that iminonitroxide is not formed during the molecular beam evaporation process but either after the condensation or because of the exposure of the thin film to the atmosphere [245].

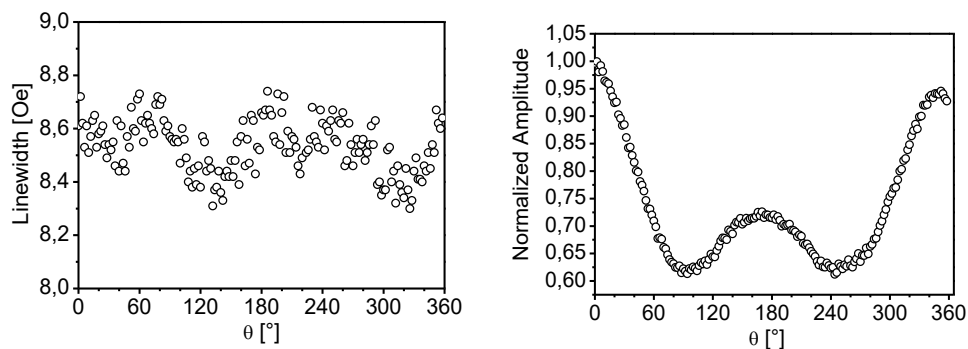


**Figure 4.31:** Angular dependence of the linewidth obtained by best fit of the spectra by Lorentzian line shape for the 4 nm thick film.  $\theta = 0^\circ$  when the magnetic field is applied parallel to the Si surface. Angular dependence of the double integral of the Lorentzian curves obtained by best fit of the spectra of the 4 nm thick film: Intensities are normalized as 1.00 at  $\theta = 0^\circ$ , when the magnetic field is applied parallel to the Si surface.

#### 4.5.1.2 Sub-monolayer regime

The low coverage thin film of NitPyn, with a nominal thickness of 0.6 nm is deposited on the SiO<sub>2</sub>/Si(111) surface. The C 1s core level spectrum of the low coverage films of NitPyn on the SiO<sub>2</sub>/Si(111) is investigated to unravel the mechanism of adsorption of the molecule on the surface of a metal-oxide substrate and the study possible variations in the electronic structures of the molecule, mainly the pyrene substituent in NitPyn, where the molecule directly interacts with the substrate.

We compare the C 1s core level photoemission spectrum of a nominally 0.6 nm thick film of NitPyn deposited on the SiO<sub>2</sub>/Si(111) with that of the thick layers. The contribution of the four different carbon atoms in NitPyn are evident from the peaks at 284.02 eV. This has contributions belongs to the C=C. At 0.28, 0.56 and 1.91 eV higher Ebs the contributions are assigned to the C-H, CH<sub>3</sub>, and C-N respectively [210]. Here, we observe no difference neither in the Ebs nor in the relative intensity of the signals related to the contributions of the four carbon atoms in the structure of NitPyn for thick and thin films. This indicates that the pyrene unit is not been perturbed upon adsorption. Regardless of the character of the molecule–substrate interaction, the specific influence of substrate on the pyrene unit remains unexplored. One possibility is that the molecule may be adsorbed on the surface in such a configuration that the pyrene part of the molecule is not bound

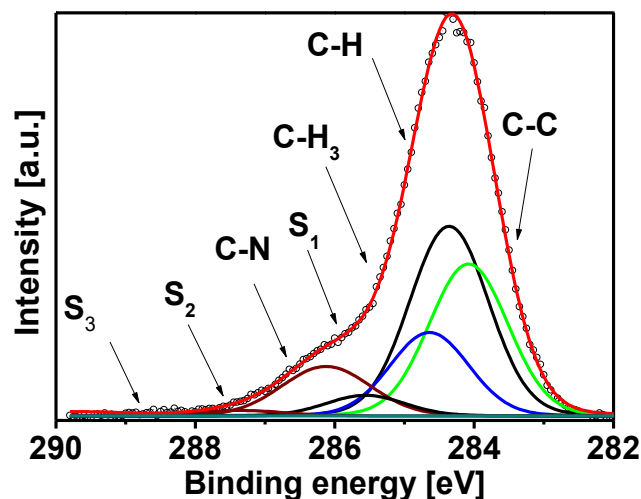


**Figure 4.32:** C 1s core level spectrum of a nominally 0.6 nm thick film of NitPyn deposited on SiO<sub>2</sub>/Si(111).

to the substrate. This has been previously observed with adsorption of NitPyn on the TiO<sub>2</sub>(110) single crystals: The N atoms are bound to the adsorption site, while the pyrene unit assembles with an orientation of approximately 48° with respect to the substrate. The other possibility is that the pyrene substituents is not influenced by the substrate because NitPyn is physisorbed or weakly chemisorbed. To further understand this aspect, we will discuss data (paragraph 4.5.2.1). The NEXAFS spectroscopy results as in the multi-layer regime, Figure 4.32 also displays two core photoelectron shake-up structures at 1.2 eV (S<sub>1</sub>) and 3.2 eV (S<sub>2</sub>) higher Eb relative to the main line. The feature visible at 285.50 eV (S<sub>1</sub>) can be attributed to the first HOMO-LUMO shake-up satellite excitation. As previously done, now we draw our attention to the N 1s core level spectrum of 0.6 nm thick film of NitPyn deposited on the amorphous SiO<sub>2</sub>/Si(111) wafer (Figure 4.33). A clear satellite feature is visible at 403.32 eV. The single peak visible at 402.4 eV indicates an intact paramagnetic character of the NitPyn molecules. The comparison of this results with those discussed in section 4.5.1.1 indicates that the paramagnetic character of the NitPyn molecules on silicon wafers, remain intact not only in the multilayer but also in the sub-monolayer. This observation is in contrast to the adsorption of the NitPyn on the surface of the TiO<sub>2</sub>(110) single crystal in which the paramagnetic properties of initial layers are perturbed. In Figure 4.33 we observe a signal tail in the Ebs between 398 and 400 eV. The percentage of the peak equals 4.8%. As discussed, the EPR study states that imino nitroxide is not formed during the molecular beam

**Table 4.6:** Energy position and relative intensity of the different components of the C 1s core level spectrum and shake-up satellites in NitPyn thin film, with nominally 0.6 nm thickness, deposited on the SiO<sub>2</sub>/Si(111).

	Energy (eV)	Lorentzian Width (eV)	Gaussian Width (eV)	Intensity (%)
<b>C-C</b>	284.02	0.08	1.24	29.55
<b>C-H</b>	284.30	0.08	1.24	37.52
<b>CH<sub>3</sub></b>	284.58	0.08	1.24	17.31
<b>C-N</b>	286.01	0.08	1.54	11.59
<b>S<sub>1</sub></b>	285.50	0.08	1.06	3.25
<b>S<sub>2</sub></b>	287.58	0.08	1.54	0.98

evaporation process but either after the condensation or because of the exposure of the thin film to the atmosphere [240].

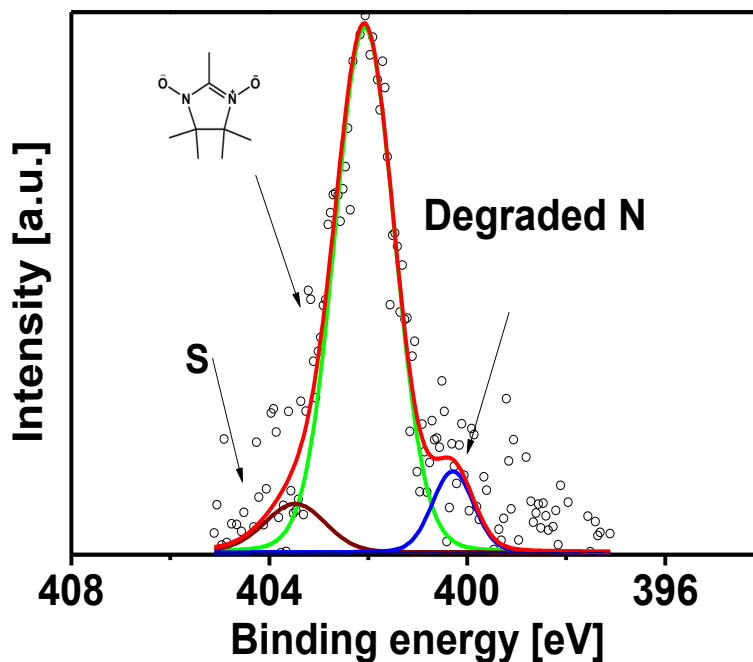


**Figure 4.33:** N 1s core level spectrum of a nominally 0.6 nm thick film of NitPyn deposited on SiO<sub>2</sub>/Si(111).

**Table 4.7:** Energy position and relative intensity of the N 1s core level spectrum and shake-up satellite of NitPyn thin film, with nominally 0.6 nm thickness, deposited on the SiO<sub>2</sub>/Si(111).

	<b>Energy</b> (eV)	<b>LorentzianWidth</b> (eV)	<b>GaussianWidth</b> (eV)	<b>Intensity</b> (%)
<b>N</b>	402.04	0.1	1.32	87.08
<b>N<sub>deg</sub></b>	398.94	0.1	1.67	4.82
<b>S<sub>1</sub></b>	403.32	0.1	1.32	1.73

## 4.5.2 NEXAFS spectra

NEXAFS spectroscopy allows us to study the electronic structure of the molecule. In addition, it provides information about the environment of specific chemical elements and is employed to determine quantitatively the orientation of the molecules forming the thin film with respect to the plane of the substrate [118].

### 4.5.2.1 C-K edge NEXAFS spectra of multilayers

C-K edge NEXAFS dichroism can be used quantitatively to determine the average spatial orientation of the molecular plane with respect to the surface of the substrate. In this particular case, this is useful to calculate the molecular plane of mostly the pyrene substituent. When a comparison is made between the in plane and out of plane polarization directions of the incident light, no significant sharp peak is observed which means that the pyrene unit does not show any preferential orientation. The direct conclusion from this finding is that the film is assembled with rather small structural domains. This small domains are oriented almost randomly. This finding is in contrast to the results of the study NitPyn on the TiO<sub>2</sub>(110) under the same preparation condition [35].

To uncover the role of the topography of the substrate on the morphology and structure in the thin film, we analyzed the results of NitPyn deposited over different substrates. The relatively small size of the structural domains of NitPyn in the case of the deposition of the molecules on the

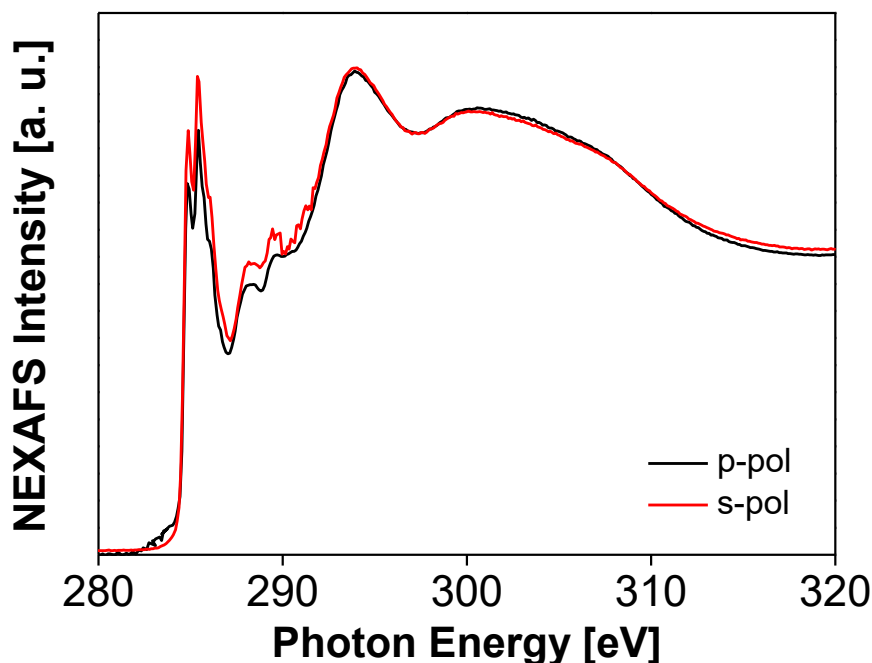


**Figure 4.34:** C-K edge NEXAFS spectra of a 15nm nominally thin film of NitPyn. The spectra are taken in grazing incidence for s-pol (red) and p-pol (black) polarization.

surface of the flat amorphous  $\text{SiO}_2/\text{Si}(111)$  shows the crucial effect of the geometry of the substrate on the nucleation of the islands in thin film formation. In order to understand to which extent the mechanism of thin film formation is controlled by the substrates, further studies are required. The comparison of our finding on NitPyn thin films deposited on the  $\text{SiO}_2/\text{Si}(111)$  surface with those obtained  $\text{TiO}_2(110)$  single crystals shows that the topography of the  $\text{TiO}_2(110)$  single crystal act as a template for morphology and structure in organic thin films.

### 4.5.3 Growth mode

The growth mode of the thin film of NitPyn on  $\text{SiO}_2/\text{Si}(111)$  can be identify by thickness dependent XPS measurements. The modes of growth can be identified by analyzing the trend of attenuation of the signal originated from the substrate with increasing thickness of the deposited films. For this purpose, the attenuation of the Si 2p core level spectra versus deposition time (i.e. thickness of the deposited thin film) is measured. The Si 2p signal decreases by increasing the thickness of the deposited layer.

The trend of decreasing of the signal from the substrate indicates the mechanism of assembly of the organic molecule on the substrate, and hence the mode of growing the thin film. The obtained data are normalized to the intensity of Si 2p signal from the clean substrate. Therefore, the relative intensity varies in the 0-1 interval. The variation in the intensity of the Si 2p signal can be classified into two groups. One of which shows a significant decrease in the signal intensity and the second shows only a slight decrease in intensity. The significant decrease caused by adsorption of the molecule indicates that the molecules are forming layers. The slow decrease in the signal intensity is observed after exceeding a certain critical thickness, nominally 1 nm (S-K transitions, see paragraph 2.3) in the case of NitPyn deposited on the SiO<sub>2</sub>/Si(111) surface, showing that three dimensional islands are forming over the deposited layers (see Figure4.35). Our XPS finding clearly shows that NitPyn grows on the SiO<sub>2</sub> /Si(111) by layer + island; S-K growth mode. Figure 4.36 shows a 2 $\mu$ m  $\times$  2  $\mu$ m AFM image of a 40 nm nominally thick layer of NitPyn on SiO<sub>2</sub>/Si(111). Figure 4.36 clearly depicts islands, confirming our XPS finding.

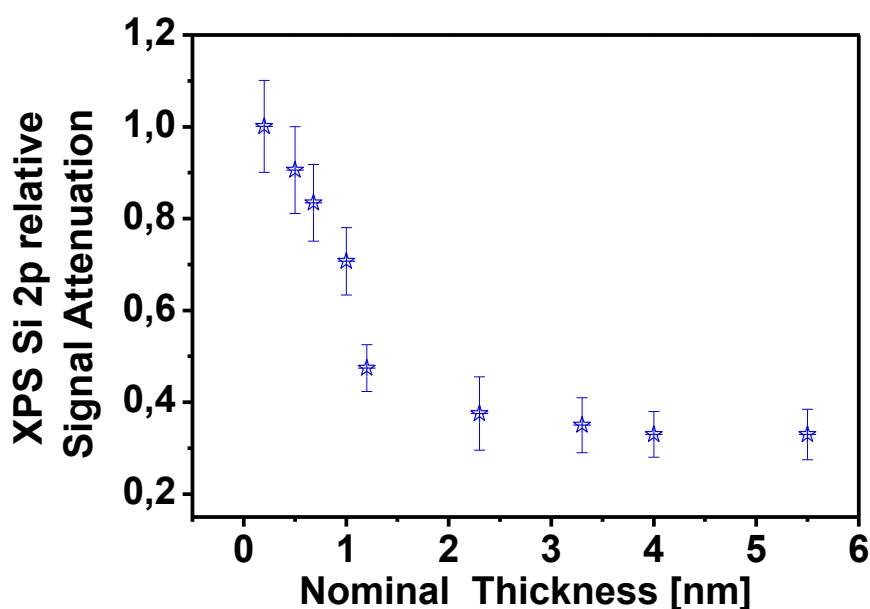


**Figure4.35:** Attenuation of Si 2p XP signal corresponding to the saturation signal as function of time during NitPyn deposition on SiO<sub>2</sub> /Si(111) at RT.

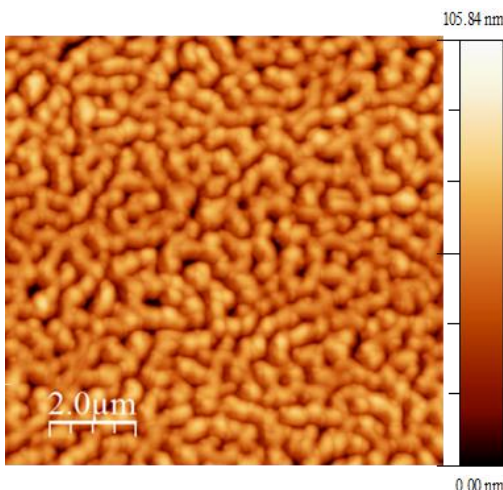


**Figure 4.36:** 2 μm × 2 μm AFM image of a 40 nm nominally thick layer of NitPyn deposited on the surface of SiO<sub>2</sub>/Si(111).

## 4.6 PPN deposition on SiO<sub>2</sub>/Si(111)

In the present experiment we focus our effort on the growing of thin films of PPN on SiO<sub>2</sub>/Si(111). XPS, NEXAFS and AFM measurements of the vapor-deposited thin films are performed to gain information on the electronic structure, paramagnetic character and morphological behavior of the PPN molecule, as well as, to understand the mechanism of thin formation of PPN on the surface of SiO<sub>2</sub>/Si(111). We also examine the vacuum and air stability of the PPN thin film. A comprehensive study of the thin film of PPN and a systematic comparison of the physical and chemical properties of the PPN molecule with NitPyn, as well as, the understanding of the origin of these interesting properties provides first-hand information about the two molecules.

In this regards, first, we concentrate on the analysis of the thick films of PPN to describe the electronic structure and the paramagnetic properties in the absence of substrate influence. Thin films in the multi-layer range are then used as a references for the investigation of the behavior of the molecule at the molecule-substrate interface.

## 4.6.1 XPS Measurement

### 4.6.1.1 Multilayer regime

This section starts by analyzing the XPS survey spectrum of the PPN deposited on the SiO<sub>2</sub>/Si(111) substrate. Figure 4.37 shows the XPS survey scan of a nominally 1 nm thick film of PPN. We concentrate on the study of the carbon and nitrogen contributions. The presence of the intense peaks in the survey spectrum visible at the 288 eV and 404.5 eV corresponding to the carbon atoms and the nitrogen atoms, respectively. This indicates the successful deposition of the PPN on the clean SiO<sub>2</sub>/Si(111) surface. Our stoichiometric calculations of the experimental curves shows a ratio of the C 1s and the N 1s intensity to be equal to 6.2 which is very close to the expected stoichiometric ratio of 6.5 (see appendix I).

In order to investigate the core level spectra of the different atoms consisting the PPN molecule, the detailed XPS spectra are analyzed by means of a curve-fitting. This analysis paved the way to understand the electronic structure, the type of the molecule – substrate interactions and the stability of the deposited thin films. The procedure of peak fitting has been explained in the section 4.4.1.1 of this thesis. The molecular structure of PPN consists of three main parts: a pyrene part which is a stable and efficient fluorophore, a radical part which play the role of a spin carrying unit and a pyrazole bridging block which plays the role of a spacer and it covalently links to the pyrene and to the radical unit [148]. Linking the spin carrying unit of the PPN, which is used as an efficient quencher of fluorescence, to the fluorophore, remarkably enhances the sensor capability of the PPN molecule [148].

The primary purpose of this set of experiments is to understand whether the electronic structure and the radical nature of the molecule after deposition remain unperturbed. For this purpose, the C 1s and N 1s core level spectra are quantitatively investigated. In this regard, the C 1s core level spectra of the thin film of PPN deposited on the SiO<sub>2</sub>/Si(111) surface are collected and the ratio between the intensity of the different components of the C 1s XP spectra are identified by peak fitting. As Figure 4.38 shows, the C 1s core level spectra are characterized by two lines. The main line, displayed in the lower E<sub>bs</sub>, can be assigned to the contributions related with the aromatic rings (C-C and C-H) and the methyl groups (CH<sub>3</sub>) and the second line, visible at rather higher E<sub>bs</sub> with respect to the main line, it is assigned to the C-N contributions. The peaks visible at the 285.36 eV, 285.74 eV, 286.02 eV and 287.45 eV are assigned to the C=C, C-H, CH<sub>3</sub> and, C-

N, respectively [<sup>210</sup>]. The relative intensity of the components are 28%, 42%, 15% and 15% for C=C, C-H, CH<sub>3</sub> and C-N respectively. This ratio is in agreement with the stoichiometry of the molecule which means that PPN deposition occurs without molecular degradation. Figure 4.38 shows two wide satellite structures visible at 286.94 eV (S<sub>1</sub>) and 289.75 eV (S<sub>2</sub>). The first feature

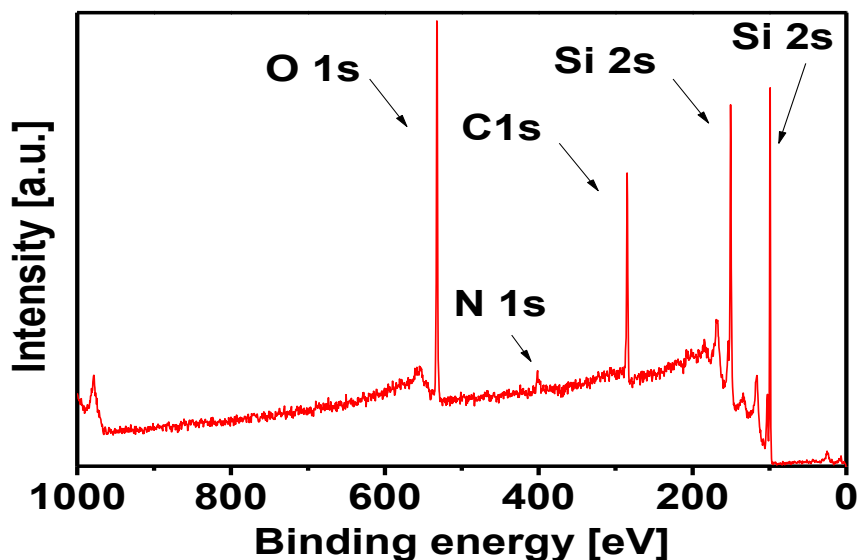


**Figure 4.37:** Survey spectrum of a 1 nm nominally thin film PPN on the SiO<sub>2</sub>/Si(111).

(S<sub>1</sub>) at 1.2 eV higher than the E<sub>b</sub> of the main line can be assigned to the first HOMO-LUMO shake-up satellite. The second feature (S<sub>2</sub>) is visible at 2.8 eV higher E<sub>b</sub>s with respect to the main line and according to stoichiometry arguments, this satellite may be related to C–N contributions.

Now, we look at the N 1s core level spectra of PPN deposited on the SiO<sub>2</sub>/Si(111) surface. The analysis of the N 1s core level spectra provides first-hand information about the nature of the radical and, consequently, the paramagnetic character of the molecule, due to the delocalization of the unpaired electron over the N–O group. Referring to the chemical structural formula of PPN, we observe three chemically different nitrogen atoms. Figure 4.39 shows the N 1s core level spectrum of a nominally 3.3 nm thick film of PPN deposited on a SiO<sub>2</sub>/Si(111) surface together with its best fit curves. The different nitrogen atoms in the PPN structure have been categorized into two main groups: the nitrogen atoms belonging to the nitronyl nitroxide radical and those belonging to the pyrazole ring. The spectrum shows a main line visible at 402.4 eV and it is

assigned to the signal of the photoelectrons from N atoms belonging to the nitronyl nitroxide radical. The environment of the N atoms in the radical unit of PPN and NitPyn are identical, This fact is verified by the finding that the photoelectron emitted from the N atoms of the nitronyl nitroxide radical in the PPN molecule are at the same  $E_b$  observed for the N 1s main line in the NitPyn thin film deposited on the Au (111) single crystal [<sup>211</sup>]. Thus, the obtained result for the N

**Table 4.8:** Energy position and relative intensity of the C 1s core level spectrum and shake-up satellites of a nominally 3.3 nm thick film of PPN deposited on the SiO<sub>2</sub>/Si(111).

	<b>Energy</b> (eV)	<b>Lorentzian Width</b> (eV)	<b>Gaussian Width</b> (eV)	<b>Intensity</b> (%)
<b>C-C</b>	285.36	0.08	1.90	26.54
<b>C-H</b>	285.74	0.08	1.90	37.86
<b>CH<sub>3</sub></b>	286.02	0.08	1.90	15.15
<b>C-N</b>	287.45	0.08	2.35	14.41
<b>S<sub>1</sub></b>	286.94	0.08	1.90	3.79
<b>S<sub>2</sub></b>	289.75	0.08	2.35	1.88

atoms in the radical unit of the NitPyn can be generalized to the PPN. Fitting the feature of the N 1s core level spectra belonging to the pyrazole ring visible at 399.9 eV results in two peaks, N<sub>1</sub> and N<sub>2</sub> in Figure 4.39, at 400.15 eV and 399.65 eV, respectively. The differences in the  $E_b$ s of N<sub>1</sub> and N<sub>2</sub> (0.5 eV) stems from their different environment in the pyrazole ring. Comparing the N 1s core level spectra with those of the PPN powder (see appendix II), one can conclude that the molecules are deposited on the silica

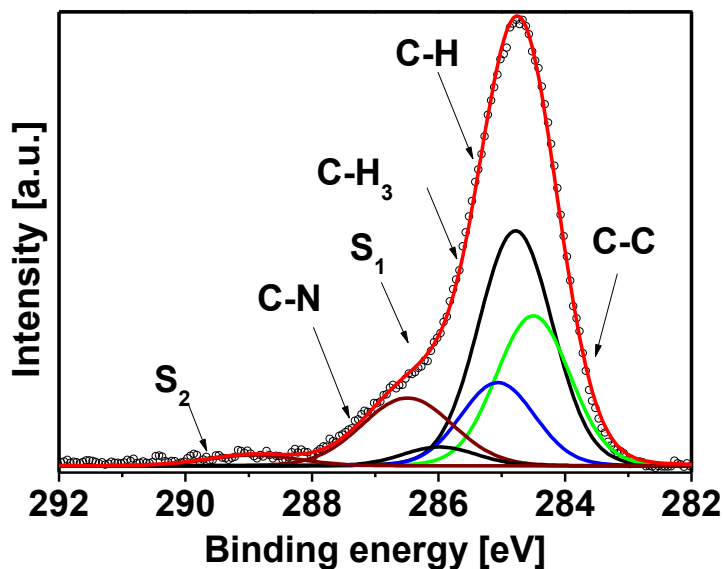


**Figure 4.38:** C 1s core level spectra of a nominally 3.3 nm thick film of PPN deposited on SiO<sub>2</sub>/Si(111).

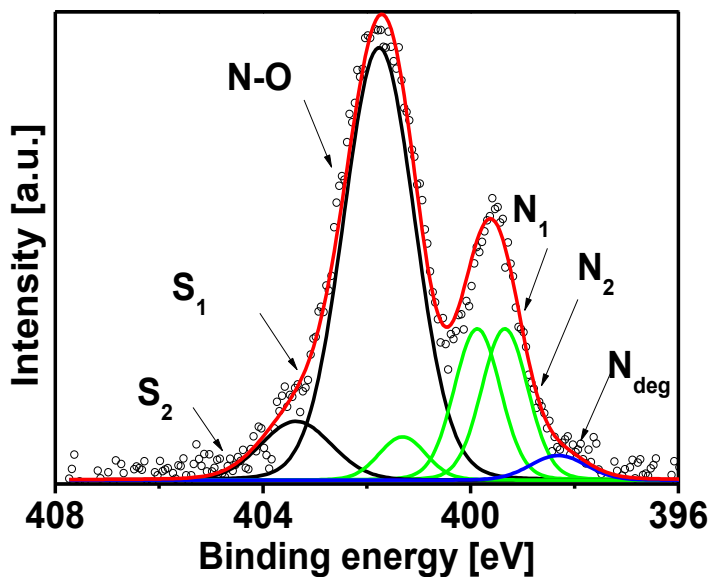


**Figure 4.39:** N 1s core level spectrum of a nominally 3.3 nm thick film of PPN deposited on SiO<sub>2</sub>/Si(111).

surface retain their radical nature, during evaporation and deposition. In addition to the main line in the N 1s core level spectra of PPN, a feature ( $S_1$ ) is visible at 1.6 eV higher  $E_b$  with respect to the main line (attributed to the N atom belonging to the radical part). As mentioned in the section 4.4.1,  $S_1$  is a shake-up satellite. According to the assignment of the shake-up satellite in the NitPyn

spectrum, S<sub>1</sub> can be assigned to the HOMO – LUMO transition. We also notice the presence of a second satellite feature at 403.32 eV. In accordance with stoichiometry arguments, the S<sub>2</sub> satellite may be related to the N atom belonging to the pyrazole ring contributions. The preserved paramagnetic nature of the deposited molecule on the surface of the substrate is related to the mechanism of the molecules-substrate interaction. In the case of PPN, the molecules are bound to the substrate by a weak physisorption that does not perturb the molecular orbital of the molecules at the interface. Figure 4.39 shows a further contributions at 398.58 eV. This contribution corresponds to 6.5% of the total intensity and is attributed to the degradation of the organic molecule. From the position of this contribution with respect to the main N 1s XPS line we can infer that the chemical environment of the contributing photoemitted electrons is less electronegative than in the intact nitroniyl nitroxide radical and the nitrogen atoms of the pyrazole ring. This finding indicates that a part of PPN (around 6.5 %) undergoes degradation either during

**Table 4.9:** Energy position and relative intensity of the different contributions in the N 1s core level spectrum and shake-up satellites of a nominally 3.3 nm thick film of PPN deposited on the SiO<sub>2</sub>/Si(111).

	<b>Energy</b> (eV)	<b>Lorentzian Width</b> (eV)	<b>GaussianWidth</b> (eV)	<b>Intensity</b> (%)
<b>N-O</b>	402.04	0.1	2.25	61.80
<b>N<sub>2</sub></b>	398.94	0.1	1.46	13.50
<b>N<sub>1</sub></b>	403.32	0.1	1.46	13.50
<b>N<sub>deg</sub></b>	398.58	0.1	1.58	6.53
<b>S<sub>1</sub></b>	401.72	0.1	1.46	1.52
<b>S<sub>2</sub></b>	402.67	0.1	2.2.5	3.10

evaporation of the molecule or when the molecule assembles on the surface to form a thin film. To understand the nature of this weak spectroscopic line, a complimentary study by EPR

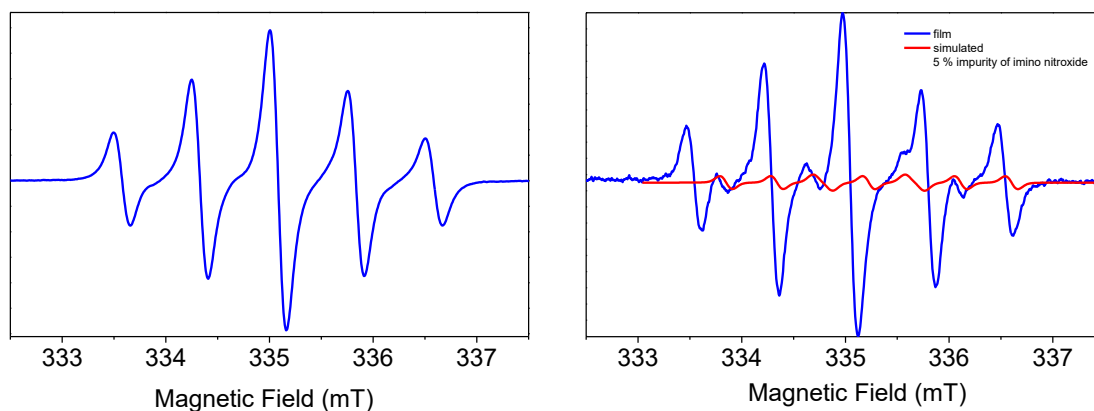


**Figure 4.40:** (Left) EPR spectrum obtained from the solution of the PPN residual powders present in the cell after several cycles of evaporation. (Right). EPR spectrum of a solution obtained from washing one of the thin films with toluene.

measurements is undertaken in collaboration with the research group of professor Baumgarten in Mainz. The EPR study is conducted on the residual powder left in the Knudsen cell after undergoing several cycles of heating as well as on the solution obtained by washing the organic layers from the substrate with toluene in order to investigate that in which part of thin film formation degradation takes place.

The EPR spectrum obtained from the solution of the PPN residual powders present in the cell after several cycles of evaporation exhibits an isotropic five line pattern due to the presence of the two equivalent nitrogen nuclei of the imidazolyl moiety (Figure 4.40- left). The relative intensity of the lines follows the typical 1:2:3:2:1 pattern. This result indicates that the evaporation does not affect the nitronyl nitroxide radical. As Figure 4.40- right shows and by considering the EPR spectrum of the powder before evaporation as reference, the EPR spectra related to the solution after washing the thin films from the substrate, mixture of nitronyl nitroxide (5 lines with two equivalent nitrogens) and imino nitroxide (7 line feature from two different nitrogen hyperfine couplings) which indicate the presence of the same patterns observed in the case of the powder, and in addition, some patterns which are attributed to the presence of the imino nitroxide radical. The results from this study indicate the formation of imino nitroxide radical as a consequence of the release of the oxygen atoms from the nitronyl nitroxide radical. Comparison of the EPR spectra

obtained from the residual powder after undergoing several cycles of heating with those obtained from the powder before heating as well as the spectra collected after washing the thin films from the substrate, shows that the imino nitroxide radical is not formed during the molecular beam evaporation process but after the condensation or because of the exposure of the thin film to either ambient atmosphere or x-ray radiation [251]. A spectral simulation [255] of the mixture of nitronyl nitroxide (5 lines with two equivalent nitrogens) and imino nitroxide (7 lines) and their added sum leads to an estimate of approximately 5% impurity of imino nitroxide. It confirms the quantitative correlation between EPR measurements and XPS study on the deposited PPN.

#### 4.6.1.2 Sub-monolayer regime

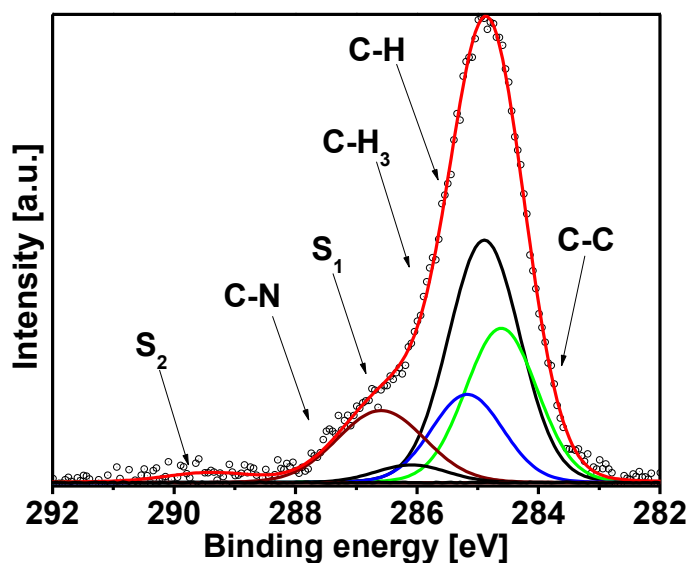
The C 1s core level spectra of PPN in the sub-monolayer regime are investigated to understand the mechanism of adsorption of PPN on the metal-oxide surfaces and the role of the molecule-substrate interaction on the properties of the deposited molecule.

Figure 4.41 shows the C 1s core level photoemission spectrum of a nominally 0.5 nm thick film of PPN deposited on SiO<sub>2</sub>/Si(111) surface together with its best fit curves. The integrated signal intensities of the different components of the C 1s core level spectra are then quantitatively analyzed. The relative intensity of the different components of the C 1s XPS spectrum agrees with the stoichiometry of the PPN molecule (see appendix I). This agreement indicates that the PPN molecules are deposited on the surface of the SiO<sub>2</sub>/Si(111) at low coverage without any alteration in the electronic structures and in the radical nature of the molecule. This finding leads us to conclude that the pyrene unit of PPN does not undergo a strong chemical interaction with the substrate.

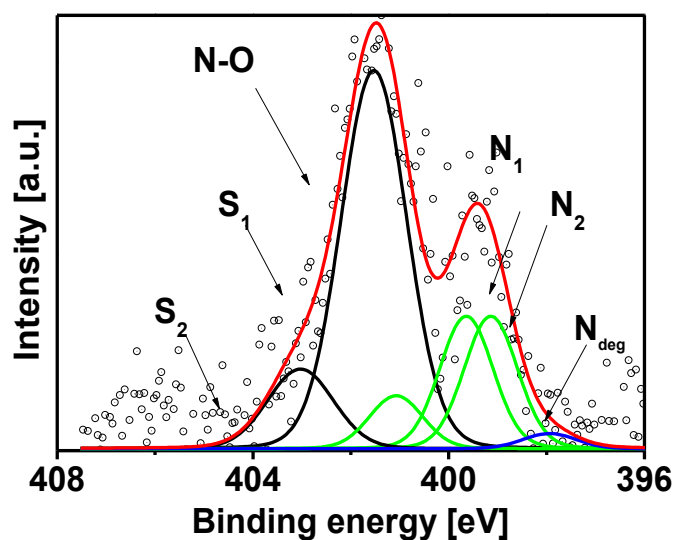
Figure 4.41 shows two satellite structures visible at 285.98 eV and 288.93 eV which are denoted as S<sub>1</sub> and S<sub>2</sub> respectively. S<sub>1</sub> can be assigned to the first HOMO-LUMO shake-up. By considering the difference in the BE of the shake-up satellite and the main C 1s core level line, on enhanced screening of the created core-hole due to its delocalization over the large aromatic system can be deduced [108].

Figure 4.42 shows the N 1s core level spectrum of a nominally 0.5 nm thick film of PPN deposited on the SiO<sub>2</sub>/Si(111) surface. The presence of the line related to the mesomeric nitrogen

atoms (N-O), shows that the paramagnetic nature has been preserved from the molecule to the thin film. A quantitative analysis of the components of the XPS spectra shows that their relative



**Figure 4.41:** C 1s core level spectrum of 0.5 nm thick film of PPN on SiO<sub>2</sub>/Si(111).



**Figure 4.42:** N 1s core level spectrum of a nominally 0.5 nm thick film of PPN deposited on SiO<sub>2</sub>/Si(111).

intensity in the N 1s core level spectra agrees well with the stoichiometry of the PPN molecule. This fact that the molecule preserve both its electronic structure and the paramagnetic nature at the molecule-SiO<sub>2</sub>/Si(111) wafer interface is interesting. Because intactness of the sensing properties

of the PPN molecules, which is in correlation to the electronic structure and the paramagnetic character of PPN, at the sub-monolayer regime of thickness pave the way to fabrication of the high sensitive systems with ultra-low thickness.

#### 4.6.1.3 Thickness dependent core level spectra

In this section we focus on the interaction between the PPN molecules and the SiO<sub>2</sub>/Si(111) substrate by means of XPS. Comparing the XPS spectra of the thin films in different layers elucidates the differences in the electronic structures of the deposited molecules at the molecule-substrate interface and at the surface of the thin films. This study also provides information about variation in the radical character of the molecule upon increasing the film thickness.

Figure 4.43 (left) shows the thickness dependent C 1s core level spectra of the PPN thin film deposited on SiO<sub>2</sub>/Si(111) surfaces. Upon increasing film thickness, a shift in the energy position towards higher E<sub>bs</sub> is observed. This shift in the E<sub>b</sub> is due to the screening of the core hole in the layer next to the substrate is assisted by the substrate. In other words, the generated core hole in the layer on top of the substrate shows a coulombic interactions with the image charge localized on the surface of the substrate. By increasing the thickness of the film and thus the distance between imagine charge and photo generated core-hole, the strength of this coulombic interaction decreases. The mechanism of core-hole screening for subsequent layers varies only slightly. This is evident from the slight variation in the E<sub>bs</sub> of the photoelectrons related to the carbon atoms in the different deposited layers in Figure 4.43 (left). The other reason for shift in the E<sub>b</sub> in the spectra and slight broadening of the XPS lines in the thinnest film maybe charging phenomena. By considering insulator nature of the SiO<sub>2</sub>/Si(111) surfaces, the charge resulted from the electron process is not immediately neutralized by electron flux. On the other words, neutralization is partial and a net charge accumulated at the surface of the substrate. The surface potential leads to an emerging electric field at the surface of the substrate which varies the E<sub>kin</sub> of the photoelectrons.

We can see the thickness dependent N 1s core level spectra of the PPN thin film deposited on SiO<sub>2</sub>/Si(111) surfaces in the Figure 4.43 (right). A slight inhomogeneous broadening is observed in the N 1s core level spectra upon increasing thickness. This may be due to the different structural and morphological environment in different layers of the thin film. Increasing the

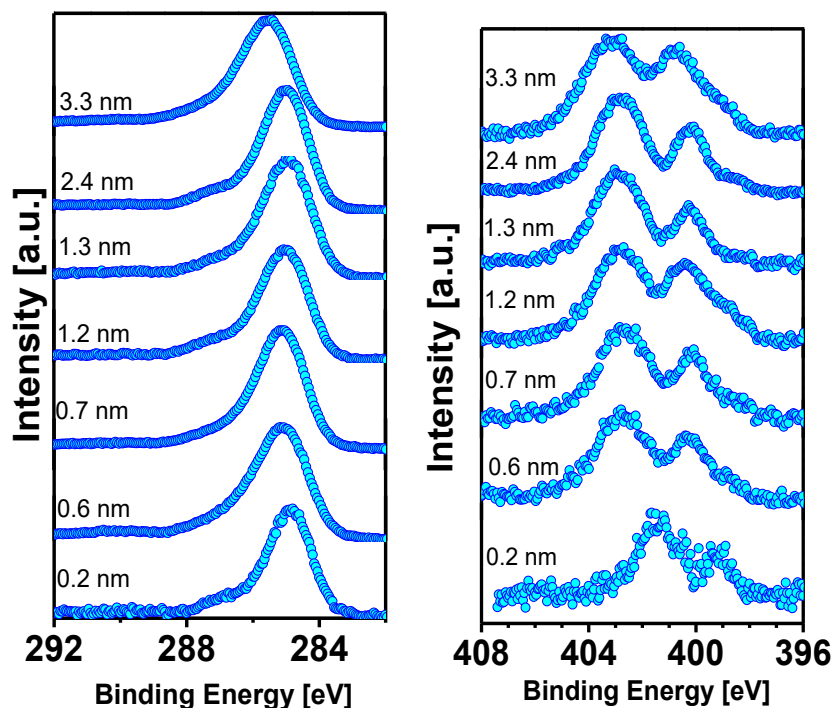


**Figure 4.43:** Thickness dependent C 1s (left) and N 1s (right) core level spectra of the PPN thin films deposited on SiO<sub>2</sub>/Si(111) surfaces.

thickness of the PPN films shows slight shift in the energy position of the C 1s and N 1s XPS main lines but the shape of both C 1s and N 1s core level spectra does not change. The similarity in the shape of the C 1s core level spectra at the molecule-substrate interface, in which the interfacial effects should be remarkable, with the C 1s core level spectra of the thicker layers indicates that the pyrene unit of PPN is not influenced by the flat and amorphous SiO<sub>2</sub>/Si(111) surface. Otherwise, it is expected that an alteration in the C 1s core level spectra at the molecule-substrate interface as a consequence of the perturbation in the molecular orbitals of the pyrene substituent is being observed.

#### 4.6.1.4 Stability of the PPN

Metal-free molecular magnets are generally considered unstable molecules due to the high density of the unpaired spins in the structure of the molecule. Synthesizing metal-free magnets that are stable either in the vacuum or in the ambient atmosphere can be a great achievement in the field of molecular magnetism. Identifying stable organic magnetic molecules in the UHV condition and ultimately in the air atmosphere provides a possibility for the technological applications of the purely organic magnets. Thus, in this section, we focus on the investigation vacuum and air

stability of PPN thin films. The next step after comparing the recent findings on PPN thin films with those obtained from NitPyn thin films, is to unravel the source of these differences. Studying electronic structure of the evaporated PPN and NitPyn indicates that differences arise from the presence of the pyrazole ring in the structure of the PPN.

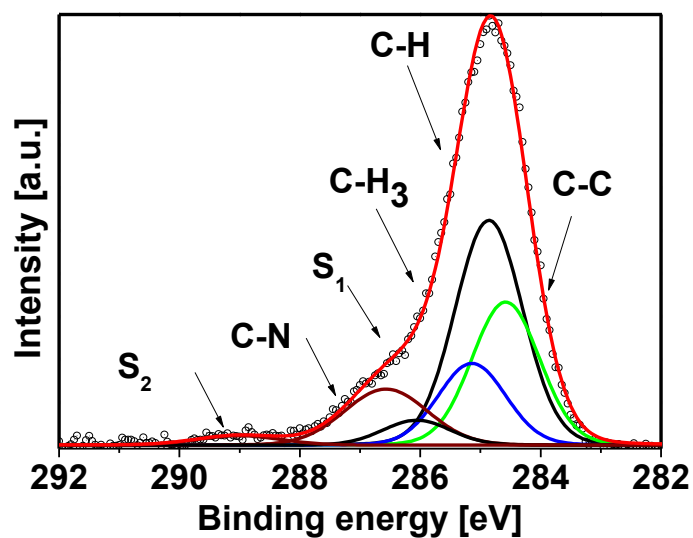
#### 4.6.1.4.1 Vacuum stability

Figure 4.44 shows the C 1s core level photoemission spectrum of a nominally 1.3 nm thick film of PPN deposited on the SiO<sub>2</sub>/Si(111) substrate kept at 10<sup>-4</sup> mbar for 30 min. The integrated signal intensities of the different components of the C 1s core level are quantitatively studied. The relative intensity of the different components of C 1s XP spectra (See Appendix II) is in agreement with the stoichiometry of the PPN molecule (see Appendix I). This indicates that keeping PPN molecules in vacuum (10<sup>-4</sup> mbar) for 30 min does not show any significant influence on the shape of the C 1s core level spectra and consequently on the pyrene unit of PPN. Here we conclude that the pyrene unit of PPN does not undergo interaction with the environment even at pressure higher than UHV condition. We further studied the N 1s core level spectra, to understand if there is a reaction between the radical part of the molecule and the environment. It is worth noting that a possible interaction of the radical part leads to the degradation of the paramagnetic character of the molecule.

Figure 4.45 shows a N 1s core level spectrum of a nominally 1.3 nm thick film of PPN deposited on the surface of SiO<sub>2</sub>/Si(111) after 30 min in the vacuum condition. The signals are attributed to the mesomeric nitrogen atoms and the nitrogen atoms belonging to the pyrazole ring in the N 1s core level spectra. The relative intensity of the integrated signals as well as the BEs of the photoelectrons are in agreement with those from core level spectra of the fresh thin films. This PPN seems to preserve its electronic structure and its radical nature in low vacuum. The thin film is kept in vacuum varying the period of time, from 30 to 1200 minutes. The stability of the thin film is examined against time to track a possible variation in the electronic structure of the PPN thin film. We focused on the radical unit, the most sensitive part of the molecule, by investigating the N 1s core level spectrum of the PPN thin film after 1200 min post deposition.

As it is shown in the Figure 4.46, no significant variation in the relative intensity of the integrated signals as well as in the BEs of the photoelectrons attributed to the different components of the nitrogen atoms of the PPN upon keeping the thin film in UHV conditions are observed (See

Table 4.11 and Table 4.12). We can infer that the molecule remains electronically and magnetically stable with time in vacuum conditions. This finding is supported by a quantitative analysis of the



**Figure 4.44:** C 1s core level spectrum of a nominally 1.3 nm thick film of PPN deposited on SiO<sub>2</sub>/Si(111) after 30 min in the vacuum condition.

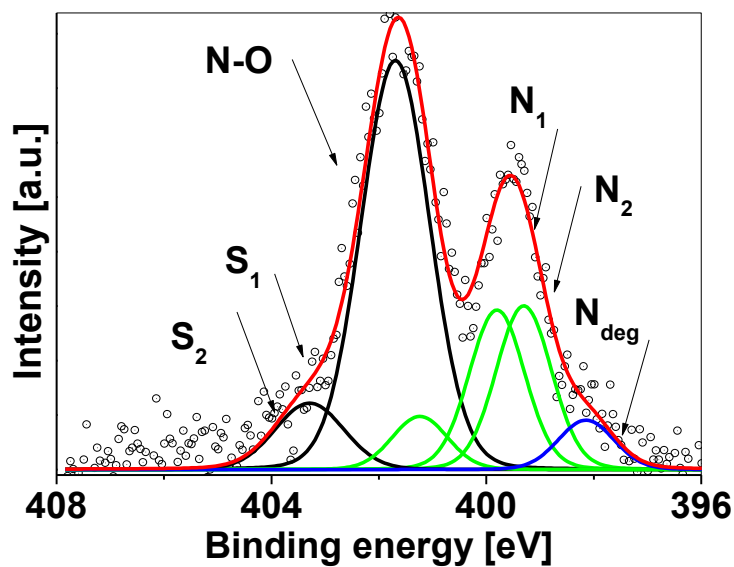


**Figure 4.45:** N 1s core level spectrum of a nominally 1.3 nm thick film of PPN deposited on SiO<sub>2</sub>/Si(111) after 30 min in the vacuum condition.

N 1s core level spectra (Table 4.12) which shows that the relative intensity of the different components agrees with the stoichiometry of PPN after 1200 min post deposition (See Appendix II).

**Table 4.10:** Energy position and relative intensity of the different contributions in the N 1s core level spectrum and shake-up satellites of a nominally 1.3 nm thick film of PPN deposited on the SiO<sub>2</sub>/Si(111) after 1200 min in vacuum.

	<b>Energy (eV)</b>	<b>Lorentzian Width (eV)</b>	<b>Gaussian Width (eV)</b>	<b>Intensity (%)</b>
<b>N-O</b>	402.04	0.1	2.25	61.80
<b>N<sub>2</sub></b>	398.94	0.1	1.46	13.50
<b>N<sub>1</sub></b>	403.32	0.1	1.46	13.50
<b>N<sub>deg</sub></b>	398.58	0.1	1.58	6.53
<b>S<sub>1</sub></b>	401.72	0.1	1.46	1.52
<b>S<sub>2</sub></b>	402.67	0.1	2.2.5	3.10

Figure 4.47 shows the intensity of the C 1s and Si 2p core level spectra versus post-deposition time. The intensity of the photoelectron signals are normalized to the intensity of the photoelectron spectra of the fresh film ( $t = 0$ ). The relative increase in the intensity of the C 1s core level signal is accompanied by a decrease in the intensity of the Si 2p core level signal. Figure 4.47 shows an increasing around 10 % in the intensity of the C 1s core level spectra which can be largely attributed to the adsorption of the contamination present in the chamber on the surface of the thin film.

As Figure 4.47 shows variations in both C 1s and Si 2p XPS spirals are limited to the range of 10%. A portion of this fluctuation lies in the data error range and can be neglected. Very small variation in the intensity of the photoelectron signals, clearly confirms the vacuum stability of the thin film of PPN. The only exception is the dramatic rise in the intensity of the C 1s spectra after 1200 min. This could be caused by the re-adsorption of molecules present in the analysis chamber. We did not observe any change in the relative intensities of the contributing components of both C 1s and N 1s core level spectra (Figure 4.46). This finding leads us to the conclusion that

desorption of the organic magnet from the surface of the SiO<sub>2</sub>/Si(111) takes place without further variation in the structure of the deposited molecule.

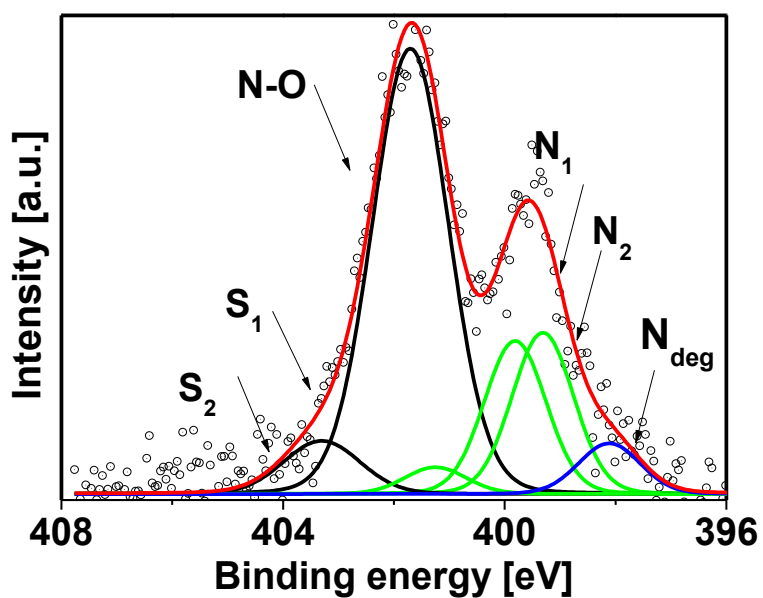


**Figure 4.46:** N 1s core level spectrum of a nominally 1.3 nm thick film of PPN deposited on SiO<sub>2</sub>/Si(111) after 1200 min in vacuum.

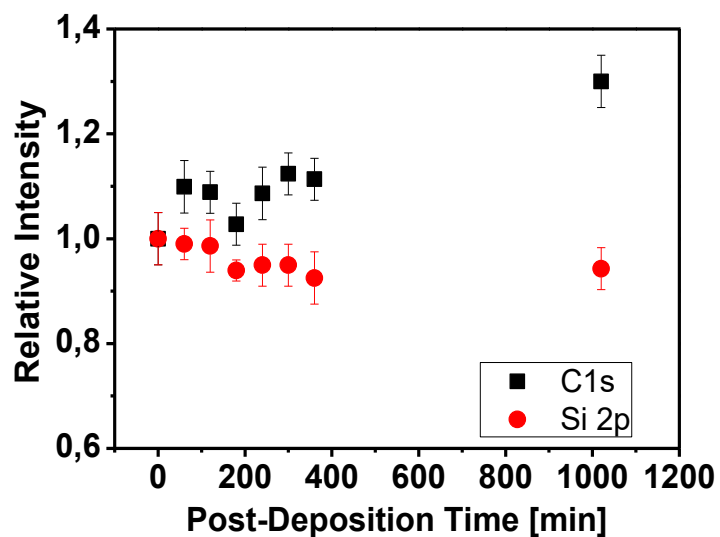


**Figure 4.47:** Temporal evolution at RT of the Si 2p and C 1s XPS signals for a 1.3 nm nominally thin film after deposition.

#### 4.6.1.4.2 Air stability

Purely organic magnets in technological applications need to be versatile: Once checked the vacuum stability, we go ahead to check their stability in air. Figure 4.48 shows the C 1s core level photoemission spectrum of a nominally 1.3 nm thick film of PPN deposited on the SiO<sub>2</sub>/Si(111) substrate kept at the ambient pressure for 25 h. The integrated signal intensities of the different components of C 1s core level are then quantitatively analyzed (see Appendix I). We see that the relative intensity of the different components of C 1s XP spectra agrees with the stoichiometry of the PPN molecule. This observation indicates that the C 1s core level spectrum, mainly dominated by the pyrene unit, remains unchanged with respect to the fresh film upon keeping PPN molecules in air atmosphere. We can deduce that the pyrene unit of the PPN molecule does not undergo interaction with the environment in air. Next we go on to examine the most sensitive part of the molecule: the radical unit, exposed to air atmosphere. We know from our previous experiments on the radical part of PPN that any interaction of this part with other species or its environment leads to the degradation of the molecule and perturbs the stability of the molecule which is reflected in the complexity of the N 1s core level spectra. Figure 4.48 shows the corresponding N 1s core level photoemission spectrum of PPN film. The presence of the mesomeric nitrogen atoms (N-O) and the nitrogen atoms belonging to the pyrazole ring (N<sub>1</sub> and N<sub>2</sub>) and the analysis of the N 1s core level components (in appendix II) shows that the radical nature of the PPN molecule is preserved in air condition.

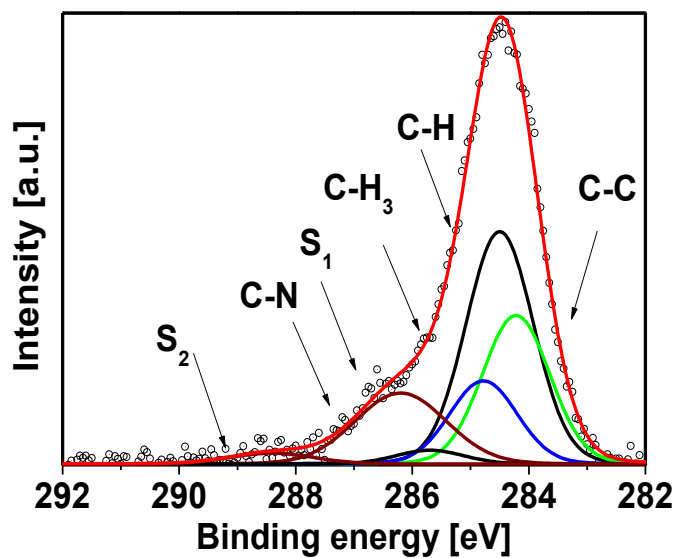


**Figure 4.48:** C 1s core level spectra of a nominally 1.3 nm thick film of PPN deposited on SiO<sub>2</sub>/Si(111) after 25h air exposure.

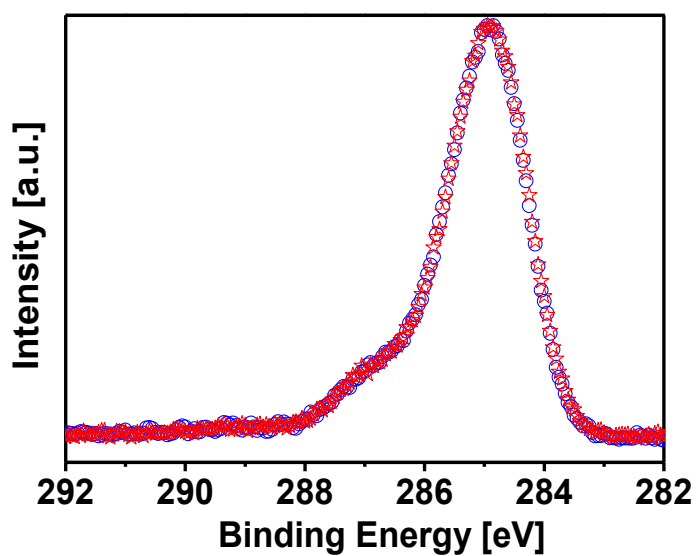


**Figure 4.49:** C 1s core level spectra of a freshly evaporated film of PPN deposited on the SiO<sub>2</sub>/Si(111) (blue curve) and after 25 h of air exposure (red curve).

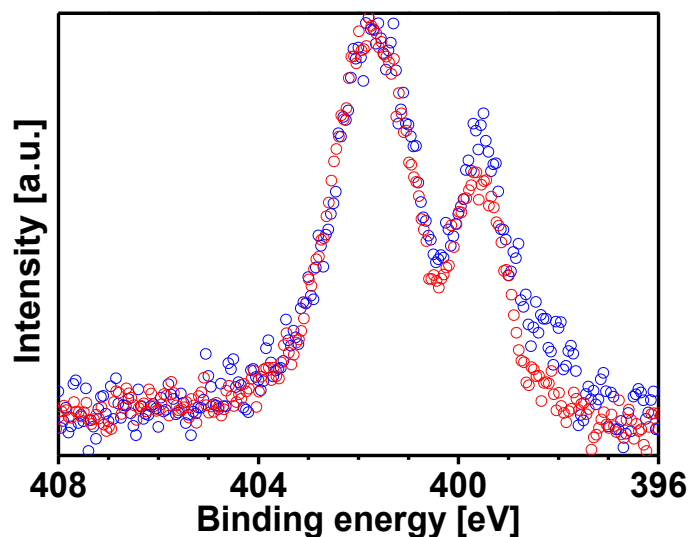


**Figure 4.50:** N 1s core level spectra of a freshly evaporated film of PPN deposited on the SiO<sub>2</sub>/Si(111) (blue curve) and after 25 h of air exposure (red curve).

Figure 4.49 and Figure 4.50 show the C 1s and N 1s core level spectra of a freshly evaporated film of PPN deposited on the SiO<sub>2</sub>/Si(111) and the same thin film after 25 h of air exposure, respectively. These Figures facilitate the comparison of C 1s and N 1s core level spectra of the thin films upon air exposure. None of the mentioned spectra shows significant variations. The molecule appears to be stable upon exposure to air in this period of time.

## 4.6.2 NEXAFS

NEXAFS spectroscopy is employed to gain information on the unoccupied states. We can investigate certain characteristics like bonding properties, local charge distributions and environment of the specific chemical elements, that could not be investigated by XPS measurement [35]. We also explore the electronic structure and, in this particular case, the paramagnetic character of thin films. These measurements are done by probing the unoccupied states while scanning the photon energy in a region several tens of eV above the edge resulting in measurement of adsorbed X-ray intensity. The intensity of the individual resonant peak in NEXAFS is directly related to the X-ray adsorption cross-section of an atom [235].

### 4.6.2.1 C-K edge NEXAFS spectra

The polarization dependent C-K edge spectra yield information mostly on the pyrene orientation with respect to the substrate [36]. The interpretation of the NEXAFS spectral features of the

molecule and the assignment of the peaks in the C-K edge NEXAFS spectra, is based on a comparison between the NEXAFS spectra data of NitPyn and pyrene as well as pyrene-based molecules [236, 237]. The C-K edge NEXAFS spectra are characterized by two main regions: the  $\pi^*$  region up to around 290 eV and the  $\sigma^*$  region that lies in the photon energy range above 290 eV. The photon energy interval from 280 to 320 eV is chosen to completely span the C-K edge and all  $\pi^*$  and  $\sigma^*$  transitions.

In the  $\pi^*$  region, sharp resonances are observed at 284.8, 285.4, 285.7 and 286.2 eV which have C=C character corresponding to the transition of the C 1s initial states of the C atoms to the LUMOs [236]. Two other features visible at 287.8 and 288.9 eV have a mixed nature ( $\sigma^*(\text{C-H})$  and  $\pi^*(\text{C=C})$ ) [237]. In the  $\sigma^*$  region (above 290 eV), which are dominated by relatively broad shapes, two resonances are visible. These have a mixed character (C-C, C=C, and C-N) and  $\pi \rightarrow \pi^*$  shake-up contribution due mainly to the transition from the 1s core levels to the  $\sigma^*$  orbitals [237]. In addition, a significant shoulder is visible at 286.6 eV that may be related to the contribution due to the carbon atoms of the pyrazole ring [246].

#### 4.6.2.1.2 Orientation analysis of NEXAFS spectroscopy

The C-K edge NEXAFS spectra is useful to determine the average orientation of the molecular plane mostly of the pyrene unit, with respect to the surface of the substrate. The transition energy and the intensity of the features in the NEXAFS spectra is related to the presence of specific elements and their chemical environments. The transitions are also depend on the orientation of the transition dipole moment, associated with the transition relative to the polarization vector of the linearly polarized X-ray beam [238]. We have focused on the study of the resonance observed at the 286.2 eV which yields a value of  $83^\circ$  in the angle between the molecular plane of the pyrene substituent and the surface of the substrate. The spatial average orientation of the pyrene substituent molecular plane is in agreement with PPN crystal structure [148]. We assume that the PPN unit cell in the thicker films is arranged with the b-axis (the long axis) almost perpendicular to the substrate surface [36]. This orientation is very often adopted by molecules in organic thin films deposited on metal oxides [39, 42, 247, 248].

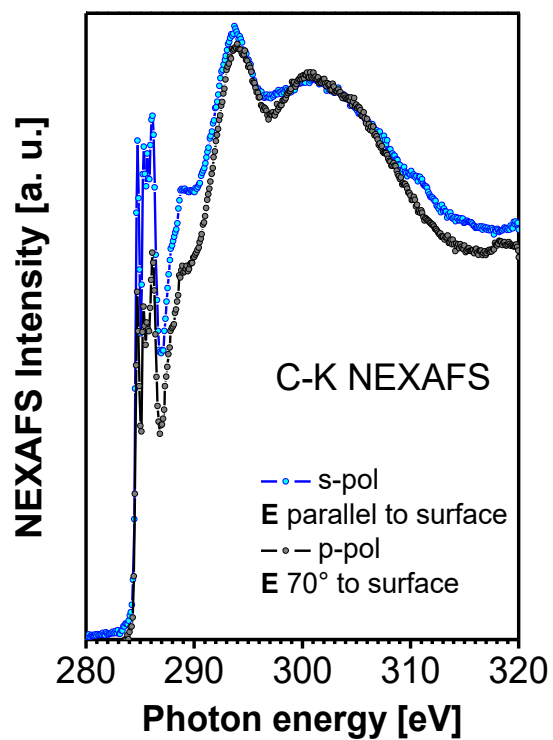


**Figure 4.51:** C-K edge NEXAFS spectra obtained from a 12 nm nominally thick film of PPN deposited on  $\text{SiO}_2/\text{Si}(111)$ . The spectra are taken in grazing incidence for p-pol (black curve) and s-pol (blue curve) polarization.

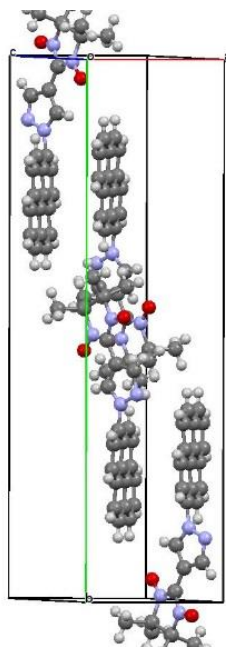


**Figure 4.52:** The unit cell of the PPN molecule.

### 4.6.2.2 N-K edge NEXAFS spectra

We look at N-K edge NEXAFS spectra of PPN. The analysis of the N-K edge NEXAFS spectra of the molecule, provides valuable information about the paramagnetic character of the molecule, due to the delocalization of the unpaired electron over the N-O group.

In the  $\pi^*$  region, several sharp resonances are observed that are related to the transitions from the N 1s initial states of the N atoms to the  $\pi^*$  antibonding molecular orbitals (see Figure 4.53). This assignment is done based on previous studies on NO [244,245], amino acids [246] and phthalocyanines [247–249]. In the  $\sigma^*$  regions, several relatively broad resonances are visible; they are due mainly to the transitions from the N 1s core levels of the N atoms to the antibonding  $\sigma^*$  orbitals of the molecule [259]. There are two reasons for the broad shape of the feature. First, they have mixed character and various contributions such as  $\sigma^*(\text{N-C})$  are included, and second, the decay probability of the electron in the continuum states is remarkably higher in comparison to the  $\pi^*$  region [250]. All the assigned feature in the 398 to 410 eV photon energy interval have analogy

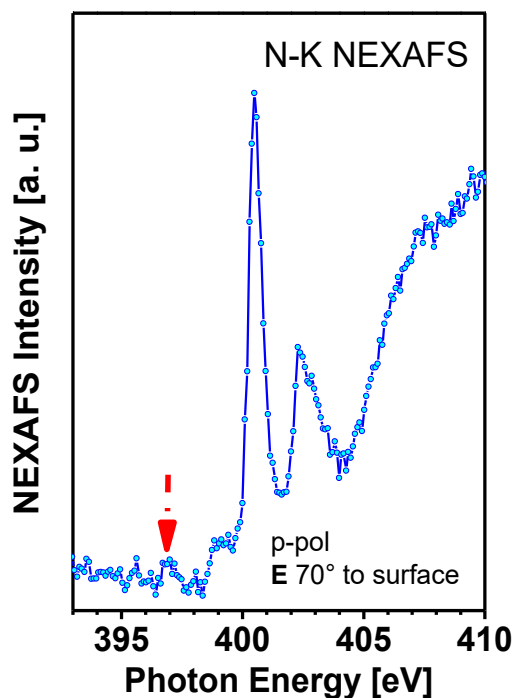


**Figure 4.53:** N-K edge NEXAFS spectrum obtained from a 12 nm nominally thick film of the PPN on SiO<sub>2</sub>/Si(111) surface. The spectrum is taken in grazing incidence for p-polarization.

with peak energy and the behavior of the features in the N-K edge NEXAFS spectra of small organic molecules [35]. The photon energy region below 398 eV is known as “pre-edge “and is characterized by a signal at the photon energy of 397.2 eV which corresponds to the transition of N-K electrons from 1s orbitals to the SOMO. The consequence of the presence of SOMO in deposited thin film is that the molecules preserve their unpaired electrons and then, their paramagnetic properties during evaporation and, ultimately, as condensed thin film of PPN.

### 4.6.3 Growth mode

The mechanisms of assembly of the PPN on the surface of the substrate, thus, the mode of growing the thin film is obtained by XPS. In this regard, the attenuation of the intensity Si 2p core level spectra upon PPN deposition is measured. The intensity of the signal from the substrate is plotted against the thickness of the deposited layer. The resulting data are normalized to the intensity of Si 2p signal from a clean substrate. Therefore, the relative intensity varies in the 0-1 interval. The intensity of the Si 2p signal, initially, decreases rapidly due to the adsorption of the molecules, indicating that the molecules are assembled as sequential layers on top of a flat substrate. When the nominal thickness of the thin film reaches 0.7 nm, the trend of the decreasing intensity of the

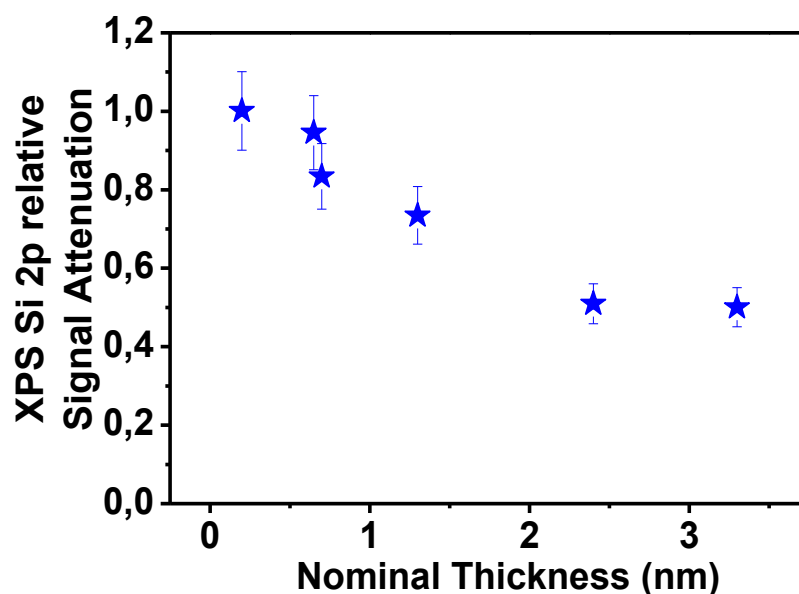


**Figure 4.54:** Attenuation of Si 2p XP signal corresponding to the saturation signal as function of time during PPN deposition on SiO<sub>2</sub>/Si(111) at RT.

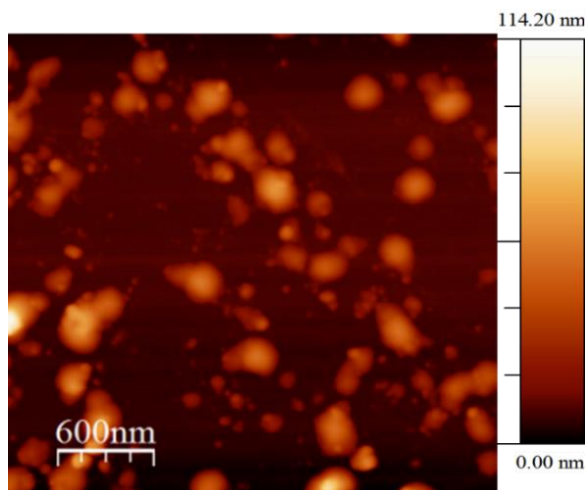


**Figure 4. 55:** 2 $\mu\text{m}$   $\times$  2 $\mu\text{m}$  AFM image of a 12 nm nominally thick layer of PPN deposited on the surface of SiO<sub>2</sub>/Si(111).

Si 2p core level signal changes indicating islands formation over the deposited layer(s). The XPS data shows that PPN grows according to the layer + island, i.e. S-K growth mode. In the next step of these set of experiments in order to study the surface of the thin film of PPN deposited on the SiO<sub>2</sub>/Si(111) as well as to investigate the growth mode of the thin film, we have performed AFM analysis. Figure 4. 55 shows a 2 $\mu\text{m}$   $\times$  2 $\mu\text{m}$  AFM image of a 12 nm nominally thick layer of PPN deposited on on the SiO<sub>2</sub>/Si(111). The AFM image clearly shows the presence of islands which supports our XPS finding.

## 4.7 PPN deposition on TiO<sub>2</sub>(110) single crystal

In this section we present our results on PPN thin films grown on the rutile TiO<sub>2</sub>(110) single crystals. We study the electronic structure and radical nature of the molecule on a vast range of thicknesses. We also study the growing mechanism of PPN thin film on the rutile TiO<sub>2</sub>(110) single crystals by means of XPS and AFM measurements. We further examine the thickness dependent electronic structure of the PPN deposited on the metal-oxide substrate.

### 4.7.1 Multilayer

This section starts with the study of the XPS survey spectrum of the thin film of PPN deposited on the TiO<sub>2</sub>(110) single crystal.

Figure 4.56 shows a survey XPS scan of a nominally 4 nm thick film of PPN deposited on the  $\text{TiO}_2(110)$  single crystal. This spectrum shows contributions of C, N, O and Ti core level spectra. The intense peaks in the survey spectrum visible at the 288 eV and 404.5 eV corresponding to carbon atoms and the nitrogen atoms, respectively, indicates the successful deposition of the PPN on the  $\text{TiO}_2(110)$  surface. Our stoichiometric calculations at the experimental curves indicates an intensity of C 1s and the N 1s equal to 6.8 which is very close to the stoichiometric ratio 6.5 (see appendix I).

As discussed in the paragraph 4.6.1.1, PPN consists of three parts: a pyrene substituent which is a fluorophore, a radical which plays the role of the quencher and a pyrazole bridging block which is a spacer covalently linked to the radical unit [148]. The C 1s spectroscopic lines are investigated to understand the PPN electronic structure. The effect of the molecule-substrate interaction on the electronic structure and on the radical character of the organic magnets is discussed in the previous sections. An analysis of the molecular orbitals of the constituent elements in the molecule and its electronic structure, elucidates the nature of the molecular interaction with

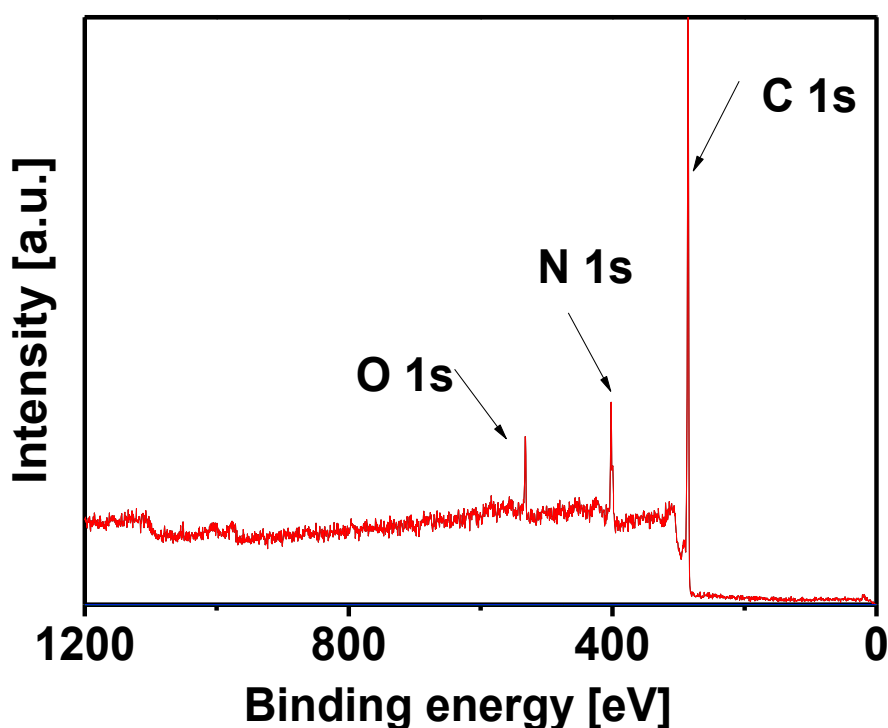


**Figure 4.56:** Survey spectrum of a nominally 4 nm thin film of PPN on rutile  $\text{TiO}_2(110)$  single crystal.

its environment. In this regard, after collecting the C 1s core level spectra of thin film of PPN deposited on the TiO<sub>2</sub>(110), the ratio between the intensity of the different components of C 1s XPS spectra is quantitatively investigated. Figure 4.57 shows a C 1s core level spectrum of a nominally 11.8 nm thick films of PPN deposited on TiO<sub>2</sub>(110). The C 1s core level spectra can be related to the contributions of the carbon atoms with different environments including C-C, C-H, CH<sub>3</sub>, and C-N [34]. The ratio of the intensity of the signal from different carbon atoms (27%, 42%, 15% and 15% for C=C, C-H, C-H<sub>3</sub>, and C-N respectively) agrees well with the stoichiometry of the molecules. Conclusively indicating that PPN has been deposited on the TiO<sub>2</sub>(110) without molecular degradation (See Appendix I).

The process of PPN adsorption on the surface of the TiO<sub>2</sub>(110) single crystal and the effect of the magnetic molecule-substrate interactions on its radical nature is studied by quantitative analysis of the different kind of nitrogen atoms in PPN (nitrogen atoms belonging to the nitronyl nitroxide radical and belonging to the pyrazole ring). This investigation consists of the study of the relative intensity of the photoelectron signals related to the different nitrogen atoms and their Ebs in the thin films with different thicknesses. We have elucidated the influence of adsorption of the NitPyn on the TiO<sub>2</sub>(110) single crystal. PPN is, in many aspects, in the particular paramagnetic nature, very similar to the NitPyn. A characterization of the electronic structure and radical nature of NitPyn paves the way for understanding the PPN/TiO<sub>2</sub>(110) single crystal system.

**Table 4.11:** Energy position and relative intensity of the different contributions in the C 1s core level spectrum and shake-up satellites of a nominally 11.8 nm thick film PPN deposited on the TiO<sub>2</sub>(110) single crystal.

	<b>Energy (eV)</b>	<b>Lorentzian Width (eV)</b>	<b>Gaussian Width (eV)</b>	<b>Intensity (%)</b>
<b>C-C</b>	284.02	0.08	1.24	29.35
<b>C-H</b>	284.30	0.08	1.24	37.58
<b>CH<sub>3</sub></b>	284.58	0.08	1.24	17.31
<b>C-N</b>	286.01	0.08	1.54	11.59

Figure 4.58 illustrates the N 1s core level photoemission spectrum of a nominally 11.8 nm thick film of PPN deposited on a TiO<sub>2</sub>(110) single crystal kept at RT. The N 1s line consists of two main contributions at 402.17 eV and at the 400.27 eV nitrogen atoms belonging to the pyrazole ring. The integrated intensities of the photoelectron signals related to the nitrogen atoms in the pyrazole ring are identical. This similarity arises from the equivalency of the two nitrogen atoms in the pyrazole ring and it is well in agreement with the stoichiometry of PPN. The presence of the contribution related to the mesomeric nitrogen atoms (N-O) coupled with the relative intensity of the spectrum of this nitrogen atoms in the N 1s core level spectrum, which agrees with the stoichiometry of the molecule, shows that the paramagnetic nature has been preserved from molecule to the thin film. This finding indicates that the molecule preserve both its electronic structure and paramagnetic nature. The intactness of the electronic structure and the radical nature of the self-assembled molecule originates from the dominating physisorption of the molecule and van-der Waals nature of the molecule-molecule interaction in thicker layers. Apart from the main lines in the N 1s core level spectrum, two well-separated satellite features are visible at 1.4 eV (S<sub>1</sub>) and 2.45 eV (S<sub>2</sub>) higher E<sub>bs</sub> than that of N 1s spectrum of the mesomeric nitrogen atoms and pyrazole nitrogen atoms respectively. These features are attributed to HOMO-LUMO shake up satellites.

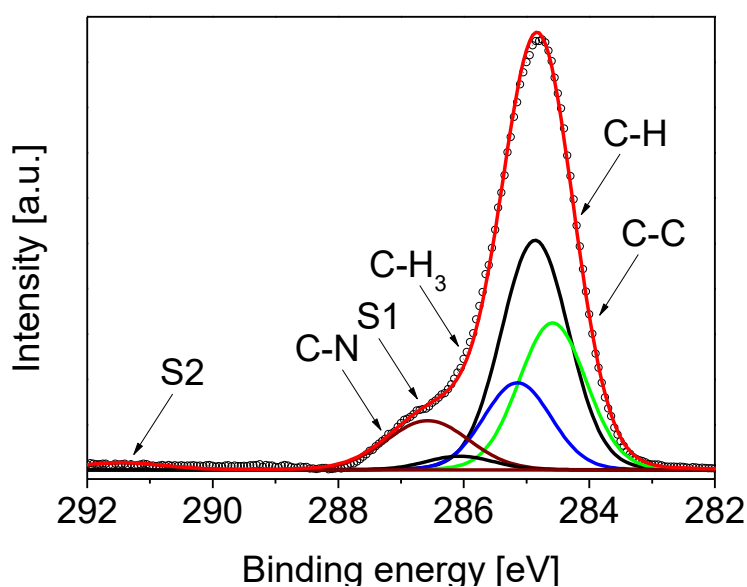


**Figure 4.57:** C 1s core level spectrum of a nominally 11.8 nm thick film of PPN deposited on TiO<sub>2</sub>(110) single crystal.

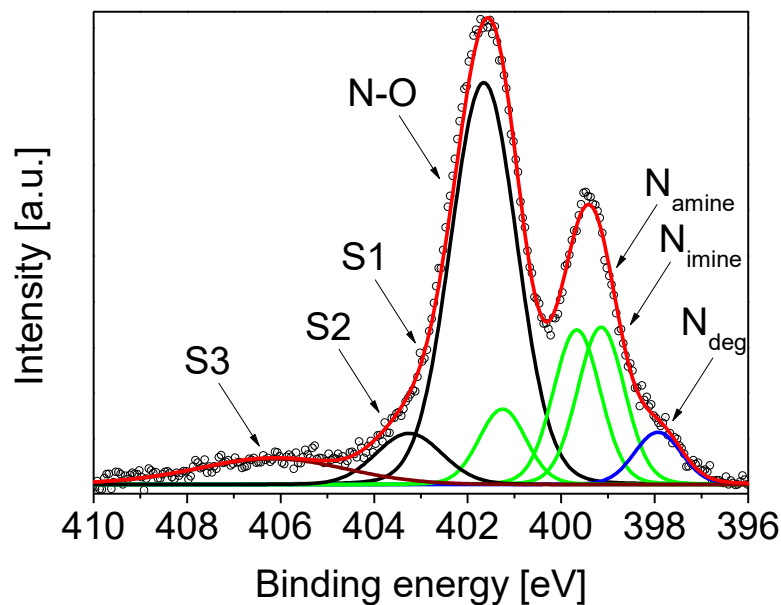


**Figure 4.58:** N 1s core level spectrum of a nominally 11.8 nm thick film of PPN deposited on the  $\text{TiO}_2(110)$  single crystal.

In this section, we focus on the interaction between the PPN molecules and the  $\text{TiO}_2(110)$  single crystal by means of XPS. Comparing the XPS spectra of the thin films in different layers elucidates the differences in the electronic structures of the deposited molecules at the interface with the substrate and at the surface of the thin films. This study also provides

**Table 4.12:** Energy position and relative intensity of the N 1s core level spectrum and shake-up satellites of a nominally 11.8 nm thick film PPN deposited on the  $\text{TiO}_2(110)$ .

	Energy (eV)	LorentzianWidth (eV)	GaussianWidth (eV)	Intensity (%)
<b>N-O</b>	402.17	0.1	2.25	61.80
<b>N<sub>2</sub></b>	400.28	0.1	1.46	13.50
<b>N<sub>1</sub></b>	399.78	0.1	1.46	13.50
<b>N<sub>deg</sub></b>	398.58	0.1	1.58	6.53
<b>S<sub>1</sub></b>	401.72	0.1	1.46	1.52
<b>S<sub>2</sub></b>	402.67	0.1	2.2.5	3.10

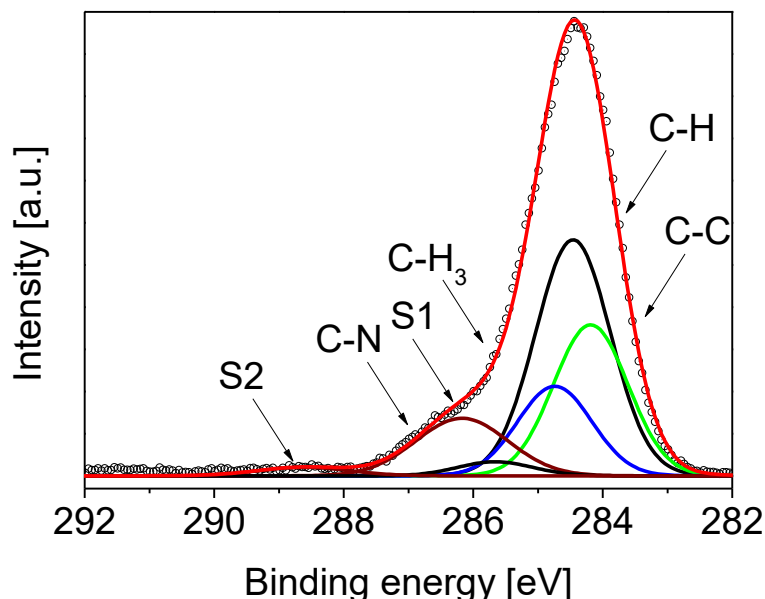


**Figure 4.59:** C 1s core level spectrum of a nominally 0.8 nm thick film of PPN deposited on TiO<sub>2</sub>(110) single crystal.

information about varying the radical character of the molecule upon increasing thin film thickness. Figure 4.61 (left) shows the thickness dependent C 1s core level spectra of the PPN thin film deposited on TiO<sub>2</sub>(110) single crystals. A shift in the C 1s core level spectra toward higher Ebs by increasing thickness of the deposited films is observed. This phenomena is exactly like the shift in the C 1s core level spectra in deposition PPN on the SiO<sub>2</sub>/Si(111) surface and it is explained in paragraph 4.6.1.3 in detail. The origin of the shifts is substrate assisted core hole screening of

**Table 4.13:** Binding energy of the N 1s core level spectrum and shake-up satellites of a nominally 0.8 nm thick film PPN deposited on the TiO<sub>2</sub>(110) single crystal.

	Energy (eV)	LorentzianWidth (eV)	GaussianWidth (eV)	Intensity (%)
<b>N-O</b>	402.24	0.1	1.63	48.59
<b>N<sub>2</sub></b>	400.25	0.1	1.14	14.61
<b>N<sub>1</sub></b>	399.73	0.1	1.14	14.62
<b>N<sub>deg</sub></b>	398.51	0.1	1.14	4.71
<b>S<sub>1</sub></b>	400.84	0,1	1.14	6.54
<b>S<sub>2</sub></b>	402.84	0.1	1.63	4.52

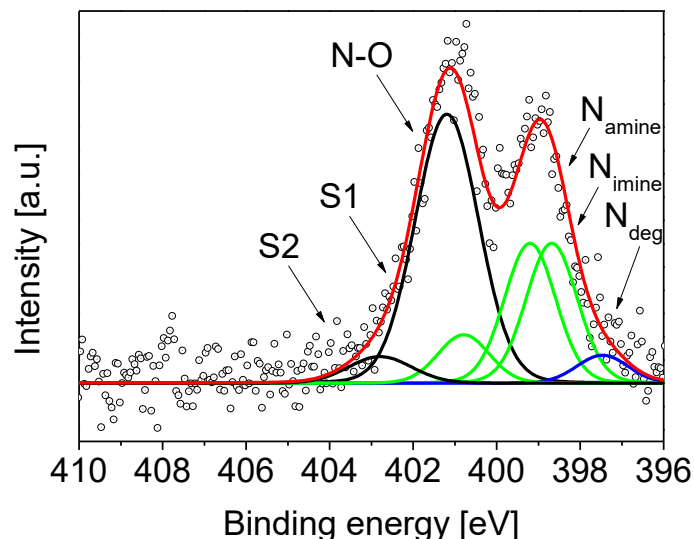


**Figure 4.60:** N 1s core level spectrum of a nominally 0.8 nm thick film of PPN deposited on TiO<sub>2</sub>(110) single crystal.

the layer next to the substrate as explained in the paragraph 4.6.1.3. No significant change in the shape of the C 1s core level spectra upon increasing the thickness of the film is observed which clearly indicates that the pyrene part of PPN is not strongly influenced by interacting with the substrate. In the case of the N 1s core level spectra, a remarkable changes in the shape of the spectra is observed when thickness increases from the sub-monolayer to the multi-layer regime. Thereafter, the shape of the spectra remains unchanged. We can infer from this observation that PPN is chemisorbed on the surface of the TiO<sub>2</sub>(110) single crystals. The origin of the slight inhomogeneous broadening observed in the N 1s core level spectra upon increasing thickness may be related to the different structural and morphological environment in different layers of the PPN thin film. The other reason for this broadening can be typical charging phenomena occurring in photoemission in organic crystals [36]. Shift in the C 1s and N 1s core level spectra upon increasing thickness of the NitPyn thin film deposited on the same substrate is not evidenced which clearly indicates larger stability of PPN with respect to the NitPyn. The shift in the core level spectra observed in NitPyn may be due to the high volatility of the molecule in the layers even next to the substrate.

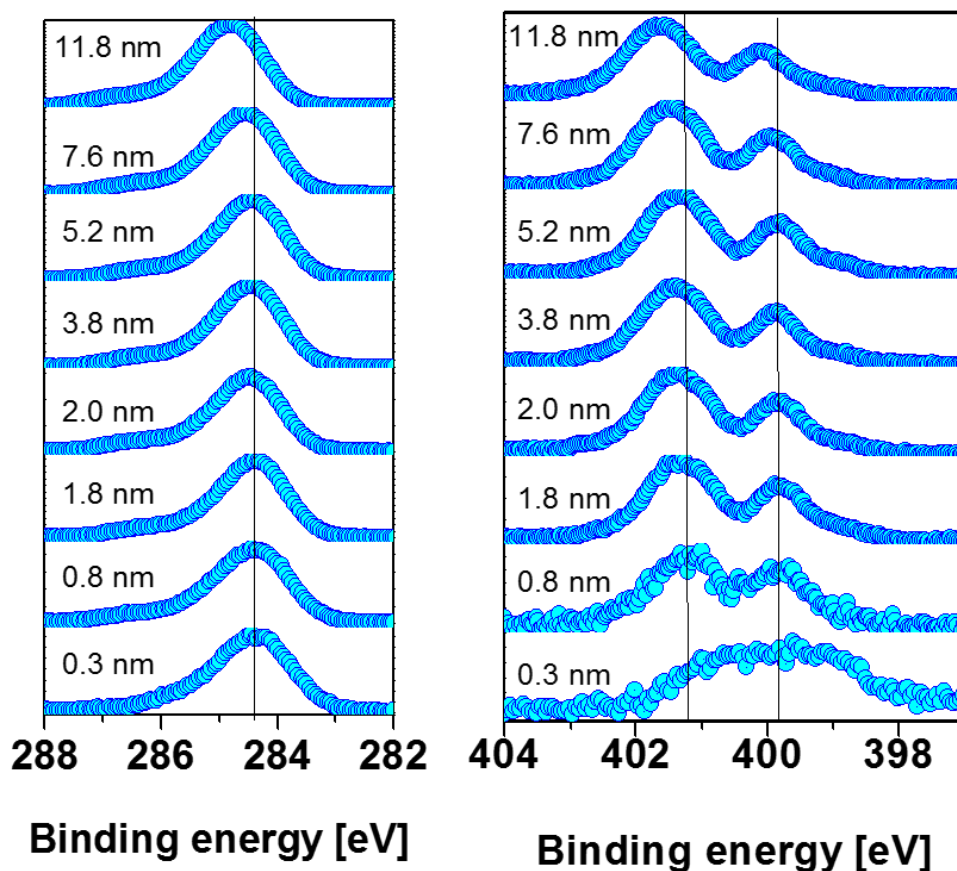


**Figure 4.61:** Thickness dependent C 1s (left) and N 1s (right) core level spectra of the PPN thin films deposited on  $\text{TiO}_2(110)$  single crystals.

### 4.7.2 Growth mode

The growth mode of the deposited thin film of PPN on  $\text{TiO}_2(110)$  single crystal can be evaluated by thickness dependent XPS measurements. As mentioned in Chapter 2, three different mode of growth can be identified by analyzing the trend of attenuation of the signal originating from the substrate with increasing thickness of the deposited thin film. For this purpose, the attenuation of the Ti 2p core level spectra versus deposition time is measured. Decreasing the Ti 2p signal of the substrate upon increasing thickness of the deposited layer, gives us information about the mechanisms of assembly of the molecules on the substrate thus the growth mode of the thin film. Figure 4.62 shows the attenuation of the Ti 2p XPS signal, as a function of time during PPN deposition on the surface of the  $\text{TiO}_2(110)$  single crystal at RT. The resulting data are normalized to the corresponding clean substrate signal. Therefore, the relative intensity varies in the 0-1 interval. Variation in the intensity of Ti 2p signal can be classified into two regions.

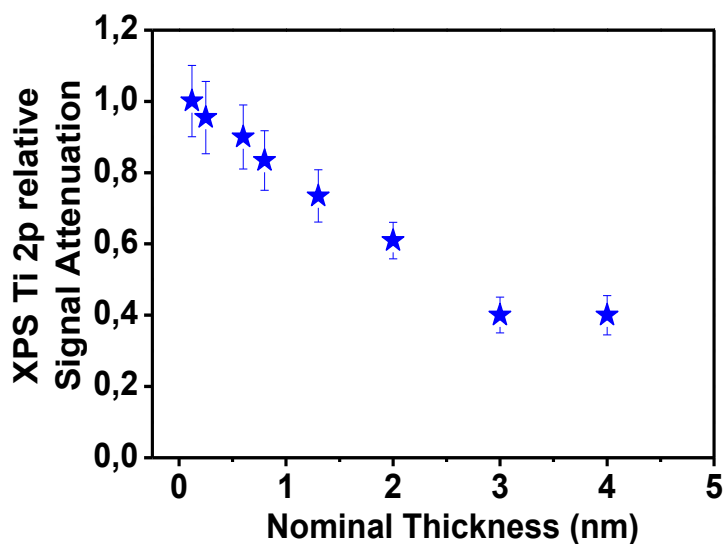


**Figure 4.62:** Attenuation of Ti 2p XP signal corresponding to the saturation signal as function of time during PPN deposition on the  $\text{TiO}_2(110)$  at RT.

The initial adsorption of the molecules causes the intensity of the signal from the substrate to decrease significantly, indicating that the molecules are forming a layer over a layer. On exceeding a certain critical thickness (nominal thickness of 3 nm) in the case of PPN the intensity decreases gently indicating that three dimensional islands are forming over the deposited layers. The deposition time at which the trend of decreasing intensity changes determines the number of layers formed before island formation begins.

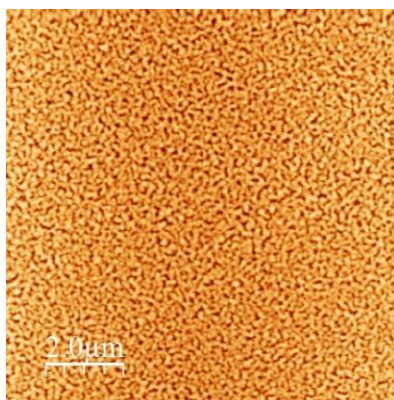


**Figure 4.63:**  $2\mu\text{m} \times 2\mu\text{m}$  AFM image of a 4 nm nominally thick layer of PPN deposited on the surface of  $\text{TiO}_2(110)$  single crystal.

Our XPS finding clearly shows that PPN on the surface of  $\text{TiO}_2(110)$  single crystal is deposited by layer + island i.e., S-K growth mode. Figure 4.63 clearly shows, island formation on the uppermost layers of the deposited PPN thin film on the surface of  $\text{TiO}_2(110)$  single crystal which verifies the S-K growth mode.

## 4.8 Bisnitroxide Diradical

The analysis of bisnitroxide diradical films deposited on the  $\text{SiO}_2/\text{Si}(111)$  surface and of  $\text{TiO}_2(110)$  single crystals starts with the analysis of the XPS survey spectrum.

Figure 4.64 shows the survey spectra before and after deposition of a bisnitroxide diradical thin film on the  $\text{SiO}_2/\text{Si}(111)$  surface. The intensity of the peaks related to the C 1s and the N 1s core level spectra in the survey spectrum after thin film deposition illustrates that the molecule has been deposited on the clean substrate. Further calculations show that the ratio between the integral intensity of the C 1s and the N 1s core level spectra is equal to 10.72 (Appendix I). The chemical

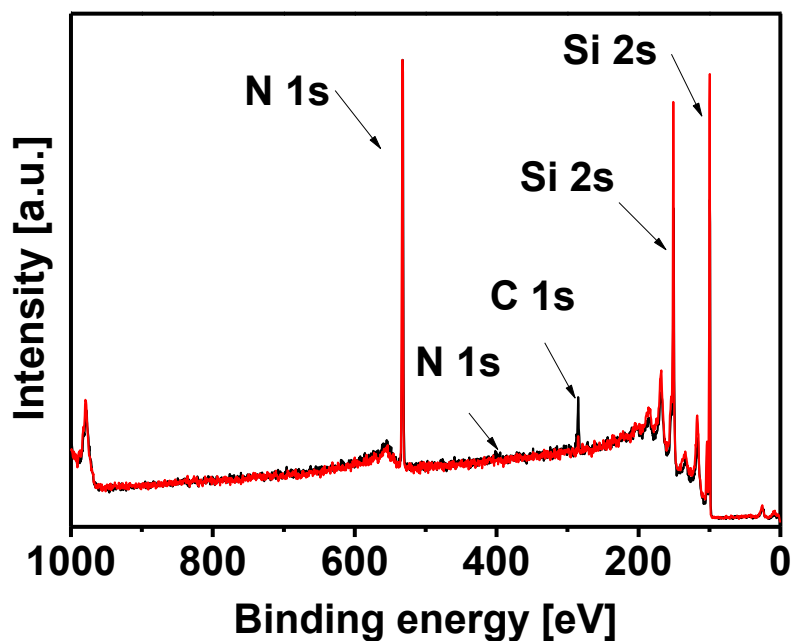


**Figure 4.64:** Survey spectra of bisnitroxide diradical thin film on the  $\text{SiO}_2/\text{Si}(111)$  before (red curve) and after 2.5 h deposition (black curve).

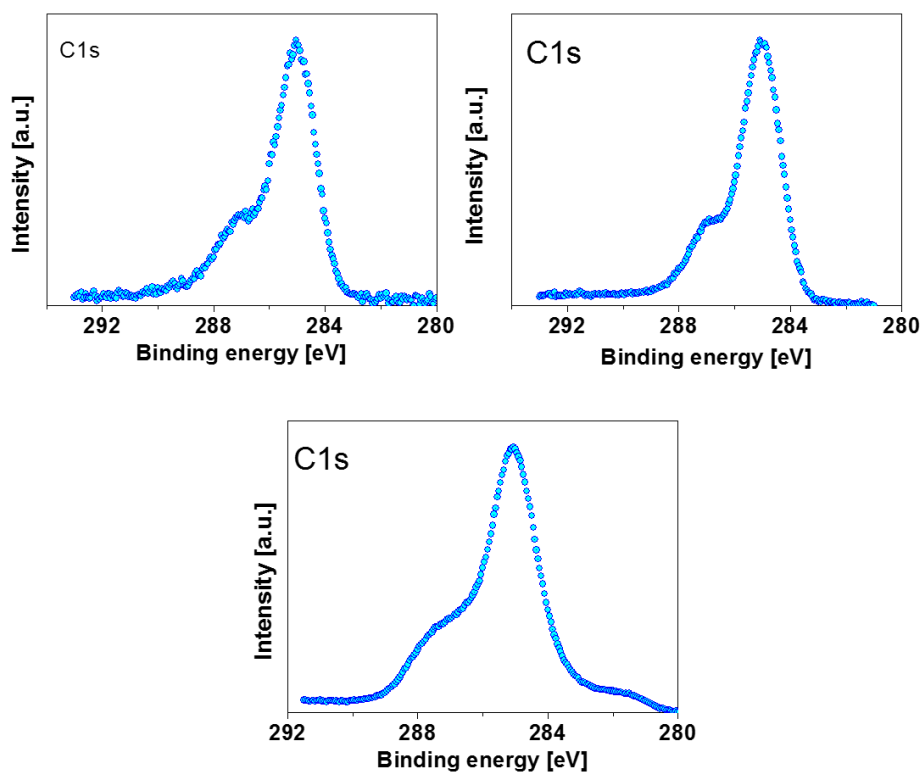


**Figure 4.65:** C 1s core level spectra of bisnitroxide diradical powder (upper panel –right), deposited on the TiO<sub>2</sub>(110) single crystal (upper panel –left) and deposited on the SiO<sub>2</sub>/Si(111) (lower panel).

formula of bisnitroxide diradical (C<sub>18</sub>H<sub>26</sub>N<sub>2</sub>O<sub>4</sub>) exhibits the presence of the 18 carbon atoms and 2 nitrogen atoms in the molecule. The ratio of the integrated signal intensities of the C 1s and N 1s core level spectra meets the expected stoichiometric ratio (C 1s / N 1s = 18/2) which is equal to 9.

The very low intensities of the N 1s signal in the survey spectra of a thin film of bisnitroxide diradical molecule on the SiO<sub>2</sub>/Si(111) surface and on the TiO<sub>2</sub>(110) single crystals, considering the remarkable evaporation time (2.5h), with evaporation rate of approximately 6 Å/min, is the source of many questions about the mechanism of deposition of the molecule on the surface of the SiO<sub>2</sub>/Si(111) and on the TiO<sub>2</sub>(110) single crystals. As it is shown in the Figure 4.66, there is no significant difference between the main lines of the C 1s core level spectra of the molecule deposited on the different substrates while a small variation in the shape and in the intensity of the feature that is attributed to the C-N contributions, is observed. Figure 4.66 shows the N 1s core level spectra of the bisnitroxide diradical powder and the thin films deposited on the TiO<sub>2</sub>(110) single crystal and on the SiO<sub>2</sub>/Si(111) surface. In contrast to the C 1s core level spectra, significant

variations in the N 1s core level spectra are observed when comparing the powder and the molecule. These variations are mirrored in different ways such as the appearance of an additional feature in rather higher Ebs at 1.1eV in the spectrum of the molecule deposited on the surface of the SiO<sub>2</sub>/Si(111) wafer and a remarkable broadening of the main N 1s core level spectra of the deposited molecule with respect to the powder. This finding would hint at the fact that the N-O groups undergo degradation.

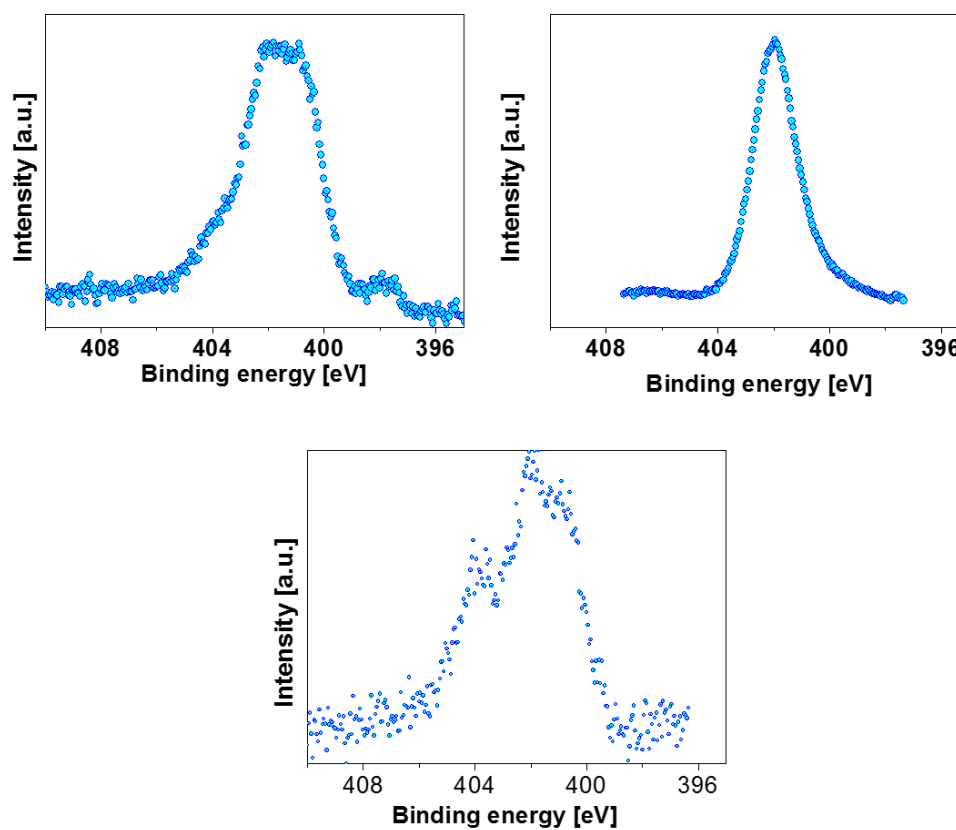


**Figure 4.66:** N 1s core level spectra of bisnitroxide biradical powder (upper panel –right), deposited on the TiO<sub>2</sub>(110) single crystal (upper panel – left) and deposited on the SiO<sub>2</sub>/Si(111) (lower panel).

# Chapter 5

## Conclusions and Outlook

### 5.1 Conclusions

The central topic of this work is the thin film processing in purely organic magnetic molecules in the shadow of a quantitative study of the electronic structures and magnetic properties of this class of quantum magnets by means of soft X-ray spectroscopic techniques and atomic force microscopy. Several metal-free magnets are deposited on well-defined metal oxide surfaces by using OMBD. The mechanism of growth of these organic systems is the focus of a widespread interest due to their crucial importance in developing organic magnetic devices.

An important aspect that is addressed is to explore the possibility to use OMBD under controlled conditions for nano-scale assembly of purely organic magnets on the solid surfaces. For this purpose, different spectroscopic techniques such as XPS and NEXAFS were employed to explore electronic structure, as well as, the paramagnetic function of the thin films of the organic radicals. The nice agreement between stoichiometry of the assembled thin film and the molecule coupled with the preserved radical nature of the deposited films indicates that OMBD is a suitable technique for nano-scale assembly of purely organic magnets.

This work provides an insight into the electronic structure of thin films of organic magnetic molecules both at the film surface, as well as, at the interfaces with the substrates. In this context, also the significant role of the physical and the chemical properties of the substrates is studied.

It has been shown that due to the co-existence of the ideal and hydroxylated surface, the mechanism of adsorption of the first NitPyn molecular layer on the  $\text{TiO}_2(110)$  single crystal surface is a mixture of strong chemisorption and weak physisorption. The molecules bound to the titanium or hydrogen atoms at the  $\text{TiO}_2(110)$  single crystal surface undergo strong chemisorption. Consequently, their initial paramagnetic character is lost, while the rest of the adsorbed molecules keep their molecules. This layer acts as a buffer for growing further intact magnetic molecules.

In contrast to the complex nature of the adsorption on the  $\text{TiO}_2(110)$  single crystal, the adsorption of NitPyn on the  $\text{SiO}_2/\text{Si}(111)$  surface has only a physisorption character. By varying the excitation energy of the light, ultimately, probing different depths we found an inhomogeneous broadening in the N 1s core level spectra which is related with the local morphological and structural alteration in the thin films.

The second molecule investigated in this work is PPN. It is also based on the nitronyl nitroxide radical attached to a fluorophore core. Our finding demonstrates that the electronic structure, as well as, the radical character of the PPN orbitals are unperturbed after vapor-deposition of the molecule on the metal-oxides. The consequence of this intactness is that the sensing capabilities of PPN are maintained in the film.

UHV and air stability of PPN is also examined by investigating the electronic and the radical nature of the film kept in the UHV and in the ambient condition. This study shows no significant alteration in the electronic structure and in the radical function upon air or UHV aging.

NEXAFS spectroscopy allowed us to elucidate the paramagnetic character of the systems and gain quantitative information on the spatial orientation of the self-assembled molecules.

NitPyn deposited on the  $\text{SiO}_2/\text{Si}(111)$  surface does not show any preferential orientation in contrast to the  $\text{TiO}_2(110)$  single crystal. The comparison between different substrates shows that the morphology of the substrates have different effects on the spatial orientation of the deposited molecule.

The same study on PPN deposited on the  $\text{SiO}_2/\text{Si}(111)$  surface reveals that the b-axis of the PPN unit cell in the multi-layer regime is oriented almost perpendicular to the plane of the surface. This orientation is very often adopted by molecules in organic thin films deposited on metal oxides.

Our study on the paramagnetic nature of the molecule is also carried out by investigating the N-K edge NEXAFS spectra of both the NitPyn and PPN. NEXAFS spectra show sharp resonances corresponding to the transition of the excited electrons from core-level to the singly occupied molecular orbital (SOMO) indicating that the magnetic function is preserved going from the molecule to the thin film.

The growth mechanism and morphology of the thin film systems are examined by means of the atomic force microscopic techniques. AFM images clearly shows island formation. These images are in agreement with the XPS measurements indicating S-K growth mode.

All these properties shows that thin films of purely organic magnetic molecules with well-controlled properties are promising candidates for designing and developing a new generation of devices operating at molecular dimensions.

## 5.2 Outlook

The work presented in this thesis demonstrates the possibility of highly controlled deposition and growth of thin films from purely organic magnets. These findings have shown the importance of precise control of the assembly of (magnetic) molecules to form thin films. In addition, various mechanisms of interactions at the interface could be worked out by comparison of different systems, which can lead to a more comprehensive understanding of the organics – metal oxide interfaces.

However, more systematic studies combined with different measurement techniques in parallel with theory for more precise calculations are required for achieving a systematic understanding and control of the thin films of this class of materials.

An important achievement to improve device performance can be employing alternative structures with controllable magnetic properties at RT, such as functionalized graphene, in order to prepare low dimensional mesoscopic quantum magnets. The other alternative is growing purely organic magnets on the novel surfaces such as topological insulator. On these substrates, due to their novel properties such as extraordinary spin-orbit coupling or RT superconductivity, the magnetic properties of the organic molecules can be governed by applying current to the substrate.



# Chapter 6

## References

1. Zhou, C. Y., Yu, T. X., & Lee, R. S. W. Drop/Impact Tests and Analysis of Typical Portable Electronic Devices. *Int. J. Mech. Sci.* **50**, 905–917 (2008).
2. Beerten, K & Vanhavere, F. The Use of Portable Electronic Devices in Accident Dosimetry. *Radiat. Prot. Dosimetry* **131**, 509–512 (2008).
3. Yu, D., Garcia, N., & Xu, S. Toward Portable Nuclear Magnetic Resonance Devices Using Atomic Magnetometers. *Concepts Magn. Reson. Part A* **34A**, 124–132 (2009).
4. Swallow, L. M., Luo, J. K., Siores, E., Patel, I. & Dodds, D. A Piezoelectric Fibre Composite Based Energy Harvesting Device for Potential Wearable Applications. *Smart Mater. Struct.* **17**, 25017 (2008).
5. Munro, B. J., Campbell, T. E., Wallace, G. G. & Steele, J. R. The Intelligent Knee Sleeve: A Wearable Biofeedback Device. *Sensors Actuators B Chem.* **131**, 541–547 (2008).
6. Wu, W., Bai, S., Yuan, M., Qin, Y., Wang, Zh., & Jing, T. Lead Zirconate Titanate Nanowire Textile Nanogenerator for Wearable Energy-Harvesting and Self-Powered Devices. *ACS Nano* **6**, 6231–6235 (2012).
7. Shim, B., Chen, W., Doty, C., Xu, C. & Kotov, N. Smart Electronic Yarns and Wearable Fabrics for Human Biomonitoring Made by Carbon Nanotube Coating with Polyelectrolytes. *Nano Lett.* **8**, 4151–7 (2008).
8. Meng, Y., Zhao, Y., Hu, Ch., Cheng, H., Hu, Y., Zhang, Z., Shi, G., & Qu, L. All-Graphene Core-Sheath Microfibers for All-Solid-State, Stretchable Fibriform Supercapacitors and Wearable Electronic Textiles. *Adv. Mater.* **25**, 2326–31 (2013).
9. Fu, Y., Cai, X., Wu, H., Lv, Zh., Hou, Sh., Peng, M., Yu, X., Zou, D: Fiber supercapacitors utilizing pen ink for flexible/wearable energy storage. *Adv. Mater.* **24**, 5713–8 (2012).
10. Kinbara, K. & Aida, T. Toward intelligent molecular machines: directed motions of biological and artificial molecules and assemblies. *Chem. Rev.* **105**, 1377–400 (2005).
11. Jayaram, B., Agrawal, S. K., Gupta, A. & Narlikar, A. V. High Temperature Superconductivity in Mixed Metal Oxides Containing Yttrium. *Japanees J. Appl. Phys.* **26**, 1004–1008 (1987).
12. Balzani, V., Credi, A. & Venturi, M. Controlled Disassembling of Self-Assembling Systems: Toward Artificial Molecular-Level Devices and Machines. *Proc. Natl. Acad. Sci. U. S. A.* **99**, 4814–7 (2002).
13. Palacio, F. A magnet made from carbon. *Nature* **413**, 690–691 (2001).
14. Verdaguer, M. Molecular Electronics Emerges from Molecular Magnetism. *Science* , **272**, 698–699 (1996).
15. Jain, R., Kabir, K., Gilory, G., Mitchell, K., Wong, K.A.R, Wong, K.C., & Hicks, R.G. High-Temperature Metal-Organic Magnets. *Nature* **445**, 291–294 (2007).
16. Morkoç, H. *Handbook of Nitride Semiconductors and Devices, Materials Properties, Physics and Growth.* (John Wiley & Sons, 2009).
17. Bogani, L. & Wernsdorfer, W. Molecular Spintronics Using Single-Molecule Magnets. *Nat. Mater.*

- 7, 179–186 (2008).
18. Miller, B. J. S. Organic Magnets- A History. *Adv. Mater.* **14**, 1105–1110 (2002).
  19. Jarillo-herrero, P. Pulling Apart Molecular Magnetism. *Science* **328**, 1362–1364 (2010).
  20. Kolasinski, K. W. *Surface Science: Foundations of Catalysis and Nanoscience*. (John Wiley & Sons, 2002).
  21. Gordon, R. G., Becker, J., Hausmann, D. & Suh, S. Vapor Deposition of Metal Oxides and Silicates : Possible Gate Insulators for Future Microelectronics. *Chem. Mater.* **13**, 2463–2464 (2001).
  22. Salahuddin, S. A New Spin on Spintronics. *Nature* **494**, 43–44 (2013).
  23. Long, J. R. Molecular Cluster Magnets. *Chem. Nanostructured Mater.* 291–315 (2003).
  24. Zhang, Y., Kahle, S., Herden, T., Stroh, S., Mayor, M., Schlickum, U., Ternes, M., Wahl, P., & Kern, K. Temperature and Magnetic field Dependence of a Kondo System in the Weak Coupling Regime. *Nat. Commun.* **4**, 2110 (2013).
  25. Palacio, F., Antorrena, G., Castro, M., Burriel, R., Rawson, J., Smith, N., Bricklebank, N., Novoa, J., & Ritter, C. High-Temperature Magnetic Ordering in a New Organic Magnet. *Phys. Rev. Lett.* **79**, 2336–2339 (1997).
  26. Kinoshita, M. P-Nitrophenyl Nitronyl Nitroxide : The First Organic Ferromagnet. *Phil.Trans.R.Soc* **357**, 2855–2872 (1999).
  27. Rønna, A. A Closer Look at the TiO<sub>2</sub>(110) Surface with STM. **2**, (Aarhus, 2003).
  28. Boratyński, P. J., Pink, M., Rajca, S. & Rajca, A. Isolation of the Triplet Ground State Aminyl Diradical. *Angew. Chem. Int. Ed. Engl.* **49**, 5459–62 (2010).
  29. Gatteschi, D. Molecular Magnetism: A Basis for New Materials. *Adv. Mater.* **6**, 635–645 (1994).
  30. Lee, J., Lee, E., Kim, S., Bang, G., Shultz, D.A., Schmidt, R.D., Forbes, M.D.E., & Lee, H. Nitronyl Nitroxide Radicals as Organic Memory Elements with Both n-and p-type Properties. *Angew. Chem. Int. Ed. Engl.* **50**, 4414–4418 (2011).
  31. Nishide, H., & Oyaizu, K., Toward Flexible Batteries. *Science* **319**, 737–739 (2008).
  32. Mannini, M., Pineider, F., Daniele, C., Totti, F., Sorace, L., Sainctavit, P., Arrio, M.-A., Otero, E., Joly, L., Cezar, J.C., Cornia, A., & Sessoli, R. Quantum Tunnelling of the Magnetization in a Monolayer of Oriented Single-Molecule Magnets. *Nature* **468**, 417–21 (2010).
  33. Nishide, H., Iwasa, Sh., Pu, Y.-J., Suga, T., Nakahara, K., & Satoh, M. Organic Radical Battery: Nitroxide Polymers as a Cathode-Active Material. *Electrochim. Acta* **50**, 827–831 (2004).
  34. Kakavandi, R., Savu, S.-A., Caneschi, A., Chassé, T. & Casu, M. B. At the Interface between Organic Radicals and TiO<sub>2</sub>(110) Single Crystals: Electronic Structure and Paramagnetic Character. *Chem. Commun. (Camb)*. **49**, 10103–5 (2013).
  35. Kakavandi, R., Savu, S.-A., Caneschi, A., & Casu, M. B. Paramagnetic Character in Thin Films of Metal-Free Organic Magnets Deposited on TiO<sub>2</sub>(110) Single Crystals. *J.Phys.Chem.C* **2**, 26675–26679 (2013).
  36. Kakavandi, R., Ravat, P., Savu, S.-A., Borozdina, Y. B., Baumgarten, M., & Casu, M.B., Electronic Structure and Stability of Fluorophore-Nitroxide Radicals from Ultrahigh Vacuum to Air Exposure. *ACS Appl. Mater. Interfaces* **7**, 1685–92 (2015).
  37. Schreiber, F. Organic Molecular Beam Deposition: Growth Studies Beyond the First Monolayer. *Phys. Status Solidi* **201**, 1037–1054 (2004).
  38. Witte, G. & Wöll, C. Growth of Aromatic Molecules on Solid Substrates for Applications in Organic

- Electronics. *J. Mater. Res.* **19**, 1889–1916 (2011).
39. Casu, M.B., Schöll, A., Bauchspiess, K. R., Huebner, D., Schmidt, T., Heske, C., & Umbach, E. Nucleation in Organic Thin Film Growth : Perylene on Al<sub>2</sub>O<sub>3</sub>/Ni<sub>3</sub>Al(111). *J. Phys. Chem. C* **113**, 10990–10996 (2009).
  40. Casu, M. B., Yu, X., Schmitt, S., Heske, C. & Umbach, E. Influence of the Preparation Conditions on the Morphology of Perylene Thin Films on Si(111) and Si(100). *J. Chem. Phys.* **129**, 244708 (2008).
  41. Savu, S.-A. Casu, M.B., Schundelmeier, S., Abb, S., Tönshoff, Ch., Bettinger, H.F., & Chasse, T. Nanoscale Assembly, Morphology and Screening Effects in Nanorods of Newly Synthesized Substituted Pentacenes. *RSC Adv.* **2**, 5112 (2012).
  42. Schuster, B.-E., Casu, M.B., Biswas, I., Hinderhofer, A., Gerlach, A., Schreiber, F., Chasse, T. Role of the Substrate in Electronic Structure, Molecular Orientation, and Morphology of Organic Thin Film: Diindenoperylene on Rutile TiO<sub>2</sub>(110). *Phys. Chem. Chem. Phys.* **11**, 9000–4 (2009).
  43. Casu, M.B., Schuster, B.-E., Biswas, I., Raisch, C., Marchetto, H., Schmidh, T., & Chasse, T. Locally Resolved Core-hole Screening , Molecular Orientation , and Morphology in Thin Films of Diindenoperylene Deposited on Au(111) Single Crystals. *Adv. Mater.* **22**, 3740–3744 (2010).
  44. Caro, J., Fraxedas, J., Juergens, O., Santino, J., Concepcio, R., Veciana, J., & Figueras A., The First Oriented Thin Films Based on a Nitronyl Nitroxide Radical. *Adv. Mater.* **10**, 608–610 (1998).
  45. Caro, J., Fraxedas, J. & Figueras, A. Thickness-dependent Spherulitic Growth Observed in Thin Films of The Molecular Organic Radical P-nitrophenyl Nitronyl Nitroxide. *J.Crys.Growth* **209**, 146–158 (2000).
  46. Molecular Electronics under the Microscope. *Nat. Chem.* **7**, 181 (2015).
  47. Forrest, S. R. Ultrathin Organic Films Grown by Organic Molecular Beam Deposition and Related Techniques. *Chem. Rev.* **97**, 1793–1896 (1997).
  48. Krause, B., Dürr, A. C., Schreiber, F., Dosch, H. & Seeck, O. H. Thermal Stability and Partial Dewetting of Crystalline Organic Thin Films: 3,4,9,10-Perylenetetra-carboxylic Dianhydride on Ag(111). *J. Chem. Phys.* **119**, 3429 (2003).
  49. Andreasson, M., Ilver, L., Kanski, J., & Andersson, T. G. Organic Molecular Beam Deposition System and Initial Studies of Organic Layer Growth. *Phys. Scr.* **T126**, 1–5 (2006).
  50. Kowarik, S., Gerlach, A. & Schreiber, F. Organic Molecular Beam Deposition: Fundamentals, Growth Dynamics, and in Situ Studies. *J. Phys. Condens. Matter* **20**, 184005 (2008).
  51. Killampalli, A.S., Interface Formation and Thin Film Deposition for Molecular and Organic Electronics. (Cornell University, 2006).
  52. Borghesi, A., Bella, L. D., Destri, S., Porzio, W. & Sassella, A. A New Apparatus for Ultra-high Vacuum Organic Molecular Beam Deposition. **9**, 437–444 (1998).
  53. Casu, M. B., Savu, S.-A., Hoffman, P., Schuster, B.-E., Menten, O.T., Nino, M.A., Locatelli, A., & Chasse, T. Direct Observation of Step-Edge Barrier Effects and General Aspects of Growth Processes: Morphology and Structure in Diindenoperylene Thin Films deposited on Au(100) Single Crystals. *CrystEngComm* **13**, 4139–4144 (2011).
  54. Hinderhofer, A. & Schreiber, F. Organic-Organic Heterostructures: Concepts and Applications. *Chemphyschem* **13**, 628–43 (2012).
  55. Ritley, K. A., Krause, B., Schreiber, F., & Dosch, H. A Portable Ultrahigh Vacuum Organic Molecular Beam Deposition System for in Situ X-ray Diffraction Measurements. *Rev. Sci. Instrum.* **72**, 1453 (2001).

56. Ohring, M. *Materials Science of Thin Films*. (Academic Press, 2001).
57. Debever, J., Bruxelles, D. & Bnandpll, B. L. C<sub>60</sub> Growth on Si(100), GaSe (0001) and GeS (001) Influence of the Substrate on the Film Crystallinity. *Appl. Phys. A* **183**, 175–183 (1993).
58. Barth, J. V, Costantini, G. & Kern, K. Engineering Atomic and Molecular Nanostructures at Surfaces. *Nature* **437**, 671–9 (2005).
59. Forrest, S. R. & Burrows, P. E. Growth Modes of Organic Semiconductor Thin Films Using Organic Molecular Beam Deposition: Epitaxy, van der Waals Epitaxy, and Quasi-Epitaxy. *Supramol. Sci.* **4**, 127–139 (1997).
60. Venables, J. A. *Introduction to Surface and Thin Film Processes*. (Cambridge University Press, 2000).
61. Hill, M. Dislocation-Free Stranski-Krastanow Growth of Ge on Si(100). *Phys. Rev. Lett.* **64**, 1943–1946 (1990).
62. Bauer, E., & van der Merwe, J. H. Structure and Growth of Crystalline Superlattices: From Monolayer to Superlattice. *Phys. Rev. B* **33**, 3657–3671 (1986).
63. Lüth, H. *Solid Surfaces, Interfaces and Thin Films*. (Springer Science & Business Media, 2010).
64. *Silicon-Germanium (SiGe) Nanostructures: Production, Properties and Applications in Electronics*. (Elsevier Science, 2011).
65. Beigmohammadi, M. Growth, Structure and Morphology of Organic Thin Films. (Rheinisch-Westfälischen Technischen Hochschule Aachen, 2007).
66. Sitter, H., Draxl, C. & Ramsey, M. *Small Organic Molecules on Surfaces: Fundamentals and Applications*. (Springer Science & Business Media, 2013).
67. *An Introduction to Electronic Materials for Engineers*. (World Scientific, 2011).
68. <http://www2.warwick.ac.uk/>
69. Lee, J. P., Jang, Y. J. & Sung, M. M. Atomic Layer Deposition of TiO<sub>2</sub> Thin Films on Mixed Self-Assembled Monolayers Studied as a Function of Surface Free Energy. *Adv. Funct. Mater.* **13**, 873–876 (2003).
70. Orr, B. G., Kessler, D., Snyder, C. W. & Sande, L. A Model for Strain-Induced Roughening and Coherent Island Growth. *Eur. Lett.* **33**, 33–38 (1992).
71. Burke, S. A., Topple, J. M. & Grütter, P. Molecular Dewetting on Insulators. *J. Phys. Condens. Matter* **21**, 423101 (2009).
72. Gauglitz, G, Moore, D. S. & Casu, M. B., & Chassé, T. *Handbook of Spectroscopy*. (Wiley-VCH Verlag GmbH & Co. KGaA, 2014). doi:10.1002/9783527654703
73. Hertz, H. Ueber einen Einfluss des ultravioletten Lichtes auf die elektrische Entladung. *Ann. Phys.* (1887).
74. Einstein, A. Über einen die Erzeugung und Verwandlung des Lichtes betreffenden Heuristischen Gesichtspunkt. *Ann. Phys.* **322**, 132–148 (1905).
75. Seah, M.P & Dench, W. A. Quantitative Electron Spectroscopy of Surfaces: A Standard Data Base for Electron Inelastic Mean Free Paths in Solids. *Surf. Interface Anal.* **1**, 1–12 (1979).
76. Oura, K., Lifshits, V.G., Saranin, A., Zotov, A.V., Katayama, M. *Surface Science - An Introduction*. (Springer, 2003).
77. Hollenstein, U., Seiler, R., Osterwalder, A., Somavilla, M., Wuest, A., Rupper, P., Willitsch, S., Greetham, G. M., Gatehouse, B-B., & Merkt, F. High-Resolution Vacuum Ultraviolet Photoelectron

- Spectroscopy. *CHIMICA* **55**, 759–762 (2001).
78. Bröker, B. Electronic and Structural Properties of Interfaces Between Electron Donor & Acceptor Molecules and Conductive Electrodes. (2010).
  79. Borstel, G. Theoretical Aspects of Photoemission. *Appl. Phys. A Solids Surfaces* **38**, 193–204 (1985).
  80. X-ray Photoelectron Spectroscopy - Damian Marrufo - Confluence.
  81. Daniel, A-R., Kirchartz, T. & Rau, U. *Advanced Characterization Techniques for Thin Film Solar Cells*. (John Wiley & Sons, 2011).
  82. Bagus, P. S., Ilton, E. S., & Nelin, C. J. The Interpretation of XPS Spectra: Insights into Materials Properties. *Surf. Sci. Rep.* **68**, 273–304 (2013).
  83. Kosugi, N., & Kuroda, H. Equivalent-Core Basis Functions to Study Core-ionized and Excited States. *Chem. Phys. Lett.* **94**, 377–382 (1982).
  84. Gao, Y. Probing the Interaction of Small Organic Molecules on Metal Oxide Surfaces. (2010).
  85. Salaneck, W.R., Bieglow, R. X-ray Photoelectron Spectroscopy of Gaseous and Solid I<sub>2</sub>: Ion-state enhanced Intermolecular Interactions. *Phys. Rev. B* **24**, 2403–2411 (1981).
  86. Berglund, C.N., Spicer, W. Photoemission Studies of Copper and Silver: Theory. *Phys. Rev. A* **136**, 1030–1038 (1964).
  87. Iijima, Y. & Tazawa, T. Application of Total Reflection X-ray Photoelectron Spectroscopy to Boron and Phosphorus on Si Wafer Surface Measurement. *Spectrochim. Acta Part B At. Spectrosc.* **59**, 1273–1276 (2004).
  88. Vickerman, J.C. & Gilmore, I. *Surface Analysis: The Principal Techniques*. (John Wiley & Sons, 2011).
  89. Tanuma, S., Powell, C. J. & Penn, D. R. Calculations of Electron Inelastic Mean Free Paths. *Surf. Interface Anal.* **37**, 1–14 (2005).
  90. Liu, T., Temprano, I., King, D. A., Driver, S. M. & Jenkins, S. J. Epitaxial Growth of Few-layer MoS<sub>2</sub>(0001) on FeS<sub>2</sub>{100}. *Chem. Commun. (Camb)*. 2–5 (2014).
  91. Herstedt, M., Herstedt, M., Maårten, S., Nyttén, A., Gustafsson, T., Rensmo, H., Siegbahn, H., Ravet, N., Armand, M., Thomas, J., & Edström, K. Surface Chemistry of Carbon-Treated LiFePO<sub>4</sub> Particles for Li-Ion Battery Cathodes Studied by PES. *Electrochem. Solid-State Lett.* **6**, A202 (2003).
  92. Tanuma, S., Shiratori, T., Kimur, T., Goto, K., Ichimura, S., & Powell, C. J. Experimental Determination of Electron Inelastic Mean Free Paths in 13 Elemental Solids in the 50 to 5000 eV Energy Range by Elastic-peak Electron spectroscopy. *Surf. Interface Anal.* **37**, 833–845 (2005).
  93. Powell, C. J. & Jablonski, A. Surface Sensitivity of X-ray Photoelectron Spectroscopy. *Nucl. Instruments Methods Phys. Res. Sect. A Accel. Spectrometers, Detect. Assoc. Equip.* **601**, 54–65 (2009).
  94. <http://www.globalsino.com/EM/image1/4809b.gif>.
  95. Aronniemi, M., Sainio, J. & Lahtinen, J. Chemical State Quantification of Iron and Chromium Oxides Using XPS: The Effect of the Background Subtraction Method. *Surf. Sci.* **578**, 108–123 (2005).
  96. Zwahlen, M. Orientation in Ultrathin Self-Assembled Organic Films for Functional Coatings: A NEXAFS Study. (2003).
  97. Shirley, D. A. High-Resolution X-Ray Photoemission Spectrum of the Valence Bands of Gold.

- Phys. Rev. B* **5**, 4709–4712 (1972).
98. Becker, U., & Shirley, D. *VUV and Soft X-Ray Photoionization*. (Springer Science & Business Media, 1996).
  99. Baker, A. & Brisk, M. . Shake-up Satellites in X-ray Photoelectron Spectroscopy. *J. Electron Spectros. Relat. Phenomena* **7**, 197–213 (1975).
  100. Hofmann, S. *Auger- and X-Ray Photoelectron Spectroscopy in Material science*. (Springer link, 2013).
  101. Maier, A., Kempgens, B., Hergenbahn, U., Neeb, M., Ruedel, A., Pincastelli, M.N., & Bradshaw, A.M. Influence of Multielectron Excitations on the O 1s Photoionization in CO<sub>2</sub>. *Phys. Rev. A* **58**, 3654–3660 (1998).
  102. Schattke, W, A. Van Hove, M. *Solid-State Photoemission and Related Methods: Theory and Experiment*. (John Wiley & Sons, 2008).
  103. Merzlikin, S. Depth Profiling by X-ray Photoelectron Spectroscopy Depth Profiling by X-ray Photoelectron Spectroscopy. (2007).
  104. Kim, K.S & Winograd, N. Charge Transfer Shake-up Satellites in X-ray Photoelectron Spectra of Cations and Anions of SrTiO<sub>3</sub>, TiO<sub>2</sub> and Sc<sub>2</sub>O<sub>3</sub>. *Chem. Phys. Lett.* **31**, 312–317 (1975).
  105. Spears, P., Fischbeck, J. & Garison, T. A. Satellite Structure in the X-Ray Photoelectron Spectra of Rare Gases and Alkali-metal Halides. *Phys. Rev. A* **9**, 1603–1611 (1974).
  106. Bancroft, G. M., Brian, D. B., & Creber, D.K. Shake-up Satellite Structure in the X-Ray Photoelectron Spectra (ESCA) of Metal Hexacarbonyls. *Inorg. Chem.* **17**, 1008–1013 (1978).
  107. Khanna, A. S. *Introduction to High Temperature Oxidation and Corrosion*. (ASM International, 2002).
  108. Abb, S., Savu, S. A., Caneschi, A., Chasse, T. & Casu, M. B. Paramagnetic Nitronyl Nitroxide Radicals on Al<sub>2</sub>O<sub>3</sub>(11-20) Single Crystals: Nanoscale Assembly, Morphology, Electronic Structure, and Paramagnetic Character Toward Future Applications. *ACS Appl. Mater. Interfaces* **5**, 13006–13011 (2013).
  109. Watts, John F. , Wolstenholme, J. *An Introduction to Surface Analysis by XPS and AES*. (2005).
  110. *X-Ray Data Booklet*. (2001).
  111. Ade, H. & Stoll, H. Near-edge X-ray Absorption Fine-structure Microscopy of Organic and Magnetic Materials. *Nat. Mater.* **8**, 281–90 (2009).
  112. Fratesi, G., Lanzilotto, V., Floreano, L. & Brivio, G. P. Azimuthal Dichroism in Near-Edge X-ray Absorption Fine Structure Spectra of Planar Molecules. *J. Phys. Chem. C* **117**, 6632–6638 (2013).
  113. Greenhough, T. J. & Helliwell, J. R. The Uses of Synchrotron X-radiation in the Crystallography of Molecular Biology. *Prog. Biophys. Mol. Biol.* **41**, 67–123 (1983).
  114. Piantek, M. Switchable Molecules on Metallic Surfaces Studied by Core-level Spectroscopies. **117**, (2009).
  115. Benny, H., Banerjee, S., Sambasivan, S., Balasubramanian, M., Fischer, D. A., Eres, G., Purtezky, A. A., Geohegan, D. Lowndes, D.H., Han, W., Misewich, J.A., & Wong, S.S., Near-Edge X-ray Absorption Fine Structure Spectroscopy as a Tool for Investigating Nanomaterials. *Small* **2**, 26–35 (2006).
  116. Ridgway, C. S. S. & M. C. *X-Ray Absorption Spectroscopy of Semiconductors*. (Springer, 2015).
  117. de Groot, F, Kotani, A. Core Level Spectroscopy of Solids (Advances in Condensed Matter Science). *Taylor & Francis Group* (2008).

118. Stöhr, J., Outka, A., Determination of Molecular Orientations on Surface from the Angular Dependence of Near-edge X-ray Absorption Fine-structure Spectra. *Phys. Rev. B* **36**, 7891–7905 (1987).
119. Zahn, D. R. T., Gavrilă, G. N. & Salvan, G. Electronic and Vibrational Spectroscopies Applied to Organic/Inorganic Interfaces. *Chem. Rev.* **107**, 1161–232 (2007).
120. Tinone, M. C. K. & Tanaka, K. Inner-shell Excitation and Site Specific Fragmentation of Poly (Methylmethacrylate ) Thin Film. **0**, 5988–5995 (1994).
121. Hähner, G. Near Edge X-ray Absorption Fine Structure Spectroscopy as a Tool to Probe Electronic and Structural Properties of Thin Organic Films and Liquids. *Chem. Soc. Rev.* **35**, 1244–55 (2006).
122. Fadley, C. S. X-ray Photoelectron Spectroscopy: Progress and Perspectives. *J. Electron Spectros. Relat. Phenomena* **178–179**, 2–32 (2010).
123. Casu, M.B., Biswas, I., Nagel , M., Nagel , P., Schuppler, S., & Chasse, T. Photoemission Electron Microscopy of Diindenoperylene Thin Films. *Physical Review B* **78**, (2008).
124. Schöll, A. High-resolution Investigation of the Electronic Structure of Organic Thin Films. (2003).
125. Benny, H-T., Banerjee ,S., Sambasivan , S., Balasubramanian, M., Fischer, D. A., Eres, G., Purtezky, A. A., Geohegan, D. B., Lowndes, D.H., Han , W., Misewich , J.A., & Wong, S.S., Imperfect Surface Order and Functionalization in Vertical Carbon Nanotube Arrays Probed by Near Edge X-ray Absorption Fine Structure Spectroscopy (NEXAFS). *Phys. Chem. Chem. Phys.* **8**, 5038–44 (2006).
126. Wurth, W., Stöhr, J., Feulner, P., Pan , X., Bauchspiess, K. R., Baba, Y., Hudel, E., Rocker, G., & Menzel, D. Bonding, Structure and Magnetism of Physisorbed and Chemisorbed O<sub>2</sub> on Pt(111). *Phys. Rev. Lett.* **65**, 2426–2429 (1990).
127. Bracco, G. & Holst, B. *Surface Science Techniques*. (Springer Science & Business Media, 2013).
128. Nakanishi, K. & Ohta, T. in *Advanced Topics in Measurements* 43–50 (2012).
129. Nakajima, R. Electron-yield Saturation Effects in L -edge X-ray Magnetic Circular Dichroism Spectra of Fe , Co , and Ni. *Phys. Rev B.* **59**, 6421–6429 (1999).
130. Schöll, A., Zou, Y., Schmidt, T., Fink, R. & Umbach, E. High-Resolution Photoemission Study of Different NTCDA Monolayers on Ag(111): Bonding and Screening Influences on the Line Shapes. *J. Phys. Chem. B* **108**, 14741–14748 (2004).
131. Dufre, Y. F. Atomic Force Microscopy , a Powerful Tool in Microbiology. *J. Bacteriol.* **184**, 5205–5213 (2002).
132. Sugimoto, Y., Pou, P., Custance, O., Jelinek, P., Abe, M., Perez, R., Morita, S. Complex Patterning by Vertical Interchange Atom Manipulation Using Atomic Force Microscopy. *Science (80- )*. **322**, 413–417 (2008).
133. To, J., Pe, R. & Terakura, K. Simulation of Tip-Surface Interactions in Atomic Force Microscopy of an InP (110) Surface with a Si Tip. *Phys. Rev. B* **60**, 639–644 (1999).
134. Bhushan, B. *Nanotribology and Nanomechanics*. (Springer-Verlag, 2008).
135. Mittal, V. & Matsko, N. B. *Analytical Imaging Techniques for Soft Matter Characterization*. (Springer Science & Business Media, 2012).
136. Leite, F. L., Mattoso, L. H. C., Oliveira Jr, O. & Herrmann Jr, P. S. P. The Atomic Force Spectroscopy as a Tool to Investigate Surface Forces : Basic Principles and Applications. *Mod. Res. Educ. Top. Microsc.* 22–24 (2007).
137. Oteyza, D.G, Gorman, P, Chen, Y-C, Wickenburg, S, Riss, A, J. Mowbray, D, Etkin, G, Pedramrazi,

- Z, Tsai, H-Z, Rubio, A, Crommie, M.F, Fischer, F. Direct Imaging of Covalent Bond Structure in Single-Molecule Chemical Reactions. *Science* **340**, 1434–1438 (2013).
138. Sahin, O. & Erina, N. High-Resolution and Large Dynamic Range Nanomechanical Mapping in Tapping-Mode Atomic Force Microscopy. *Nanotechnology* **19**, 445717 (2008).
139. Hansma, P. K., Cleveland, J. P., Radmacher, M., Walters, D. A., Hillner, P. E., Bezanilla, M., Fritz, M., Vie, D., Hansma, H. G., Prater, C. B., Massie, J., Fukunaga, L., Gurley, J., & Elings V. Tapping mode atomic force microscopy in liquids. *Appl. Phys. Lett.* **64**, 1738 (1994).
140. [www.spmtips.com](http://www.spmtips.com).
141. *JPK NanoWizard Handbook*. (2005).
142. Ratera, I. & Veciana, J. Playing With Organic Radicals as Building Blocks for Functional Molecular Materials. *Chem. Soc. Rev.* **41**, 303–349 (2012).
143. *Magnetism: A Synchrotron Radiation Approach*. (Springer Science & Business Media, 2006).
144. Borozdina, Y. B. Aminoxyl Radicals - Pure Organic Materials With Tunable Magnetic and Sensing Properties. (Johannes Gutenberg-Universität, Mainz, 2012).
145. Abb, S. Controlled Growth of Paramagnetic Organic Radicals on Al<sub>2</sub>O<sub>3</sub>(11-20) Single Crystals. **3**, (Tuebingen, 2012).
146. Oldfarb, J. I. L. G. & Uuberg, E. R. I. C. M. S. Vapor Pressures and Thermodynamics of Oxygen-Containing Polycyclic Aromatic Hydrocarbons Measured Using Knudsen Effusion. *Environ. Toxicological Chem.* **27**, 1244–1249 (2008).
147. *Stable Radicals: Fundamentals and Applied Aspects of Odd-Electron Compounds*. (John Wiley & Sons, 2011).
148. Borozdina, Y. B., Kamm, V., Laquai, F. & Baumgarten, M. Tuning the Sensitivity of Fluorophore–Nitroxide Radicals. *J. Mater. Chem.* **22**, 13260–13267 (2012).
149. Sholle, V.D, Rozantsev, E. . Synthesis and Reaction of Stable Nitroxyl Radicals. *Synthesis (Stuttg)*. **4**, 190–202 (1971).
150. Ravat, P. Tuning of Magnetic Exchange Interactions between Organic Radicals through Bond and Space. (Johannes Gutenberg-Universität Mainz, 2014).
151. Rajca, A., Takahashi, M. & Pink, M. Conformationally Constrained, Stable, Triplet Ground State (S= 1) Nitroxide Diradicals. Antiferromagnetic Chains of S= 1 Diradicals. *J. Am. Chem. Soc.* **129**, 10159–10170 (2007).
152. Coupling, S., State, G. & Wroclawska, P. Organic Diradicals and Poiradicals: From Spin Coupling to Magnetism? *Chem. Rev.* **94**, 871–893 (1994).
153. Blundell, S. J. & Pratt, F. L. Organic and Molecular Magnets. *J. Phys. Condens. Matter* **16**, R771–R828 (2004).
154. Acosta-Torres, L. S., López-Marín, L. M., Núñez-Anita, R. E., Hernández-Padrón, G. & Castaño, V. M. Biocompatible Metal-Oxide Nanoparticles: Nanotechnology Improvement of Conventional Prosthetic Acrylic Resins. *J. Nanomater.* **2011**, 1–8 (2011).
155. Solanki, P. R., Kaushik, A., Agrawal, V. V. & Malhotra, B. D. Nanostructured Metal Oxide-Based Biosensors. *NPG Asia Mater.* **3**, 17–24 (2011).
156. Rodionov, I. V. Application of the Air-Thermal Oxidation Technology for Producing Biocompatible Oxide Coatings on Periosteal Osteofixation Devices from Stainless Steel. *Inorg. Mater. Appl. Res.* **4**, 119–126 (2013).
157. Xiang, B., Zhang, Y., Wang, Z., Luo, X H., Zhu, Y.W., Zhang, H Z., & Yu, D.P, Field-Emission

- Properties of TiO<sub>2</sub> Nanowire Arrays. *J. Phys. D. Appl. Phys.* **38**, 1152–1155 (2005).
158. Marcos Fernández-García, J. A. R. *Metal Oxide Nanoparticles*. (2007).
159. Urushibara, A., Asamitsu, A. & Sr, L. Insulator-Metal Transition and Giant Magnetoresistance in La<sub>0.7</sub>Sr<sub>0.3</sub>MnO<sub>3</sub>. *Phys. Rev. A* **51**, 103–109 (1995).
160. Venevtsev, Y. N., Bogatko, V. V., Popadeikin, I. A. & Tomashpolski, Y. Y. A. High Temperature Superconductivity and Ferroelectricity in Metal Oxides. *Ferroelectrics* **94**, 463–464 (1989).
161. Matsumoto, Y., Murakami, M., Shono, T., Hasegawa, T., Fukumura, T., Kawasaki, M., Ahmet, P., Chikyow, T., Koshihara, S., & Koinuma, H. Room-Temperature Ferromagnetism in Transparent Transition Metal – Doped Titanium Dioxide. *Science* **291**, 854–857 (2001).
162. Yang, H. G., Sun, Ch. H., Qiao, Sh. Zh., Zou, J., Liu, G., Smith, S. C., Cheng, H. M., Lu, G.Q., Anatase TiO<sub>2</sub> Single Crystals with a Large Percentage of Reactive Facets. *Nature* **453**, 638–41 (2008).
163. Kielbassa, S. Well-Defined Au /TiO<sub>2</sub> (110) Model Catalysts on Fully Oxidized Substrates. **2**, (Ulm, 2008).
164. Hodgskiss, S. W. Electron Spin Resonance Studies of Impurity Ions in Rutile. (1981).
165. Diebold, U. The Surface Science of Titanium Dioxide. *Surf. Sci. Rep.* **48**, 53–229 (2003).
166. Walle, L. E. Surface Science Studies of TiO<sub>2</sub> Single Crystal Systems. (Norwegian University of Science and Technology, 2009).
167. Brown, Jr, G. E., Henrich, V., William, C., Clark, D., Eggleston, C., Felmy, A., Goodman, D. W., Gratzel, M., Gary, M., McCarthy, M.I., Nealson, K.H., Sverjensky, D., Toney, M., & Zachara J. M. Metal Oxide Surfaces and Their Interactions with Aqueous Solutions and Microbial Organisms. *Chem. Soc. Rev.* **99**, 77–174 (1999).
168. *Complex Metallic Alloys: Fundamentals and Applications*. (John Wiley & Sons, 2010).
169. Himpsel, F.J., McFeely, F.R., Taleb-Ibrahimi, A., Yarmof, J. A., & Hollinger, G. Microscopic Structure of the SiO<sub>2</sub>/Si Interface. *Phys. Rev. B* **38**, 6084–6096 (1988).
170. Razeghi, M. *Technology of Quantum Devices*. (Springer, 2009).
171. Wang, Y.-L., Guo, H.-M., Qin, Z.-H., Ma, H.-F. & Gao, H.-J. Toward a Detailed Understanding of Si(111)- 7 × 7 Surface and Adsorbed Ge Nanostructures: Fabrications, Structures, and Calculations. *J. Nanomater.* **2008**, 1–18 (2008).
172. Lu, Q. Lu, Qiang Yeo, Yee Chia Yang, Kevin J, Lin, Ronald, Polishchuk, Igor, King, Tsu-jae Hu, Chenming, Song, S C, Luan, H F, Kwong, Two Silicon Nitride Technologies for Post- SiO<sub>2</sub> MOSFET Gate Dielectric. *IEEE Electron device Lett.* **22**, 324–326 (2001).
173. Trompe, R., Rubloff, G.W., Balk, P., Le Gouse, F.K., & Van Loenen, E. High Temperature SiO<sub>2</sub> Decomposition at the SiO<sub>2</sub>/Si Interface. *Phys. Rev. Lett.* **55**, 2332–2337 (1985).
174. Green, M. L., Gusev, E. P., Degraeve, R. & Garfunkel, E. L. Ultrathin (SiO<sub>2</sub> and Si–O–N Gate Dielectric Layers for Silicon Microelectronics: Understanding the Processing, Structure, and Physical and Electrical Limits. *J. Appl. Phys.* **90**, 2057–2121 (2001).
175. Horowitz, G. Organic Field-Effect Transistors. *Adv. Mater.* **10**, 365–377 (1998).
176. De Boer, R. W. I., Klapwijk, T. M. & Morpurgo, A. F. Field-Effect Transistors on Tetracene Single Crystals. *Appl. Phys. Lett.* **83**, 4345 (2003).
177. Silicon Nanoworld: Si(111) Surface and 7×7 Reconstruction.
178. Heide, P. van der. *X-Ray Photoelectron Spectroscopy*. (2012).

179. Friedbacher, G, Bubert, H. *Surface and Thin Film Analysis: A Compendium of Principles, Instrumentation, and Applications*. John (Wiley-VCH Verlag GmbH & Co. KGaA, 2011).
180. X-Ray Photoelectron Spectroscopy. *Encycl. Phys. Sci. Technol.* 921–938
181. Michael, R. An X-Ray Spectroscopic Study of Novel Materials for Electronic Applications. (University of Osnabrück, 2009).
182. CHA Details.
183. Claessen, R., Schäfer, J. & Sing, M. *Very High Resolution Photoelectron Spectroscopy. Dimension Contemporary German Arts And Letters* **715**, (Springer Berlin Heidelberg, 2007).
184. Willmott, P. & PhD. *An Introduction to Synchrotron Radiation: Techniques and Applications*. (John Wiley & Sons, 2011).
185. Jamison, S. X-Ray Science: X-Ray FEL Shines Brightly. *Nat. Photonics* **4**, 589–591 (2010).
186. Eland, J. H. D. *Photoelectron Spectroscopy: An Introduction to Ultraviolet Photoelectron Spectroscopy in the Gas Phase*. (Elsevier, 2013).
187. Ashcroft, N. W. & Mermin, D. N. *Festkörperphysik*. (Oldenbourg Verlag, 2012).
188. Wagner, N., Brümmer, O. & Sauer, N. Photoemission Studies of Titanium Oxides. *Cryst. Res. Technol.* **17**, 1151–1158 (1982).
189. Lun Pang, C., Lindsay, R. & Thornton, G. Chemical Reactions on Rutile TiO<sub>2</sub>(110). *Chem. Soc. Rev.* **37**, 2328–53 (2008).
190. T.K. SHAM, M. S. L. X-Ray Photoelectron Spectroscopy Studies of Clean and Hydrated TiO<sub>2</sub> (RUTILE) Surfaces. *Chem. Phys. Lett.* **68**, 426–432 (1979).
191. Nolan, M. Elliott, S. D. Electronic Structure of Point Defects in Controlled self-Doping of the TiO<sub>2</sub> (110) Surface: Combined photoemission spectroscopy and density functional theory study. *Phys. Rev. B* **77**, 235424 (2008).
192. Proceedings of the Symposium on Compatability of Biomedical Implants. in **0**, 397 (The Electrochemical Society, 1994).
193. Tang, J., Durrant, J. R. & Klug, D. R. Mechanism of Photocatalytic Water Splitting in TiO<sub>2</sub> . Reaction of Water with Photoholes , Importance of Charge Carrier Dynamics , and Evidence for Four-Hole Chemistry. *J. Am. Chem. Soc.* **127**, 13885–13891 (2008).
194. Zhang, D., Yang, M. & Dong, S. Hydroxylation of the Rutile TiO<sub>2</sub>(110) Surface Enhancing Its Reducing Power for Photocatalysis. *J. Phys. Chem. C* **2**, 150109085144001 (2015).
195. Wang, L.-Q., Baer, D. R., Engelhard, M. H. & Shultz, A. N. The Adsorption of Liquid and Vapor Water on TiO<sub>2</sub>(110) Surfaces: the Role of Defects. *Surf. Sci.* **344**, 237–250 (1995).
196. Mayer, J.T. , Diebold, U , Madey , T.E. , Garfunkel, E. Titanium and Reduced Titania Overlayers on Titanium Dioxide (110). *J. Electron Spectros. Relat. Phenomena* **73**, 1–11 (1995).
197. Sen , S.K., & Verbist, R. 2s and 2p X-Ray Photoelectron Spectra of Ti<sup>4+</sup> ion in TiO<sub>2</sub>. *J. Chem. Phys. Lett.* **39**, 560–564 (1976).
198. Scrocco, M. X-Ray Photoelectron Spectra of Ti<sup>4+</sup> in TiO<sub>2</sub>. Evidence of Band Structure. *Chem. Phys. Lett.* **61**, 453–456 (1979).
199. Wendt, S., Schaub, R., Matthiesen, J., Vestergaard, EK., Wahlström, E., Rasmussen, MD., Thostrup, P., Molina, LM., Lægsgaard, E., Stensgaard, I., Hammer, B., Besenbacher, F. Oxygen Vacancies on TiO<sub>2</sub>(110) and their Interaction with H<sub>2</sub>O and O<sub>2</sub>: A Combined High-Resolution STM and DFT Study. *Surf. Sci.* **598**, 226–245 (2005).

200. Valentin, C. Di, Pacchioni, G. & Selloni, A. Electronic Structure of Defect States in Hydroxylated and Reduced Rutile TiO<sub>2</sub>(110) Surfaces. *Phys. Rev. Lett.* **166803**, (2006).
201. Duncan, D. A., Allegretti, F., & Woodruff, D. P. Water Does Partially Dissociate on the Perfect TiO<sub>2</sub>(110) Surface: A Quantitative Structure Determination. *Phys. Rev. B* **86**, 45411–45414 (2012).
202. Guillemot, F., Porté, M. ., Labrugère, C. & Baquey, C. Ti<sup>4+</sup> to Ti<sup>3+</sup> Conversion of TiO<sub>2</sub> Uppermost Layer by Low-Temperature Vacuum Annealing: Interest for Titanium Biomedical Applications. *J. Colloid Interface Sci.* **255**, 75–78 (2002).
203. Henderson, M. A., Otero-tapia, S. & Castro, M. E. The Chemistry of Methanol on the TiO<sub>2</sub>(110) Surface: the Influence of Vacancies and Coadsorbed Species. *Faraday Discuss.* **114**, 313–329 (2000).
204. Henderson, M. A. An HREELS and TPD Study of Water on TiO<sub>2</sub>(110): the Extent of Molecular Versus Dissociative Adsorption. *Surf. Sci* **355**, 151–166 (1996).
205. Walle, L. E., Borg, A., Johansson, E. M. J., Plogmaker, S., Rensmo, H., Uvdal, P., & Sandell, A. Mixed Dissociative and Molecular Water Adsorption on Anatase TiO<sub>2</sub>(101). *Phys. Chem. C* **2**, 9545–9550 (2011).
206. Bredow, T. & Jug, K. Theoretical Investigation of Water Adsorption at Rutile and Anatase Surfaces. *Surf. Sci.* **327**, 398–408 (1995).
207. Fleming, G. J. Adib, K., Rodriguez, J.A., Barteau, M.A., White, J. M., & Idriss, H. The Adsorption and Reactions of the Amino Acid Proline on Rutile TiO<sub>2</sub>(110) Surfaces. *Surf. Sci.* **602**, 2029–2038 (2008).
208. Unterberger, W, Lertholi, T. J., Kröger, E. AM., Knight, J., Duncan, D. A., Kreikemeyer-Lorenzo, D., Hogan, K. A., Jackson, D. C., Włodarczyk, R., Sierka, M., Sauer, J., & Woodruff, D. P. Local hydroxyl adsorption geometry on TiO<sub>2</sub>(110). *Phys. Rev. B* **84**, 115461 (2011).
209. Schaub, R., Thostrup, P., Lopez, N., Lægsgaard, E., Stensgaard, I., Nørskov, J. K., & Besenbacher, F. Oxygen Vacancies as Active Sites for Water Dissociation on Rutile TiO<sub>2</sub>(110). *Phys. Rev. Lett.* **87**, 266104 (2001).
210. Savu, S.-A. Casu, M.B., Schundelmeier, S., Abb, S., Tönshoff, Ch., Bettinger, H.F., & Chasse, T. Nanoscale Assembly, Morphology and Screening Effects in Nanorods of Newly Synthesized Substituted Pentacenes. *RSC Adv.* **2**, 5112 (2012).
211. Savu, S.-A., Biswas, I., Sorace, L., Mannini, M., Rovai, D., Caneschi, A., Chasse, T., & Casu, M.B. Nanoscale Assembly of Paramagnetic Organic Radicals on Au(111) Single Crystals. *Chemistry* **19**, 3445–3450 (2013).
212. Schöll, A., Zou, Y., Kilian, L., Hübner, D. & Gador, D. Electron-Vibron Coupling in High-Resolution X-ray Absorption Spectra of Organic Materials: NTCDA on Ag(111). *Phys. Rev Lett.* **93**, 146406–146410 (2004).
213. Schöll, A., Hübner, D., Schmidt, Th, Urquhart, S. G. Fink, R., Umbach, E. Anharmonicity of the Core-excited State Potential of an Organic Molecule from NEXAFS Vibronic Fine Structure. *Chem. Phys. Lett.* **392**, 297–302 (2004).
214. Schöll, A., Zou, Y., Schmidt, T., Fink, Rainer., Umbach, E., Line Shapes and Satellites in High-resolution X-ray Photoelectron Spectra of Large Pi-conjugated Organic Molecules. *J. Chem. Phys.* **121**, 10260–7 (2004).
215. Sjögren, B., Svensson, S., deBrito, A. Naves, Correia, N. Keane, M. P., Enkvist, C. Lunell, S. The C 1s Core Shake-up Spectra of Alkene Molecules: An Experimental and Theoretical Study. *J. Chem. Phys.* **96**, 6389 (1992).

216. Ebel, H., Ebel, M. F., Wernisch, J. & Jablonsiu, A. The Influence of Elastic Scattering of Electron on Measured X-ray Photoelectron Signals. *J. Electron Spectros. Relat. Phenomena* **34**, 355–362 (1984).
217. Rocco, M. L. Haeming, M., Batchelor, DR., Fink, R., Schöll, A., Umbach, E. Electronic Relaxation Effects in Condensed Polyacenes: A High-Resolution Photoemission Study. *J. Chem. Phys.* **129**, 74702 (2008).
218. Ottaviano, L., Lozzi, L., Ramondo, F., Picozzi, P. & Santucci, S. Copper Hexadecafluoro Phthalocyanine and Naphthalocyanine : The Role of Shake up Excitations in the Interpretation and Electronic Distinction of High-Resolution X-Ray Photoelectron Spectroscopy Measurements. *J. Electron Spectros. Relat. Phenomena* **105**, 145–154 (1999).
219. Bigelow, R. W., Weagley, R. J. & Freund, H.-J. Core-Hole Spectra of D<sup>+</sup>-Ar A<sup>-</sup> Molecules in the Solid State (D = Dialkylamino, A = Pyridinium, Pirylium, Thiapyrylium). *J. Electron Spectros. Relat. Phenomena* **28**, 149–170 (1982).
220. Pauling, L. *The Nature of the Chemical Bond and the Structure of Molecules and Crystals: An Introduction to Modern Structural Chemistry*. (Cornell University Press, 1960).
221. IUPAC Gold Book - Mesomerism.
222. Atkins, P. & Paula, J. de. *Physical Chemistry Vol 2: Quantum Chemistry*. (W. H. Freeman, 2009).
223. Finar, I. L. *Organic Chemistry: The Fundamental Principles*. (Longmans, Green, 1960).
224. Müller, K, Seitsonen, A.P, Brugger, Th, Westover, J, Greber, Th, Jung, & Th, Kara, A. Electronic Structure of an Organic/Metal Interface: Pentacene/ Cu(110). *J. Phys. Chem. C* **116**, 2465–23471 (2012).
225. Jouan, P.-Y., Peignon, M.-C.,Cardinaud, Ch., & Lempérière,G. Characterisation of TiN Coatings and of the TiN/Si Interface by X-Ray Photoelectron Spectroscopy and Auger Electron Spectroscopy. *Appl. Surf. Sci.* **68**, 595–603 (1993).
226. Saha, N. C. & Tompkins, H. G. Titanium Nitride Oxidation Chemistry: An X-Ray Photoelectron Spectroscopy Study. *J. Appl. Phys.* **72**, 3072 (1992).
227. Ullman, E. F., Call, L. . & Osiecki, H. Stable Free Radicals. VIII. New Imino, Amidino, and Carbamoyl Nitroxides. *J.Org.Chem* **35**, 3623–3632 (1970).
228. Bundaleski, N., Silva, A. G., Schröder, U., Moutinho, A.M. C. & Teodoro, O. M. N. D. Adsorption Dynamics of Water on the Surface of TiO<sub>2</sub>(110). *J. Phys. Conf. Ser.* **257**, 12008 (2010).
229. Casu, M. B., Zou, Y., Kera, S., Batchelor, D., Schmidt, T., & Umbach, E. Investigation of Polarization Effects in Organic Thin Films by Surface Core-Level Shifts. *Phys. Rev. B* **76**, 193311–193314 (2007).
230. Casu, M. B. Evidence for Efficient Screening in Organic Materials. *Phys. status solidi – Rapid Res. Lett.* **2**, 40–42 (2008).
231. Ueda, K., Hoshino, M.,Tanaka,T., Kitajima, M.,Tanaka, H.,deFanis,A.,Tamenori,Y., Ehara, M., Oyagi, F., Kuramoto, K., Nakatsuji, H. Symmetry-Resolved Vibrational Spectra of Carbon K-Shell Photoelectron Satellites in Carbon Monoxides: Experiment and Theory. *Phys. Rev. Lett.* **94**, 243004 (2005).
- 232.Rennie,E., Kempgens, B., Köppe, H. M., Hergenahh, U., Feldhaus, J., Itchkawitz, B. S., Kilcoyne, A. L.D., Kivimäki, A., Maier, K., Piancastelli, M. N., Polcik, M., Rüdél, A., & Bradshaw, A. M. A Comprehensive Photoabsorption, Photoionization, and Shake-up Excitation Study of the C 1s Cross Section of Benzene. *J. Chem. Phys.* **113**, 7362 (2000)
233. Piancastelli, M. N., Ferrett , T. A. , Lindle., D. W. , Medhurst, L. J. , Heimann, P. A. , Liu , S. H. ,

- & Shirley, D. A. Resonant Processes above the Carbon 1s Ionization Threshold in Benzene and Ethylene. *J. Chem. Phys.* **90**, 3004 (1989).
234. Söderström, J., Söderström, J., Mårtensson, N., Travnikova, O., Patanen, M., Miron, C., Sæthre, L., J., Børve, K. J., Rehr, J. J., Kas, J. J., Vila, F. D., Thomas, T. D., & Svensson, S., Nonstoichiometric Intensities in Core Photoelectron Spectroscopy. *Phys. Rev. Lett.* **108**, 193005 (2012).
235. Koch, N., Uneo, N., & Wee, A. T. *The Molecule-Metal Interface*. (John Wiley & Sons, 2013).
236. Sandi, G., Song, K., Karrado, K. A., Winans, R. A NEXAFS Determination of the Electronic Structure of Carbons for Lithium-Ion Cells. *Carbon N. Y.* **36**, 1755–1758 (1998).
237. Lucas, L. A., DeLongchamp, D. M., Richter, L. J., Kline, R. J., Fischer, D. A., Kaafarani, B. R., & Jabbour, Gh. E. Thin Film Microstructure of a Solution Processable Pyrene-Based Organic Semiconductor. *Chem. Mater.* **20**, 5743–5749 (2008).
238. Fu, J. Linear Dichroism in the NEXAFS Spectroscopy of N-Alkane Thin Films. (Saskatoon, 2006).
239. Sugano, T., Blundell, S. J., Lancaster, T., Pratt, F. L., & Mori, H. Magnetic Order in the Purely Organic Quasi-One-Dimensional Ferromagnet 2-Benzimidazolyl Nitronyl Nitroxide. *Phys. Rev. B* **82**, 180401 (2010).
240. Molas, S., Coulon, C., & Fraxedas, J. Magnetic Properties of thin  $\alpha$ -p-Nitrophenyl Nitronyl Nitroxide Films. *CrystEngComm* **5**, 310 (2003).
241. Clancy, P. Application of Molecular Simulation Techniques to the Study of Factors Affecting the Thin-Film Morphology of Small-Molecule Organic Semiconductors. *Chem. Mater.* **23**, 522–543 (2011).
242. Savu, S.-A., Abb, S., Schundelmeier, S., Saathoff, J. D., Stevenson, J. M., Tönshoff, Ch., Bettinger, H. F., Clancy, P., Casu, M. B., & Chassé, T. Pentacene-Based Nanorods on Au(111) Single Crystals: Charge Transfer, Diffusion, and Step-Edge Barriers. *Nano Res.* **6**, 449–459 (2013).
243. Gallani, J. L., Moigne, J. Le, Oswald, L., Bernard, M., & Turek, P. Induced Ferromagnetic Interactions in Langmuir - Blodgett Films of an Organic Radical. *Langmuir* **17**, 1104–1109 (2001).
244. Moigne, J. L., Gallani, J. L., Wautelet, P., Moroni, M., Oswald, L., Cruz, C., Galerne, Y., Arnault, J. C., Duran, R., & Garrett, M. Nitronyl Nitroxide and Imino Nitroxide Mono- and Biradicals in Langmuir and Langmuir - Blodgett Films. 7484–7492 (1998).
245. Kakavandi, R., Savu, S.-A., Sorace, L., Rovai, D., Mannini, M., & Casu, M. B. Core-Hole Screening, Electronic Structure, and Paramagnetic Character in Thin Films of Organic Radicals Deposited on SiO<sub>2</sub>/Si(111). *J. Phys. Chem. C* **118**, 8044–8049 (2014).
246. Shen, C., Haryono, M., Grohmann, A., Buck, M., Weidner, T., Ballav, N., & Zharnikov, M. Self-Assembled Monolayers of a Bis-Pyrazol-1-yl) Pyridine-Substituted Thiol on Au(111). *langmuir* **24**, 12883–12891 (2008).
247. Liscio, F., Albonetti, C., Broch, K., Shehu, A., Quiroga, S. D., Ferlauto, L., Frank, C., Kowarik, S., Nervo, R., Gerlach, A., Milita, S., Schreiber, F., & Biscarini, F. Molecular Reorganization in Organic Field-Effect Transistors and Its Effect on Two-Dimensional Charge Transport Pathways. *ACS Nano* **7**, 1257–1264 (2013).
248. Kowarik, S., Gerlach, A., Sellner, S., Schreiber, F., Cavalcanti, L., and Konovalov, O. Real-Time Observation of Structural and Orientational Transitions during Growth of Organic Thin Films. *Phys. Rev Lett.* **96**, 125504 (2006).



# Chapter 7

## Appendix I

### A) NitPyn ( $C_{23}H_{21}N_2O_2$ )

**Deposited on  $TiO_2(110)$  single crystal**

$$C = 30616/0.25 = 122464$$

$$N = 4354/0.4 = 10885$$

$$C/N = 11.25$$

**Powder**

$$C = 34029963/0.25 = 1361198.52$$

$$N = 50757/0.4 = 126892.5$$

$$C/N = 10.72$$

**Deposited on  $SiO_2/Si(111)$**

$$C = 63193/0.25 = 252772$$

$$N = 7673/0.4 = 22146$$

$$C/N = 11.41$$

### B) PPN ( $C_{26}H_{23}N_4O_2$ )

**Deposited on  $TiO_2(110)$  single crystal**

$$C = 3141292/0.25 = 12565168$$

$$N = 718009.60/0.4 = 1795024$$

$$C/N = 7$$

**Powder**

$$C = 94750.646/0.25 = 19002.584$$

$$N = 1165.80/0.4 = 2914.51$$

$$C/N = 6.52$$

**Deposited on SiO<sub>2</sub>/Si(111)**

$$C = 64108/0.25 = 256432$$

$$N = 16544 /0.4 = 41360$$

$$C/N = 6.2$$

**C) Bisnitroxide Diradical (C<sub>18</sub> H<sub>26</sub> N<sub>2</sub> O<sub>4</sub>)****Deposited on TiO<sub>2</sub>(110) single crystal**

$$C = 34029963/0.25 = 1361198.52$$

$$N = 50757/0.4 = 126892.5$$

$$C/N = 10.72$$

**Powder**

$$C = 85926.122/0.25 = 343704.5$$

$$N = 12085.137/0.4 = 30212.84$$

$$C/N = 11.37$$

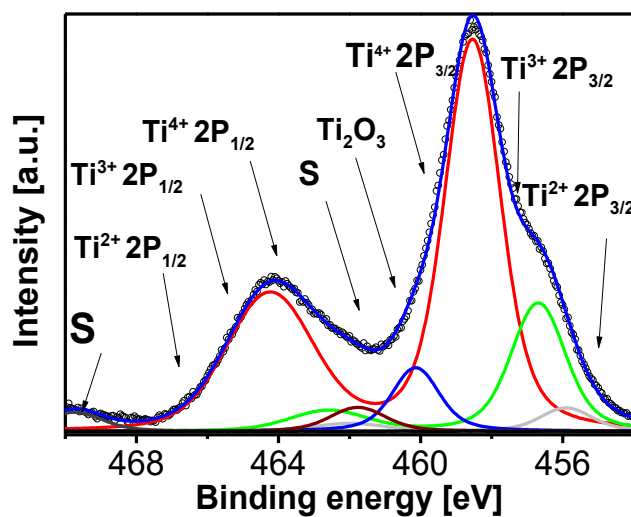
**Deposited on SiO<sub>2</sub>/Si(111)**

$$C = 63193/0.25 = 252772$$

$$N = 7673/0.4 = 22146$$

$$C/N = 11.4$$

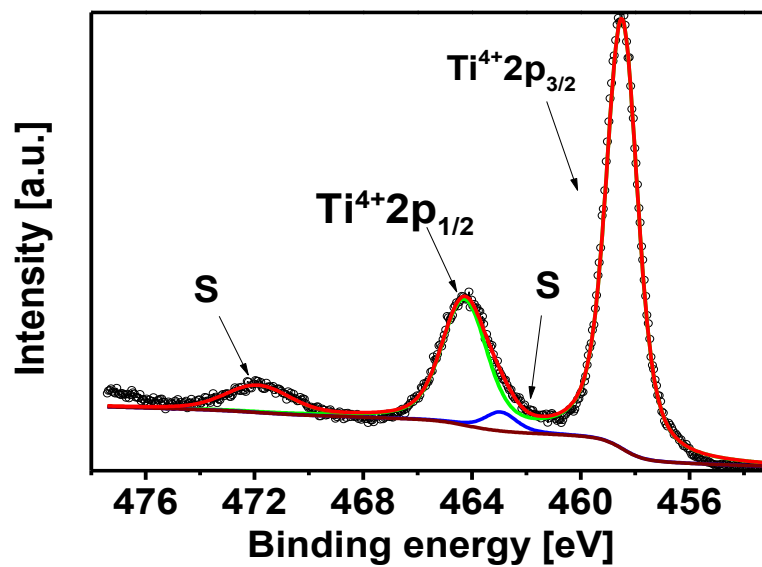
## Appendix II



**Figure A.1:** Ti 2p core level spectrum of clean  $\text{TiO}_2(110)$  single crystal.

**Table A.1:** Binding energy of the Ti 2p core level spectrum of clean  $\text{TiO}_2(110)$  single crystal.

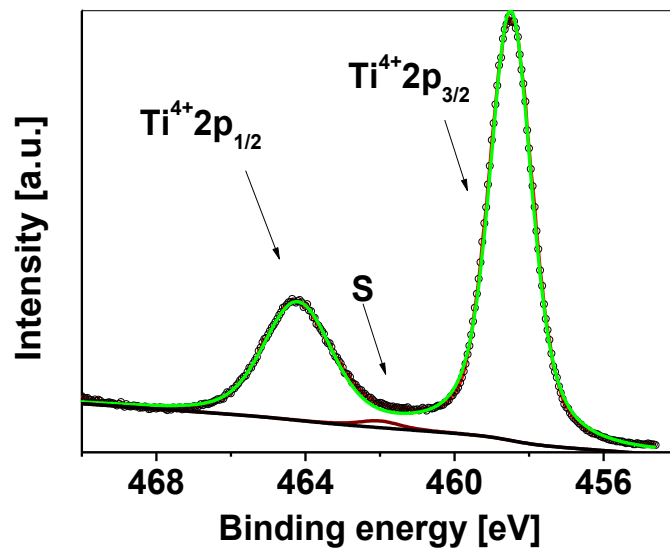
	Energy (eV)	Lorentzian Width (eV)	Gaussian Width (eV)	Intensity (%)
$\text{Ti}^{4+}(2p_{3/2})$	458.50	0.70	1.45	44.71
$\text{Ti}^{4+}(2p_{1/2})$	464.20	0.70	2.52	23.18
$\text{Ti}^{3+}(2p_{3/2})$	456.60	0.70	1.41	14.29
$\text{Ti}^{3+}(2p_{1/2})$	462.50	0.70	1.66	3.05
$\text{Ti}^{2+}(2p_{3/2})$	455.83	0.70	1.35	2.46
$\text{Ti}^{2+}(2p_{1/2})$	461.93	0.70	1.22	1.08
$\text{Ti}_2\text{O}_3$	460.05	0.70	1.13	6.30
$\text{S}_1$	461.68	0.70	1.45	2.73
$\text{S}_2$	468.68	0.70	1.45	2.18



**Figure A.2:** XPS spectrum of clean TiO<sub>2</sub>(110) single crystal.

**Table A.2:** Binding energy of the Ti 2p core level spectrum of clean TiO<sub>2</sub>(110) single crystal.

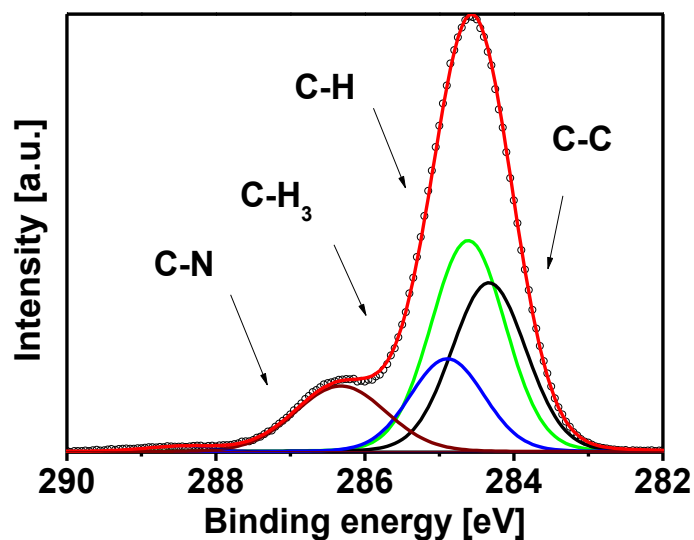
	Energy (eV)	Lorentzian Width (eV)	Gaussian Width (eV)	Intensity (%)
Ti <sup>4+</sup> (2p <sub>3/2</sub> )	458.50	0.70	0.96	64.96
Ti <sup>4+</sup> (2p <sub>1/2</sub> )	464.20	0.70	1.55	24.96
S <sub>1</sub>	462.95	0.70	0.96	2.87
S <sub>2</sub>	472.89	0.70	2.40	7.20



**Figure A.3:** Ti 2p core level spectrum of clean TiO<sub>2</sub>(110) single crystal.

**Table A.3:** Binding energy of the Ti 2p core level spectrum of clean TiO<sub>2</sub>(110) single crystal.

	Energy (eV)	Lorentzian Width (eV)	Gaussian Width (eV)	Intensity (%)
Ti <sup>4+</sup> (2p <sub>3/2</sub> )	458.50	0.53	1.06	70.03
Ti <sup>4+</sup> (2p <sub>1/2</sub> )	464.21	0.53	1.84	28.06
S	461.95	0.53	1.06	07.04
S	472.49	0.53	1.06	1.70

NitPyn deposited on TiO<sub>2</sub>(110) single crystal

**Figure A.4:** C 1s core level spectrum of nominally 2 nm NitPyn deposited on TiO<sub>2</sub>(110) single crystal.

**Table A.4:** Binding energy of the different components of the C 1s core level spectrum and shake-up satellites in NitPyn deposited on TiO<sub>2</sub>(110) single crystal.

	Energy (eV)	Lorentzian Width (eV)	Gaussian Width (eV)	Intensity (%)
C-C	284.40	0.08	1.12	31.30
C-H	284.68	0.08	1.12	39.10
CH <sub>3</sub>	284.96	0.08	1.12	17.20
C-N	286.39	0.08	1.45	12.40

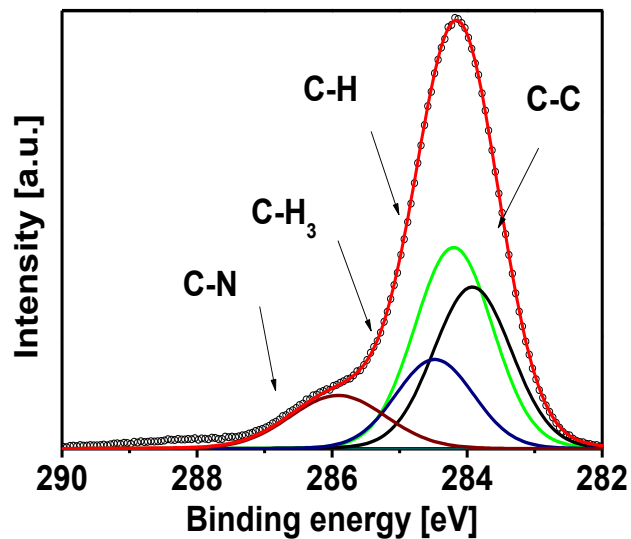


**Figure A.5:** C 1s core level spectrum of nominally 0.5 nm NitPyn deposited on TiO<sub>2</sub>(110) single crystal.

**Table A.5:** Binding energy of the different components of the C 1s core level spectrum and shake-up satellites of nominally 0.5 nm NitPyn deposited on TiO<sub>2</sub>(110) single crystal.

	Energy (eV)	Lorentzian Width (eV)	Gaussian Width (eV)	Intensity (%)
<b>C-C</b>	284.02	0.08	1.32	31.30
<b>C-H</b>	284.30	0.08	1.32	39.10
<b>CH<sub>3</sub></b>	284.58	0.08	1.32	17.20
<b>C-N</b>	286.01	0.08	1.68	12.40

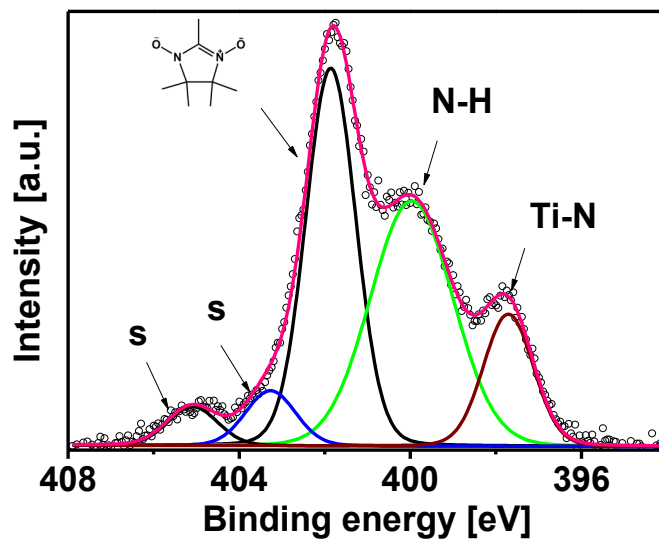


**Figure A.6:** N 1s core level spectrum of nominally 0.5 nm NitPyn deposited on TiO<sub>2</sub>(110) single crystal.

**Table A.6:** Binding energy of the different components of the N 1s core level spectrum and shake-up satellites of nominally 0.5 nm NitPyn deposited on TiO<sub>2</sub>(110) single crystal.

	Energy (eV)	Lorentzian Width (eV)	Gaussian Width (eV)	Intensity (%)
<b>C-N</b>	401.92	0.1	1.32	47.58
<b>N-H</b>	400.03	0.1	2.35	33.40
<b>Ti-N</b>	398.02	0.1	1.32	10.60
<b>S<sub>1</sub></b>	403.32	0.1	1.32	4.48
<b>S<sub>2</sub></b>	405.15	0.1	1.32	3.88

**Figure A.7:** N 1s core level spectrum of nominally 3 nm NitPyn deposited on TiO<sub>2</sub>(110) single crystal.

**Table A.7:** Binding energy of the different components of the N 1s core level spectrum and shake-up satellites of nominally 3 nm NitPyn deposited on TiO<sub>2</sub>(110) single crystal.

	<b>Energy (eV)</b>	<b>LorentzianWidth (eV)</b>	<b>GaussianWidth (eV)</b>	<b>Intensity (%)</b>
<b>N-H</b>	400.03	0.1	2.35	83.37
<b>Ti-N</b>	397.75	0.1	1.33	13.47
<b>S<sub>1</sub></b>	402.93	0.1	2.03	3.16

**Figure A.8:** O 1s core level spectrum of nominally 2 nm NitPyn deposited on TiO<sub>2</sub>(110) single crystal.

**Table A.8:** Binding energy of the different components of the O 1s core level spectrum and shake-up satellites of nominally 2 nm NitPyn deposited on TiO<sub>2</sub>(110) single crystal.

	<b>Energy (eV)</b>	<b>LorentzianWidth (eV)</b>	<b>GaussianWidth (eV)</b>	<b>Intensity (%)</b>
<b>O</b>	529.75	0.1	1.14	60.72
<b>O-H</b>	531.14	0.1	0.93	1.02
<b>O (Nitpyn)</b>	531.13	0.1	1.39	30.86
<b>Terminal O</b>	532.05	0.1	1.71	1.71
<b>S</b>	532.54	0.1	0.93	1.43

**Figure A.9:** O 1s core level spectrum of clean TiO<sub>2</sub>(110) single crystal.

**Table A.9:** Binding energy of the different components of the O 1s core level spectrum and shake-up satellites of clean TiO<sub>2</sub>(110) single crystal.

	<b>Energy (eV)</b>	<b>LorentzianWidth (eV)</b>	<b>GaussianWidth (eV)</b>	<b>Intensity (%)</b>
<b>O</b>	529.75	0.1	1.47	97.94
<b>O-H</b>	531.14	0.1	1.19	2.06

**Figure A.10:** N 1s core level spectrum of nominally 2.3 nm NitPyn deposited on TiO<sub>2</sub>(110) single crystal (excitation energy = 1000 eV).

**Table A.10:** Binding energy of the different components of the N 1s core level spectrum and shake-up satellites of nominally 2.3 nm NitPyn deposited on TiO<sub>2</sub>(110) single crystal (excitation energy = 1000 eV).

	<b>Energy (eV)</b>	<b>Lorentzian Width (eV)</b>	<b>Gaussian Width (eV)</b>	<b>Intensity (%)</b>
<b>C-N</b>	402.04	0.1	1.41	77.51
<b>N-H</b>	400.15	0.1	2.12	9.07
<b>Ti-N</b>	398.15	0.1	1.41	4.63
<b>S<sub>1</sub></b>	403.44	0.1	1.41	4.86
<b>S<sub>2</sub></b>	405.21	0.1	1.41	3.92

**Figure A.11:** N 1s core level spectrum of nominally 2.3 nm NitPyn deposited on TiO<sub>2</sub>(110) single crystal (excitation energy = 640 eV).

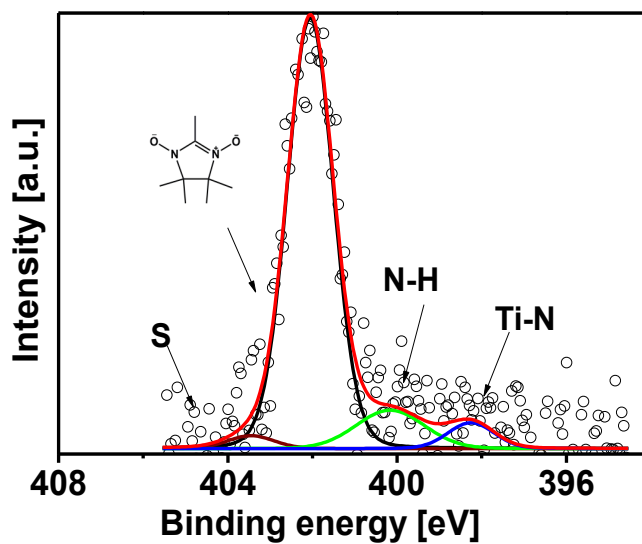
**Table A.11:** Binding energy of the different components of the N 1s core level spectrum and shake-up satellites of nominally 2.3 nm NitPyn deposited on TiO<sub>2</sub>(110) single crystal (excitation energy = 640 eV).

	<b>Energy (eV)</b>	<b>Lorentzian Width (eV)</b>	<b>GaussianWidth (eV)</b>	<b>Intensity (%)</b>
<b>C-N</b>	402.04	0.1	1.39	77.13
<b>N-H</b>	400.15	0.1	1.39	10.26
<b>Ti-N</b>	398.15	0.1	2.17	11.07
<b>S<sub>1</sub></b>	405.21	0.1	1.39	1.54

**Figure A.12:** N 1s core level spectrum of nominally 0.5 nm NitPyn deposited on TiO<sub>2</sub>(110) single crystal (excitation energy = 1000 eV).

**Table A.12:** Binding energy of the different components of the N 1s core level spectrum and shake-up satellites of nominally 0.5 nm NitPyn deposited on TiO<sub>2</sub>(110) single crystal (excitation energy = 1000 eV).

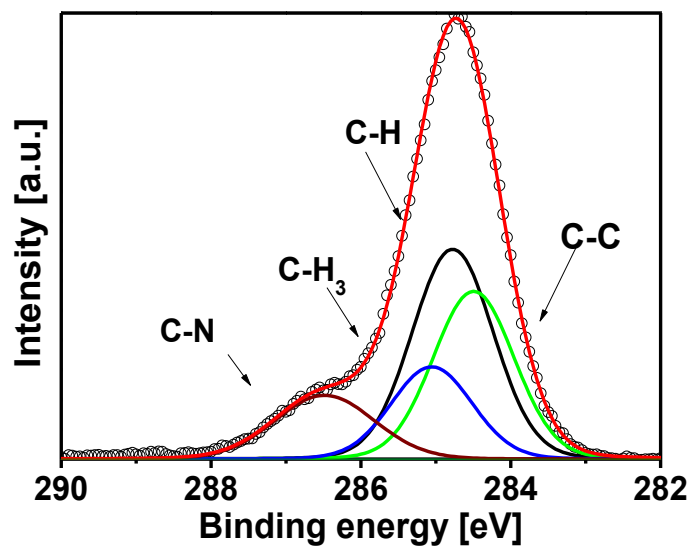
	<b>Energy (eV)</b>	<b>LorentzianWidth (eV)</b>	<b>Gaussian Width (eV)</b>	<b>Intensity (%)</b>
<b>C-N</b>	402.04	0.1	1.35	28.43
<b>N-H</b>	400.15	0.1	3.12	52.68
<b>Ti-N</b>	398.45	0.1	1.35	4.79
<b>S<sub>1</sub></b>	403.44	0.1	1.35	3.92
<b>S<sub>2</sub></b>	405.33	0.1	1.35	2.51



**Figure A.13:** N 1s core level spectrum of nominally 1.5 nm NitPyn deposited on TiO<sub>2</sub>(110) single crystal (excitation energy = 640 eV).

**Table A.13:** Binding energy of the different components of the N 1s core level spectrum and shake-up satellites of nominally 1.5 nm NitPyn deposited on TiO<sub>2</sub>(110) single crystal (excitation energy = 640 eV).

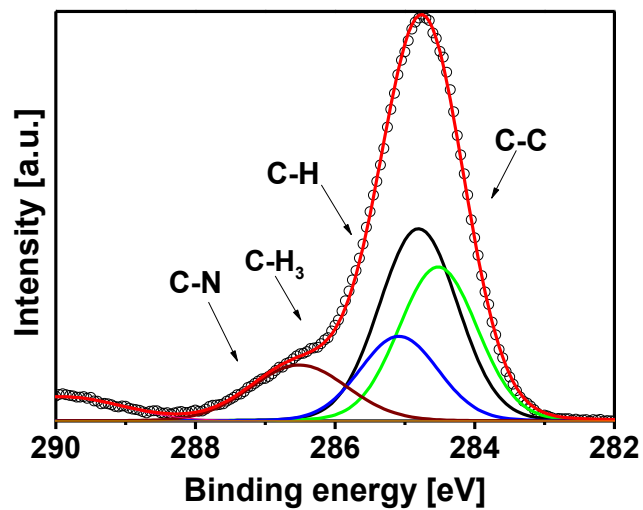
	Energy (eV)	Lorentzian Width (eV)	Gaussian Width (eV)	Intensity (%)
<b>C-N</b>	402.04	0.1	1.23	81.49
<b>N-H</b>	400.15	0.1	1.84	10.67
<b>Ti-N</b>	398.45	0.1	1.23	4.92
<b>S<sub>1</sub></b>	403.44	0.1	1.23	2.54



**Figure A.14:** C 1s core level spectrum of nominally 2.3 nm NitPyn deposited on TiO<sub>2</sub>(110) single crystal (excitation energy = 1000 eV).

**Table A.14:** Binding energy of the different components of the C 1s core level spectrum and shake-up satellites of nominally 2.3 nm NitPyn deposited on TiO<sub>2</sub>(110) single crystal (excitation energy = 1000 eV).

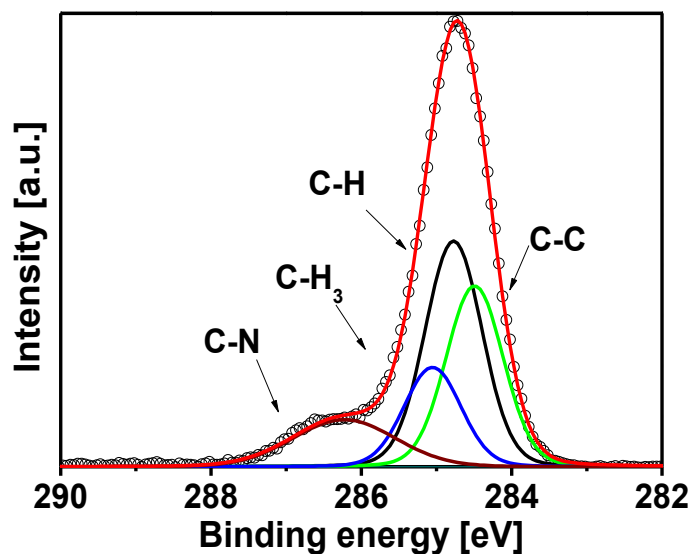
	Energy (eV)	Lorentzian Width (eV)	Gaussian Width (eV)	Intensity (%)
<b>C-C</b>	284.50	0.08	1.23	30.59
<b>C-H</b>	284.76	0.08	1.23	38.33
<b>CH<sub>3</sub></b>	285.04	0.08	1.23	16.83
<b>C-N</b>	286.47	0.08	1.52	14.25



**Figure A.15:** C 1s core level spectrum of nominally 2.3 nm NitPyn deposited on TiO<sub>2</sub>(110) single crystal (excitation energy = 640 eV).

**Table A.15:** Binding energy of the different components of the C 1s core level spectrum and shake-up satellites of nominally 2.3 nm NitPyn deposited on TiO<sub>2</sub>(110) single crystal (excitation energy = 640 eV).

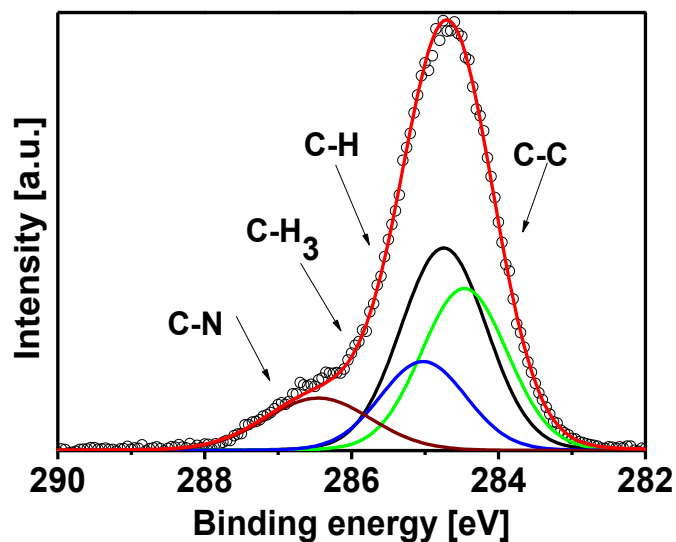
	Energy (eV)	Lorentzian Width (eV)	Gaussian Width (eV)	Intensity (%)
<b>C-C</b>	284.50	0.08	1.28	28.74
<b>C-H</b>	284.76	0.08	1.28	35.85
<b>CH<sub>3</sub></b>	285.04	0.08	1.28	15.79
<b>C-N</b>	286.49	0.08	1.58	12.79



**Figure A.15:** C 1s core level spectrum of nominally 2.3 nm NitPyn deposited on TiO<sub>2</sub>(110) single crystal (excitation energy = 330 eV).

**Table A.15:** Binding energy of the different components of the C 1s core level spectrum and shake-up satellites of nominally 2.3 nm NitPyn deposited on TiO<sub>2</sub>(110) single crystal (excitation energy = 330 eV).

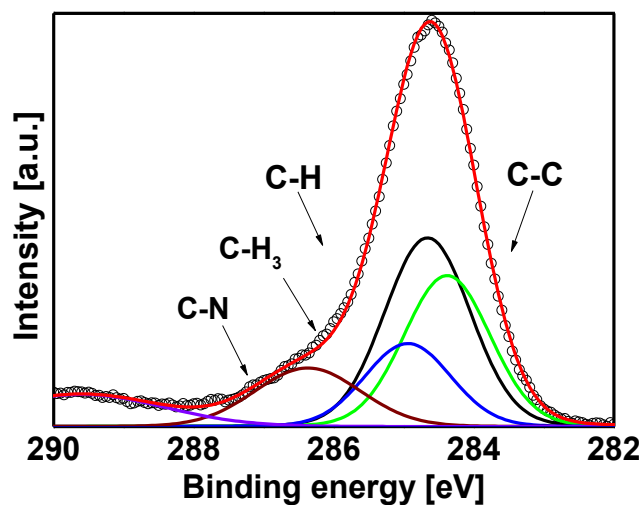
	Energy (eV)	Lorentzian Width (eV)	Gaussian Width (eV)	Intensity (%)
<b>C-C</b>	284.50	0.08	0.96	31.47
<b>C-H</b>	284.78	0.08	0.96	39.26
<b>CH<sub>3</sub></b>	285.06	0.08	0.96	17.28
<b>C-N</b>	286.49	0.08	1.19	11.98



**Figure A.16:** C 1s core level spectrum of nominally 0.5 nm NitPyn deposited on TiO<sub>2</sub>(110) single crystal (excitation energy = 1000 eV).

**Table A.16:** Binding energy of the different components of the C 1s core level spectrum and shake-up satellites of nominally 0.5 nm NitPyn deposited on TiO<sub>2</sub>(110) single crystal (excitation energy = 1000 eV).

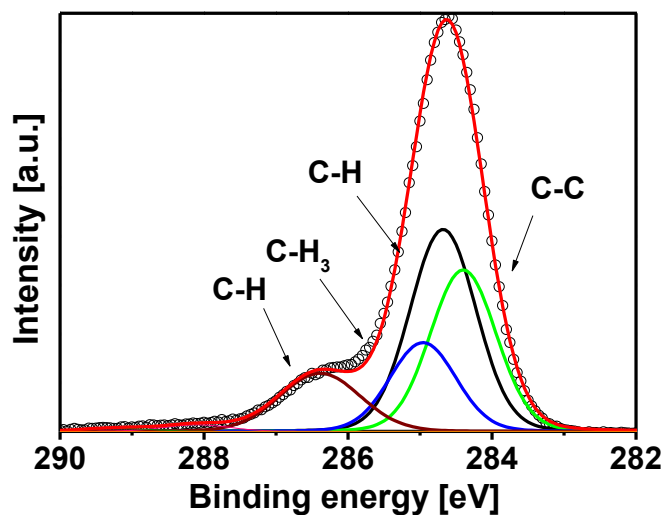
	Energy (eV)	Lorentzian Width (eV)	Gaussian Width (eV)	Intensity (%)
<b>C-C</b>	284.40	0.08	1.47	31.30
<b>C-H</b>	284.68	0.08	1.47	39.10
<b>CH<sub>3</sub></b>	284.96	0.08	1.47	17.20
<b>C-N</b>	286.39	0.08	1.82	12.40



**Figure A.17:** C 1s core level spectrum of nominally 0.5 nm NitPyn deposited on TiO<sub>2</sub>(110) single crystal (excitation energy = 640 eV).

**Table A.17:** Binding energy of the different components of the C 1s core level spectrum and shake-up satellites of nominally 0.5 nm NitPyn deposited on TiO<sub>2</sub>(110) single crystal (excitation energy = 640 eV).

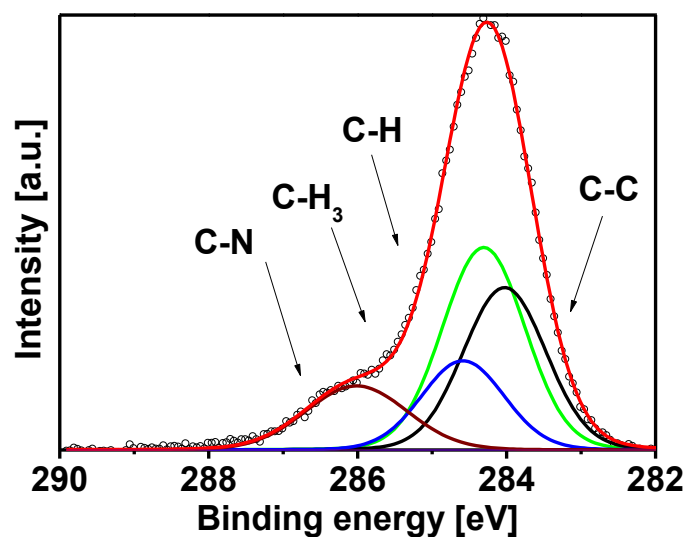
	Energy (eV)	LorentzianWidth (eV)	GaussianWidth (eV)	Intensity (%)
<b>C-C</b>	284.40	0.08	1.40	27.20
<b>C-H</b>	284.68	0.08	1.40	34.00
<b>CH<sub>3</sub></b>	285.96	0.08	1.40	14.95
<b>C-N</b>	286.39	0.08	1.73	12.51



**Figure A.18:** C 1s core level spectrum of nominally 0.5 nm NitPyn deposited on TiO<sub>2</sub>(110) single crystal (excitation energy = 330 eV).

**Table A.18:** Binding energy of the different components of the C 1s core level spectrum and shake-up satellites of nominally 0.5 nm NitPyn deposited on TiO<sub>2</sub>(110) single crystal (excitation energy = 330 eV).

	Energy (eV)	LorentzianWidth (eV)	GaussianWidth (eV)	Intensity (%)
<b>C-C</b>	284.40	0.08	1.03	30.26
<b>C-H</b>	284.68	0.08	1.03	37.93
<b>CH<sub>3</sub></b>	285.96	0.08	1.03	16.66
<b>C-N</b>	286.39	0.08	1.28	13.32

NitPyn deposited on SiO<sub>2</sub>/ Si(111)

**Figure A.19:** C 1s core level spectrum of nominally 6 nm NitPyn deposited on SiO<sub>2</sub>/Si(111) (excitation energy = 1000 eV).

**Table A.19:** Binding energy of the different components of the C 1s core level spectrum and shake-up satellites of nominally 6 nm NitPyn deposited on SiO<sub>2</sub>/Si(111) (excitation energy = 1000 eV).

	Energy (eV)	LorentzianWidth (eV)	GaussianWidth (eV)	Intensity (%)
C-C	284.02	0.08	1.26	30.53
C-H	284.30	0.08	1.26	38.00
CH <sub>3</sub>	284.58	0.08	1.26	16.56
C-N	286.01	0.08	1.56	14.71

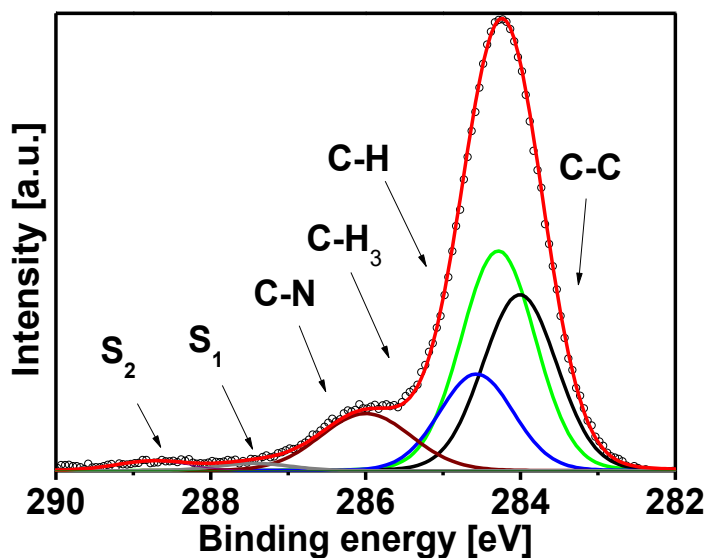


**Figure A.20:** C 1s core level spectrum of nominally 6 nm NitPyn deposited on SiO<sub>2</sub>/Si(111) (excitation energy = 640 eV).

**Table A.20:** Binding energy of the different components of the C 1s core level spectrum and shake-up satellites of nominally 6 nm NitPyn deposited on SiO<sub>2</sub>/Si(111) (excitation energy = 640 eV).

	Energy (eV)	LorentzianWidth (eV)	Gaussian Width (eV)	Intensity (%)
<b>C-C</b>	284.02	0.08	1.08	31.39
<b>C-H</b>	284.30	0.08	1.08	39.32
<b>CH<sub>3</sub></b>	284.58	0.08	1.08	17.26
<b>C-N</b>	286.01	0.08	1.34	12.03

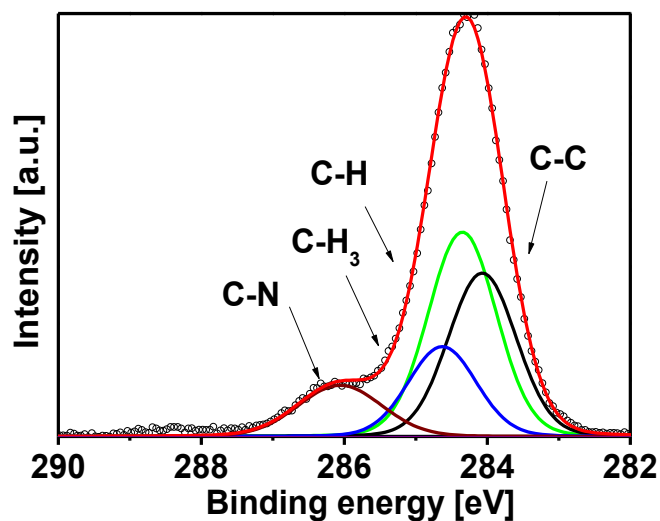


**Figure A.21:** C 1s core level spectrum of nominally 6 nm NitPyn deposited on SiO<sub>2</sub>/Si(111) (excitation energy = 330 eV).

**Table A.21:** Binding energy of the different components of the C 1s core level spectrum and shake-up satellites of nominally 6 nm NitPyn deposited on SiO<sub>2</sub>/Si(111) (excitation energy = 330 eV).

	<b>Energy (eV)</b>	<b>Lorentzian Width (eV)</b>	<b>Gaussian Width (eV)</b>	<b>Intensity (%)</b>
<b>C-C</b>	284.02	0.08	1.08	31.39
<b>C-H</b>	284.30	0.08	1.08	39.32
<b>CH<sub>3</sub></b>	284.58	0.08	1.08	17.26
<b>C-N</b>	286.01	0.08	1.34	12.03

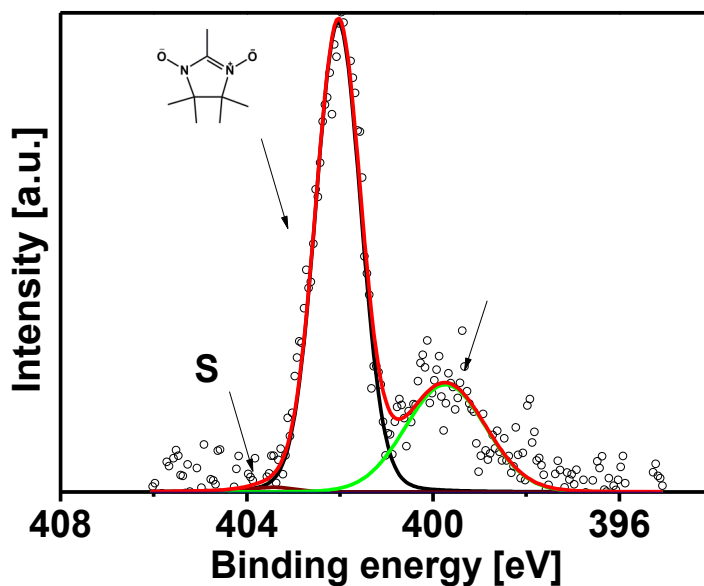


**Figure A.22:** N 1s core level spectrum of nominally 6 nm NitPyn deposited on SiO<sub>2</sub>/Si(111) (excitation energy = 640 eV).

**Table A.22:** Binding energy of the different components of the N 1s core level spectrum and shake-up satellites of nominally 6 nm NitPyn deposited on SiO<sub>2</sub>/Si(111) (excitation energy = 640 eV).

	Energy (eV)	LorentzianWidth (eV)	GaussianWidth (eV)	Intensity (%)
C-N	402.04	0.1	1.09	70.81
S	403.44	0.1	1.09	1.00

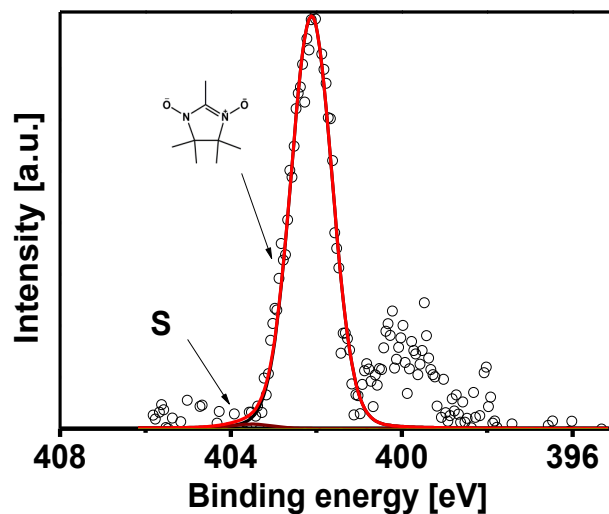


**Figure A.23:** C 1s core level spectrum of nominally 6 nm NitPyn deposited on SiO<sub>2</sub>/Si(111) (excitation energy = 1000 eV).

**Table A.23:** Binding energy of the different components of the C 1s core level spectrum and shake-up satellites of nominally 6 nm NitPyn deposited on SiO<sub>2</sub>/Si(111) (excitation energy = 1000 eV).

	Energy (eV)	LorentzianWidth (eV)	GaussianWidth (eV)	Intensity (%)
C-N	402.04	0.1	1.09	70.81
S	403.44	0.1	1.09	1.00

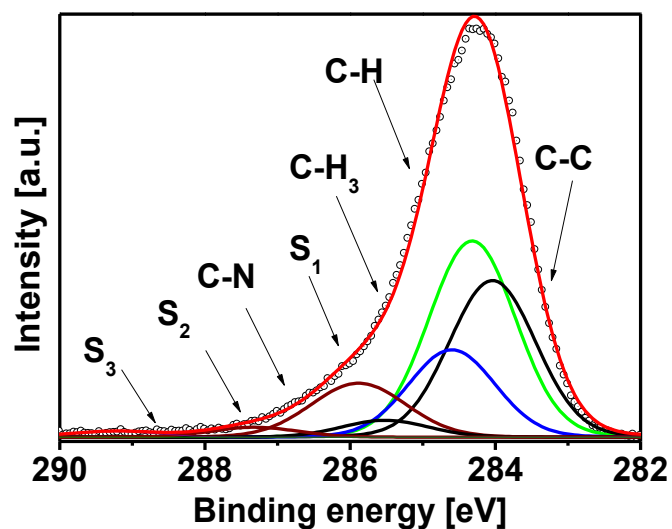


**Figure A.24:** C 1s core level spectrum of nominally 15 nm NitPyn deposited on SiO<sub>2</sub>/Si(111) (excitation energy = 330 eV).

**Table A.24:** Binding energy of the different components of the C 1s core level spectrum and shake-up satellites of nominally 15 nm NitPyn deposited on SiO<sub>2</sub>/Si(111) (excitation energy = 330 eV).

	Energy (eV)	Lorentzian Width (eV)	Gaussian Width (eV)	Intensity (%)
<b>C-C</b>	284.02	0.08	1.36	29.46
<b>C-H</b>	284.30	0.08	1.36	36.90
<b>CH<sub>3</sub></b>	284.58	0.08	1.36	16.43
<b>C-N</b>	286.01	0.08	1.47	11.12
<b>S<sub>1</sub></b>	285.50	0.08	1.36	3.17
<b>S<sub>2</sub></b>	287.30	0.08	1.47	1.86
<b>S<sub>3</sub></b>	289.30	0.08	1.36	1.06

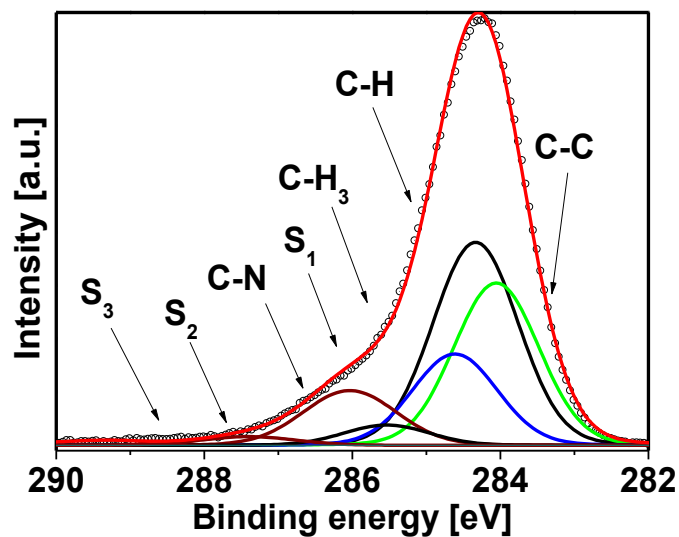


**Figure A.25:** C 1s core level spectrum of nominally 15 nm NitPyn deposited on SiO<sub>2</sub>/Si(111) (excitation energy = 640 eV).

**Table A.25:** Binding energy of the different components of the C 1s core level spectrum and shake-up satellites of nominally 15 nm NitPyn deposited on SiO<sub>2</sub>/Si(111) (excitation energy = 640 eV).

	Energy (eV)	Lorentzian Width (eV)	Gaussian Width (eV)	Intensity (%)
C-C	284.02	0.08	1.30	29.43
C-H	284.30	0.08	1.30	36.87
CH <sub>3</sub>	284.58	0.08	1.30	16.56
C-N	286.00	0.08	1.44	10.89
S <sub>1</sub>	285.50	0.08	1.30	3.70
S <sub>2</sub>	287.30	0.08	1.44	1.73
S <sub>3</sub>	289.30	0.08	1.30	0.83

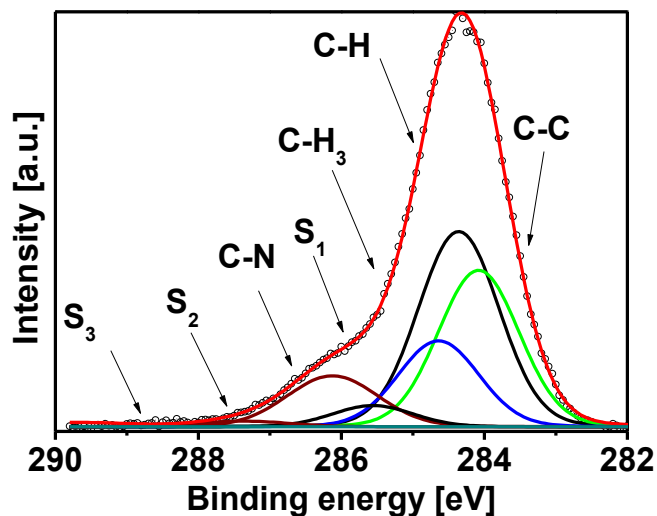


**Figure A.26:** C 1s core level spectrum of nominally 15 nm NitPyn deposited on SiO<sub>2</sub>/Si(111) (excitation energy = 1000 eV).

**Table A.26:** Binding energy of the different components of the C 1s core level spectrum and shake-up satellites of nominally 15 nm NitPyn deposited on SiO<sub>2</sub>/Si(111) (excitation energy = 1000 eV).

	Energy (eV)	Lorentzian Width (eV)	Gaussian Width (eV)	Intensity (%)
C-C	284.02	0.08	1.29	29.81
C-H	284.30	0.08	1.29	37.19
CH <sub>3</sub>	284.58	0.08	1.29	16.36
C-N	286.00	0.08	1.66	10.89
S <sub>1</sub>	285.50	0.08	1.29	4.03
S <sub>2</sub>	287.30	0.08	1.66	1.20
S <sub>3</sub>	289.30	0.08	1.29	0.53

**Figure A.27:** N 1s core level spectrum of nominally 15 nm NitPyn deposited on SiO<sub>2</sub>/Si(111) (excitation energy = 640 eV).

**Table A.27:** Binding energy of the different components of the C 1s core level spectrum and shake-up satellites of nominally 15 nm NitPyn deposited on SiO<sub>2</sub>/Si(111) (excitation energy = 640 eV).

	<b>Energy</b> (eV)	<b>LorentzianWidth</b> (eV)	<b>GaussianWidth</b> (eV)	<b>Intensity</b> (%)
<b>C-N</b>	402.04	0.1	1.29	88.55
<b>S</b>	403.44	0.1	1.29	11.45

**Figure A.28:** N 1s core level spectrum of nominally 15 nm NitPyn deposited on SiO<sub>2</sub>/Si(111) (excitation energy = 1000 eV).

**Table A.28:** Binding energy of the different components of the N 1s core level spectrum and shake-up satellites of nominally 15 nm NitPyn deposited on SiO<sub>2</sub>/Si(111) (excitation energy = 1000 eV).

	<b>Energy</b> (eV)	<b>LorentzianWidth</b> (eV)	<b>GaussianWidth</b> (eV)	<b>Intensity</b> (%)
<b>C-N</b>	402.04	0.1	1.54	94.97
<b>S</b>	403.44	0.1	1.54	5.03

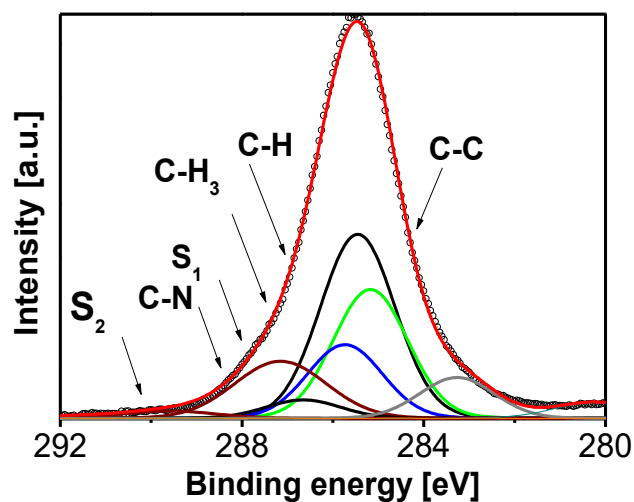
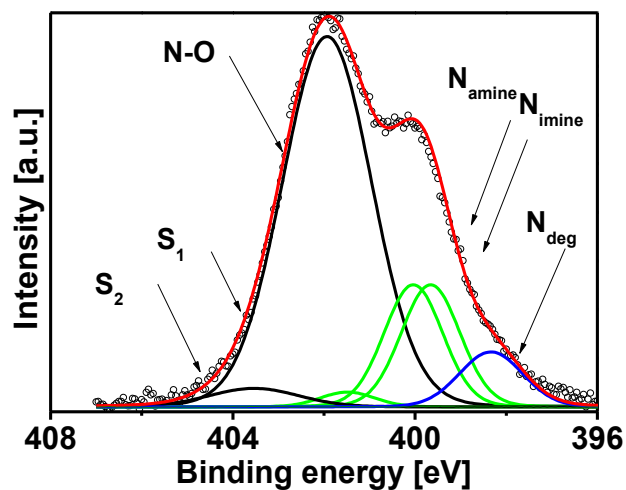
PPN deposited on TiO<sub>2</sub>(110) single crystal

Figure A.29: C 1s core level spectrum of PPN powder

Table A.29: Binding energy of the different components of PPN powder

	Energy (eV)	Lorentzian Width (eV)	Gaussian Width (eV)	Intensity (%)
<b>C-C</b>	285.36	0.08	1.90	23.68
<b>C-H</b>	285.74	0.08	1.90	33.75
<b>CH<sub>3</sub></b>	286.02	0.08	1.90	13.52
<b>C-N</b>	287.45	0.08	2.35	12.68
<b>S<sub>1</sub></b>	286.94	0.08	1.90	3.38
<b>S<sub>2</sub></b>	289.75	0.08	2.35	1.68



**Figure A.30:** N 1s core level spectrum of PPN powder

**Table A.30:** Binding energy of the different components of the N 1s core level spectrum and shake-up satellites of PPN powder.

	Energy (eV)	Lorentzian Width (eV)	Gaussian Width (eV)	Intensity (%)
N-O	402.17	0.1	2.25	61.80
N <sub>1</sub>	400.28	0.1	1.46	13.50
N <sub>2</sub>	399.78	0.1	1.46	13.50
N <sub>deg</sub>	398.58	0.1	1.58	6.53
S <sub>1</sub>	401.72	0.1	1.46	1.52
S <sub>2</sub>	402.67	0.1	2.25	3.10

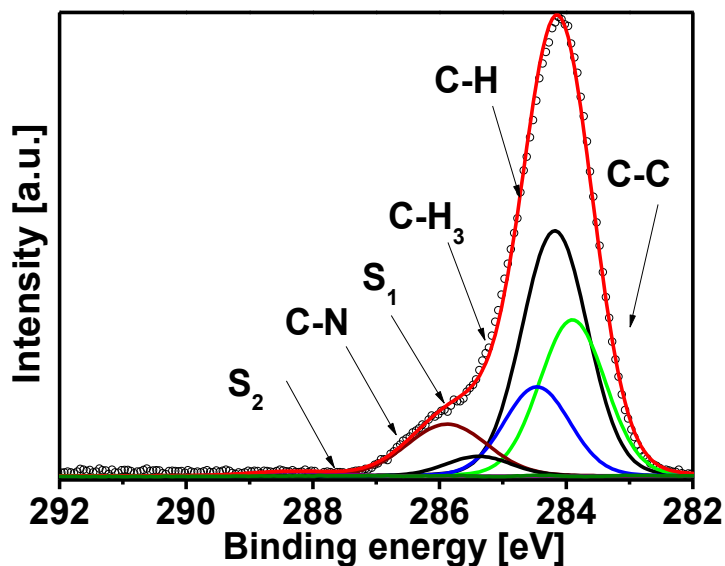


**Figure A.31:** C 1s core level spectrum of nominally 0.5 nm PPN deposited on TiO<sub>2</sub>(110) single crystal (excitation energy = 640 eV).

**Table A.31:** Binding energy of the different components of the N 1s core level spectrum and shake-up satellites of nominally 2.3 nm NitPyn deposited on TiO<sub>2</sub>(110) single crystal (excitation energy = 1000 eV).

	Energy (eV)	Lorentzian Width (eV)	Gaussian Width (eV)	Intensity (%)
C-C	283.90	0.08	1.18	27.01
C-H	284.18	0.08	1.18	42.39
C-H <sub>3</sub>	285.56	0.08	1.18	15.41
C-N	285.89	0.08	1.45	10.94
S <sub>1</sub>	285.38	0.08	1.18	3.39
S <sub>2</sub>	288.33	0.08	1.45	1.00

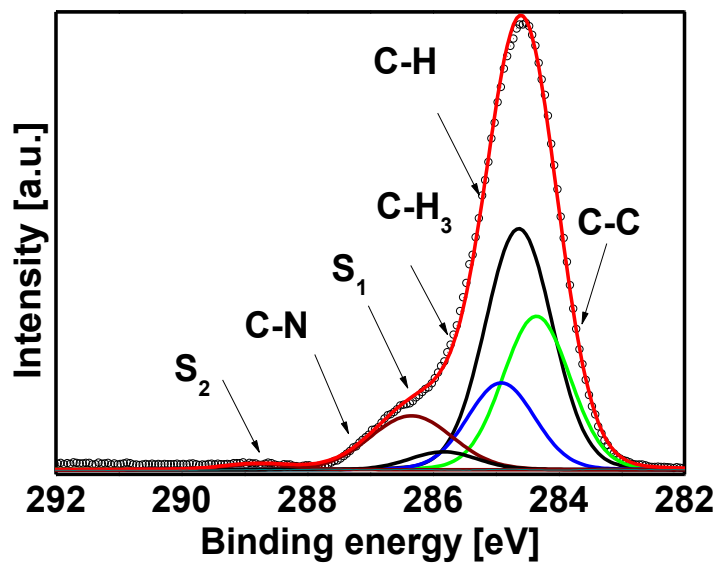


**Figure A.32:** C 1s core level spectrum of nominally 6 nm PPN deposited on TiO<sub>2</sub>(110) single crystal.

**Table A.32:** Binding energy of the different components of the C 1s core level spectrum and shake-up satellites of nominally 6 nm PPN deposited on TiO<sub>2</sub>(110) single crystal.

	Energy (eV)	Lorentzian Width (eV)	Gaussian Width (eV)	Intensity (%)
C-C	284.36	0.08	1.21	26.88
C-H	284.64	0.08	1.21	42.26
C-H <sub>3</sub>	286.02	0.08	1.21	15.19
C-N	286.35	0.08	1.49	11.55
S <sub>1</sub>	285.84	0.08	1.21	3.13
S <sub>2</sub>	288.80	0.08	1.49	1.00

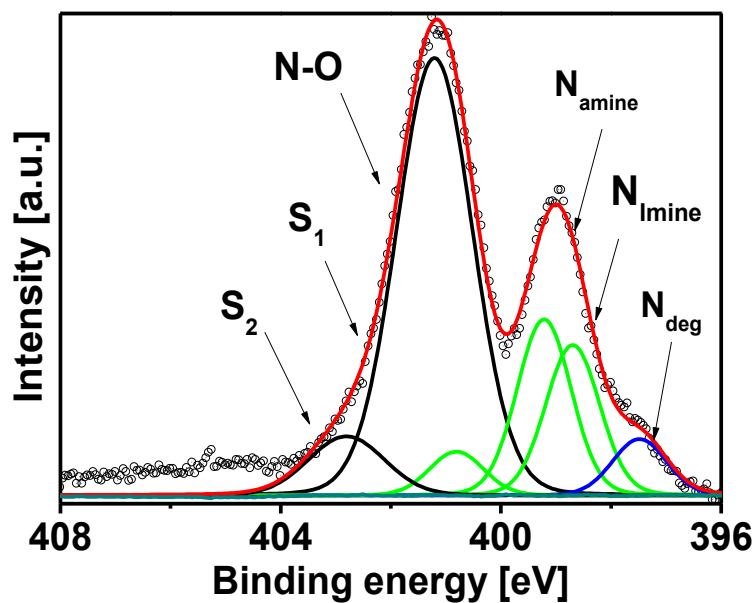


**Figure A.33:** N 1s core level spectrum of nominally 6 nm PPN deposited on TiO<sub>2</sub>(110) single crystal.

**Table A.33:** Binding energy of the different components of the N 1s core level spectrum and shake-up satellites of nominally 6 nm PPN deposited on TiO<sub>2</sub>(110) single crystal.

	Energy (eV)	Lorentzian Width (eV)	Gaussian Width (eV)	Intensity (%)
N-O	401.22	0.1	1.61	54.65
N <sub>2</sub>	399.23	0.1	1.13	15.08
N <sub>1</sub>	398.71	0.1	1.13	14.08
N <sub>deg</sub>	397.50	0.1	1.13	4.42
S <sub>1</sub>	400.82	0.1	1.13	4.70
S <sub>2</sub>	402.82	0.1	1.61	7.06

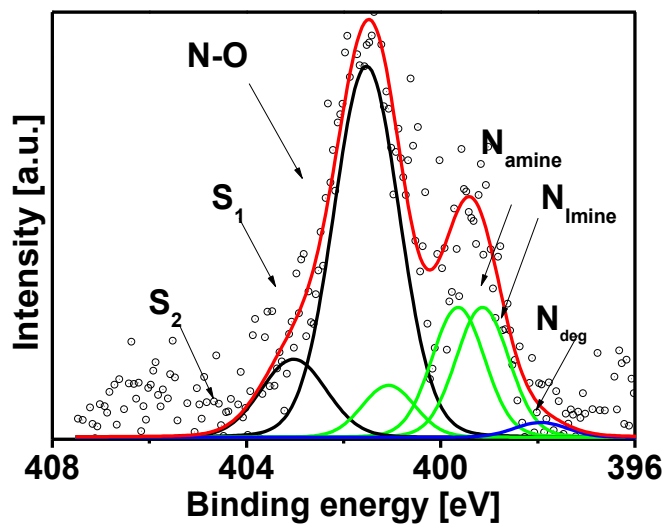


**Figure A.34:** N 1s core level spectrum of nominally 0.5 nm PPN deposited on SiO<sub>2</sub>/Si(111) .

**Table A.34:** Binding energy of the different components of the N 1s core level spectrum and shake-up satellites of nominally 0.5 nm PPN deposited on SiO<sub>2</sub>/Si(111) .

	Energy (eV)	Lorentzian Width (eV)	Gaussian Width (eV)	Intensity (%)
<b>N-O</b>	401.53	0.1	1.49	50.94
<b>N<sub>2</sub></b>	399.64	0.1	1.20	16.39
<b>N<sub>1</sub></b>	399.14	0.1	1.20	16.39
<b>N<sub>deg</sub></b>	397.94	0.1	1.20	2.05
<b>S<sub>1</sub></b>	400.09	0.1	1.20	5.74
<b>S<sub>2</sub></b>	403.13	0.1	1.49	8.94

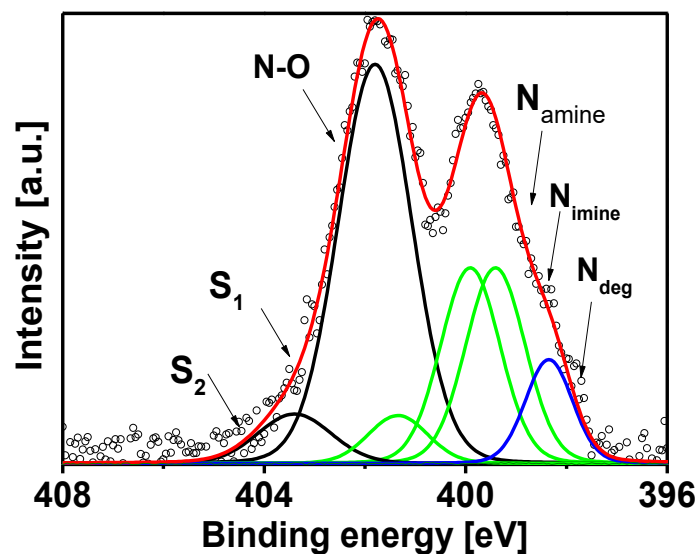


**Figure A.35:** N 1s core level spectrum of nominally 2 nm PPN deposited on SiO<sub>2</sub>/Si(111) .

**Table A.35:** Binding energy of the different components of the N 1s core level spectrum and shake-up satellites of nominally 2 nm PPN deposited on SiO<sub>2</sub>/Si(111) .

	Energy (eV)	Lorentzian Width (eV)	Gaussian Width (eV)	Intensity (%)
<b>N-O</b>	401.73	0.1	1.67	45.79
<b>N<sub>2</sub></b>	399.84	0.1	1.33	18.19
<b>N<sub>1</sub></b>	399.24	0.1	1.33	18.19
<b>N<sub>deg</sub></b>	397.94	0.1	1.05	7.71
<b>S<sub>1</sub></b>	400.09	0.1	1.33	4.46
<b>S<sub>2</sub></b>	403.13	0.1	1.67	5.66

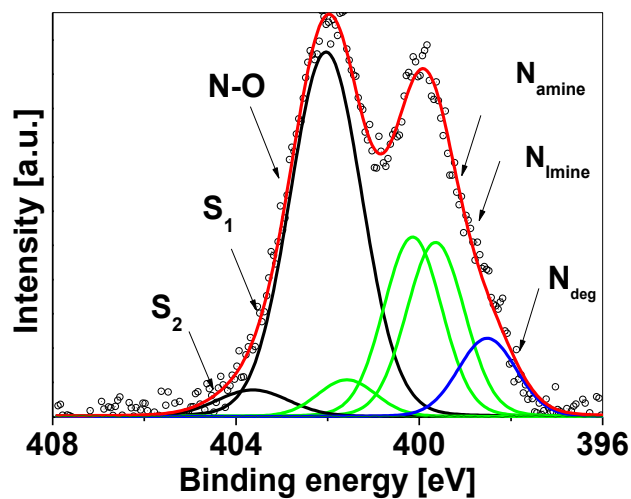


**Figure A.36:** N 1s core level spectrum of nominally 5 nm PPN deposited on SiO<sub>2</sub>/Si(111) .

**Table A.36:** Binding energy of the different components of the N 1s core level spectrum and shake-up satellites of nominally 5 nm PPN deposited on SiO<sub>2</sub>/Si(111) .

	Energy (eV)	Lorentzian Width (eV)	Gaussian Width (eV)	Intensity (%)
<b>N-O</b>	402.04	0.1	1.79	47.31
<b>N<sub>2</sub></b>	400.15	0.1	1.44	18.88
<b>N<sub>1</sub></b>	399.65	0.1	1.44	18.31
<b>N<sub>deg</sub></b>	398.64	0.1	1.44	8.21
<b>S<sub>1</sub></b>	401.59	0.1	1.44	3.84
<b>S<sub>2</sub></b>	403.64	0.1	1.79	3.44

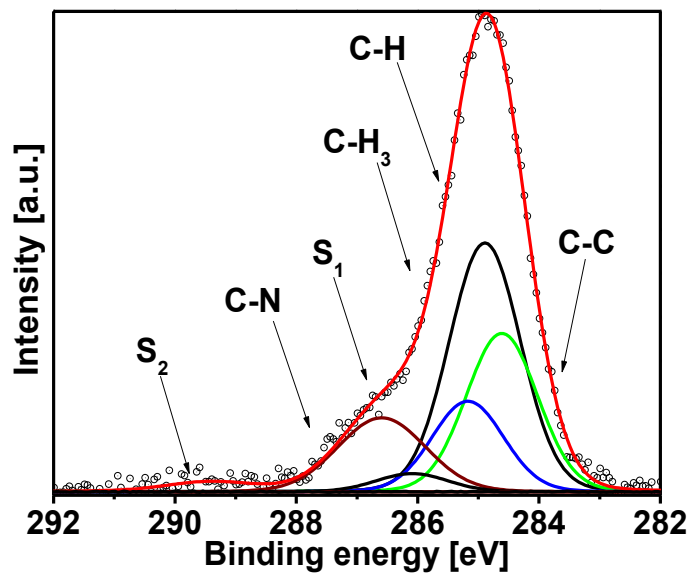


**Figure A.37:** C 1s core level spectrum of nominally 0.5 nm PPN deposited on SiO<sub>2</sub>/Si(111) .

**Table A.37:** Binding energy of the different components of the C 1s core level spectrum and shake-up satellites of nominally 0.5 nm PPN deposited on SiO<sub>2</sub>/Si(111) .

	Energy (eV)	Lorentzian Width (eV)	Gaussian Width (eV)	Intensity (%)
C-C	284.62	0.08	1.34	25.63
C-H	284.90	0.08	1.34	40.20
C-H <sub>3</sub>	285.18	0.08	1.34	14.64
C-N	286.61	0.08	1.66	14.62
S <sub>1</sub>	286.10	0.08	1.34	2.94
S <sub>2</sub>	289.05	0.08	1.66	1.91

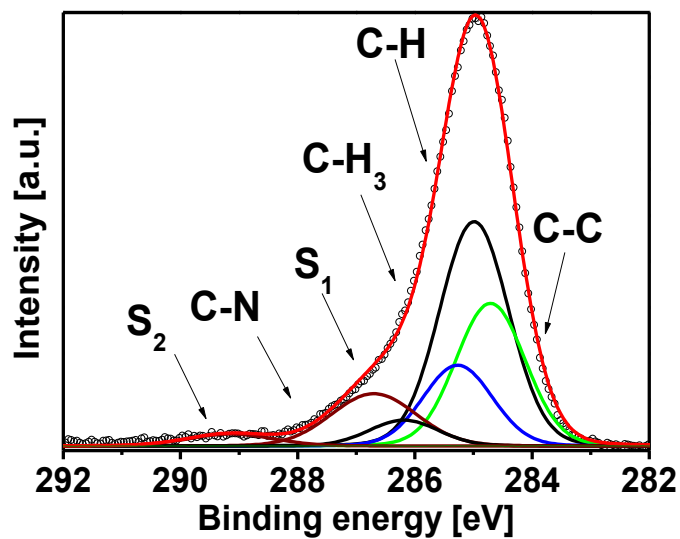


**Figure A.38:** C 1s core level spectrum of nominally 2 nm PPN deposited on SiO<sub>2</sub>/Si(111) .

**Table A.38:** Binding energy of the different components of the C 1s core level spectrum and shake-up satellites of nominally 2 nm PPN deposited on SiO<sub>2</sub>/Si(111) .

	Energy (eV)	Lorentzian Width (eV)	Gaussian Width (eV)	Intensity (%)
<b>C-C</b>	284.70	0.08	1.35	25.82
<b>C-H</b>	284.98	0.08	1.35	40.66
<b>C-H<sub>3</sub></b>	285.26	0.08	1.35	14.61
<b>C-N</b>	286.71	0.08	1.67	11.59
<b>S<sub>1</sub></b>	286.20	0.08	1.35	4.68
<b>S<sub>2</sub></b>	289.15	0.08	1.67	2.65

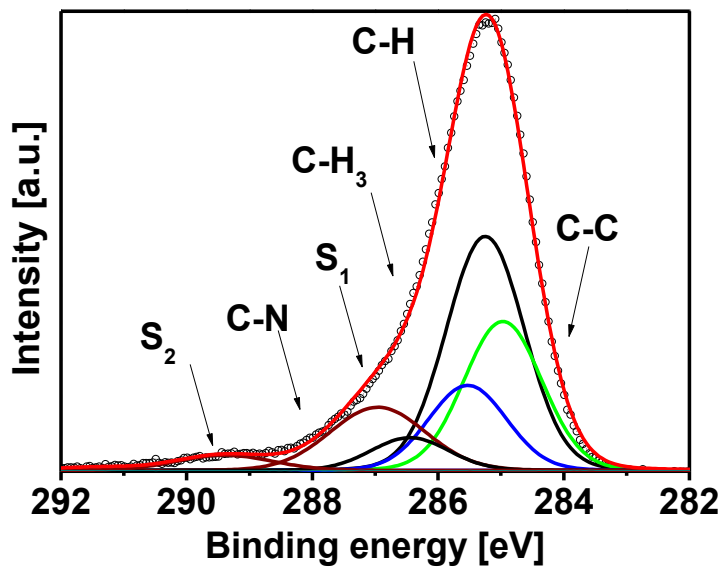


**Figure A.39:** C 1s core level spectrum of nominally 5 nm PPN deposited on SiO<sub>2</sub>/Si(111) .

**Table A.39:** Binding energy of the different components of the C 1s core level spectrum and shake-up satellites of nominally 5 nm PPN deposited on SiO<sub>2</sub>/Si(111) .

	Energy (eV)	Lorentzian Width (eV)	Gaussian Width (eV)	Intensity (%)
C-C	284.98	0.08	1.42	24.84
C-H	285.26	0.08	1.42	39.98
C-H <sub>3</sub>	285.54	0.08	1.34	14.18
C-N	286.97	0.08	1.75	12.91
S <sub>1</sub>	286.46	0.08	1.42	5.46
S <sub>2</sub>	289.41	0.08	1.75	3.12

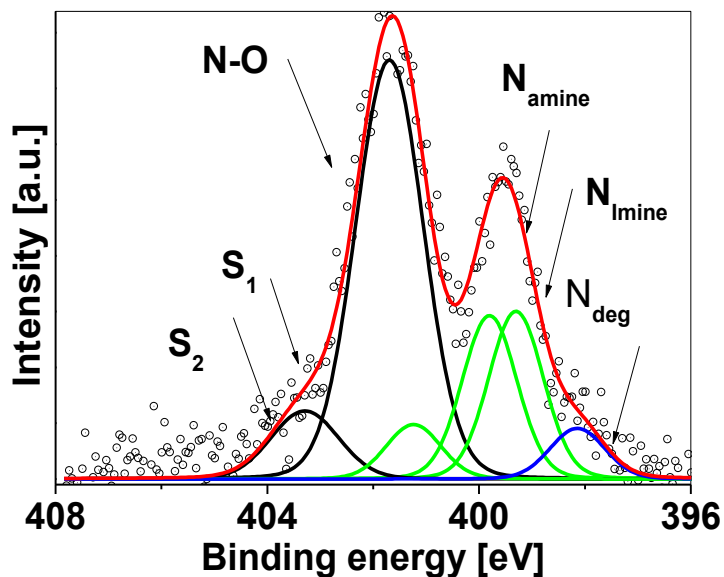


**Figure A.40:** N 1s core level spectrum (the first one) of nominally 5 nm PPN deposited on SiO<sub>2</sub>/Si(111) .

The sample was mounted in low vacuum for 30 min.

**Table A.40:** Binding energy of the different components of the N 1s core level spectrum and shake-up satellites (the first one) of nominally 5 nm PPN deposited on SiO<sub>2</sub>/Si(111) .

The sample was mounted in low vacuum for 30 min.

	Energy (eV)	Lorentzian Width (eV)	Gaussian Width (eV)	Intensity (%)
N-O	401.70	0.1	1.45	49.80
N <sub>1</sub>	399.81	0.1	1.16	15.78
N <sub>2</sub>	399.31	0.1	1.16	16.19
N <sub>deg</sub>	398.11	0.1	1.16	4.88
S <sub>2</sub>	401.25	0.1	1.16	5.26
S <sub>1</sub>	403.30	0.1	1.45	8.09

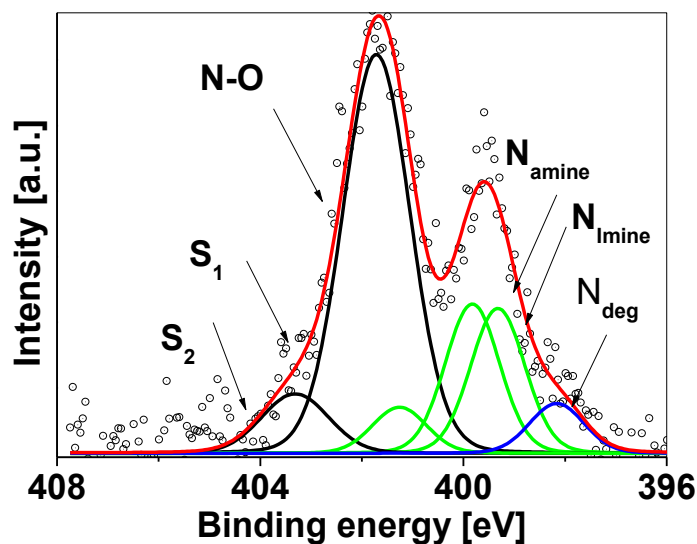


**Figure A.41:** N 1s core level spectrum (the last one) of nominally 5 nm PPN deposited on SiO<sub>2</sub>/Si(111) .

The sample was mounted in low vacuum for 30 min.

**Table A.41:** Binding energy of the different components of the N 1s core level spectrum and shake-up satellites (the last one) of nominally 5 nm PPN deposited on SiO<sub>2</sub>/Si(111) .

The sample was mounted in low vacuum for 30 min.

	Energy (eV)	Lorentzian Width (eV)	Gaussian Width (eV)	Intensity (%)
N-O	401.70	0.1	1.50	51.47
N <sub>1</sub>	399.81	0.1	1.20	15.65
N <sub>2</sub>	399.31	0.1	1.20	16.18
N <sub>deg</sub>	398.11	0.1	1.20	5.21
S <sub>1</sub>	401.25	0.1	1.20	4.82
S <sub>2</sub>	403.30	0.1	1.50	7.66

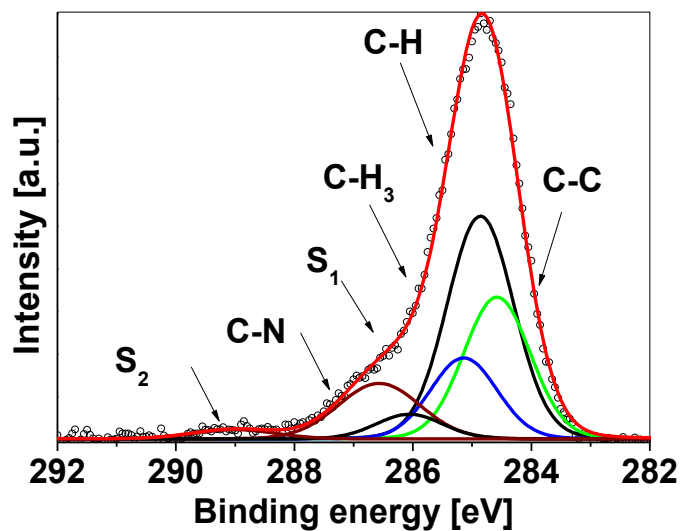


**Figure A.42:** C 1s core level spectrum (the first one) of nominally 4 nm PPN deposited on SiO<sub>2</sub>/Si(111) .

The sample was mounted in low vacuum for 30 min.

**Table A.42:** Binding energy of the different components of the C 1s core level spectrum and shake-up satellites (the first one) of nominally 4 nm PPN deposited on SiO<sub>2</sub>/Si(111) .

The sample was mounted in low vacuum for 30 min

	Energy (eV)	Lorentzian Width (eV)	Gaussian Width (eV)	Intensity (%)
<b>C-C</b>	284.55	0.08	1.28	25.81
<b>C-H</b>	284.83	0.08	1.28	40.51
<b>C-H<sub>3</sub></b>	285.11	0.08	1.28	14.73
<b>C-N</b>	286.54	0.08	1.58	12.38
<b>S<sub>1</sub></b>	286.03	0.08	1.28	4.49
<b>S<sub>2</sub></b>	288.98	0.08	1.58	2.07

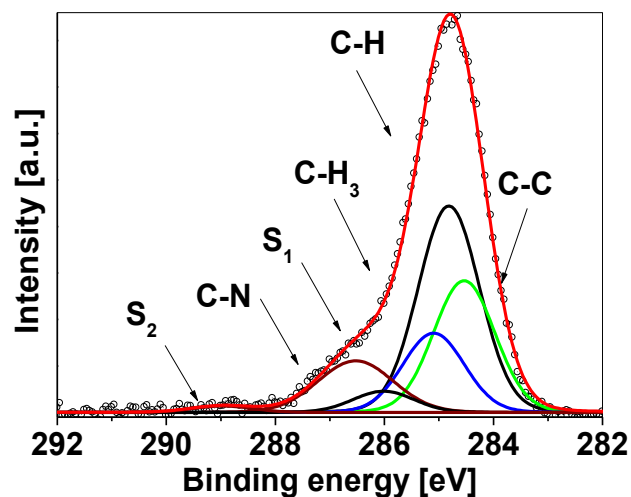


**Figure A.43:** C 1s core level spectrum (the first one) of nominally 4 nm PPN deposited on SiO<sub>2</sub>/Si(111) .

The sample was mounted in low vacuum for 30 min.

**Table A.43:** Binding energy of the different components of the C 1s core level spectrum and shake-up satellites (the first one) of nominally 4 nm PPN deposited on SiO<sub>2</sub>/Si(111) .

The sample was mounted in low vacuum for 30 min

	Energy (eV)	LorentzianWidth (eV)	GaussianWidth (eV)	Intensity (%)
<b>C-C</b>	284.55	0.08	1.28	25.94
<b>C-H</b>	284.83	0.08	1.28	40.58
<b>C-H<sub>3</sub></b>	285.11	0.08	1.28	15.61
<b>C-N</b>	286.54	0.08	1.58	12.43
<b>S<sub>1</sub></b>	286.03	0.08	1.28	4.18
<b>S<sub>2</sub></b>	288.98	0.08	1.58	1.26

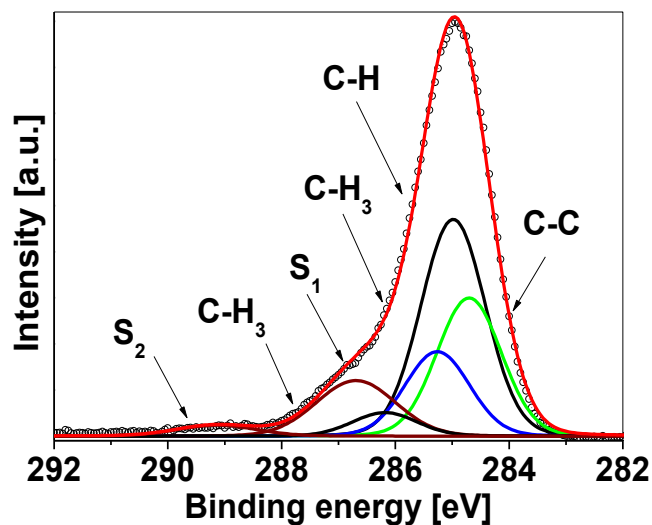


**Figure A.44:** C 1s core level spectrum (the last one) of nominally 4 nm PPN deposited on SiO<sub>2</sub>/Si(111) .

The sample was mounted in low vacuum for 30 min.

**Table A.44:** Binding energy of the different components of the C 1s core level spectrum and shake-up satellites (the last one) of nominally 4 nm PPN deposited on SiO<sub>2</sub>/Si(111) .

The sample was mounted in low vacuum for 30 min

	Energy (eV)	LorentzianWidth (eV)	GaussianWidth (eV)	Intensity (%)
<b>C-C</b>	284.55	0.08	1.28	25.38
<b>C-H</b>	284.83	0.08	1.28	39.84
<b>C-H<sub>3</sub></b>	285.11	0.08	1.28	15.53
<b>C-N</b>	286.54	0.08	1.58	12.49
<b>S<sub>1</sub></b>	286.03	0.08	1.28	4.33
<b>S<sub>2</sub></b>	288.98	0.08	1.58	2.44

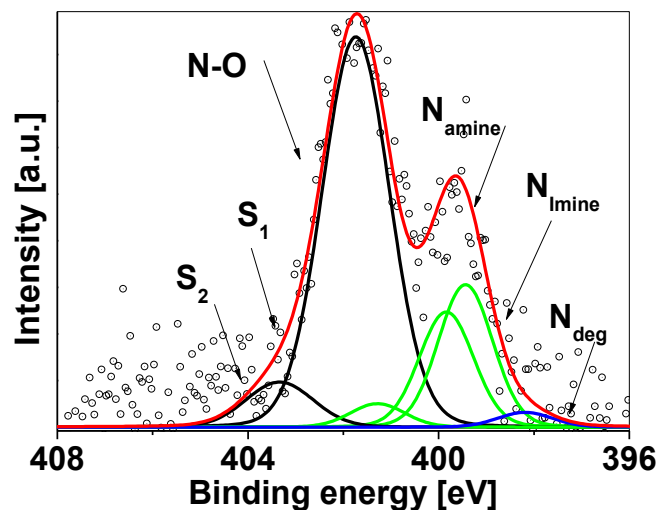


**Figure A.45:** N 1s core level spectrum (the first one) of nominally 1 nm PPN deposited on SiO<sub>2</sub>/Si(111) .

The sample was mounted in low vacuum for 30 min and in the air exposure for 25 h.

**Table A.45:** Binding energy of the different components of the N 1s core level spectrum and shake-up satellites (the first one) of nominally 1 nm PPN deposited on SiO<sub>2</sub>/Si(111) .

The sample was mounted in low vacuum for 30 min and in the air exposure for 25 h.

	Energy (eV)	Lorentzian Width (eV)	Gaussian Width (eV)	Intensity (%)
<b>N-O</b>	401.77	0.1	1.60	58.14
<b>N<sub>1</sub></b>	399.87	0.1	1.28	13.91
<b>N<sub>2</sub></b>	399.38	0.1	1.28	17.21
<b>N<sub>deg</sub></b>	398.18	0.1	1.28	1.70
<b>S<sub>1</sub></b>	401.32	0.1	1.28	2.36
<b>S<sub>2</sub></b>	403.37	0.1	1.60	6.68

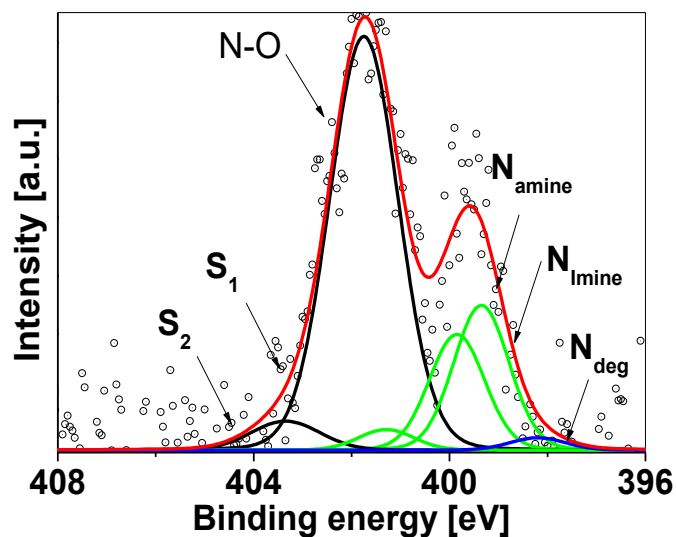


**Figure A.46:** N 1s core level spectrum (the last one) of nominally 1 nm PPN deposited on SiO<sub>2</sub>/Si(111) .

The sample was mounted in low vacuum for 30 min and in the air exposure for 25 h.

**Table A.46:** Binding energy of the different components of the N 1s core level spectrum and shake-up satellites (the last one) of nominally 1 nm PPN deposited on SiO<sub>2</sub>/Si(111) .

The sample was mounted in low vacuum for 30 min and in the air exposure for 25 h.

	Energy (eV)	LorentzianWidth (eV)	GaussianWidth (eV)	Intensity (%)
<b>N-O</b>	401.77	0.1	1.60	60.76
<b>N<sub>1</sub></b>	399.87	0.1	1.28	13.80
<b>N<sub>2</sub></b>	399.38	0.1	1.28	17.24
<b>N<sub>deg</sub></b>	398.18	0.1	1.28	1.48
<b>S<sub>1</sub></b>	401.32	0.1	1.28	2.36
<b>S<sub>2</sub></b>	403.37	0.1	1.60	6.68

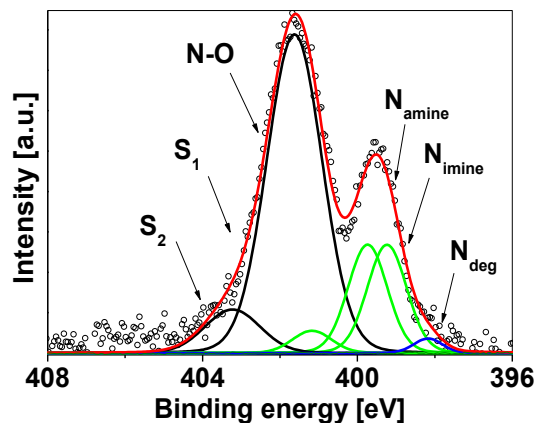


**Figure A.47:** N 1s core level spectrum (the added one) of nominally 1 nm PPN deposited on SiO<sub>2</sub>/Si(111)

The sample was mounted in low vacuum for 30 min and in the air exposure for 25 h.

**Table A.47:** Binding energy of the different components of the N 1s core level spectrum and shake-up satellites (the added one) of nominally 1 nm PPN deposited on SiO<sub>2</sub>/Si(111) .

The sample was mounted in low vacuum for 30 min and in the air exposure for 25 h.

	Energy (eV)	LorentzianWidth (eV)	GaussianWidth (eV)	Intensity (%)
<b>N-O</b>	401.77	0.1	1.63	58.89
<b>N<sub>1</sub></b>	399.88	0.1	1.14	14.36
<b>N<sub>2</sub></b>	399.38	0.1	1.14	14.34
<b>N<sub>deg</sub></b>	398.18	0.1	0.82	1.42
<b>S<sub>1</sub></b>	401.32	0.1	1.14	2.95
<b>S<sub>2</sub></b>	403.37	0.1	1.63	8.04

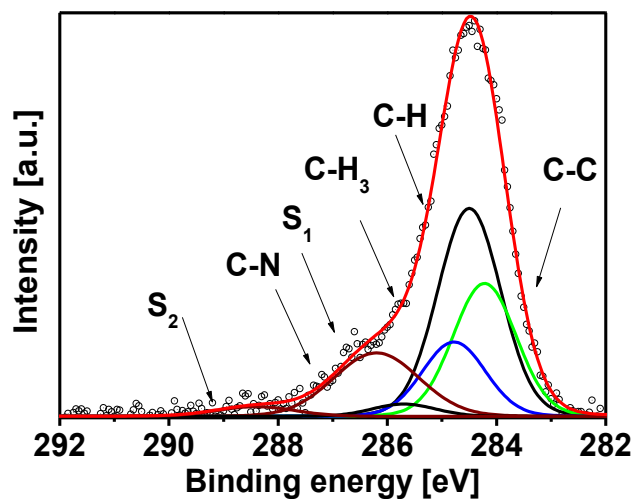


**Figure A.48:** C 1s core level spectrum (the first one) of nominally 1 nm PPN deposited on SiO<sub>2</sub>/Si(111) .

The sample was mounted in low vacuum for 30 min and in the air exposure for 25 h.

**Table A.48:** Binding energy of the different components of the C 1s core level spectrum and shake-up satellites (the first one) of nominally 1 nm PPN deposited on SiO<sub>2</sub>/Si(111) .

The sample was mounted in low vacuum for 30 min and in the air exposure for 25 h.

	Energy (eV)	LorentzianWidth (eV)	GaussianWidth (eV)	Intensity (%)
<b>C-C</b>	284.50	0.08	1.32	25.37
<b>C-H</b>	284.78	0.08	1.32	39.62
<b>C-H<sub>3</sub></b>	285.06	0.08	1.32	14.19
<b>C-N</b>	286.49	0.08	1.80	16.03
<b>S<sub>1</sub></b>	285.98	0.08	1.32	2.53
<b>S<sub>2</sub></b>	288.93	0.08	1.80	2.27

**Figure A.49:** C 1s core level spectrum (the last one) of nominally 1 nm PPN deposited on SiO<sub>2</sub>/Si(111) .

The sample was mounted in low vacuum for 30 min and in the air exposure for 25 h.

**Table A.49:** Binding energy of the different components of the C 1s core level spectrum and shake-up satellites (the last one) of nominally 1 nm PPN deposited on SiO<sub>2</sub>/Si(111) .

The sample was mounted in low vacuum for 30 min and in the air exposure for 25 h.

	<b>Energy (eV)</b>	<b>LorentzianWidth (eV)</b>	<b>GaussianWidth (eV)</b>	<b>Intensity (%)</b>
<b>C-C</b>	284.50	0.08	1.33	25.12
<b>C-H</b>	284.78	0.08	1.33	39.42
<b>C-H<sub>3</sub></b>	285.06	0.08	1.33	14.39
<b>C-N</b>	286.49	0.08	1.65	14.70
<b>S<sub>1</sub></b>	285.98	0.08	1.33	4.37
<b>S<sub>2</sub></b>	288.93	0.08	1.65	1.99

**Figure A.50:** C 1s core level spectrum (the added one) of nominally 1 nm PPN deposited on SiO<sub>2</sub>/Si(111)

The sample was mounted in low vacuum for 30 min and in the air exposure for 25 h.

**Table A.50:** Binding energy of the different components of the C 1s core level spectrum and shake-up satellites (the added one) of nominally 1 nm PPN deposited on SiO<sub>2</sub>/Si(111) .

The sample was mounted in low vacuum for 30 min and in the air exposure for 25 h.

	<b>Energy (eV)</b>	<b>LorentzianWidth (eV)</b>	<b>GaussianWidth (eV)</b>	<b>Intensity (%)</b>
<b>C-C</b>	284.50	0.08	1.31	25.15
<b>C-H</b>	284.78	0.08	1.31	39.40
<b>C-H<sub>3</sub></b>	285.06	0.08	1.31	14.35
<b>C-N</b>	286.49	0.08	1.84	14.91
<b>S<sub>1</sub></b>	285.98	0.08	1.33	4.13
<b>S<sub>2</sub></b>	288.93	0.08	1.84	2.05

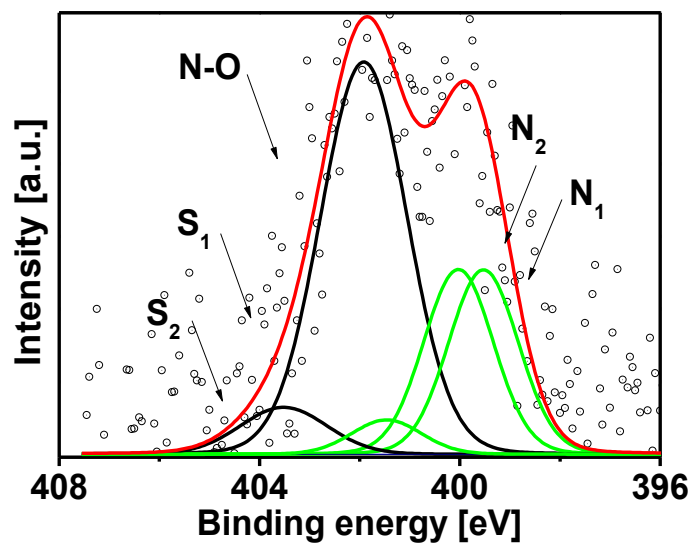


**Figure A.51:** N 1s core level spectrum of nominally 3 nm PPN deposited on SiO<sub>2</sub>/Si(111) (excitation energy = 640 eV).

**Table A.51:** Binding energy of the different components of the N 1s core level spectrum and shake-up satellites of nominally 3 nm PPN deposited on SiO<sub>2</sub>/Si(111) (excitation energy = 640 eV).

	Energy (eV)	LorentzianWidth (eV)	GaussianWidth (eV)	Intensity (%)
N-O	401.92	0.1	1.99	51.22
N <sub>1</sub>	400.03	0.1	1.59	19.53
N <sub>2</sub>	399.54	0.1	1.59	19.49
N <sub>deg</sub>	398.33	0.1	1.59	0.00
S <sub>1</sub>	401.47	0.1	1.59	3.63
S <sub>2</sub>	403.52	0.1	1.99	6.13

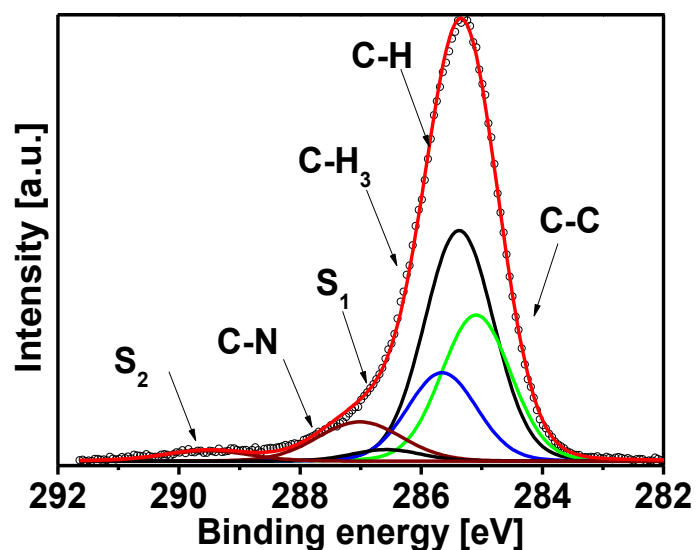


**Figure A.52:** C 1s core level spectrum of nominally 3 nm PPN deposited on SiO<sub>2</sub>/Si(111) (excitation energy = 330 eV).

**Table A.52:** Binding energy of the different components of the C 1s core level spectrum and shake-up satellites of nominally 3 nm PPN deposited on SiO<sub>2</sub>/Si(111) (excitation energy = 330 eV).

	Energy (eV)	Lorentzian Width (eV)	Gaussian Width (eV)	Intensity (%)
<b>C-C</b>	285.07	0.08	1.29	27.18
<b>C-H</b>	285.35	0.08	1.29	42.92
<b>C-H<sub>3</sub></b>	285.63	0.08	1.29	16.46
<b>C-N</b>	287.06	0.08	1.59	8.91
<b>S<sub>1</sub></b>	286.55	0.08	1.29	2.15
<b>S<sub>2</sub></b>	289.40	0.08	1.59	2.38

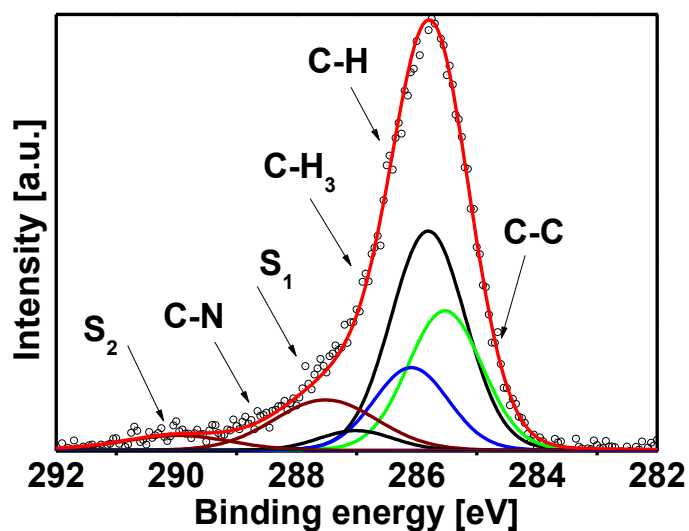


**Figure A.53:** C 1s core level spectrum of nominally 3 nm PPN deposited on SiO<sub>2</sub>/Si(111) (excitation energy = 640 eV).

**Table A.53:** Binding energy of the different components of the C 1s core level spectrum and shake-up satellites of nominally 3 nm PPN deposited on SiO<sub>2</sub>/Si(111) (excitation energy = 640 eV).

	Energy (eV)	LorentzianWidth (eV)	GaussianWidth (eV)	Intensity (%)
C-C	285.07	0.08	1.42	25.29
C-H	285.35	0.08	1.42	391
C-H <sub>3</sub>	285.63	0.08	1.42	14.99
C-N	287.06	0.08	1.98	12.61
S <sub>1</sub>	286.55	0.08	1.42	3.57
S <sub>2</sub>	289.40	0.08	1.98	3.82

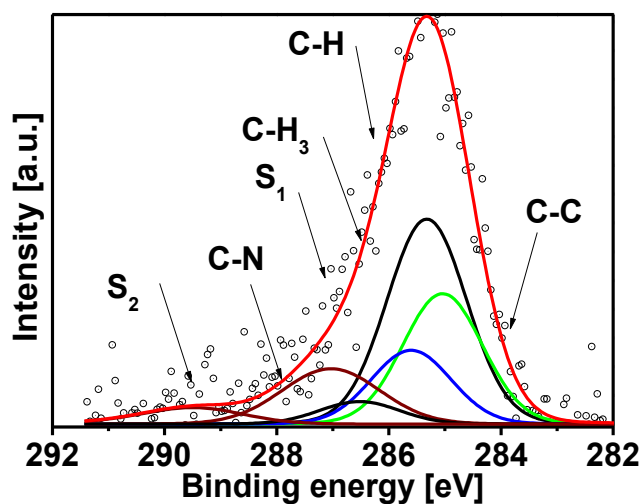


**Figure A.54:** C 1s core level spectrum of nominally 3 nm PPN deposited on SiO<sub>2</sub>/Si(111) (excitation energy = 1000 eV).

**Table A.54:** Binding energy of the different components of the C 1s core level spectrum and shake-up satellites of nominally 3 nm PPN deposited on SiO<sub>2</sub>/Si(111) (excitation energy = 1000 eV).

	Energy (eV)	Lorentzian Width (eV)	Gaussian Width (eV)	Intensity (%)
C-C	285.07	0.08	1.63	25.06
C-H	285.35	0.08	1.63	39.37
C-H <sub>3</sub>	285.63	0.08	1.63	14.19
C-N	287.06	0.08	2.02	13.04
S <sub>1</sub>	286.55	0.08	1.63	4.33
S <sub>2</sub>	289.40	0.08	2.02	4.00

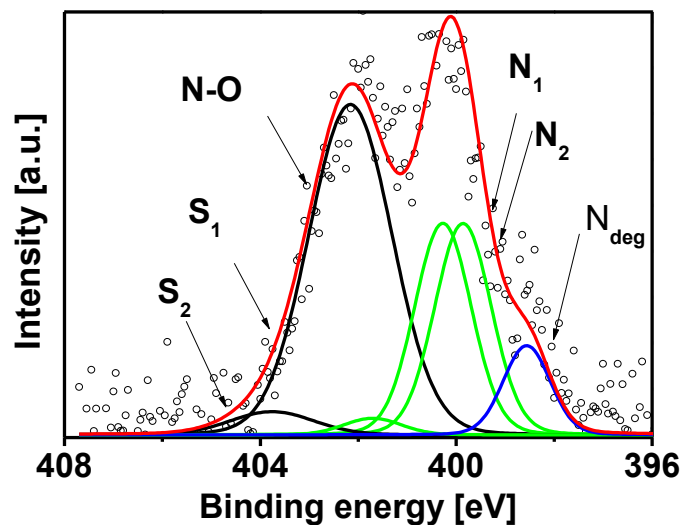


**Figure A.55:** N 1s core level spectrum of nominally 12 nm PPN deposited on SiO<sub>2</sub>/Si(111) (excitation energy = 640 eV).

**Table A.55:** Binding energy of the different components of the N 1s core level spectrum and shake-up satellites of nominally 12 nm PPN deposited on SiO<sub>2</sub>/Si(111) (excitation energy = 640 eV).

	Energy (eV)	Lorentzian Width (eV)	Gaussian Width (eV)	Intensity (%)
N-O	402.17	0.1	1.95	46.79
N <sub>1</sub>	400.28	0.1	1.31	20.55
N <sub>2</sub>	399.78	0.1	1.31	20.55
N <sub>deg</sub>	398.58	0.1	1.07	7.21
S <sub>1</sub>	401.72	0.1	1.54	1.63
S <sub>2</sub>	402.67	0.1	1.95	3.27

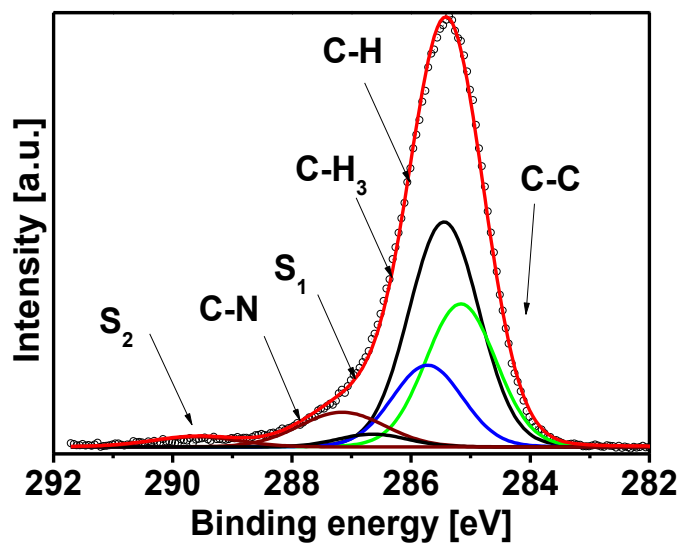


**Figure A.56:** C 1s core level spectrum of nominally 12 nm PPN deposited on SiO<sub>2</sub>/Si(111) (excitation energy = 330 eV).

**Table A.56:** Binding energy of the different components of the C 1s core level spectrum and shake-up satellites of nominally 12 nm PPN deposited on SiO<sub>2</sub>/Si(111) (excitation energy = 330 eV).

	Energy (eV)	Lorentzian Width (eV)	Gaussian Width (eV)	Intensity (%)
C-C	285.16	0.08	1.34	27.61
C-H	285.44	0.08	1.34	43.45
C-H <sub>3</sub>	285.72	0.08	1.34	15.80
C-N	287.15	0.08	1.66	8.21
S <sub>1</sub>	286.64	0.08	1.34	2.47
S <sub>2</sub>	289.45	0.08	1.66	2.45

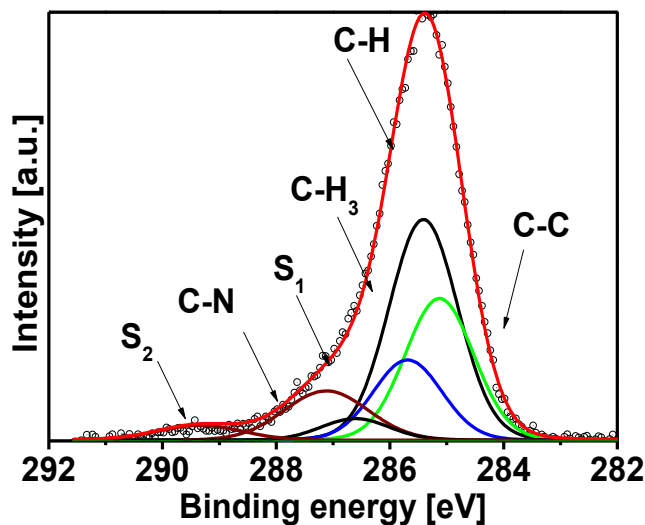


**Figure A.57:** C 1s core level spectrum of nominally 12 nm PPN deposited on SiO<sub>2</sub>/Si(111) (excitation energy = 330 eV).

**Table A.57:** Binding energy of the different components of the N 1s core level spectrum and shake-up satellites of nominally 12 nm PPN deposited on SiO<sub>2</sub>/Si(111) (excitation energy = 330 eV).

	Energy (eV)	Lorentzian Width (eV)	Gaussian Width (eV)	Intensity (%)
C-C	285.16	0.08	1.38	26.06
C-H	285.44	0.08	1.38	40.65
C-H <sub>3</sub>	285.72	0.08	1.38	14.77
C-N	287.15	0.08	1.70	11.11
S <sub>1</sub>	286.64	0.08	1.38	4.00
S <sub>2</sub>	289.45	0.08	1.70	3.50

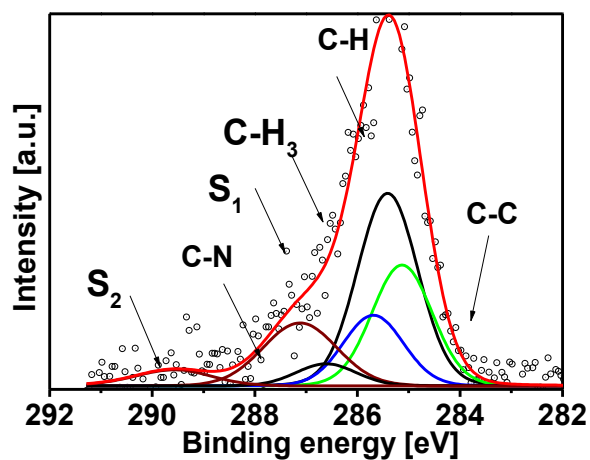


**Figure A.58:** C 1s core level spectrum of nominally 12 nm PPN deposited on SiO<sub>2</sub>/Si(111) (excitation energy = 1000 eV).

**Table A.58:** Binding energy of the different components of the C 1s core level spectrum and shake-up satellites of nominally 12 nm PPN deposited on SiO<sub>2</sub>/Si(111) (excitation energy = 1000 eV).

	Energy (eV)	Lorentzian Width (eV)	Gaussian Width (eV)	Intensity (%)
C-C	285.16	0.08	1.43	25.19
C-H	285.44	0.08	1.43	39.52
C-H <sub>3</sub>	285.72	0.08	1.43	14.39
C-N	287.15	0.08	1.77	12.54
S <sub>1</sub>	286.64	0.08	1.43	4.40
S <sub>2</sub>	289.45	0.08	1.77	4.03



# List of Publications

1. At the interface between organic radicals and TiO<sub>2</sub>(110) single crystals: electronic structure and paramagnetic character  
R. Kakavandi, S.-A. Savu, A. Caneschi, T. Chassé, M. B. Casu. *Chem. Communications*. 49, (2013), 10103-10105.
2. Paramagnetic Character in Thin Films of Organic Magnets Deposited on TiO<sub>2</sub>(110) Single Crystals  
R. Kakavandi, S.A. Savu, A. Caneschi, M. B. Casu. *J. Phys. Chem. C* 117, (2013), 26675-26679.
3. Core-Hole Screening, Electronic Structure, and Paramagnetic Character in Thin Films of Paramagnetic Metal-Free Organic Molecules Deposited on SiO<sub>2</sub>/Si(111)  
R. Kakavandi, S.A. Savu, L. Sorace, M. Mannini, T. Chassé, M. B. Casu. *J. Phys. Chem. C* 118, (2014), 8044-8049.
4. Electronic Structure of Thin Films of Metal Free Magnetic Fluorophore-Nitroxide Radicals: from Ultra High Vacuum to Air Exposure  
R. Kakavandi, P. Ravat, S.-A. Savu, Y. B. Borozdina M. Baumgarten, M. B. Casu. *ACS Applied Materials & Interfaces* 7-3, (2015), 1685-1692.



# Credits

Dr. L.Sorace, and, M.Mannini performed EPR characterizations, which are described in Section 4.4 and 4.5.

Prof. M. Baumgarten, P. Ravat and Y. B. Borozdina performed have done EPR characterization, which are described in Section 4.6 and 4.7.

All AFM images are measured out by S.A Savu. She also joined the beam time at BESSY II

All NEXAFS spectra shown in this work are evaluated and normalized by PD. Dr. Maria Benedetta Casu. Dr. Casu also joined the beam time at BESSY II.



# Acknowledgements

For all those who have contributed to the success of this work, I have an opportunity to thank you cordially.

First, I would like to express my gratitude thanks to PD. Dr. Maria Benedetta Casu to give me the opportunity to work in the framework of her DFG project (CA 852 / 5-1) and listen to my questions and for the thousand time correcting without comment - almost. The discussions with her have been very constructive and I have always been very motivated, even when they have turned a hundred times in a circle. Her interest in my work has inspired me further.

A great thank you is addressed to Prof. Thomas Chassé for the opportunity to access his photoelectron lab at the Institute of Physical and Theoretical Chemistry and for helpful discussions.

My sincere thanks go to Mr. Wolfgang Neu and Mrs. Elke Nadler for technical supports

I would like to thank Deutsche Forschungs gemeinschaft (DFG) under the contract number CA 852/5-1 and Helmholtz-Zentrum Berlin für Materialien und Energie (HZB) for funding the projects which I was involved in during three years.

I particularly thank all my colleagues, current and former for their help in numerous aspects, for creating a friendly atmosphere and for the good times shared in and outside the laboratory.

I would like to thank all my friends for their help and moral support during these years: Mohammad Soltanabadi, Kazem Abdolsamadi, Roozbeh Shokri, Reza Safari and Khosrow Rahimi.

I am deeply and forever indebted to my family and my wife for their love, support and encouragement throughout my entire life.



# Curriculum Vitae

Name	Reza Kakavandi
Date of birth	30.08.1978
Place of birth	Kermanshah, Iran
Nationality	Iranian

## Ph.D.

11/2011 - /2015	Research Assistant Institute of Theoretical and Physical Chemistry, University of Tuebingen, Tuebingen, Germany
08/2010 - 11/2011	Research Assistant, Freiburger Materialforschungszentrums Freiburg, Germany

## University Education

2003 - 2007	M.Sc., Solid State Physics, University of Razi, Kermanshah, Iran.
1998 - 2003	B.Sc., Physics, University of Bu-Ali Sina Hamedan, Iran.

## School education

1993 – 1997	High school, Mathematics and Physics, Kermanshah, Iran
1990 – 1993	Middle school, Kermanshah, Iran
1985 – 1990	Primary school, Kermanshah, Iran